

nature

HEAD TO HEAD

Were *Homo habilis*
and *Homo erectus*
contemporaries?

WAVEPOWER
How cilia make
your body work

**DRUG
REDISCOVERY**
Scanning the
back catalogue

X-RAY HOLOGRAPHY
Dusting off Newton's
old technique

NATURE JOBS
Join us today



Strife on the seven seas

The sight of nations jockeying for position on the high seas is becoming more common. An international treaty exists to deal with such disputes and it is time for the US Senate to ratify it.

The resources of the world's oceans, from fish to oil and minerals, are vast, but finite. And it is quickly becoming apparent that nations will increasingly be squaring up over how these marine riches should be divided.

Fortunately, the United Nations Convention on the Law of the Sea provides a comprehensive and reasonably robust framework for the peaceful resolution of such disputes — and much else besides. Less fortunately, the US Senate has yet to ratify the country's membership of the convention. It should do so immediately, so that the United States can play a grown-up role in the development of the framework established by the treaty. The same argument applies to another two dozen or so other nations, from Turkey to Peru, that have yet to ratify the convention.

The current, prolonged boom in prices for oil, gas and minerals is bringing to the fore resource issues that the UN convention was designed to help untangle. Last week's placement of a Russian flag on the sea floor at the North Pole (see *Nature* **448**, 520–521; 2007) offered an aptly melodramatic foretaste of the difficulties that are likely to transpire as nations engage in a scramble for the oceans.

And it won't just be old European powers that will be staking their claims. In this issue, we report how India's oceanographic research interests, for example, are already stretching from the Equator to the poles (see page 642). When humans were less able to harm the sea — skating on its surface in wooden boats and taking resources in relatively small quantities — it could be a lawless common. But now our society must manage the sea very carefully, lest the waters become a lifeless waste.

As much as any other scientific discipline, oceanography is inextricably tied up with the material and military exploitation of the territory that it studies. The UN convention sets out the factors that should determine which waters fall under the economic control of each nation. The undersea Russian flag is merely the symbolic component of an ongoing petition about its marine rights, which are linked to geology. If Russia can convince a commission set up under the convention that its continental shelf does indeed extend far beneath the Arctic ice, it will

be able to claim exclusive rights over valuable oil and gas deposits.

The convention also sets out rules for shipping: protecting the right of 'innocent passage' for ships to pass through territorial waters without special permission. It prohibits piracy and includes environmental safeguards, requiring, for example, that nations set sustainable fishing policies and refrain from damaging the interests of other nations with pollution emanating from their waters.

And it includes a right to conduct scientific research anywhere on the immense swathe of ocean that is not controlled by any country, as long as the work is peaceful, noncommercial and disseminated freely. The treaty's scope can expand as fresh issues arise: at the convention's most recent meeting, in May in New York, a framework for dealing with marine genetic resources was discussed.

In practice, the United States already abides by nearly all of these provisions. So why has the treaty languished there since 1994 without its ratification even being considered on the Senate floor? At one point, opposition focused on a section on seabed mining that representatives of some nations considered too restrictive. But since that was rewritten, also in 1994, opposition has been confined primarily to a dozen or so conservative senators who are philosophically opposed to the encroachment of UN rules on what they regard as the United States' rights as a sovereign nation.

Everyone else, from the environmental lobby and the oil industry to the US Navy and the administration of President George W. Bush, is now publicly backing ratification. Last week's flag-planting prompted a spokesman from the Department of State to call on the Senate to ratify the law in the United States' own interests, saying he was "hopeful that when Congress comes back in session they'll give it due consideration".

It is up to Senator Joseph Biden (Democrat, Delaware), chair of the Senate Committee on Foreign Relations, to bring a resolution of ratification through his committee to the Senate floor. He should do so at the earliest available opportunity. ■

"When humans were less able to harm the sea, it could be a lawless common."

Clinical precision

Disease advocates should influence, but not dictate, research priorities.

Disease lobby groups have always made energetic efforts to ensure that the formidable resources of the US National Institutes of Health (NIH) are brought to bear on the health issues that interest them; and that is as it should be. When these resources are expanding, there has been room for most of the participants in

the process to feel that they are winning. Now that the budget of the largest research agency in the world is effectively frozen, there are likely to be more losers.

In the case of research into autism — a common but poorly understood developmental disorder — effective advocacy has seen a generous increase in NIH support specifically targeted at the disease, even since the real growth in the agency's total budget came to an end in 2003. Unfortunately, some of autism's success may have come at the expense of research into other children's diseases (see page 628).

Autism research also garners an unusually strong level of support from private sources, including funds raised by the disease group

Autism Speaks and contributed by philanthropists such as Jim Simons, a mathematician and hedge-fund billionaire whose daughter suffers from the condition. This year, these sources will spend some \$50 million — roughly half what the NIH is spending on autism research. Typically, disease groups can muster charitable funding that is only a small fraction of what the NIH spends (see *Nature* **447**, 248–254; 2007). That leaves them scrambling for slices of a pie that is no longer growing.

Scientists, especially those involved in the basic biomedical sciences, are also scrambling for a share of these funds. The NIH's success has been built on a tacit accommodation between scientists, who run its 27 institutes and centres on a day-to-day basis, and the public, as represented by Congress. Institutes have been established — often against the scientists' advice — to deal with specific conditions or diseases of particular organ systems. Then Congress has, in large part, left the researchers and physicians in the agencies to pursue their work as they see fit, without indulging in too much micromanagement.

This has enabled the NIH to maintain a formidable reputation for scientific integrity and excellence, while also appearing to be reasonably responsive to patient needs. It has produced an agency that does a great deal of basic scientific research — with unknown and largely serendipitous benefits for the development of drugs and

devices — as well as plenty of laboratory and clinical work devoted to particular ailments.

The public is paying for the NIH's annual budget of \$29 billion, and it is entirely appropriate that it should energetically articulate its demands of the agency. That is one of the roles of the disease-advocacy groups, and their input, as any NIH institute director will attest, provides invaluable assistance in assigning research directions and priorities.

That said, the power of some advocacy groups must be tempered to some degree — especially in today's difficult funding environment. Otherwise, these groups' ability to influence budgets is likely to dominate, to the detriment of both basic laboratory science and of research targeted at diseases that have weaker constituencies.

It falls to the scientist-administrators who run the NIH to work closely with members of the congressional appropriations committees that fund the agency to make sure that this does not happen. Both groups understand the careful political balance that has allowed the agency to thrive; they must act as moderators whenever the more energetic lobby groups are pushing the agency's agenda too far in the direction of one public-health issue at the expense of others. ■

"The power of some advocacy groups must be tempered to some degree."

A risky business

The White House risk-assessment bulletin should be put out of its misery.

Last November, the US National Academy of Sciences delivered a stinging verdict on a White House plan to change the rules on how the government's agencies measure risks, such as those resulting from chemical exposure or from smoking cigarettes. The academy said that a draft risk-assessment bulletin containing the plan was "fundamentally flawed" and ought to be completely withdrawn.

Ten months later, the bulletin is still very much alive. After some hesitancy, Susan Dudley, head of the Office of Information and Regulatory Affairs at the White House Office of Management and Budget (OMB), has indicated that it is still under review and likely to be finalized in some shape or form.

Risk assessment is a complex and exacting activity, and the National Academies have played a globally acknowledged role over many years in providing guidance on how it should be done. But the academy panel, chaired by John Ahearne, a former president of the Nuclear Regulatory Commission and director of ethics at the scientific society Sigma Xi, said that the bulletin was wrong in attempting to impose a "one-size-fits-all" approach to risk assessment overseen by so political an office as the OMB. It also charged that the bulletin failed to take account of the different approaches appropriate to the various fields of science and engineering, or of risks to particular groups, such as children or pregnant women.

Outside critics were even more direct. They saw the bulletin as a barely disguised power grab, a cynical attempt by the White House

to exercise an unprecedented degree of control over all the branches of the federal government, with a view to making it harder for major regulators such as the Environmental Protection Agency to do their jobs (see *Nature* **442**, 242–243; 2006). Indeed, the main objective of the bulletin seems to be to weaken these regulators 'through the back door', by imposing arcane bureaucratic requirements that the broader public won't understand, or even know about.

In that regard, the proposed bulletin resembles several earlier efforts, including rules on 'information quality' and requirements for cost-benefit analyses, that make use of the OMB's extensive powers to weaken all forms of regulation. These efforts have been under way from the very start of the Bush administration and they continue to this day.

Thankfully, Congress is now reacting to this strategy and applying some oversight to the OMB. In May, for example, Senators Jeff Bingaman (Democrat, New Mexico) and Joe Lieberman (Independent, Connecticut) wrote to Rob Portman, then director of the OMB, to seek assurances that it would take the National Academy of Sciences' advice and withdraw the risk-assessment bulletin.

In an evasive response, Portman would say only that his office would "not finalize the bulletin without revision" — indicating, in effect, that it is planning to press ahead with the exercise in a revised form.

Now the senators have written to the OMB again, asking its officials to state by next week exactly how they intend to proceed, given the devastating critique issued by the academy panel last year. "We began our review of the draft bulletin thinking we would only be recommending changes," said Ahearne at the time. "But the more we dug into it, the more we realized that from a scientific and technical standpoint, it should be withdrawn altogether." The White House specifically went out and sought this advice: why won't it take it? ■

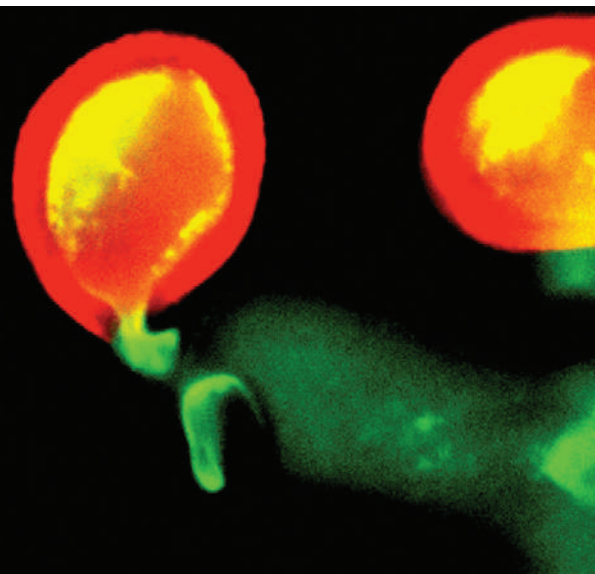
RESEARCH HIGHLIGHTS

Female to male communication*Science* 317, 656–660 (2007)

Fertilization in plants depends on the female sexual apparatus detecting and accommodating its species' pollen. Research led by Ueli Grossniklaus of the University of Zürich in Switzerland has identified a receptor-like protein on certain cells of a flower's female reproductive structure that is key to this recognition process.

When a pollen grain (red in picture) arrives at the female structure, it begins to grow a pollen tube (green) towards the reproductive cells, through which the male gamete contained within the grain is delivered to the egg. *Arabidopsis thaliana* plants lacking a protein known as FER fail to arrest the pollen tube's growth and to ensure that it ruptures in the right place, meaning that fertilization does not occur.

It may be possible to manipulate this system to allow cross-species fertilization, but it is not yet known what molecule on the pollen grain FER binds.



J.-M. ESCOBAR-RESTREPO

TOXICOLOGY**Plastic changes to a diet***Proc. Natl Acad. Sci. USA* doi:10.1073/pnas.0703739104 (2007)

Dietary supplements seem to protect developing mouse embryos from the effects of a worrying chemical. Bisphenol A (BPA), a hardening agent used in consumer plastics, has been shown to damage mouse eggs and produce problems later in life through epigenetic changes — heritable alterations to the genome that affect gene regulation.

Randy Jirtle and his colleagues at Duke University in Durham, North Carolina, investigated the effects of BPA in a mouse model in which epigenetic alterations cause the mouse's coat to change colour between brown and yellow. Offspring of mice exposed to BPA were more likely to be yellow than those of control mice. If expectant mothers exposed to BPA were also fed a diet high in folic acid or genistein, a phytoestrogen found in soy, this effect disappeared.

CANCER BIOLOGY**Microbial tumour fighters***J. Clin. Invest.* doi:10.1172/JCI32205 (2007)

The gut's microbial flora may stimulate the immune system's fight against tumours, report researchers from the US National Cancer Institute.

Chrysal Paulos, Nicholas Restifo and their colleagues studied a treatment in which cancer patients are irradiated and then given tumour-specific immune cells that find and kill the cancer cells. The radiation was thought to help by killing other immune cells

that would interfere with this process and by boosting the production of helpful proteins. But this team found that radiation also benefits mutant mice that already lack these interfering cells and beneficial proteins.

The researchers propose that this is because radiation breaks down the barriers of the gut, enabling bacterial molecules to travel into the serum and lymph nodes. Once there, they are thought to nudge the immune system into greater action. Antibiotics or elimination of the bacterial molecules reduced the positive effects of radiation.

PHYSICS**Turned out right***Phys. Rev. Lett.* 99, 050401 (2007)

Two experimental teams on opposite sides of the globe have joined forces to put Einstein's theory of relativity to a stringent test.

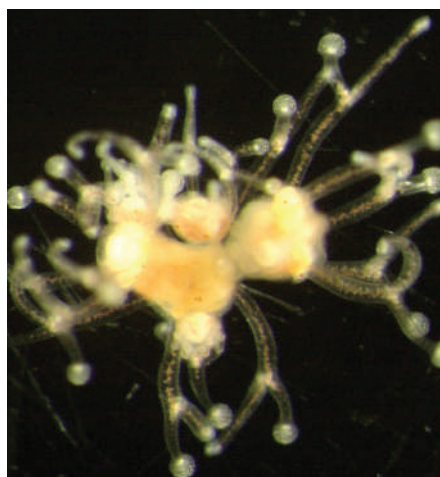
Holger Müller of Stanford University in California and his colleagues looked for violations of Lorentz invariance — the assumption in relativity that the laws of physics are the same in all reference frames — by combining data from experiments in Berlin, Germany, and Perth, Australia. The first data set compares the frequencies of light resonating in two quartz cavities, the second the frequencies of microwaves in two sapphire crystals. Together, these test the behaviour of both photons and electrons. Each experiment was rotated to change the reference frame it probed.

Some physical theories predict Lorentz violations, but relativity survived this test. Data recorded over a period of more than a year set simultaneous constraints on the possible size of 14 Lorentz violation parameters that are between 3 and 50 times smaller than the previous best limits.

GENETICS**Two heads better than one?***PloS One* 2, e694 (2007)

Silencing a single gene can induce a jellyfish to grow multiple heads, Wolfgang Jakob and Bernd Schierwater of the University of Veterinary Medicine Hannover, Germany, have found.

The researchers used RNA interference to switch off *Cnox* genes in the jellyfish, *Eleutheria dichotoma*. *Cnox* genes help to shape development of the organism's body plan, similar to the *Hox* genes found in other animals, including humans. Inhibiting one or both of the genes *Cnox-2* and *Cnox-3* produced multiple 'heads' (pictured left),



W. JAKOB

whereas inhibiting *Cnox-1* resulted in additional tentacles.

Related genes are found in Cnidaria including jellyfish, anemones and coral. These genes may have had a role in the evolution of some colony-forming Cnidaria that have multiple heads sharing a stomach.

DRUG DISCOVERY

Challenging drug resistance

Nature Chem. Biol. doi:10.1038/nchembio.2007.21 (2007)

Bacteria that have become resistant to certain antibiotics may meet their match in lactivicin — an antibiotic with an unusual architecture.

Lactivicin inhibits enzymes, known as penicillin-binding proteins, essential to building the bacterial cell wall. Several other antibiotics also target these enzymes, but their activity is underpinned by a β -lactam group, which lactivicin lacks. From crystal structures, Christopher Schofield, at the University of Oxford, UK, and Andréa Dessen, of the Jean-Pierre Ebel Institute of Structural Biology in Grenoble, France, and their colleagues have deciphered how lactivicin inhibits these enzymes.

They also report that lactivicin can inhibit a mutated form of the enzyme from bacteria that are resistant to β -lactam antibiotics. The results may spur the design of a new suite of antibiotics.

IMMUNOLOGY

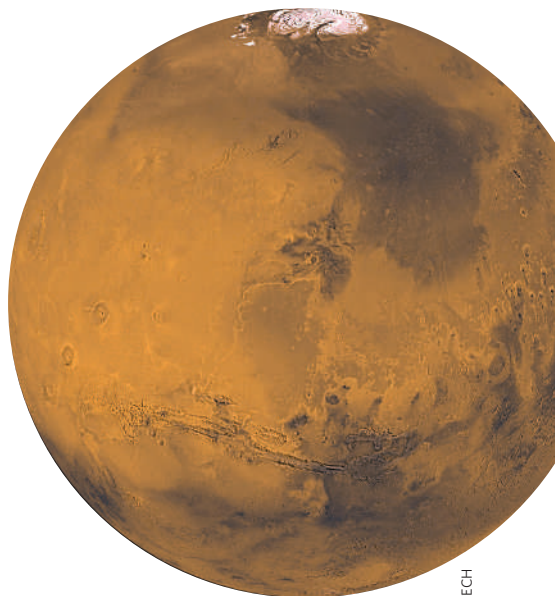
The mouse gap

Nature Immunol. doi: 10.1038/ni1500, doi: 10.1038/ni1496 and doi: 10.1038/ni1497 (2007)

Three papers offer new details about how the immune system's T_H -17 cells develop. The work indicates that mice are of limited use as models for the development of such cells in the human immune system.

Michael Lohoff, of Philipps University Marburg in Germany, and his colleagues studied mice, and found that T_H -17 cell formation requires a protein known as interferon-regulatory factor 4.

Two additional reports — one by Federica Sallusto, Eva Acosta-Rodriguez and their colleagues at the Institute for Research in Biomedicine in Bellinzona, Switzerland, and another by Rene de Waal Malefyt of Schering-Plough Biopharma in Palo Alto, California, and his colleagues — catalogue the proteins involved in differentiation of T_H -17 cells in humans. These reports reveal unexpected differences in this process between humans and mice.



NASA/JPL-CALTECH

PLANETARY SCIENCE

Volcanic roots

Geophys. Res. Lett. **34**, L14202 (2007)

Researchers in Germany have come up with a mechanism to explain how volcanoes on Mars — some of which can be seen in the image above — have remained active for much of the planet's life.

Evidence from spacecraft suggests that some volcanic flows on the red planet formed as recently as 2 million years ago, long after the planet's surface was expected to be cold and geologically dead. One hypothesis is that a mantle plume sustained the volcanism. Sandra Schumacher of the University of Münster and Doris Breuer of the German Aerospace Center in Berlin-Adlershof present a rival theory. They calculate that the crust in the major volcanic regions, which is thicker than elsewhere, can trap enough of the heat coming from the planet's interior to melt the rock beneath the crust.

CHEMICAL BIOLOGY

Minds made up

J. Am. Chem. Soc. **129**, 9258–9259 (2007)

Researchers have found a chemical that can transform muscle cells into neuron-like cells. The work could lead to treatments for neurodegenerative disease if these cells prove able to develop into fully fledged neurons.

Injae Shin and his co-workers at Yonsei University in Seoul, Korea, screened a library of molecules and found one, dubbed neurodazine, that triggers mouse and human muscle cells to display neuron-like behaviour. The treated cells start to produce neuron-specific proteins and to generate and exchange synaptic vesicles, the structures that transport neurotransmitters within nerve cells.

Previous methods to grow neurons from other cell types have either relied on chemicals with potentially disruptive biochemical effects or worked only in embryonic stem cells.

JOURNAL CLUB

Michael Purugganan
New York University, USA

An evolutionary geneticist wonders why certain crops were 'invented' not once but multiple times.

Crop species have always captured my imagination — perhaps because Darwin saw domestication as a model for the evolutionary process, or maybe because I am an inveterate foodie. Whatever the reason, I work on the evolution of crop species as diverse as rice, barley and cauliflower, using genomic methods to trace their origins.

I was struck by two recent molecular studies that indicate that key crops may have evolved more than once in association with different cultures, after Neolithic farmers began to cultivate various wild plants and select desirable traits 12,000 years ago.

Rice seems to have originated from the wild rice *Oryza rufipogon* separately in China and in India and southeast Asia (J. P. Londo *et al. Proc. Natl Acad. Sci. USA* **103**, 9578–9583; 2006). Meanwhile, barley, which originated once in the Fertile Crescent — a region defined by an arc through Lebanon, Syria, Turkey and Iraq, and home to the oldest archaeological evidence for agriculture — may also have had a second origin in present-day eastern Iran (P. L. Morrell and M. T. Clegg *Proc. Natl Acad. Sci. USA* **104**, 3289–3294; 2007).

Previous genetic mapping studies of the loss of seed shattering in rice and barley suggests that the trait is controlled by different genes in different lineages of these crops. This makes sense in the light of a multiple-origins scenario.

The pattern is not unique — cattle, sheep and goats were also domesticated multiple times. So did different cultures learn how to go about domesticating wild plants and animals from each other, or did they arrive at the same evolutionary solutions independently when faced with similar challenges? Hopefully the genetic data will motivate archaeologists to dig for evidence of how groups of people went about developing these crops.

Discuss these papers at <http://blogs.nature.com/nature/journalclub>

SPECIAL REPORT

Autism Speaks: the United States pays up

In recent years, autism has become the golden child of the fund-raising circuit. **Meredith Wadman** looks at a US public-relations success that is driving research funds and expertise towards this childhood condition, and asks who is missing out.

Toni Braxton, Matthew Broderick, Bill Cosby — perhaps not names you would associate with social or communication difficulties, and yet in one night, they helped raise \$1.45 million at a fund-raiser for research into one of the least-understood disorders affecting children: autism.

Star-studded events such as that fund-raiser at New York's swanky Lincoln Center in April are the latest front of a public-relations battle to raise money for research into childhood diseases. In the United States, it's a battle that autism seems to be winning.

"I was sitting in the nosebleed section and it was \$1,500 a ticket up there," recalls neurologist Gary Goldstein, president of the Kennedy Krieger Institute in Baltimore and chair of the scientific advisory committee for Autism Speaks, the group that organized the event. Goldstein recalls a 2005 Hollywood fund-raising concert featuring Jerry Seinfeld and Paul Simon. "Every four months there's something like that, and that doesn't count all the golf classics," Goldstein says.

In less than three years, autism has emerged from relative obscurity on the fund-raising circuit to become the disease *du jour*. The 1,000 biggest US private foundations nearly doubled their autism-related giving to \$2.7 million between 1998 and 2005, according to the New York-based Foundation Center. The Autism Society of America, the founding father of autism groups, has also seen its budget grow steadily to \$20 million. More striking are the contributions of two newcomers: Autism Speaks alone raised more than \$33 million in 2006, its first full year of operation, and it is well on target to meet its goal of \$55 million in 2007. And the lower-profile Simons Foundation, which began funding autism research

in 2003, has spent more than \$40 million and plans to spend another \$100 million over the next five years.

The commonly held belief that the prevalence of autism is rising may be partly responsible for the cash flow. Previously reported as affecting fewer than 1 in 2,000 children, studies over the past five years have found a dramatically increased prevalence: 1 in 150 eight-year-olds in the United States, according to a February report by the Centers for Disease Control and Prevention (CDC) in Atlanta, Georgia; or 1 in 86 nine-to-ten-year-olds, according to research in one UK region (G. Baird *et al. Lancet* 368, 210–215; 2006). Experts attribute much of this rise to better diagnosis and reporting and to a broadened definition of autism that includes milder forms of the disease.

The purported link to childhood vaccines (see *Nature Med.* 13, 896–897; 2007) — which has since been denounced by scientists — has also raised the public profile of the condition.

But in the past two years, two people have had perhaps a greater impact on autism's visibility — and coffers — than any other single force, essentially rewriting the book on how to raise money for disease-specific research: Bob and Suzanne Wright, who founded Autism Speaks in 2005 after learning that their grandson had the poorly-understood condition.

Bob Wright, then chairman and chief executive of media and entertainment conglomerate NBC Universal, provided his business savvy and his extensive connections to a *Who's Who* of American stardom. He also brought urgency. "I know how devastating this problem is to families. I am reminded of it daily," says Wright.

In 2004, Goldstein pre-



Making moves: performances from stars such as Toni Braxton have raised the profile of autism.



Paul Simon and Jerry Seinfeld took part in a 2005 fund-raising concert.



SHOULD MEAT-EATERS GUIDE CONSERVATION?

Researchers disagree over whether predators reflect biodiversity.

www.nature.com/news

GETTY IMAGES

the rate the group is growing, I'd be shocked if five years from now it's not raising \$100 million a year," observes Goldstein.

Although there are other private groups focused on research and treatment, in the past the public's awareness of autism has not been as high as it could have been. "We were really out there by ourselves on awareness," says Wright. A public-relations coup changed that: last year, the group won a three-year campaign of free, slick publicity from the Advertising Council.

The New York-based Simons Foundation is a very different player. Formed by Jim Simons, a mathematician and hedge-fund billionaire who has an autistic daughter, the organization is spending tens of millions funding individual researchers. It's also financing a \$12-million collection of genetic information and cell lines from 2,000 affected families that will be made freely available to other scientists. The database is called the Simons Simplex collection, and is to be stored at Rutgers University, New Jersey.

In 2006, Simons recruited Gerald Fischbach, the former director of the National Institute of Neurological Disorders and Stroke, as his scientific director. Taking the job, says Fischbach, was "a chance to focus on just the very best science".

Terrific scientists

According to Fischbach, the swell of interest in the disease has been boosted by new genetic techniques and imaging tools. He notes that 11 of the 18 scientists to whom the foundation will soon make three-year grants of up to \$3 million are new to the field. "You couldn't attract terrific scientists if there were no good ways to approach the disease," Fischbach says.

The upward trend in money and interest has been mirrored at the National Institutes of Health (NIH), where funding for autism research has grown from \$22 million in 1997 to \$108 million this year — with 16% of that growth happening since 2003, while the rest of the NIH has been essentially flat-funded.

At the CDC, which in 2000 spent just over \$1 million on epidemiological research on autism, spending has soared to \$15.1 million in 2007. Even the Department of Defense is getting in on the act, spending \$7.5 million on autism



Autism Speaks has rewritten the rules on fund-raising since it was founded by Suzanne and Bob Wright in 2005.

research this year, largely thanks to Autism Speaks, which successfully lobbied Congress for the money on the grounds that autism in military families costs more than \$200 million to treat annually.

The most recent legislative achievement of the autism-research advocacy groups is the Combating Autism Act, which was passed in December 2006 after intense lobbying. It guarantees that the spotlight will stay on the disease, requiring for the first time that the government draw up an annual strategic plan for autism research, identifying gaps and opportunities, all with the input of affected families.

"The advocacy groups here have had an enormous impact," says Tom Insel, the director of the National Institute of Mental Health, which with its \$62-million spending in 2006 made the largest financial contribution of the five NIH institutes that fund autism research. Insel, who also chairs an inter-agency committee that coordinates autism research for the fed-

eral government, says of the advocates: "They hold our feet to the fire, and make sure we are relevant and accountable."

But something distinguishes autism advocates, especially Autism Speaks. "They are actually raising very substantial amounts of funds to do a lot of the science themselves," adds Insel.

Bigger share

That fund-raising prowess has generated both admiration and envy from disease groups that could be considered competitors. For example, since the doubling of the NIH budget ended in 2003, NIH's cystic fibrosis funding has fallen from \$117 million to \$85 million; funding for childhood leukaemia from \$70 million to \$53 million; and funding for Down's syndrome, which is about one-fifth as prevalent as autism, from \$23 million to \$13 million.

"Why is Down's syndrome funding low? Autism I think is a big contributor," says Jon Colman, the chief operating officer of the National Down Syndrome Society. "It's dominating priorities."

Fischbach concedes that what's good for autism has to be bad for others that rely on NIH funding. As long as the biomedical agency's budget continues to be frozen year after year, he argues, pouring new NIH millions into autism necessarily means funding less research on some other diseases. "There is a dark side" to the surge in autism funding, he admits.

But other disease groups say that they have benefited from the rise in autism's profile — some by learning from Autism Speaks' example, and others because autism can coexist with other, lesser-known diseases such as tuberous sclerosis and fragile X syndrome, which causes mental retardation. "People are beginning to talk about the probable genetic basis for most autism. And then often, if not always, they mention fragile X as an example," says Robert Miller, the executive director of the National Fragile X Foundation in Walnut Creek, California, who was pleased when a recent cover story on autism in *Newsweek* made a passing mention of fragile X.

But despite its new visibility and funding, autism remains a little-understood and untreatable disease, and it is unclear how much this well-managed public-relations exercise will change that. Insel is optimistic, though. "Autism has attracted the attention of the most stellar geneticists and neuroscientists," he points out. "So I'm hopeful."

See Editorial, page 623.

"There is a dark side to the surge in autism funding."

Chemists synthesize a natural-born killer

It took 22 years and involved 64 chemical transformations, but chemists have finally succeeded in making a synthetic version of the natural insecticide azadirachtin. It is the longest-running project that Steven Ley's group, at the University of Cambridge, UK, has ever completed.

But it is unlikely that this 'total synthesis' will ever be repeated — even though Ley is confident that he could more than halve the number of steps — because it is much easier to extract azadirachtin from the seeds of the Indian neem tree (*Azadirachta indica*). For some chemists, these sorts of *tours de force* seem increasingly irrelevant.

Natural-product synthesis emerged in the 1820s when Friedrich Wöhler synthesized urea, showing for the first time that a chemical made by nature could be recreated in the lab. It has spawned some serendipitous discoveries: William Perkin made the first synthetic dye, mauveine, in 1856 while trying to synthesize the drug quinine at the Royal College of Chemistry, now part of Imperial College London.

But for the past 20 years there's been a growing consensus among chemists that the routes to some target molecules are so complicated and low-yielding that making them in this way is pointless. Synthetic azadirachtin is unlikely ever to be used. "Sixty-four steps is not going to be possible for anyone to make on any scale," says Gemma Veitch, who helped derive the synthesis.

In fact, the trend now is to extract pesticides from their natural sources and to move away from either naturally based or purely synthetic

compounds such as DDT (dichlorodiphenyl-trichloroethane), says John Pickett, head of biochemistry research at Rothamsted Research in the United Kingdom.

But Ley insists that his quest was not in vain. "We won't quit now," he says. "We want to understand a lot more about the biology of the compound." He also expects to make simpler, more effective analogues of azadirachtin that lessen some of the sensitivity the compound shows towards light, acids and bases. Ley says he has also identified the protein in insects that binds to azadirachtin, and that without total synthesis, none of these things would have been possible. The full synthesis appears in the journal *Angewandte Chemie* (G. E. Veitch

et al. Angew. Chem. doi:10.1002/anie.200703027; 2007).

Derek Lowe, a medicinal chemist and author of the blog 'In the pipeline', is a vocal critic of total synthesis. He says that

the traditional justifications for the process, such as structure determination, have evaporated as characterization techniques including nuclear magnetic resonance spectroscopy and mass spectrometry have advanced. He also dismisses the need to make complicated molecules, calling it a trophy-grabbing exercise. "Making the molecule just for the sake of being able to do it is a waste of time," he says. "Some groups have lost track of the reason they're doing total synthesis."

"In the past we were peacocks, we liked to show off," Ley admits. But his attitude has changed. "Today it's all about the value of what you do." There is no point in going after "Everest" challenges, he says. "I don't have to

"There is nothing more noble than what we're trying to achieve."



be first; the elegance of the approach is what interests me."

Paul Wender, a synthetic chemist at Stanford University, suggests a different approach. Rather than attempting a very complex molecule, why not design simple but related target molecules, based on the structure and function of the complex natural product, he asks. "This addresses a major problem that many voice about complex molecule synthesis, namely that the targets, although exciting in function, are often too complex to be made in a practical fashion," Wender says.

Other total-synthesis chemists vehemently defend their craft. Phil Baran, from the Scripps Research Institute in La Jolla, California,

A genetic switch for gender bending

Female mice missing a gene involved in pheromone detection show the same sexual behaviour as males, researchers report this week (T. Kimchi *et al. Nature* doi:10.1038/nature06089; 2007).

The striking finding, by Catherine Dulac's group at Harvard University implies that female mice have a 'male behaviour' circuit in their

brains, which can be activated by the flick of a single genetic switch.

Female mice genetically engineered to lack a gene called *Trpc2* engaged in exclusively male traits, such as pelvic thrusting, male calls and mounting other mice, both female and male. The TRPC2 protein is essential for the functioning of the vomeronasal

organ — a part of the mouse nose that is involved in sensing pheromones.

The results prompt a rethink about how the brain regulates sexual behaviour according to gender, but some query whether they could simply be an effect of the lab environment, or of the types of mice used.

Lab conditions, says Dulac, might cause mice to be more limited in their behaviour than they otherwise would be. So, her group tested the same mutant mice under more natural conditions, leaving them in a larger enclosure for a month. The *Trpc2*-knockout mice still behaved sexually as if they were males.

The genetic make-up of lab mice



M. GUELDRY/SPL

Better times? The jury is out on whether natural-product synthesis has a place in modern chemistry.

admits that total synthesis is not a fashionable pursuit but he insists that it will endure. "Anybody who downplays the Ley achievement as anything other than a landmark is simply jealous." Baran is driven by what he describes as "the creation of beauty" and says: "If you focus on generating complexity in new ways, you have the opportunity to open up new realms of chemical space." He cites examples of important reactions discovered in the course of solving a seemingly intractable synthesis, including a reaction called the Nozaki-Hiyama-Kishi coupling to form carbon-carbon bonds.

Lowe dismisses this idea. "You're more likely to find new chemistry if you're looking for it," he says. But he admits that Ley's work is different, because Ley invented new reagents and general synthetic routes to reach his goal.

Ley himself is well aware of the debates surrounding total synthesis, which he attributes to a squeeze on funding, and says that those who criticize are those who are unwilling to do the tough chemistry themselves. "There is nothing more noble than what we're trying to achieve," he says.

Katharine Sanderson

might also affect the results. There are three types of mouse, says geneticist Fernando Pardo-Manuel de Villena, of the University of North Carolina in Chapel Hill. There are the classical lab mice, descended from one original pool of pets, bred to be less aggressive than average; wild-derived lab strains, which are not bred on the basis of behaviour; and wild mice. Wild and lab mice are

effectively chalk and cheese, with "strikingly different behaviour", says Pardo-Manuel de Villena.

Dulac's group bred two of the most common classical lab mouse strains — the C57BL and the 129/Sv types — together, and used the offspring in their experiments. But wild mice may behave very differently, points out mouse geneticist Elissa Chesler, of Oak

Ridge National Laboratory in Tennessee. "Would there be any compensation for this gene if this mutant was crossed to wild mice?"

Dulac's group is aware of this problem and is now breeding wild mice with the *Trpc2*-mutant mice, to experiment with a 'wilder' version.

Kerri Smith

See News & Views,

doi:10.1038/nature05892



KOREAN STEM CELLS UNMASKED

Disgraced biologist's cell line was first of its kind, but not cloned.

www.nature.com/news

LEE JIN-MAN/AP

US genetics bill blocked again

US Senator Tom Coburn is single-handedly blocking the passage of a bill through the Senate that aims to protect people from genetic discrimination.

Coburn (Republican, Oklahoma) is using a legislative tactic called a hold to block a Senate vote on the Genetic Information Nondiscrimination Act (GINA), which was passed in April by the House of Representatives on a vote of 420 to 3 (see *Nature* 447, 14–15; 2007). The bill would make it illegal for employers or insurers to use genetic information in hiring, firing, promotion or insurance-coverage decisions. President George W. Bush has promised to sign the bill into law should it reach his desk.

"I believe the bill, as drafted, contains unintended consequences," Coburn wrote in a 1 August letter to his constituents, who have since deluged his office with complaining letters, e-mails and phone calls. "Congress has both the moral and legal responsibility to pay

"The goalposts keep moving." attention to details and get them right. I want to assure you that my hold on

GINA is not because I oppose the bill's purpose, but because I am concerned about its lack of precision."

Coburn, who has holds on 87 bills, voted for essentially the same bill when the Senate passed it unanimously in 2005. At that time, both the House and Senate were controlled by Republicans, but the House refused to bring the bill to a vote. With Democrats now in charge of both, the bill is just one senator away from becoming law.

Coburn wants changes in the bill that would make it harder for victims to sue employers in some cases. He also says that the bill's definition of genetic tests isn't identical in the sections dealing with employers and insurers.

But its advocates dismiss these concerns as manufactured excuses. "The goalposts keep moving," says Kathy Hudson, director of the Genetics and Public Policy Center at Johns Hopkins University in Baltimore, Maryland. "He raises a concern and that concern gets addressed or negated and all of a sudden there is a new concern."

Meredith Wadman

WORDWATCH

Embiggen

In a case of theoretical physics imitating art, 'embiggen', first coined by *The Simpsons* character Jebediah Springfield, has now been used in a paper on string theory by Stanford University's Shamit Kachru. In case you need a definition, it means 'to grow or expand'. Obviously.

SCORECARD



Regret-free tattoos

The pain of removing that no-longer-hip tattoo could soon be a thing of the past, with the advent of ink-filled polymer capsules that can be injected under the skin, and later ruptured to disperse the ink.



Virtual gambling

Administrators of the booming virtual world Second Life have forbidden all casino games, in line with the US blanket ban on online gambling.

ZOO NEWS

Bear minimum

To feed the public's (and our) obsession with Knut, keepers at Berlin Zoo have announced that they are putting the cub on a diet. Bizarrely, the world's most famous polar bear was previously allowed to eat croissants, but not any more — he's looking quite chubby at around 60 kilograms.



JEAN-LUC

3 GOOD REASONS...

...to have sex

According to research in this month's *Archives of Sexual Behavior*, there are a staggering 237 reasons why people might choose to mate. Here is a brief selection.

- 1 The most common: "I was attracted to the person."
- 2 The prosaic: "It seemed like good exercise."
- 3 And the refreshingly honest: "The opportunity presented itself."

Sources: *Scientific American*, *The Guardian*, *The Times*, *Der Spiegel*, *New York Times*

Academic accused of living on borrowed lines

A shockwave could be about to hit the normally tranquil waters of social science. A German economist, specializing in environmental science and technology, has allegedly committed serial plagiarism and invented academic affiliations going back decades. The case should act as a warning sign to editors about how widespread plagiarism and deception may be, experts say.

Events may only now be catching up with Hans Werner Gottinger, 63, who is drifting into retirement in the town of Ingolstadt, Germany. This week the journal *Research Policy* is set to retract a 1993 paper by Gottinger, which analysed demand for spin-off technologies from Ronald Reagan's Strategic Defense Initiative. An accompanying editorial explains that two referees concluded that the article substantially plagiarized a paper published in 1980 in the *Journal of Business* by Frank Bass, then an economist at Purdue University in West Lafayette, Indiana. The editorial also profiles other cases of plagiarism.

Gottinger claims that he has "only scant recollection" of events so long in the past, but insists that he did not intend to plagiarize. He adds that he has "sincerely apologized" for any misunderstandings.

Problems with his paper came to the journal editors' attention in June, when a student noted that whole paragraphs and strings of complex mathematical equations in the Bass paper — which analysed demand for consumer-durable technologies — had been repeated almost exactly in Gottinger's paper. Gottinger did not acknowledge the Bass paper in his work.

Further investigations by one of the journal editors, Ben Martin, an expert in science policy at the University of Sussex in Brighton, UK, revealed that this was not the first such case. In 1999, the editors of the economics journal *Kyklos* had withdrawn a 1996 paper by Gottinger after finding that it had plagiarized a 1992 paper in the journal *Economics of Innovation and New Technology*. And by googling various strings of text from half a dozen other Gottinger papers, Martin identified yet another case — a 2002 paper by Gottinger about an economic model of global warming in the *International Journal of Global Energy Issues*, in which whole sections were remarkably similar to a 1997 article in the *Journal of Environmental Economics and Management*,

by economist Zhiqi Chen of Carleton University in Ottawa, Canada.

"I was shocked and saddened that someone in my profession could do something like that," Chen says. For his part, Gottinger says that the papers were "clearly designed as review papers and did not claim any novel ideas".

Martin then contacted Gottinger's supposed employer, Maastricht University in the Netherlands, about the cases. But the university says that Gottinger has never been appointed or affiliated with it in any capacity. "We have written to Gottinger and asked him to remove from the web all reference to an affiliation with our university," says university spokeswoman Jeanine Hermans. Gottinger told *Nature* that the affiliation was a "misguided muddling" of

"Plagiarism may be much more common than we previously thought."

other institutes in Maastricht with which he claims to have been affiliated, and says he has contacted all the web pages he can think of to correct matters.

Nature has checked other claims made by Gottinger, including membership of professional societies and editorships of several influential journals. We failed to confirm membership of any of the societies, and some of the journals deny he was ever an editor with them. He was, however, removed from the advisory board of *Technology Forecasting and Social Change* in 2003, after the journal became aware of the issue of the *Kyklos* plagiarism.

A chequered career

Gottinger started out in 1973 as a faculty member at the University of Bielefeld in northern Germany, until his resignation in 1980. His co-worker Peter Weingart remembers him as someone strongly orientated towards mathematical approaches, which was unusual in a sociology department. "He was considered highly intelligent but reserved," Weingart says.

In 1979, Gottinger was sacked from the GSF national research centre in Munich because of deception relating to a European Union grant application. From the mid-1980s on, he started to list Maastricht University as his academic affiliation on papers. In 1988 he was appointed as director of the Fraunhofer Institute for Technological Trend Analysis in Euskirchen near Bonn. He says he left over professional differences of opinion; current director Uwe Wiemken says the appointment "didn't end peacefully".



ORANG-UTANS ARE CUNNING COMMUNICATORS

Apes modify their gestures depending on human response.

www.nature.com/news

E. CARTMILL

CORBIS



Duplicated text alerted editors of the journal *Research Policy* to a wider web of deception.

Gottinger then moved abroad, working at the Oxford Institute for Energy Studies in the United Kingdom, and also at Norway's Centre for International Climate and Environmental Research in Oslo. In the mid-1990s he was involved with a private business school in the small town of Bad Waldsee in southwest Germany. Over the past decade, Gottinger has held various positions in Japan as well as an appointment at Rensselaer Polytechnic Institute in Troy, New York, that lasted only a

matter of weeks. At one point he received a special fellowship from the Carisal Foundation in Salerno, Italy, on the strength of the impressive CV he submitted.

During his career, Gottinger has clocked up more than 100 articles in reputable journals, and was shortlisted for the rectorship of the University of Klagenfurt in Austria in 1995, coming within a whisker of being elected.

Institutions that employed him are reluctant to discuss details of his case. *Nature* has inves-

tigated other affiliations claimed by Gottinger at different times and found many to be inaccurate — including Osaka University in Japan, which Gottinger attributes to a “sloppy misrepresentation” of claimed affiliations with two other institutes in the city.

So how could he have got away with so much alleged deception for so long? Detecting plagiarism is not easy (see ‘Copycat trap’). Martin also speculates that the highly mathematical nature of Gottinger’s work, unusual in the social sciences, may have been tough on referees. “It’s frightening — it suggests plagiarism may be much more common than we previously thought,” says Martin. “It undermines the basis of trust we have — and must continue to have — in our academic literature and our research community.”

Most scientists who had contact with Gottinger refer to him as a lone operator — only occasionally did he have a co-author. One of these was Peter Weimann, now a professor at the University of Applied Sciences in Berlin. (None of his co-authored papers is suspected of having plagiarized work.) Weimann says that Gottinger was “hard to work with because he was not very communicative”.

In a final twist, Martin has found that one of Gottinger’s papers (in 1992) may itself have been plagiarized — in 2005, by an academic from Zimbabwe.

Alison Abbott, with additional reporting by David Cyranoski, Emiliano Feresin and Carina Lenotti

Copycat trap

Plagiarists should beware. The next time they submit a paper to a journal, a red flag may pop up on the editors’ screen warning them that the article’s word patterns are suspiciously similar to those of a published paper. A pilot of this computer cop, called CrossCheck, was launched on 1 August by CrossRef, a group of 2,046 scholarly publishers.

Commercial software of this kind has been available for some time, but until now subscription firewalls have prevented its use with online literature. CrossCheck is able to access the databases of its member publishers.

Six publishers are taking part in the pilot: the Association for Computing Machinery, BMJ Publishing Group, Elsevier, the Institute of Electrical and Electronics Engineers, Taylor & Francis, and Wiley-Blackwell.

Like a search engine on the web, the program computes the similarity of word strings to yield an originality score. Suspect scores are flagged-up, and it displays similar excerpts of text from different sources. But an editor will need to examine the flagged up papers to confirm plagiarism.

If all goes well, the service could be available as soon as November and other

software providers could request access in the future, says Geoffrey Bilder, director of strategic initiatives at CrossRef. Publishers could also get authors to test their papers before submission, which would spread out the work and allow honest authors to check they hadn’t inadvertently ‘cut and paste’ verbatim, says Bilder.

The downside, he notes, is that the program would let hardened plagiarists play the system, by rewording detected passages. “It might just force people to become more sophisticated plagiarists.”

Declan Butler

Strike threat over jailed primatologist

Scientists in Brazil are considering strike action or “civil disobedience of another form” in protest over the imprisonment of a renowned primatologist. The case, they say, is a visible part of a wider government crackdown on scientists working in tropical areas around the world.

Dutch-born maverick Marc van Roosmalen has spent more than 20 years living and working in the Amazon, where he has discovered various new species of mammal, including several primates. A Brazilian national since 1997, much of his research career has been spent in a quest to save the rainforest, occasionally bending the rules to achieve this end.

But in 2002, van Roosmalen was charged with taking four monkeys from the forest northwest of Manaus without permits. The charges led to a federal congressional inquiry, a criminal case and, in June this year, a prison sentence of 15 years and 9 months. Van Roosmalen was convicted of keeping monkeys in a rehabilitation facility at his Manaus home without permits; auctioning names of new primate species to wealthy donors; and selling materials that had been donated to his former employer, the National Institute for Amazonian Research (INPA) in Manaus.

The sentence has other researchers in Brazil worried. “My main concern is the precedent,” says ecologist Regina Luizão of INPA in Manaus. “If this is happening to him now, how can we tell that we are not next?”

Ostensibly, the restrictions imposed on scientists are to limit biopiracy, whereby people profit from selling or patenting the properties of indigenous biomaterial without compensating the communities that they come from. The Brazilian authorities say the country has a serious problem with biopiracy and cannot afford to deal lightly with violations such as those committed by van Roosmalen. Vanessa Grazziotin, federal deputy for the State of Amazonas, who led the inquiry into van Roosmalen's case, is reported as saying at the time: “There is a vast biopiracy network infiltrating the research institutes.” (Grazziotin was unavailable for comment



E. PERES/AP PHOTO

Marc van Roosmalen was charged with crimes including keeping primates at his rehabilitation centre without permits.

when approached by *Nature*.)

But researchers say the authorities are going too far and limiting the nation's scientific potential. As a result, says INPA ecologist Philip Fearnside, Brazil and other nations will lose out. “Brazil has lost all kinds of money and intellectual importance because of its attempts to protect biodiversity from international interference,” he says.

In July, 287 researchers from 31 countries attending the annual meeting of the Association for Tropical Biology and Conservation in Morelia, Mexico, signed a petition protesting that van Roosmalen's sentencing was “out of proportion with his alleged crimes” and is “indicative of governmental restrictions on scientists” in Brazil. And, on 2 August, a group of top researchers organized by the Brazilian Society

for the Advancement of Science (SBPC) met to discuss its strategy in response to the Roosmalen case and the larger issues it represents in relation to scientists' ability to work in Brazil.

The group will meet again this week, says Leandro Salles of the National Museum in Rio de Janeiro. “Van Roosmalen is a specific case, within a broader context that is very sad

for the country,” Salles says. “Under the current laws, researchers are treated as potential criminals.”

Salles adds that researchers are fed up with increasing restrictions on their activities, including the jailing of scientists for minor infractions of permit laws, tougher biopiracy regulations that came into effect in 2001, and new rules that give the Brazilian military the authority to reject research project applications with foreign collaborators. Salles says the SBPC working group has been trying for several years to convince the government to change aspects of the laws with little success, and sees the van Roosmalen case as a last straw.

“One more letter of complaint, one more meeting in Brasilia isn't going to change anything,” Salles says. “So there is now a group that is ready to propose more forceful political acts, which could include strikes or civil disobedience of another form.”

Scientists outside Brazil say they are also facing increasing difficulty when working in the tropics, where governments are cracking down on research in the name of combating biopiracy. In 2006, for instance, the Gandhi Agricultural University in Raipur, India, charged a former professor with illegally giving plants to a UK-based company.

Erika Check and Thomas Hayden

Search is on for origin of UK foot-and-mouth outbreak

The British government is investigating the source of a fresh outbreak of foot-and-mouth disease detected in cattle at two farms in Surrey on 3 and 7 August.

The inquiries have focused on an animal-research facility at Pirbright, around 7 kilometres from the farms. The strain of the virus found is believed to be one used to make vaccines in laboratories, including Pirbright, although test results had not been confirmed as *Nature* went to press.

The Institute for Animal Health — run by the UK Biotechnology and Biological Sciences Research Council — and the vaccine manufacturer Merial Animal Health share occupancy of the Pirbright facility. A national ban on the movement of livestock has been implemented.

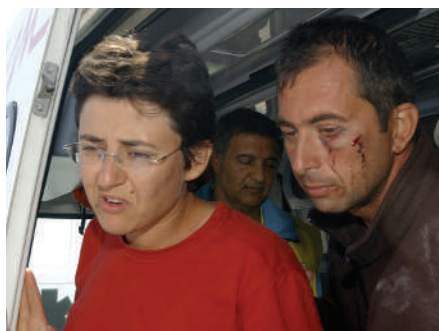
A previous outbreak of foot-and-mouth disease in 2001 led to the culling of more than 6 million cattle and cost the UK economy an estimated £8 billion (US\$16 billion).

Researcher drowns after vessel collision

A Russian marine biologist was drowned and an Italian colleague badly injured when the Italian research vessel *Thetis* sank off the coast of Sicily on 3 August.

Eight researchers and a crew of six were aboard the 200-tonne ship, testing laser instrumentation to measure biomass, when it was rammed in morning fog by a 55,000-tonne container ship registered in Panama.

The research ship sank within a few minutes, but Petr Mikhejchik, a scientist at the Russian Federal Research Institute of Fishery and Oceanography in Moscow, was trapped inside it. His body was



Vincenzo di Stefano (left) and Giusy Buscaino survived the sinking of the research vessel *Thetis*.

recovered by divers three days later.

The *Thetis* was commissioned in 2000 by the CNR Institute for Coastal Marine Environment in Naples and had been used in a wide range of research. Scientists are hoping to recover some instrumentation from the wreck.

Congress backs doubling of physics budget

The US Congress has passed a landmark bill that aims to double the budgets of the main agencies that fund research in engineering and the physical sciences.

The 21st Century Competitiveness Act recommends doubling the budgets of the National Science Foundation and the Department of Energy's Office of Science over seven years, and that of most programmes at the National Institute of Standards and Technology over ten years.

The act boosts funding for science education and the transfer of technology from laboratories to industry. It also backs the creation of an office in the energy department to support high-risk research (see *Nature* 448, 524; 2007).

The bill was passed by both the House

and the Senate on 2 August and will become law if signed by President George W. Bush. The agencies' annual budgets are actually set by appropriations committees, and these are widely expected to follow the bill's recommendations, at least in the short term.

India hopes cash will lure youngsters to science

In a bid to attract more young people into scientific careers, India's government is boosting stipends for graduate students and postdocs by 50%. Under the plan, graduate students will now receive 12,000 rupees (US\$300) per month, and postdocs will start out on 16,000 rupees.

Announcing the move on 1 August, science secretary Thirumalachari Ramasami said that the government will spend 1.2 billion rupees each year to increase the stipends it pays to students at universities and government research labs.

The rise has been welcomed by the country's scientists. "This is an excellent step to enrich the research pool," says Rajan Sankaranarayanan, a structural biologist at the Centre for Cellular and Molecular Biology in Hyderabad.

Bush to veto additional spending on water projects

President George W. Bush has threatened to veto a water-projects bill that would spend some \$20 billion on coastal, lake and wetland management and restoration projects.

Administration officials say that they object to the cost of the Water Resources Development Act, which is expected to be passed by the Senate and sent to the president this week. The bill includes hundreds of specific water projects, many of them favoured by environmentalists.

April Gromnicki, director of ecosystem restoration at the National Audubon Society, says the bill is long overdue, and that it includes \$6 billion for urgently needed restoration projects. And Senator Barbara Boxer (Democrat, California), chair of the Senate Committee on Environment and Public Works, says that the bill has enough support in both houses of Congress to overturn a presidential veto.

Archaeologists resume quest for hobbit remains

After a three-year hiatus, archaeologists are once more hunting for hobbits. A team from Indonesia and Australia has returned to the remote site on the island of Flores that yielded the first specimen of *Homo floresiensis*, metre-tall relatives of humans dubbed 'hobbits' on account of their stature.

Researchers from the Indonesian Centre for Archaeology in Jakarta and their colleagues resumed excavations at Liang Bua cave (pictured) on Flores in Indonesia last month. They hope to unearth more fossils of *H. floresiensis*, which lived until about 18,000 years ago.

The team has so far excavated to a depth of about six metres, reaching layers rich in artefacts and animal bones. These include bones of pygmy elephants, which are believed to have been eaten by hobbits. But no hominin bones have so far been found.



Foo's paradise (cont.)

Why aren't the aliens here? How can young scientists escape the fear of scooping and communicate openly? Where next for the gut microbiome? These and many other equally stimulating questions occupied 200 scientists and technologists gathered at the Googleplex in Mountain View, California, at this year's SciFoo (see *Nature* 442, 848; 2006). Bloggers were there in force. Go to www.nature.com/scifoo to see what they encountered.

BUSINESS

China tightens up

Plans to revamp drug regulation in China have yet to convince the sceptics, as **Jane Qiu** reports.

After a series of scandals that climaxed on 10 July with the execution of Zheng Xiaoyu, former chief of the State Food and Drug Administration (SFDA), China has announced a regime that, it says, will mark a clean start for its approach to drug regulation.

The government says that the changes will place the drug-approval system under public scrutiny and avoid misuse of power. But drug regulation is a tricky business, and critics doubt that China will be able to put the mechanisms in place to do it properly.

Since 1998, Chinese drug regulators have, in theory, adopted many of the rules that govern the US Food and Drug Administration (FDA) — the largest and, arguably, most thorough drug regulator in the world. But the Chinese outfit resembles the FDA more in form than in substance, according to Jia Wei, associate dean of the pharmacy school at Shanghai Jiao Tong University. Most importantly, he says, the SFDA doesn't have the internal checks and balances that the FDA has — or its level of transparency.

The result, the Chinese government now concedes, has been rampant fraud and corruption (see *Nature* **446**, 598; 2007). “Zheng's case reflects flaws in the drug-regulatory system,” says Yan Jiangying, deputy director of policy and regulation at the SFDA.

When they take effect on 1 October, the new rules will give individual officials responsibility for coordinating evaluations, but drugs will now be approved by a consensus of panels from several divisions of the SFDA. “This will prevent concentration of power in a single person or department,” says Wu Zhen, the agency's deputy commissioner.

An important theme of the new regulations is transparency. The SFDA will publicize the names of the evaluators and publish progress reports on its website, so people will be able to track the approval process. “Transparency is the worst enemy of corruption,” says Wu, who adds that he thinks the new rules will solve the country's drug-regulatory problems.

Few would go that far. “Drug regulation in China is an immense challenge for a very young

organization,” says Wang Mingwei, director of the National Centre for Drug Screening at the Shanghai Institute of Materia Medica. “The new rules are a step in the right direction, and will put a stop to the ‘black-box’ operation of the previous administration,” he says. But Nathan Xin Zhang, chief executive of Beijing-based drug company Sinocro, calls the changes “superficial” and says that the government has “failed to grab the bull by the horns”.

Checking up

Part of the problem facing drug regulation in China has been the extensive practice of filing applications based on false data or even drug samples that have been obtained illicitly. To tackle this, the SFDA states that it will validate the authenticity of the companies' work. Its inspectors will be empowered to make spot inspections, check experiments and samples, and examine raw data.

For some products, such as vaccines, the SFDA says it will place full-time inspectors in drug companies to conduct long-term surveillance. Companies who provide false information will be fined, blacklisted and banned from applying for drug approvals for up to five years. Such measures will “stop the problem at its source,” says Wu.

But China has more than 4,000 drug companies, and critics question the feasibility of the inspection plans, especially because the agency will rely on its existing staff of 1,800.

The FDA, by contrast, has 9,000 employees, including 2,125 scientific staff involved in drug evaluation — half of whom have postgraduate degrees. It assesses a more manageable number of applications from

considerably fewer companies. It also relies heavily on external panels for advice. The SFDA won't provide information about the skill-levels of its employees, but sources close to it say that it has several hundred scientific staff devoted to drug approval.

“It takes time, commitment and funding to build up this kind of infrastructure,” says Susan Wood, a biologist at George Washington University in Washington DC and former head of the FDA's Office of Women's Health. “If



“Zheng's case reflects flaws in the drug-regulatory system.”

— Yan Jiangying



the SFDA has a small team and the ability and expertise of its staff are limited, China should rely more on outside expertise.” But according to Shan Yuandong, director of the Centre for Clinical Pharmacology Research at Peking Union Medical College Hospital, the new rules do not enlarge the role of outside scientists in the approval process.

External issues

Yan says the SFDA recognizes the importance of outside expertise and that it will be reflected in future development of the agency. She claims, however, that the use of outsiders raises legal issues: “SFDA evaluators are employed by the government, but outside experts are not. So how would responsibility be attributed?”

That might prove to be a minor issue for the regulator, given the context. “Corruption is a widespread problem in China,” notes one Beijing-based researcher, who asked not to be named. “The SFDA scandal is just the tip of the iceberg.”

And despite rules released back in February that prohibit SFDA staff from having direct financial ties with the companies they regulate, staff still aren't formally required to disclose all their sources of income, as regulatory officials are required to do in many other countries.

But even the existing rules are not enforced effectively, especially at the provincial level, says Pang Ming of Eastway, a drug consultancy

G. BAKER/AP



L. JIN/AFP PHOTO

A clamp-down on corruption is part of China's plan to regulate its 4,000 or so drug companies.

firm in Hong Kong. China does have a Central Commission for Discipline Inspection, which monitors staff conduct from its office inside the SFDA. And another bureau is due to be established later this year to tackle corruption among state officials. But "that's government overseeing government," says Zhang. "It doesn't usually work."

What's really needed, says Pang, are genuinely independent watchdogs to oversee the SFDA and other branches of the government. He cites Hong Kong's Independent Commission against Corruption, which helped to turn the city from one well known for corruption into one of the 'cleanest' places to do business in Asia.

That sort of clean-up is something that China has yet to embrace. Daniel Chow, a law professor at Ohio State University in Columbia who specializes in intellectual-property issues in China says that the new SFDA rules, although encouraging, deal with only a small part of the problem. Real transparency, a culture of accountability and a mature legal system are what really matter, he says — and none of them are yet in place in China. "It will take time and patience to build up those elements, but the world is yet to see the country's commitment — not in words but in action," he says. ■

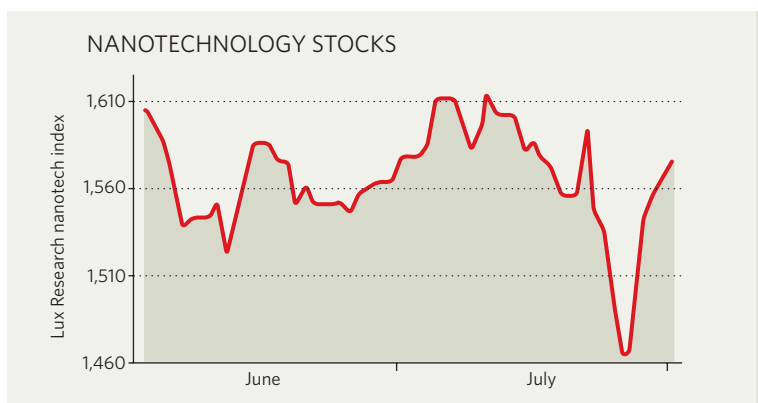
IN BRIEF

NO WITHDRAWAL An advisory panel to the US Food and Drug Administration (FDA) has said that the diabetes drug Avandia (rosiglitazone) raises the risk of heart attack, but recommended against pulling it from the market, on a vote of 22 to 1. The drug, which generated £1.6 billion (US\$3.1 billion) in sales last year for London-based GlaxoSmithKline, has come under scrutiny since a meta-analysis published by the *New England Journal of Medicine* found that it boosted heart attacks risk by 43% (see *Nature* 447, 512–513; 2007). The FDA usually follows the advice of its external advisers: in this case, however, its senior staff are said to be divided on how best to proceed.

PHYSICS BUY-OUT The Japanese company Sumitomo Chemical has said it will buy British materials developer Cambridge Display Technology for US\$285 million. The Cambridge-based company, founded in 1992 by physicist Richard Friend and his colleagues, specializes in developing polymers for use in light-emitting diodes. The offer valued the company's shares at \$12 — almost twice their closing price on 30 July, the day before the deal was announced. The size of the premium has been encouraging to other small companies in the nanotechnology industry (see below).

TIME TO LAY-OFF Disappointing quarterly results have led to a clutch of lay-off announcements by major drug companies. Britain's AstraZeneca has said that it will reduce its workforce by 11%, or 7,600 people, and Johnson & Johnson of New Jersey has said its staff numbers will fall by more than 4,000. Bristol-Myers Squibb, based in New York, has also said it will cut an unspecified number of positions. The reductions come on top of similar announcements by Merck and Pfizer earlier in the year, and reflect industry-wide concerns about prospects for profitability and for developing new, best-

MARKET WATCH



Nanotechnology stocks dipped sharply when wider stock markets got the jitters late in July. But a buy-out of a British company at the end of the month helped the sector to bounce back.

The Lux Research nanotech index, which tracks companies that develop, sell and use nanotechnology-related products, had been performing steadily if not outstandingly until the dip in July (see graph). When the wider stock market fell back, the index exaggerated the underlying trend — as it usually does, given the number of small, high-risk companies in its make-up.

Peter Hebert, chief executive of Lux, the New York consultancy firm that compiles the index, says that overall sentiment towards the sector remains positive — especially for materials companies.

However, some constituents of the index had a difficult summer. Flamel Technologies, a French specialist in drug delivery, has almost halved in value since

the start of June, because sales of the drugs it helps to deliver are lower than anticipated. And Symyx Technologies, a Californian company with diverse nanotech-related interests, dipped in late July, on news that deals it had struck with larger corporations are set to end.

Accelrys of San Diego, which sells software for modelling the behaviour of materials at a very small scale, fared better. Its shares rose sharply in July on the expectation of good financial results, which it duly announced on 1 August.

But it was the 31 July purchase of Cambridge Display Technology by Japanese company Sumitomo Chemical (see 'Physics buy-out', above) for almost twice its quoted value that boosted the sector. "That's a significant premium for a publicly-traded company," says Hebert. "It's good news for the materials business, and it obviously helped the index." ■

Colin Macilwain

Tails of the unexpected

No longer just cellular janitors, cilia are making a clean sweep for biological greatness. **Claire Ainsworth** explores how they may hold the secret of multicellular development.

As orgies go, it's pretty wild. Hundreds of whip-wielding participants pile into a seething ball. Stripping naked, they entwine and embrace, striving to make an intimate connection and consummate the union. If beaten to it by a rival, they move on to another partner until they get lucky. And chances are, it's all carrying on right now in your garden.

But don't call the police or reach for your camcorder yet. These swinging debauchers aren't human, they're single-celled algae called *Chlamydomonas*, commonly found in soil and water. Affectionately nicknamed 'chlamy' by the scientists who study them, these slimy green organisms and their rumbustious sex lives have a surprising connection with us and how our bodies work. Dissecting that connection is leading researchers to uncover a story that starts more than half-a-billion years ago and ends in modern-day illnesses such as diabetes, cancer and obesity. Along the way it touches the origin of bodies, beauty and symmetry, even helping reveal what makes individuals unique.

The link that brings these together is the whips brandished by our revellers; they're actually flagella that propel chlamy through the environment and are integral to their reproduction. In addition to providing locomotion, this tail-like

structure acts as an antenna, allowing the cells to sense their environment by detecting signals that indicate the presence of food, predators or mates. When mates meet, their flagella intertwine, sticking together and triggering a cascade of chemical signals that directs the cells to fuse.

This signalling, cooperation and clustering is reminiscent of a momentous biological step. "It's a flirtation with multicellularity as far as I'm concerned," says Bill Snell, a cell biologist and expert on chlamy at the University of Texas Southwestern Medical School in Dallas. About 700 million years ago, single cells clubbed together perhaps using flagella and other similar structures to cooperate and communicate, forming the first multicellular organisms. Now, biologists are realizing that signs of this unicellular ancestry are etched on almost every single cell of our bodies in the form of cilia, shortened versions of flagella that our unicellular ancestors used to flit through Precambrian seas.

As is the case with chlamy, these primitive flagella probably also worked as antennae, receiving signals transmitted by other cells as well as channelling information from the environment. There is growing evidence that cilia are performing similar tasks in our bodies today, sensing and responding to fluid flow and physical stress, helping cells to navigate and move as our bodies develop, and acting as communication conduits.

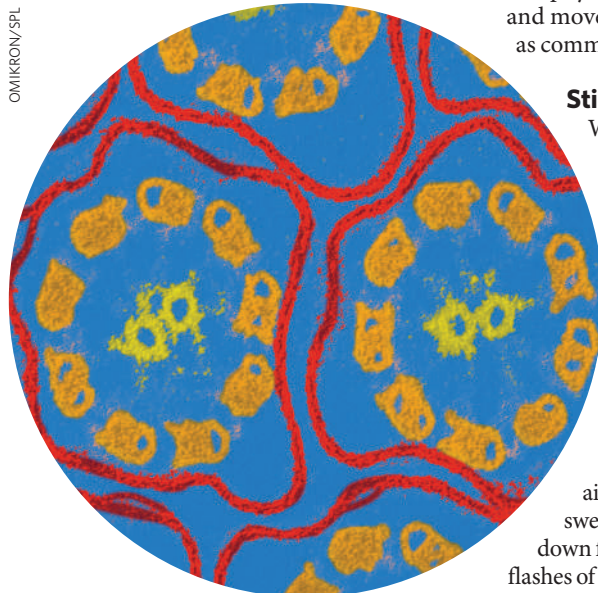
Stirring things up

Where they once ignored or overlooked cilia, biologists are now seeing them everywhere and are having to rethink aspects of their fields. "I think it's quite a surprise to developmental biologists," says John Wallingford, a developmental biologist himself at the University of Texas, Austin. And, he adds, "I think a lot of the cell biologists are saying, 'I told you so.'"

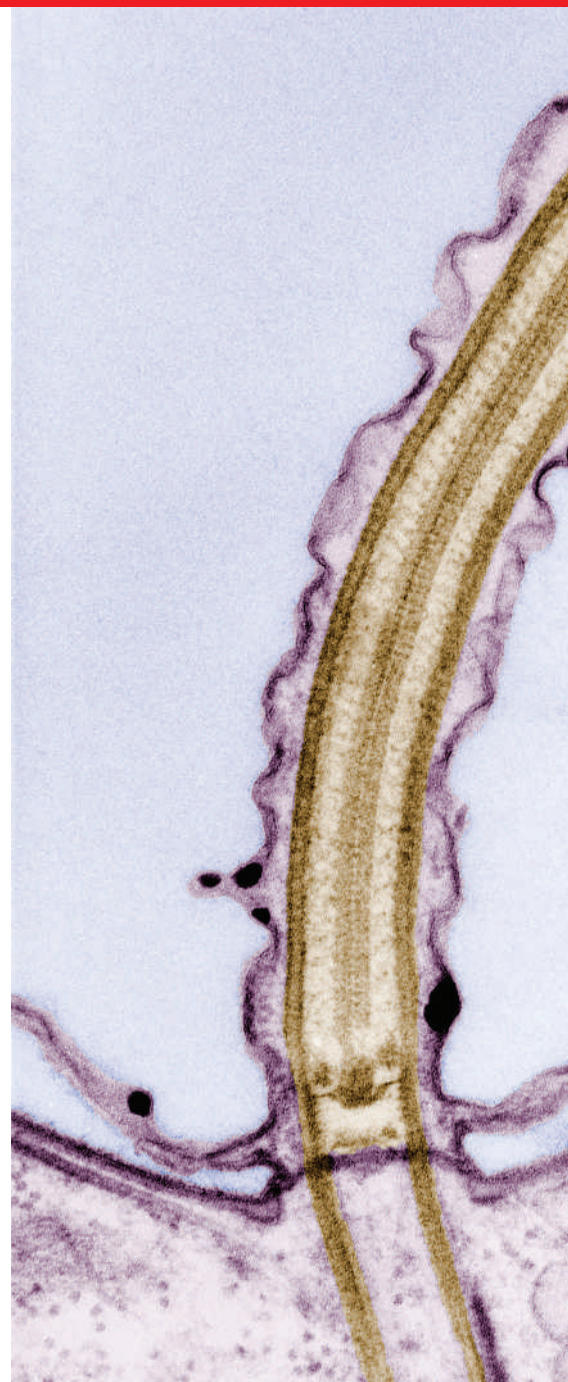
For a long time, cilia were regarded as lowly janitors, lining our airways and beating in coordination to sweep up dirt and mucus, or wafting eggs down fallopian tubes. True, they had shown flashes of brilliance: single cilia, called kinocilia

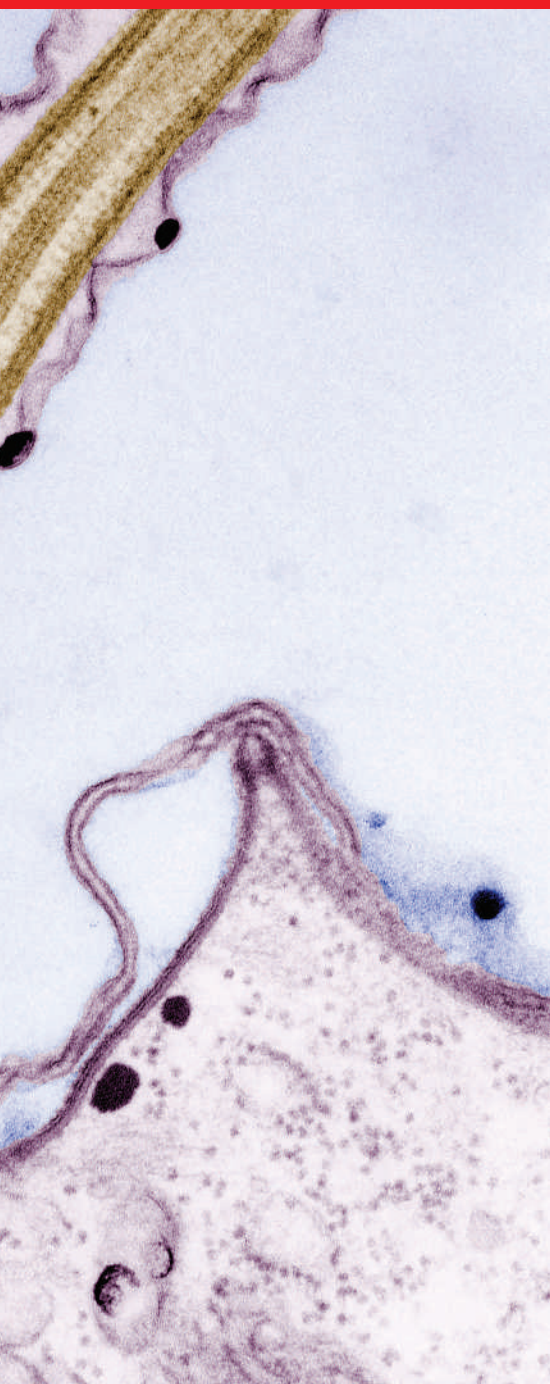
on the hair cells in the inner ear, for example, help us to hear. Cilia play similar roles in sight and smell, but biologists have only recently started to realize that cells carrying cilia are far from exceptions. Almost every cell in the human body carries a cilium, even neurons buried deep in the brain.

The first hint at the primacy of cilia came in 1976, when a Swedish biologist called Björn Afzelius reported the first link between faulty cilia and human disease. Afzelius was studying four infertile men. They were prone to chronic bronchitis, and, bizarrely, three of them had their internal organs placed on the wrong side of their bodies, a rare condition known as situs inversus. Using electron microscopy Afzelius showed that their sperm flagella lacked a key protein component, the dynein arms that help give flagella their kick. The cilia lining



OMIKRON/SPL





OMIKRON/SPL

Cilia and flagella project whip-like from cells, playing diverse roles in cells and organisms. A cross-section reveals the special arrangement of microtubules within them.

the men's airways had similar faults and did not sweep their lungs effectively. But the *situs inversus* was more puzzling¹.

Afzelius proposed that during development, cilia in particular positions in the embryo determined the placement of the organs by their coordinated beating. But no one knew where these cilia might be. More than two decades later, developmental biologist Nobutaka Hirokawa and his team at the University of Tokyo in Japan pinpointed them. Working on mouse embryos that lacked a protein needed for cilia to form properly, they showed that a patch of cilia in a tiny pit on the surface of

very young embryos beat to create a leftward flow of fluid². The team suggested that the fluid contained molecules that could accumulate on the left side of the embryo, breaking its bilateral symmetry and allowing the embryo to tell left from right. "This was a very big surprise for us," recalls Hirokawa.

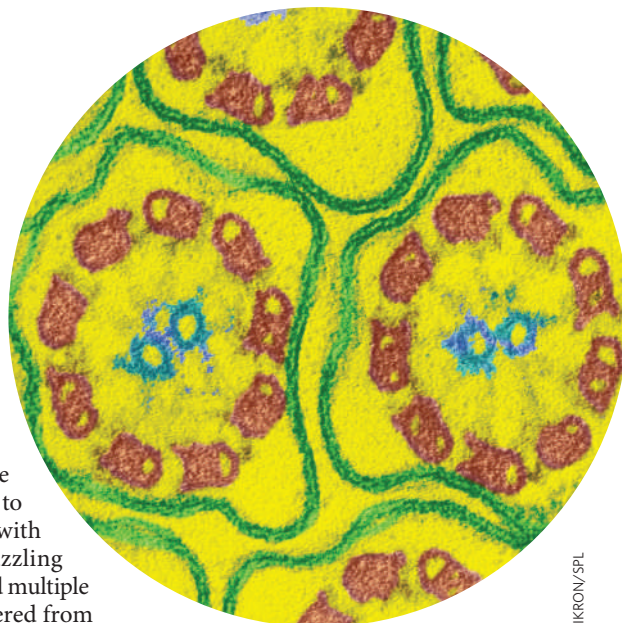
In the intervening decades more clues to the roles of cilia have come to light. Scientists studying patients with faulty cilia found a number of puzzling symptoms. Some patients developed multiple cysts in their kidneys. Others suffered from hydrocephalus, an accumulation of fluid on the brain. Cilia seemed to have their fingers in a lot of pies, but no one could work out how or why.

Dissecting cilia function

Biologists needed to find out what cilia were made of and how all the pieces worked together. This is where model organisms like *chlamy* helped. "Cilia are turning out to be really important organelles in cells, but we don't have any way to biochemically study them in vertebrates," explains Snell. Vertebrate cells are hard to separate from their cilia, but *chlamy* cells give up their two flagella more readily, making it possible to perform studies on intact organelles. "Just lower the pH and off they come," says Snell. Genetic experiments on *chlamy* can then determine the functions of flagella components.

Thanks to a number of studies in *chlamy* and other organisms such as fruitflies, nematodes and mice, biologists have pieced together a detailed picture of the structure of cilia and are now learning more about how they function (see "The cilium dissected"). One key to understanding their role in multicellular bodies came from work in *chlamy* on the system that builds and maintains cilia intraflagellar transport (IFT). In this system, motor proteins rapidly move bundles of cilium components and other molecules up or down the cilium's microtubule scaffolding. The system is balanced between motors that build and those that dismantle a cilium and if IFT fails, a cilium will eventually break down.

Mutating IFT genes in mice, unsurprisingly, disrupts their ability to form cilia. Curiously, it also leads to kidney cysts similar to those found in patients with faulty cilia syndromes and to those found in patients with polycystic kidney disease, the most common inherited single-gene disease in humans³. Biologists now know that cilia in the kidney bend in



OMIKRON/SPL

response to passing fluid, allowing the cells to sense flow. Many other cell types also have flow-sensing cilia, including those in the liver.

Already drawing attention, research on cilia yielded more surprises in the early 2000s. One revelation was a clutch of studies linking faults in ciliary proteins with a complex human genetic disease called Bardet-Biedl syndrome, a condition characterized by obesity, kidney failure, blindness and extra fingers (see 'Cilia roles in obesity and diabetes'). Another was the realization that a number of signal receptor proteins — such as receptors for the cell-growth control signal PDGF and the neurotransmitters serotonin and somatostatin — seemed to be concentrated in cilia. This raised the possibility that cilia might be involved in receiving molecular messages from other cells. So, are cilia just passive receptor-holders, or are

they actively involved in transmitting signals to the inside of the cell?

Snell and his team tackled this question by exploiting a quirk of *chlamy* genetics so they could switch IFT on and off at will. "It allows us to have cells with a full-length

flagellum, but which are completely depleted of intraflagellar transport machinery," he explains. IFT-depleted cells can stick to each other, but none of the signals reach the inside of the cell, leaving them unable to fuse⁴. Last year, Snell's team showed that IFT proteins are needed for a key signalling molecule to move to the correct locations within a cilium during the signalling process, implying a direct role for IFT in transducing the signal⁵. "The IFT system doesn't just deliver things," says Snell. "It participates directly."

As well as helping single cells find love, there is now strong evidence that IFT and the structural components of cilia are also needed to relay signals in multicellular bodies, such as those of vertebrates. Many of these signals are

"If you'd have told me I'd be up to my eyeballs in cilia, I'd have laughed."
— John Wallingford

involved in coordinating body plans. One such set of signals is that of the oddly named hedgehog protein family. Hedgehog was first discovered in fruitflies, and is so named because larvae lacking it have disrupted body plans and are covered in prickles.

From hedgehogs to guinea pigs

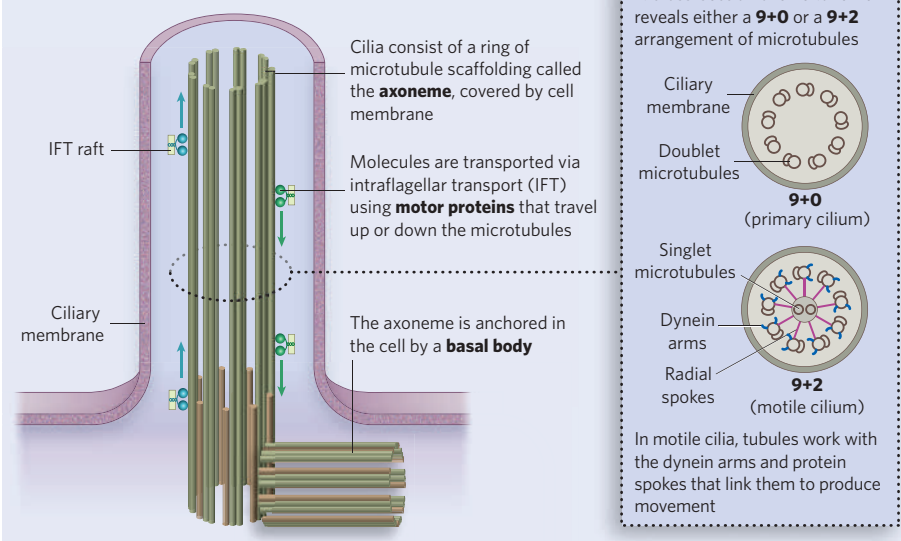
Similar molecules exist in many animals, including mammals, where they coordinate a vast range of cell behaviours. For example, hedgehog signals direct the correct ordering of fingers, the development of lungs and neurons and the spacing of facial features. Stem cells also rely on hedgehog signalling to repair damaged tissue, and several cancers result when it goes wrong. And it seems that it all comes down to cilia. "I think the idea that hedgehog depends on cilia is quite compelling," says Kathryn Anderson, a developmental biologist who studies hedgehog signalling at the Sloan-Kettering Institute in New York.

Anderson and her team stumbled across the link between IFT and hedgehog when they were looking for mutations that disrupted the development of mouse embryos. They found a set of mutants that looked like hedgehog mutants, and were surprised to find that the mutations were in genes coding for IFT proteins, which indicated that intact cilia and IFT were needed for signalling to work⁶. "We weren't looking for cilia, they found us," says Anderson.

Exactly how the system works is unclear. One suggestion is that cilia concentrate signalling components together in one place, an idea supported by the findings that hedgehog signalling proteins are localized in cilia. "I think cilia are more complicated than that," says Anderson. Earlier this year, her team showed that hedgehog-signalling components are tethered or released from the internal scaffolding of cilia in response to signalling, pointing to the spatial organization of the cilium being important⁷. And just last month, Matthew Scott and his team at Stanford University School of Medicine, California, showed that key components of the hedgehog-signal reception system move in or out of cilia as part of the signalling process⁸.

Hirokawa has added another twist to the tale. His team found that, as well as generating flow, cilia respond to the signals being wafted to the left-hand side of the embryo. Cilia located on left cells do this by seizing and opening large fatty packets of the signalling molecules needed for creating the asymmetry and

THE CILIUM DISSECTED



then relaying the signal to their cells. "So the cilium works as a capturing mechanism," says Hirokawa.

But cilia do even more during development: they help individual cells determine where they are within the plane of a sheet of cells. This phenomenon, called planar cell polarity (PCP), ensures, for example, that the hairs in a cat's coat point sleekly in the same direction, or that the hair cells in your inner ear stack the right way to let you hear. It also helps cells to navigate when they move, such as when the neural tube, which forms the developing brain and spinal cord, closes. When PCP is disrupted, the results range from the quirky, such as the rosetted fur beloved of guinea-pig fanciers, to the devastating, such as the neural-tube defect spina bifida.

Wallingford was studying PCP and neural-tube defects in *Xenopus* frogs when he stumbled upon cilia. He and his team had isolated the frog equivalents of two PCP-related genes found in flies.

When they knocked out the functions of these genes, they found neural-tube defects, as expected. But, oddly, the embryos also had problems consistent with faulty hedgehog signalling⁹. This, and the fact that the genes were expressed at high levels in ciliated skin cells made Wallingford consider cilia. "If you had told me two years ago that I was going to be up to my eyeballs in cilia, I'd have laughed," he says.

A cellular compass

Looking at the cell's internal skeleton, or cytoskeleton, Wallingford found that the PCP-related genes controlled the behaviour of actin — the main cytoskeleton protein — during cilium formation and that actin controlled where in the cell the cilium was positioned⁹. This work and that of other scientists supports the idea that the cellular signalling that underlies PCP somehow interacts with the systems that build cilia. The jury is still out on whether, like hedgehog, PCP signals are transduced via cilia, or whether cilia need PCP to form. Wallingford favours the suggestion that the PCP system governs a cilium's position on the cell, denoting its up-down axis, perhaps angling the basal body in the right direction, allowing the cell to determine its orientation.

This compass is also important in making sure cilia, in the airway for example, all beat in the same direction. "When cilia are beating, if there's directed fluid flow across it based on cilia, there has to be a planar polarity there," says Wallingford. His team is now probing possible links between PCP and lung diseases



Guinea-pig fanciers have cilia to thank for rosetted fur.

such as asthma, where cilia go awry. The team has turned to the cilia that line the slimy skins of *Xenopus* tadpoles — uncannily similar to the lining of our airways — and in unpublished work, they have already identified a suite of new genes involved in generating them.

Although cilia's relationship with cell signalling has come as a surprise to biologists, it may have been signalling that drove them to evolve in the first place. Detlev Arendt and his postdoc Gáspár Jékely at the European Molecular Biology Laboratory in Heidelberg, Germany, were running some bioinformatics studies on IFT proteins when Jékely noticed that they bore a striking resemblance to some of the protein complexes involved in transporting vesicles around the cell¹⁰. This led them to speculate on the origins of cilia, which have been debated for many years. Lynn Margulis of the University of Massachusetts, Amherst, and her colleagues have suggested that, like mitochondria — the powerhouse of the cell — cilia are derived from bacteria subsumed by other cells. Arendt and Jékely's findings suggest an alternative: that cilia arose from within cells, evolving from an existing signalling system. "It's a good assumption that the original function of the cilium was sensory," says Arendt.

Further analysis indicated that IFT structures and sequences of IFT proteins were related to cellular proteins involved in transporting receptors rather than bacterial proteins¹⁰. Jékely and Arendt propose that cilia started out as a sensory patch on the surface of a primitive cell.

Cilia roles in obesity and diabetes

There is growing evidence that cilia — relatives of the tails that our unicellular ancestors used to move around and sense the environment — are connected with the cellular signalling involved in modern illnesses such as obesity and diabetes.

Ciliopathies, for example, are rare genetic diseases resulting from faulty cilia. The best-known example is Bardet-Biedl syndrome, but a similar condition, Alström syndrome results in early-onset obesity and diabetes.

However, cilia could be related to a number of other conditions. Philip Beales, a geneticist at the Institute of Child Health in London, has probably seen more Bardet-Biedl cases than anyone else,

and thinks that there are at least 25 more ciliopathies to be found. "I am sure we are just seeing the tip of the iceberg," he says.

While screening a medical database for syndromes that had the telltale signs of ciliary defects, Beales and his colleagues recently identified another, Jeune syndrome, caused by defective IFT¹¹.

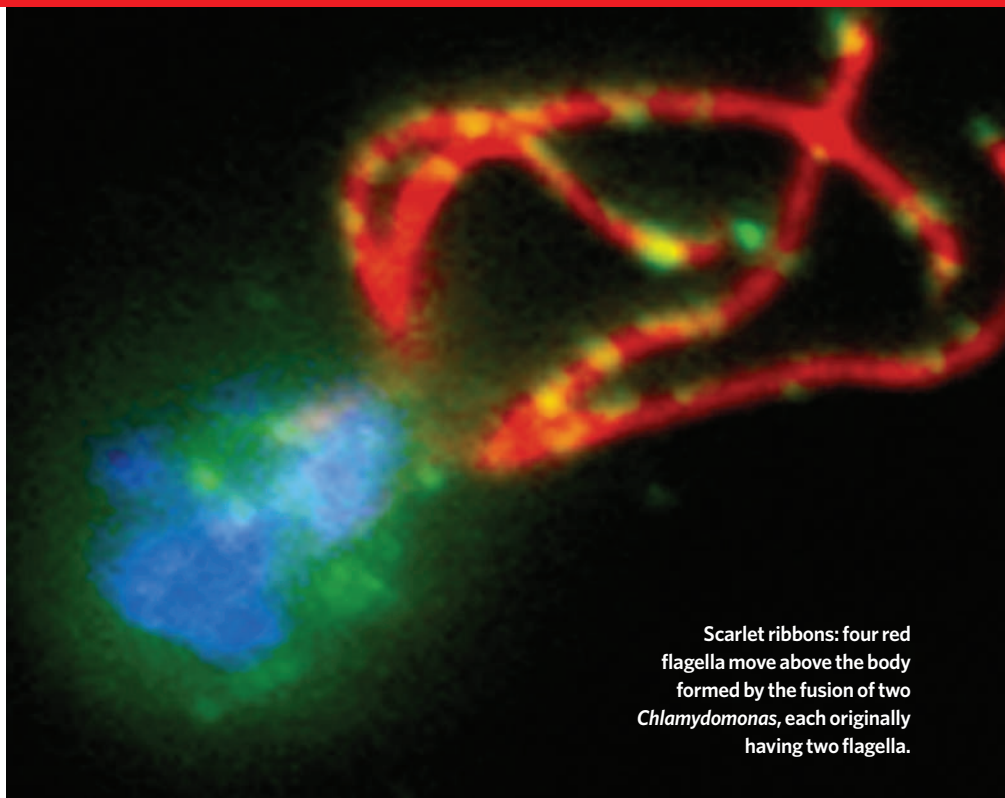
Ciliopathy symptoms often vary in severity, and, unlike many inherited diseases, they are not always caused by mutations in a single gene. Some Bardet-Biedl patients, for example, need to carry mutations in three different genes before any symptoms appear¹². Such conditions are a half-way house between classic single-gene disorders and

complex diseases such as obesity that involve many genes, and they may help biologists work out how gene variants interact to cause disease.

They also hint that the collection of variations in cilia-related genes an individual inherits could influence how he or she responds to environmental influences such as a calorie-rich diet.

It's possible that the syndromes represent one end of a range of genetic variations in cilium function, with apparently normal individuals at the other. "Time will tell which [genes] are the most important and to what extent they work with each other or the environment," says Beales.

C.A.



Scarlet ribbons: four red flagella move above the body formed by the fusion of two *Chlamydomonas*, each originally having two flagella.

Natural selection would favour patches that bulged out from the surface of the cell, as this would increase the patches' sensitivity.

As signalling between cells probably played a role in the shift to multicellular life, cilia are likely to have helped. Nicole King, an evolutionary biologist at the University of California, Berkeley, has been investigating the role of signalling and the origins of multicellularity by studying choanoflagellates, the closest living single-celled relatives of multicellular animals. "We think that the common ancestor of choanoflagellates and the first animals had a single

flagellum," she says. For the moment, little is known about the choanoflagellate flagellum, but more insights will come from genome projects now underway. Although choanoflagellates share some signalling systems with multicellular animals, they lack many others. For example, they have fragments of gene sequence that are similar to hedgehog, but, as yet, there is no evidence that they have hedgehog signalling themselves. The full range of signals first shows up in sponges — primitive multicellular animals — suggesting that the raw material of signalling was there in single-celled animals, and expanded upon as multicellularity developed. "It's easy to see how signalling may have been a pre-adaptation to multicellularity and that it might have been co-opted," King says.

It's an intriguing thought that a tiny structure sitting on almost every cell in our bodies links back to a time when cilia were helping cells first get together, and that it still plays a key part in keeping cells together today. As biologists discover yet more roles for cilia, these once obscure organelles seem set for the limelight.

Claire Ainsworth is a freelance writer in Southampton, UK.

1. Afzelius, B. A. *Science* **193**, 317–319 (1976).
2. Nonaka, S. *et al. Cell* **95**, 829–837 (1998).
3. Panzour, G. J. *et al. J. Cell Biol.* **151**, 709–718 (2000).
4. Pan, J. & Snell, W. J. *Mol. Biol. Cell* **13**, 1417–1426 (2002).
5. Wang, Q., Pan, J. & Snell, W. J. *Cell*, **125**, 549–562 (2006).
6. Huangfu, D. & Anderson, K. V. *Proc. Natl. Acad. Sci. USA* **102**, 11325–11330 (2005).
7. Caspary, T., Larkins, C. E. & Andersen, K. V. *Dev. Cell* **12**, 767–778 (2007).
8. Rohatgi, R., Milenkovic, L. & Scott, M. P. *Science* **317**, 372–376 (2007).
9. Park, Y.J., Haigo, S. L. & Wallingford, J. B. *Nat. Gen.* **38**, 303–311 (2006).
10. Jékely, G. & Arendt, D. *Bioessays* **28**, 191–198 (2006).
11. Beales, P. L. *et al. Nat. Gen.* **39**, 727–729 (2007).
12. Katsanis, N. *et al. Science* **293**, 2256–2259 (2005).

Q. WANG

Steaming ahead

India's new Ministry of Earth Sciences is at the helm of ambitious plans to advance deep-sea and polar research.

K. S. Jayaraman reports.

India, despite being the only country with an ocean named after it, has not always been a global driving force in the field of oceanography, with most of its research focused on the seas close to its shores. Now Indian researchers are pushing beyond this traditional base, with a \$100-million-a-year drive deeper into their own waters and farther afield to the poles (see 'Push for the poles').

For instance, the Indian government is planning a new deep-sea research vessel to complement the *Sagar Kanya*, the flagship of the Indian research fleet. In collaboration with Russia, India is also building a robotic underwater vehicle that can dive up to 6 kilometres deep. And on the drawing board are dreams for a manned underwater submersible that Indian scientists believe would put the country on a par with more developed nations.

"I am really excited about the idea of India becoming a major blue-water research institution," says Henry Dick, a senior scientist at the Woods Hole Oceanographic Institution in Massachusetts, who is on the editorial board of the *Indian Journal of Marine Sciences*. "Indians have a tremendous contribution to make, and I see that as a great asset to the international community."

India is, after all, in an excellent geographical location — a suitable launching point for expeditions to the relatively little-explored Indian and Southern Oceans. Both play important roles in the formation of the Indian monsoon, and both contain underwater geological features of interest — such as the Southwest Indian Ridge, where oceanic plates are pulling apart at one of the slowest rates in the world. "This portion of the global plate-boundary system is the most poorly explored region on the globe," says Dick. "Basically, this is where the frontier of oceanographic research is, and India is located next to it." In addition, nearly 40% of the Southern Ocean can be reached only from the launching-off points of India and Australia, adds Maruthadu Sudhakar, senior scientist at the National Centre for



Floating labs: research vessels, such as *Sagar Kanya*, will assist deep-sea mineral extraction.

Antarctic and Ocean Research (NCAOR), which together with India's other government-funded laboratory of oceanography — the National Institute of Oceanography (NIO) — is located in the state of Goa.

Out of disaster

Still, Indian oceanography is a relatively new field. "Systematic oceanography in India really started with the International Indian Ocean Expedition in the 1960s," says Satish Ramnath Shetye, director of the NIO. That expedition produced the first oceanographic atlas of the Indian Ocean, and the core group of scientists set up the NIO in 1966. Today, with more than 200 researchers, the NIO is "the largest institution dedicated to ocean sciences in this part of the world," says Shetye.

The entire field got an unexpected boost after the official monsoon forecast failed to predict the driest season for decades in 2002 (see *Nature* **418**, 713; 2002). The Indian government asked

atmospheric physicist Roddam Narasimha to suggest ways to revamp the country's meteorology department, and his report concluded that India needed an agency more along the lines of the US National Oceanic and Atmospheric Administration. The recommendation might have remained just that but for C. N. R. Rao, chair of the science advisory council to the prime minister, who pushed hard to implement it — and whose group met for the first time to discuss it just after the devastating tsunami of 26 December 2004.

That disaster apparently convinced the government that oceans and atmosphere should be brought under the same umbrella. India's space and nuclear scientists have left their marks on global science, says seismologist Harsh Gupta, former secretary of the government's Department of Ocean Development and a driving force behind the new initiatives. "It is now the turn of oceanographers," he says. In July 2006, the new Ministry of Earth Sciences was born, bringing

M. M. SUBRAMANIAM & M. SUDHAKAR/NCAOR

together national programmes in ocean science, meteorology, climate, environment, seismology and polar research. In its first year, the ministry has been allocated US\$240 million and is staffed by some 8,000 scientists.

India's interest in the ocean that surrounds it is economic as well as scientific. The country's exclusive economic zone, or EEZ, extends by almost two-thirds of the land area, and India has long set its sights on deep-sea mining. In October, the state-funded National Institute of Ocean Technology (NIOT) in Chennai anticipates getting a new \$70-million research vessel, which is being built in Italy. It will be the mother ship for a \$5-million unmanned submersible, expected to be ready in two years with Russian help, whose main goal is to recover manganese-rich nodules of rock and sediment from the sea floor. A prototype dived to 205 metres last October, says Subramaniam Kathirolu, director of NIOT. A manned exploration vehicle remains something of a dream, with a token allocation of \$1.25 million in this year's budget for 'development'.

Ocean secrets

Although some researchers now see deep-sea mining as economically unfeasible (see *Nature* 447, 246–247; 2007), India continues to pursue it. A pilot plant in Udaipur that extracts copper, nickel and cobalt from manganese nodules dredged from the sea floor, has been operating for several years at a rate of 500 kilograms of nodules processed per day. India has also been looking at underwater volcanic mountains — seamounts — as potential sources for mining cobalt. The cobalt-rich crusts capping the seamounts are available at shallower depths than the manganese nodules, which are up to 4 kilometres deep. The cobalt content of the crusts is three to six times greater than that of nodules. Virupaxa Banakar, a senior researcher at the NIO, says there are promising results from the Afanasy-Nikitin seamount in the

Push for the poles

Even as India puts more resources into exploring its surrounding ocean, the research focus pushes farther afield towards the poles.

India already has two polar research bases in Antarctica, and a third, a US\$10-million base to be built at Larsemann Hills in Princess Elizabeth Land, was approved this spring (see *Nature* 447, 9; 2007). It also maintains a \$25-million ice-core laboratory run by Thamban Meloth at the National Centre for Antarctic and Ocean Research (NCAOR), which

holds samples gathered from Antarctic expeditions.

Forays were made into the Arctic as early as 1991, to study how Indian soldiers fighting at high altitude in the conflict with Pakistan might cope with the cold.

Now Indian scientists are embarking on their first fully fledged expedition into the Arctic, in collaboration with the Norwegian Polar Research Institute, which has a research facility on the island of Spitsbergen. "Our scientists are keen to give India's polar science programme a bipolar

perspective," says Rasik Ravindra, director of the NCAOR.

The first expedition will be split into two groups. The first left for Spitsbergen last week, and the second will go in February next year. The project, costing \$250,000 this year, is expected to run for several years.

India is also pursuing the possibility of building an Arctic-class research vessel. The design has been selected and it will be built in the next four or five years, says Ravindra.

K. S. J.

equatorial Indian Ocean — which is in international waters and cannot be mined without additional permits — and at several sites within India's EEZ.

Yet the secrecy with which India treats the oceanographic data from its EEZ is not going down well with the international community. "That is a great way to retard progress," says Dick. Indian researchers say they are bound by the guidelines of a 1975 parliamentary committee report that calls for "strict scrutiny" of foreign participation "in all aspects of oceanographic research related to ocean resources and coastal areas". For instance, India's forthcoming petition to claim an additional 1.5 million square kilometres of seabed will not contain magnetic or seismic data on the region, says Sivaramakrishnan Rajan, a senior scientist at the NCAOR.

Indian collaboration with foreign scientists might be helped, though, by the fact that India is on the verge of joining the Integrated Ocean Drilling Programme (IODP). The United States,

Japan and a coalition of 17 European countries are the primary members of this deep-sea drilling programme; India is looking to join as an associate member, as China is already. As part of the IODP, the Indian government plans to explore its energy and mineral resources beneath the sea and also investigate the geology of the Indian plate. Of particular interest are three potential drill sites: one each in the Arabian Sea, the western Andamans, and the Bay of Bengal, whose floor is carpeted by the world's thickest sediments, at 22 kilometres thick. The drilling, however, has to take place far offshore. "We cannot allow drilling by foreign ships within our EEZ unless there is a policy change," says Rasik Ravindra, director of the NCAOR.

But interacting with the scientific community of the IODP could be valuable for young Indian scientists. And India desperately needs to alleviate a creeping manpower shortage in this field. Last year, Mangalore University, one of four universities in India that teaches oceanography, closed its marine-geology programme because it had only two students.

"We need 20 fresh scientists a year," says Shetye, "but it is hard to find them." Many of the marine geophysicists trained at the NIO are poached by offshore oil companies, he adds. The NIO gives 12-week courses to 300 university students each year in the hope that some will opt for a career in this area, and the new ministry has created nine ocean science and technology cells in universities.

But the results are yet to be seen. "We will not survive," says Shetye, "if we don't produce enough manpower to do research."

K. S. Jayaraman writes for *Nature* from Bangalore.

See Editorial, page 623.

S. R. SHETYE/NIO



Marine ambition: the National Institute of Oceanography, based in Goa, has led ocean research in India since 1966.

Public engagement means listening as well as talking

SIR — The Editorial 'Enough talk already' (*Nature* **448**, 1–2; 2007) concludes that governments should respond to the public concern expressed in engagement exercises, and invest in research on the health and environmental risks of nanotechnologies. I agree. I would, however, suggest that this is not enough.

Although we need more scientific research on the risks of nanotechnologies, we also need to encourage broader dialogue on notions of progress, quality of life, human needs and our visions of the future — both with and without nanotechnology.

In the social sciences, the concept of uncertainty has been extended beyond that of risk and a lack of research. First, within complex, open and interacting social and natural systems, there is an inherent and irreducible form of uncertainty that prevents the full range of impacts being delimited. An additional form of uncertainty results from the diverse values, interests and positions held on questions such as what actually constitutes social and environmental health. Finally, given the novel properties used within nanotechnologies, there will also inevitably be novel impacts that we are currently simply ignorant about. This is ignorance about the right questions to ask, rather than ignorance about the answers.

This means that we need a broader dialogue to take place, about the real-life value of potential applications coming from nanotechnology. Otherwise we risk falling into the trap of believing we can base decisions about nanotechnologies on an assessment of their potential impacts alone, disregarding our values in the face of multiple forms of uncertainty.

Public-engagement exercises can begin this kind of dialogue — but not if their purpose is simply building public trust in order to win acceptance of potentially controversial technologies.

Fern Wickson

Centre for the Study of the Sciences and the Humanities, University of Bergen,
PO Box 7800, 5020 Bergen, Norway

Public engagement: both sides need to be realistic

SIR — Your Editorial on engaging the public over nanotechnology ('Enough talk already' *Nature* **448**, 1–2; 2007) captured many of the key achievements stemming from the convergence of high technology and new democratic practice, as well as the challenges still faced.

As director of the public-participation

organization Involve (www.involve.org.uk), I would like to add that we need a more mature relationship between science and society, whereby both sides are open about their concerns and aspirations and realistic about what they can offer.

Too often science is equated to evidence. But having, in an earlier role, commissioned scientific research for the UK Department for Environment, Food and Rural Affairs, I am aware that the answer you get can depend to a large extent on who does the research and how their contract is configured. Because trust is built through experiencing openness and honesty, the public need to understand science, warts and all.

A good start would be to move away from portraying narrowly calculated technological risks as accepted facts (when they rarely are) to being open about the great expanse of uncertainty that scientists are constantly navigating.

Science is almost always a journey into the unknown. That includes unpredictable benefits and uncertain costs.

Richard Wilson

Involve, 212 High Holborn, London WC1V 7BF, UK

Physics Nobels should favour inventions

SIR — Alfred Nobel left a fortune to finance annual prizes to be awarded "to those who, during the preceding year, shall have conferred the greatest benefit on mankind". One part, he stated, should be given "to the person who shall have made the most important discovery or invention within the field of physics".

Nobel did not emphasize discoveries. But these are much more respected by the scientific community than are inventions: 77% of Nobel prizes in physics have been given to discoveries, compared with only 23% to inventions.

This emphasis on discoveries has moved the Nobel prize away from its original intention of rewarding the greatest contribution to society in the preceding year.

Discoveries and inventions depend on each other. Many discoveries were only made possible through the invention of certain measurement instruments, and without earlier theories, many inventions would have been inconceivable.

The fundamental difference between the two, however, is that the result of an invention is typically an artefact or process, whereas a discovery is an abstract theory. Although both require prior theories and a process of experimentation, and both have a utilitarian function, discoveries aim to be as general as possible, whereas inventions strive to be concrete.

A closer look at the 17 inventions that won

Nobel prizes before 2005 reveals that 11 of them (64%) are measurement instruments, for example the scanning tunnelling microscope.

Only three winning inventions have had direct practical applications to society: the gas regulator-controlled buoys made by Nils Gustaf Dalén were subsequently used in lighthouses; the transistor invented by John Bardeen, Walter Brattain and William Shockley is widely used in electronic devices; and Jack Kilby's work on the integrated circuit led to the development of personal computers.

Awarding more Nobel prizes for inventions would encourage inventors to tackle important problems such as global warming or the gap between the developed and developing worlds. The award given to Kilby for the development of the integrated circuit is a good example.

The invention of the electric telephone, first patented by Graham Bell, was a missed opportunity for a Nobel prize to acknowledge an invention that has brought the world closer together. But there is still hope for Tim Berners-Lee's invention of the World Wide Web.

Christoph Bartneck, Matthias Rauterberg

Department of Industrial Design, Eindhoven University of Technology, Den Dolech 2, 5600MB Eindhoven, The Netherlands

Traditional remedies put animal species at risk

SIR — Both your Editorial 'Hard to swallow' and your News Feature 'A culture in the balance' on traditional Chinese medicine (*Nature* **448**, 106 and 126–128; 2007) focused on herbal remedies. However, although herbal formulations make up the bulk of traditional Chinese medicine, many animal-based remedies are also used.

These often expensive remedies are increasingly sought after in China, and although only a small proportion of the tissue used comes from endangered species such as rhinoceroses and tigers, the demand is having destructive effects on many organisms. In particular, populations of many turtle and tortoise species, both in China and around the world, are declining rapidly as they are captured in the wild and their shells ground into a jelly that is thought to cure diseases such as cancer.

The ecological effects of the use of wild-caught animal tissues as part of traditional Chinese medicine are an important issue that must be part of any discussion of its merits and disadvantages.

Margaret B. Murphy

Department of Biology and Chemistry, City University of Hong Kong, 83 Tat Chee Avenue, Kowloon, Hong Kong

COMMENTARY

New uses for old drugs

It takes too long and costs too much to bring new drugs to market. So let's beef up efforts to screen existing drugs for new uses, argue **Curtis R. Chong** and **David J. Sullivan Jr.**

Fast, affordable drug development is a vision that contrasts sharply with the current state of drug discovery — which also neglects too many diseases of the poor. An analysis¹ of 68 approved drugs estimated that it takes an average of 15 years and US\$800 million to bring a single drug to market. And despite a doubling in research spending by the US National Institutes of Health (NIH) to \$27 billion in 2003, the number of new drugs approved by the US Food and Drug Administration (FDA) each year remains constant at 20–30 compounds². At this rate it will take more than 300 years for the number of drugs in the world to double.

The current costly and time-consuming paradigm of drug discovery is ill-equipped to combat rapidly emerging diseases, such as avian flu, drug-resistant pathogens and diseases that have a small financial market. One solution is to identify new uses for existing drugs. As the pharmacologist and Nobel laureate James Black said, “the most fruitful basis for the discovery of a new drug is to start with an old drug.” Because existing drugs have known pharmacokinetics and safety profiles and are often approved by regulatory agencies for human use, any newly identified use can be rapidly evaluated in phase II clinical trials, which typically last two years and cost \$17 million¹. In this way, drug developers can bypass almost 40% of the overall cost of bringing a drug to market by eliminating much of the toxicological and pharmacokinetic assessments¹.

This back-to-basics approach is growing in popularity. At least 17 existing drugs are in various stages of clinical and animal testing for new uses (see Supplementary information), and a further 24 are already being remarketed by the pharmaceutical industry for new uses³. Although most successful crossovers have been

the result of chance observations or educated guesses, exceptions include the antibiotic ceftriaxone, which is a potential treatment for amyotrophic lateral sclerosis⁴, and whose new activity was discovered following the screening of 1,040 compounds from the National Institute of Neurological Disorders and Stroke (NINDS) custom collection in Gaylordsville, Connecticut. In the past, individual labs were limited to screening perhaps hundreds of compounds. Now, clinical drug collections like the NINDS library and the Prestwick Chemical Library in Washington DC offer more than 1,000 approved drugs for small-scale lab screening. In our view, what is needed is a more systematic approach to drug rediscovery that takes these valuable resources to the next level.

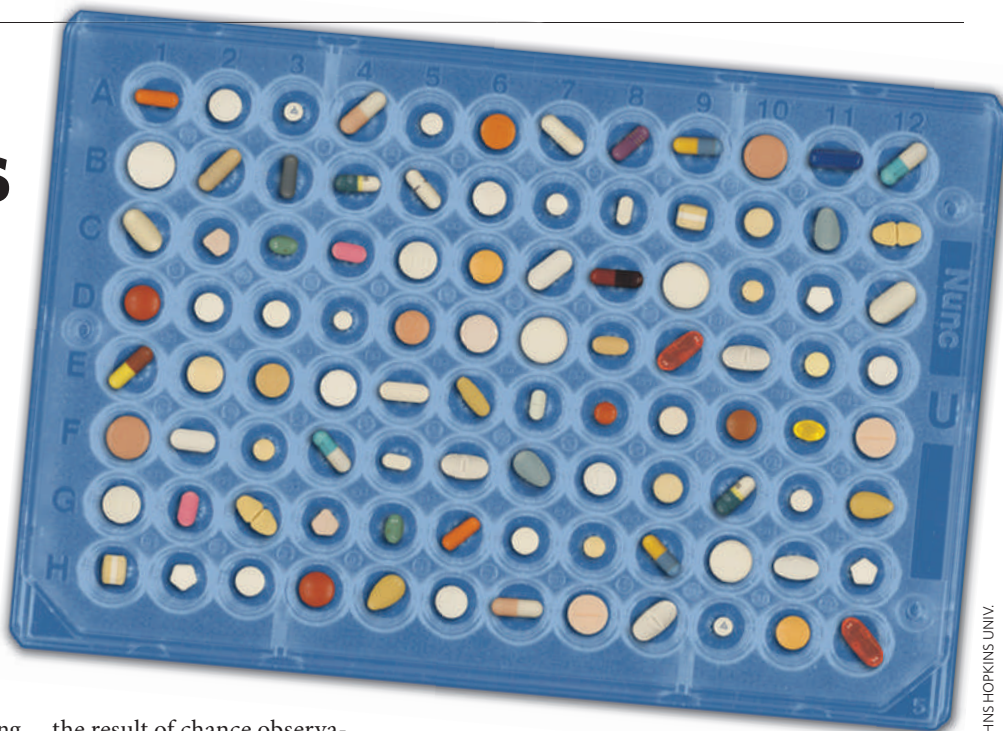
Historically, ‘repurposing’ old drugs has proved successful in bringing new therapies to the developing world. Today, even with the billions of research dollars available to create new drugs through public–private partnerships, and the promise of genomic data, there remains an enormous unmet need for therapies for neglected diseases⁵. A recent example of a repurposed drug is miltefosine, initially developed for breast cancer but now used for treating visceral leishmaniasis⁶. This disease is caused by a sand-fly-transmitted parasite and kills an estimated 500,000 people each year. In fact, miltefosine failed phase II testing for tumour reduction and the drug was never approved by the FDA for cancer therapy. However, *in vitro* and

animal studies indicated anti-infective activity, and phase II trials confirmed miltefosine as a viable treatment for visceral leishmaniasis⁶.

Cost cutting

Cost is one reason to revisit existing drugs: roughly 1,000 of the 10,000 or so drugs ever tested in clinical medicine are covered by patents, so most drugs can affordably be redeployed in the developing world. Safety is another compelling reason. Phase IV clinical studies, which monitor post-marketing safety, cost around \$100 million per drug to perform in developed countries¹ and are nearly impossible in countries without an established healthcare infrastructure. Because many existing drugs have undergone phase IV surveillance in millions of patients, the same stringent safety standards required by users in developed countries can be offered to patients with neglected diseases in the developing world.

Despite the promise of finding new uses for existing drugs, a comprehensive collection of the approximately 9,990 drugs known to clinical medicine does not exist. This number includes 2,933 unique drugs approved by the FDA since 1938 (ref. 7), 1,107 drugs in the 2006 FDA Orange Book, 888 drugs in the 2006 Physician Desk Reference, and 7,057 drugs that are either approved abroad or have entered phase II clinical trials, as indicated by a US Adopted Name or International Non-proprietary Name⁸. Excluding antiseptics, pharmaceutical aids, therapeutic plant or animal extracts, and vaccines, we estimate that there are 8,850



S. BLACKBURN/JOHNS HOPKINS UNIV.

“The most fruitful basis for the discovery of a new drug is to start with an old drug.”

The largest publicly accessible collection of existing drugs is the Johns Hopkins Clinical Compound Library (JHCCL; www.jhccsi.org), where we both work. This now has 1,500 available compounds, which together with the NINDS collection represents 22% of drugs that have ever entered the clinic⁷. An estimated 1,600 additional approved drugs can be purchased by researchers, expanding coverage to nearly 40% of the existing drug space (Fig. 1). These compounds are the low-hanging fruit as far as cost and patent restrictions are concerned.

To build a library of all 8,850 clinical compounds will require organic synthesis or donation of the remaining 60%. A comprehensive library should also include major drug metabolites, as these often have distinct pharmacological properties. For example, fexofenadine, which is a non-sedating antihistamine, lacks the cardiotoxic side effects of its parent terfenadine⁹, and isoniazid (for tuberculosis) and primaquine (for malaria) are not active unless first metabolized¹⁰. Adding metabolites might increase the size of the library by as much as 25%.

Chemical synthesis of drugs and metabolites that cannot be purchased will be costly, perhaps running to several millions of dollars. This is a substantial investment, yet, in our view, identifying just one new clinical use for an existing drug would more than make up for the resources invested in the library, given the

And although a collection of 10,000 compounds sounds ambitious, it pales in comparison with the libraries of novel unmarketed compounds (100,000 or more) held by pharmaceutical companies. Unlike *de novo* drug discovery, which requires specialized robotics to screen hundreds of thousands of compounds, the smaller size of the proposed clinical compound library makes screening feasible in virtually any laboratory. JHHCL currently provides its collection of drugs in 24×96 -well plates, and this could easily be scaled up to 27×384 -well plates for a library of 10,000 or more. At this scale, specialized screening centres (as used by the NIH Roadmap initiative) will not be necessary.

Once the clinical compound library is complete, it should become a public resource available to the scientific community for screening on any disease target. As an open repository, the collection should be distributed rapidly and provided at minimal cost to investigators from both academia and industry with reasonable screening proposals. The existing JHCCL collection is now available to any laboratory for a small charge of \$5,000 to cover shipping and replacement costs. In our view, access to the library should complement the decentralized, independent spirit of academia and should not entail a lengthy or complicated review process. An excellent example of an open repository is the synthetic and natural products collection maintained by the Developmental Therapeutics Program of the National Cancer Institute¹¹.

"We challenge the scientific community to create a comprehensive clinical drug library to screen every neglected disease by 2011."

The only requirement to access the library should be agreement to deposit results in an open database upon publication, just as the raw data from structural biology and microarray experiments are made publicly available now. To aid the interpretation of initial screening results, researchers will need a comprehensive public database containing the pharmacokinetics and clinical properties of the drugs in the library. For example, knowledge of the peak blood-plasma levels of drugs is helpful in determining whether novel activities discovered by screening are clinically significant. These data are often held by drug manufacturers or the FDA, but are not always publicly available in the scientific literature, although they can be found after some time and expense in the patent literature.

Genetic information on the biological target of each drug in the database will assist in identifying other diseases for which it might be used. The not-for-profit bioinformatics resource DrugBank in Canada has already linked genetic targets with around 1,000 drugs¹². JHCCL has plans for a relational database of this sort, although curating such information requires additional resources. Still, Wikipedia has already compiled descriptions of more than 1,800 drugs currently in use by relying on the work of volunteers.

Finding new uses for existing drugs is a proven short cut between the lab and the clinic. We challenge the scientific community to create a comprehensive clinical drug library and use it to screen every neglected disease by 2011. To build on past successes in drug rediscovery will mean screening all known pharmacological space in a systematic way.

Curtis R. Chong is in the Department of Pharmacology and Molecular Sciences, Johns Hopkins University School of Medicine, Baltimore, Maryland 21205, USA.

David J. Sullivan Jr is at the Malaria Research Institute, Johns Hopkins Bloomberg School of Public Health, Baltimore, Maryland 21205, USA.

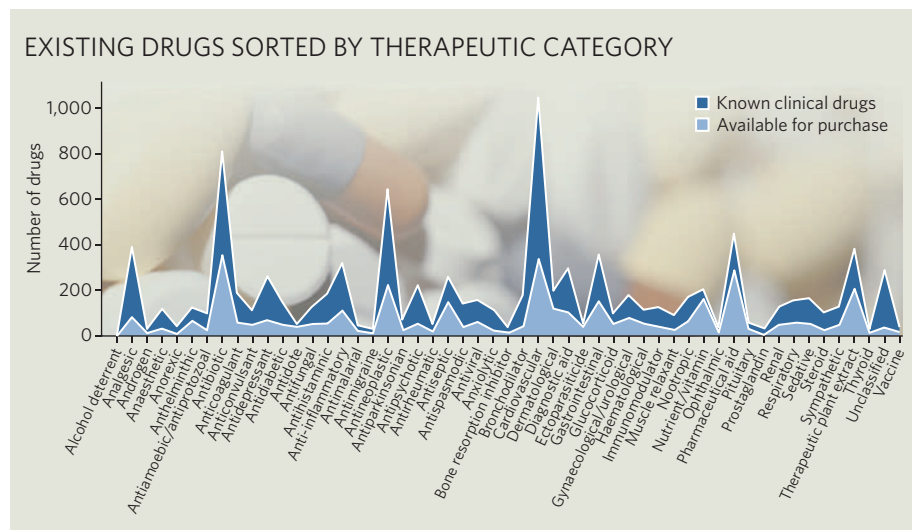


Figure 1 | The existing universe of 9,990 drugs and their availability.

- DiMasi, J. A., Hansen, R. W. & Grabowski, H. G. *J. Health Econ.* **22**, 151-185 (2003).
- Cohen, F. J. *Nature Rev. Drug Discov.* **4**, 78-84 (2005).
- Ashburn, T. T. & Thor, K. B. *Nature Rev. Drug Discov.* **3**, 673-683 (2004).
- Rothstein, J. D. *et al. Nature* **433**, 73-77 (2005).
- Moran, M. *PLoS Med.* **2**, e302 (2005).
- Sundar, S. *et al. N. Engl. J. Med.* **347**, 1739-1746 (2002).
- Chong, C. R. *et al. Nature Chem. Biol.* **2**, 415-416 (2006).
- Lipinski, C. A. *et al. Adv. Drug Deliv. Rev.* **46**, 3-26 (2001).
- Sussman, G. L. *et al. J. Allergy Clin. Immunol.* **104**, 100-106 (1999).
- Weber, W. W. *Mol. Diagn.* **4**, 299-307 (1999).
- Voigt, J. H. *et al. J. Chem. Inf. Comput. Sci.* **41**, 702-712 (2001).
- Wishart, D. S. *et al. Nucleic Acids Res.* **34**, D668-D672 (2006).

Supplementary information is linked to the online version of this article at www.nature.com/nature

Acknowledgements

Acknowledgements
We thank Walter Pudelko for invaluable help with Supplementary Table 2.

BOOKS & ARTS

Social science goes virtual

Mathematical models could help us re-engage with reality rather than trying to reinvent it.

Complex Adaptive Systems: An Introduction to Computational Models of Social Life

by John H. Miller & Scott E. Page
Princeton University Press: 2007. 284 pp.
\$24.95, £14.95 (pbk); \$65.00, £38.95 (hbk)

Generative Social Science: Studies in Agent Based Computational Modeling

by Joshua M. Epstein
Princeton University Press: 2007. 352 pp.
\$49.50, £29.95

Philip Ball

The idea that the social sciences have anything to learn from the physical sciences has raised many hackles. Some social scientists suggest that to use particle-like models of 'agents' that interact via simple rules to explore the emergence of complex collective behaviour is to neglect the sociologist's obligation to explain why individuals behave the way they do. Ironically, this position displays a curious indifference to the 'social' aspects of life. In his recent book *The Flight from Reality in the Human Sciences* (Princeton Univ. Press, 2005), political scientist Ian Shapiro lamented what might be called the 'physicization' of social science. He claimed that mathematical models that mimic physics fail to engage with the political landscape of the real world and instead disgorge "stylized facts that turn out on close inspection not to bear much relationship to any political reality".

At face value, *Complex Adaptive Systems* by John Miller and Scott Page and *Generative Social Science* by Joshua Epstein seem to encapsulate all that Shapiro deplores, but in reality they are part of the solution, not the problem. Shapiro's complaint hinges on the way social scientists have embraced models taken from economics, which themselves emulate physics. This qualifier is in fact the central issue, which Miller and Page examine in illuminating detail. As Shapiro puts it, economic theory has developed "a perverse sense of rigor, where the dread of being thought insufficiently scientific spawns a fear of not flying among young scholars". The result is that the models take no account of real human behaviour, which is far too messy to permit any theorems that can be proved rigorously. So economic models become citadels of crystalline mathematical perfection that would shatter if touched by the harsh rays of reality.

It would be grossly unfair to suggest that this describes everything that happens in eco-



Computer simulations probe how the Anasazi culture spread in the American southwest.

nomics, let alone in all social sciences. But it is widespread, and is reflected in Miller and Page's comment that economists are scandalized to discover how cavalier physicists are in making conjectures that lack any fundamental justification. The irony is that some of the foundational aspects of statistical physics, which provided economists with the early conceptual framework for the neoclassical theory of market equilibrium, remain unproven in any rigorous mathematical sense.

It is absurd that a science as complicated and ill-posed as economics should demand a degree of rigour that not even physics enjoys. That's why these two books are part of an important trend in the social sciences. Both argue for the value of agent-based modelling (ABM) in social science. This approach involves "growing societies from the bottom up", as Epstein has put it, rather than devising analytically airtight theorems from first principles that are tractable but transparently wrong in what they assume and imply about human behaviour.

The aim of ABM is to study whether the macroscopic patterns or regularities that we observe in society, such as price equilibria or the appearance of behavioural norms, can be generated from decentralized, local interactions between collections of agents.

Epstein's book is a collection of papers that use this approach to explore phenomena as diverse as civil violence, retirement, the emer-

gence of classes and the spread of epidemics. His classic example is the modelling of the demographics of the Anasazi culture of the American southwest between AD 800 and 1300 on the basis of archaeological evidence. Miller and Page, meanwhile, aim to outline a general programme of what ABM is and how it might be conducted. Both books show that computational modelling is slowly beginning to take root in the social sciences. Economics, however, continues largely to resist the idea, as it is incompatible with the standard assumption that the economic system is at equilibrium.

ABM gives access to virtual worlds that rigorous theory cannot touch. In these worlds the actors may differ; they have access to limited, mostly local, information and are limited in their ability to use it; they learn from experience, make mistakes, switch allegiances and copy others. No one should mistake these realms for our own, but they certainly sound closer to it than the neoclassical model of identical rationalizing agents, in which there often seems to be no populations with sizes between two and infinity.

Newcomers to this field might nevertheless find the degree of abstraction unnerving. They might ask, for example, whether Epstein's ring of agents making binary choices based on majority polling of their neighbours, or the forest-fire models presented by Miller and Page, could possibly map onto a real social situation. Aren't

these just offering vague metaphors of untested relevance? Indeed, if I have a criticism of Miller and Page, it is that they don't sufficiently address the fearsome question of how such testing might be done. This is discussed in some detail in Scott de Marchi's *Computational and Mathematical Modeling in the Social Sciences* (Cambridge Univ. Press, 2005). But in any event, that isn't really the point. Shapiro suggests that the role of political theorists is to rove the political landscape "debunking myths and misunderstandings that shape political practice". Properly applied, ABM might do just that.

The famous segregation model of economist Thomas Schelling, who pioneered the

ABM approach in the 1970s, showed that a high degree of social segregation does not, as one might assume, imply extreme intolerance. Conversely, and relevant to today's political climate, it showed that a combination of mobility and choice may amplify marginal preferences or imbalances into major social divisions. Agent-based models may not describe reality, but they can show how interaction and nonlinearity produce social outcomes that could not be predicted simply by inspecting the behavioural rules. They undermine the common political presumption that group behaviour is a multiplied version of individual behaviour. They expose how ideas such as market efficiency may

mutate from predictions of simplistic theories into dogmas that are applied insistently to the real economy. They might not tell us why certain social phenomena happen, but they offer mechanisms for how they might.

The challenge, which cannot be over-emphasized, is to ensure that ABM does not get above its station. It is a tool, not just another method for imprinting belief and prejudice with the false authority of 'theory'. As such, these models could form part of a toolbox that helps social scientists to re-engage with reality rather than trying to reinvent it.

Philip Ball is author of *Critical Mass* and a consultant editor for *Nature*.

In the eye of the storm

Storm World: Hurricanes, Politics, and the Battle Over Global Warming

by Chris Mooney

Harcourt: July 2007. 392 pp. \$26

James Elsner

Chris Mooney's follow-up to his *The Republican War on Science* (Basic Books, 2005) is a reconnaissance flight into the turbulent debate over a link between hurricane activity and global warming. The flight log is compelling enough for Hollywood. It records a clash between the empiricist climate scientist William Gray (think Ian McKellen) at Colorado State University and the theoretician Kerry Emanuel (think Tom Hanks) at the Massachusetts Institute of Technology. Journalist Mooney has a scriptwriter's flair for pitting his protagonists against each other and dishing the historical and methodological back story in vivid prose: "If we're really making the deadliest storms on Earth still deadlier, it will represent one of humanity's all-time greatest foot-shooting episodes."

The debate swirls about the cause of the

recent upswing in severe hurricanes, especially over the Atlantic where evidence for a change is most compelling. Warmer tropical oceans will increase the potential intensity of tropical cyclones, but for Gray the causal chain ends with the ocean. "Nobody knows how the atmosphere works," he says, feeling that it is far too complicated to be captured by a computer. Emanuel, on the other hand, adds a further link to the chain, placing the blame on human meddling with the composition of the atmosphere.

Just a month before Hurricane Katrina's devastating strike on America's south coast on 29 August 2005, Emanuel published a paper in this journal (*Nature* **436**, 686–688; 2005) that ignited a scientific debate by linking storm strength to ocean temperatures. It also triggered a maelstrom of media coverage that resulted in the US National Oceanic and Atmospheric Administration (NOAA) closing ranks and claiming unequivocally that the increase in Atlantic hurricane activity since 1995 could be attributed solely to an ocean cycle unrelated to greenhouse warming. Mooney is at his best when describing

this sort of political tempest. By allowing what Emanuel calls the "party line" while discouraging dissenters, NOAA was, in Mooney's words, "gaming the release of information and trying to shift the debate in their favoured direction".

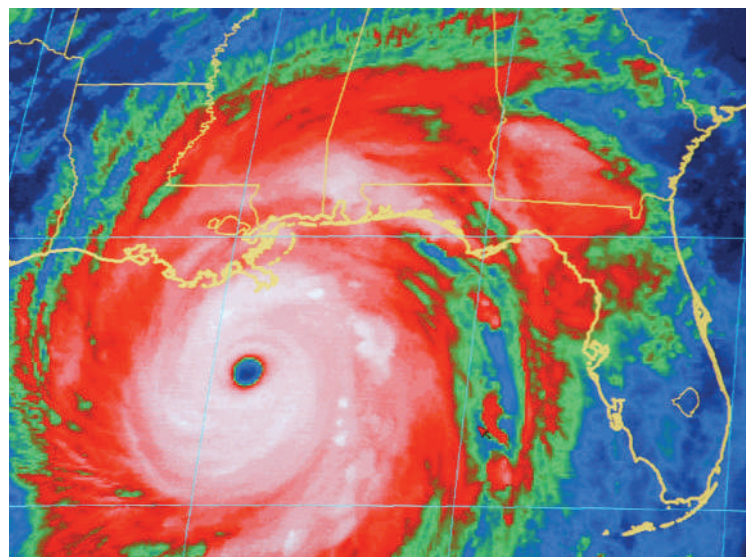
Mooney revisits his call, propounded in his earlier book and in subsequent newspaper and magazine columns, for scientists to do a better job of communicating science to the public and media. He urges researchers to stop pretending that they are nothing but objective "fact machines" and to instead give more general interpretations of their results and put them into a broader context.

Drawing on scientific conferences and on interviews with hurricane and climate scientists during 2006, Mooney covers plenty of ground, from heat engines and synoptic meteorology to computer modelling, and all without equations. At times *Storm World* feels hurried, US-centric and somewhat uneven, jumping between history, science and politics. But Mooney presents an accurate account of the clash between two of the most prominent climate scientists today. He is a good writer — "Scientists, like hurricanes, do extraordinary things at high wind speeds" — and his stories are consistently about people, giving the book a wide appeal.

In the end, he does give a clear picture of what the hurricane–climate change debate is about and where it might go next. As there are no answers, the book provides none. Not surprisingly, Mooney takes a liking to Gray, but cannot recommend his view that global warming has nothing to do with hurricane activity. Amusingly, Mooney also implies that, for storm climatologists, science sometimes plays second fiddle to entertaining soundbites.

Many scientists are contributing to one of the most important climate debates in history. Neither side is completely wrong and both would do well to study the full breadth of literature, to which *Storm World* is a useful addition. It's a great summer read, while the story continues. Let's hope there are more answers in the sequel.

James Elsner is a professor of geography at Florida State University, Tallahassee, Florida 32306, USA.



Debate swirls about the recent upswing in severe hurricanes such as Katrina.

NOAA/AP

Remarkable but not so unusual

The Comet Sweeper: Caroline Herschel's Astronomical Ambition

by Claire Brock

Icon Books: May 2007. 208 pp. £9.99

Judith P. Zinsser

Dava Sobel and Patricia Fara have proved that there is an audience for popular yet scholarly stories of the adventures of scientists at the beginning of the modern age. Claire Brock's brief study of the astronomer Caroline Herschel (1750–1848) intends to please these same readers. The easy prose of *The Comet Sweeper* is laced with quotations from Herschel's two autobiographies and her astronomical diaries. All the important facts of this interesting woman's life — from her youth in the German principality of Hanover in the late eighteenth century to her work with her astronomer brother, William — are here. Brock describes Herschel's considerable accomplishments, which included the discovery of comets and nebulae and the publication of two extensive astronomical guides: a revised edition of John Flamsteed's *Historiae Coelestis*, a catalogue of the 'fixed stars' and the standard authority on the heavens, and a catalogue of star clusters and nebulae, a similar listing that she and her brother made from their meticulous nightly sweeps of the sky.

Unfortunately, Brock has an agenda that leads her into some of the pitfalls often encountered by biographers of famous women in history. Brock describes her task as "rehabilitating Caroline Herschel". She criticizes historians whom she feels acknowledged Herschel's dis-



Caroline Herschel discovered comets and nebulae.

coveries but did not give proper attention to the astronomer's considerable ambition and desire for "independence". Brock wants to prove that Herschel was not the dutiful daughter and sister usually portrayed, but an autodidact struggling against the constraints of her day. This leads Brock to overdramatize these constraints, to comb Herschel's personal writings for hints of rebellion and to offer mismatched psychological interpretations.

Herschel was certainly as disadvantaged as

any younger sister in a large family — she was one of ten children — of no particular education or rank and with limited financial resources. Disfigured by smallpox as a young child, with no hope of a dowry from her musician father and no gift for women's trades, despite some lessons from a milliner, it was not a cruel mother, as Brock suggests, that left Herschel with little prospect of marriage or respectable employment outside the household. Her brother William must have felt he was providing generously for his unfortunate sibling by bringing her to England to run his household, allowing her to sing with his choir and to copy their musical scores.

Brock acknowledges that Herschel often wrote of her desire to be "useful" and that she defined this utility within the confines of service to her family. When William

trained her to become his assistant in his new-found avocation for astronomical observation, he gave her no independence, but he did give her the means to scientific accomplishment and fame. Without William, there would have been no discoveries and no recognition.

The root of the problem with the way Brock has chosen to frame her biography may be that although Herschel indeed deserves her fame, her life was not so unusual for the times. Brock writes that Herschel grew up "exploited

BRIDGEMAN ART LIBRARY

EXHIBITION

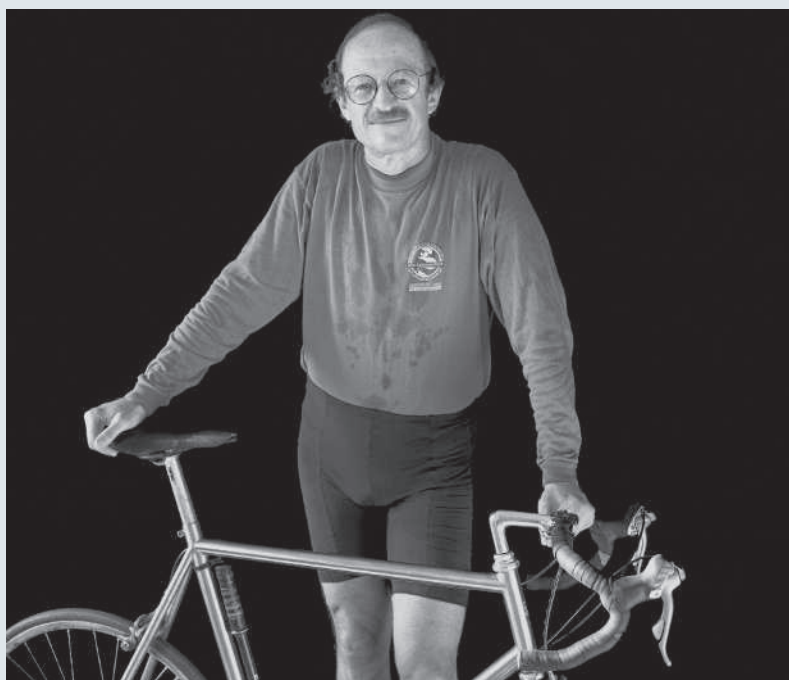
Famous faces

This arresting portrait of Nobel prizewinner Harold Varmus is one of many images of scientific luminaries by Mariana Cook on public display in the *Faces of Science* exhibition at the US National Academy of Sciences in Washington DC until 30 September.

Cook, who studied with the pioneering nature photographer Ansel Adams, hopes to "humanize" scientists through her work, to illuminate individual characters and explore possible commonalities.

Each portrait is paired with a short essay explaining how the subject became drawn to his or her chosen field — as in Cook's book of the same name (W. W. Norton, 2005). Other leading researchers captured in iconic shots include E. O. Wilson, Elizabeth Blackburn and Frederick Sanger.

Wilson sits beatifically in a pile of autumn leaves; Sanger smiles beneath an orchid. Sitters such as these share "an elasticity of mind uncommon to most of us", Cook has said. Collections of her photographs are also held by the Museum of Modern Art and the Metropolitan Museum of Art in New York.



M. COOK

and enslaved" by the drudgery of housework. Brock characterizes a father's caution not to expect an offer of marriage as "obviously" having a "devastating impact" on the young girl. European women's history shows us that Herschel was neither enslaved nor devastated but, like other women of accomplishment, made the best of her circumstances. Earlier in the eighteenth century the women of the famous Winkemann family of Prussian astronomers also had the patience and skill to watch the stars for hours at a time, and to record their

observations with care. In this exciting period of early modern science, amateurs, whether female or male, if in the right place at the right time, could make significant contributions to knowledge.

I wish that Brock had let go of the rehabilitation project and focused instead on the richness of Herschel's autobiographies, which she does recognize. They have already been edited by Michael Hoskin, an eminent historian of astronomy, but Brock, with her literary training, has an excellent eye for

the vivid quotation. An analysis of the two versions of her past that this remarkable woman created in her old age would make a fascinating double journey from eighteenth-century Hanover to Bath to Windsor, and back to Hanover 50 years later — revealing what Herschel herself chose to illuminate, cloud, or hide altogether. ■

Judith P. Zinsser is author of the recently published *La Dame d'Esprit: A Biography of the Marquise Du Châtelet* and is a professor of history at Miami University, Oxford, Ohio 45056, USA.

EXHIBITION

Palaeontology meets Hanna-Barbera

The Homo species

by Hyungkoo Lee

Korean Pavilion, 52nd Venice Biennale, Venice, Italy
(until 21 November)

Colin Martin

Korean artist Hyungkoo Lee's quirky take on palaeontology is a showstopper among the acres of international contemporary art on offer at the 52nd Venice Biennale. Lee, the first artist to have a solo show in his country's pavilion, immediately grabs the attention of visitors with a dramatically spotlighted moment from the world's geological past, staged in the centre of a darkened room. The skeleton of a predator, pouncing on its transfixed, smaller prey, initially evokes the natural history tableaux encountered in museums. Closer examination reveals that the exaggerated quality of Lee's tableau owes more to cartoon animators William Hanna and Richard Barbera than to palaeontologists. Reading the exhibit titles, *Mus Animatus* and *Felis Catus* [sic] *Animatus*, confirms that we're looking at Tom and Jerry, caught in their perpetual cycle of tragedy narrowly averted, with Jerry outwitting Tom to escape in the nick of time. This work is part of Lee's *Animatus* series, in which he "explores hypothetical anatomical possibilities of beings without existential evidence".

By exploring two layers of unreality, Lee achieves a double deception. He transforms familiar animated two-dimensional cartoon characters, which we know to be unreal, into intricately realized three-dimensional 'fossils' created from his imagination. He might give the appearance of working in a quasi-scientific manner but, unlike palaeontologists, he fakes the fossilized remains he uses. "Merely seeing Lee's work gives no clues to the complexity of its creation," comments Asian art specialist Howard Rutkowski. In this exhibition, however, Lee carefully documents his working methods and displays this evidence of his deception throughout the pavilion, as a



Intended to deceive: Hyungkoo Lee's *Mus Animatus* and *Felis Catus Animatus*.

context for viewing his finished works.

In an adjacent room, Lee reveals his artistic sleight of hand in a semicircular vitrine that contains bones of real animals, various implements, anatomical drawings of real animals and their animations, chemicals, modelling tools and fake bones. The assorted tools and chemicals not only emphasize the artist's intention to deceive, but also beseech the viewer to believe anyway. A large black-and-white

photograph also evokes scientific research by showing technicians in white coats in a laboratory. It is obviously staged, however, and they are pouring plaster into moulds to create the fake fossils. Lee's jokes and stories involve narrative build-up before revealing their punch lines. He works backwards, showing us the denouement first and then revealing what preceded it, like a cartoon screened in reverse. ■

Colin Martin is a writer based in London.

NEWS & VIEWS

FEMTOPHYSICS

Double vision

Andrea Cavalleri

By cunningly diffracting X-rays twice from an exploding nanometre-scale sphere, holographic images can be made of a tiny system evolving at lightning speed. The technique could be used to picture atomic dynamics.

On page 676 of this issue¹, Chapman *et al.* demonstrate how coherent, ultrafast X-ray pulses from a free-electron laser² can be used to yield a series of femtosecond-resolved holographic images of an evolving nanometre-scale object. This exquisite resolution in both time and space brings us closer to a long-sought-after goal — the ability to observe atomic-scale processes as they happen.

The femtosecond (10^{-15} s) is the natural timescale of atomic motions. Optical pulses of femtosecond duration thus allow us a glimpse of the evolution of chemical reactions, phase transitions and other elementary atomic interactions — processes that could otherwise be followed only indirectly. Traditional time-resolved optical techniques operating at near-visible wavelengths can often only establish how fast many of these phenomena occur, being blind to what exactly is happening. This is because they are only sensitive to spectroscopic signatures that are difficult to interpret without knowledge of the atomic structures that produced them. Ideally, these structures should also be sampled on the femtosecond timescale.

This frontier territory has recently been conquered with a first generation of X-ray and electron sources, including both 'table-top' equipment^{3,4} and accelerator-based techniques⁵. Measurements of femtosecond atomic-structural dynamics have thus become possible^{6–8}. But the ultimate goal — the determination of all atomic positions of a solid or a molecule with the same sort of time resolution — requires short pulses of X-rays or electrons to be combined with other advanced crystallographic concepts and techniques.

Specifically, optical imaging requires the 'inversion' of a pattern of light scattered (diffracted) from an object. This diffraction pattern is related to the shape of an object through a mathematical operation known as a Fourier transformation, which encodes the image in propagation directions and phases of the electromagnetic field. To obtain an image, one must be able to invert the Fourier transformation. Lenses do precisely that: they can, in fact, be thought of as physical computers that perform an inversion by recombining

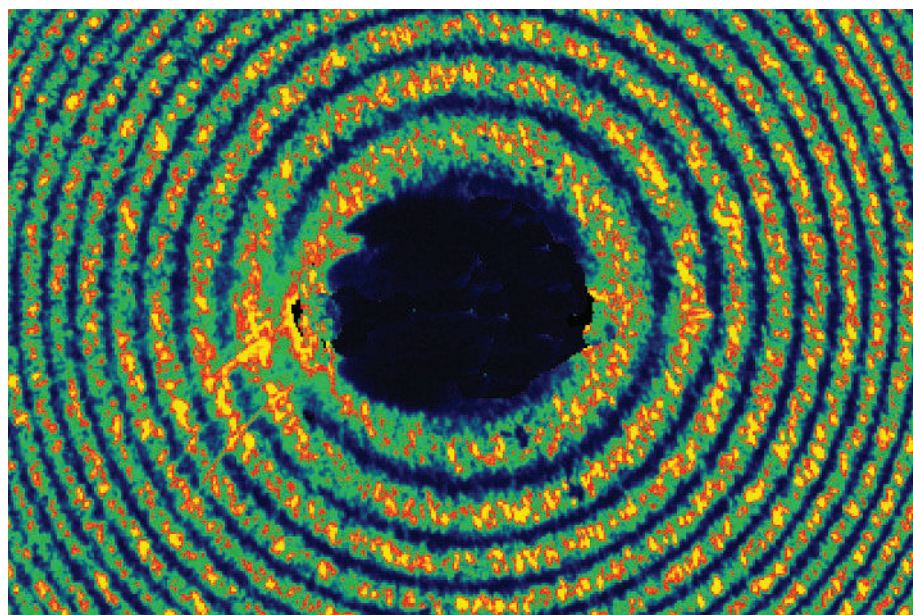


Figure 1 | Nano-explosion. A typical two-pass coherent diffraction pattern encoding shape and evolution of an object, as used by Chapman *et al.*¹ for their nanometre-scale, femtosecond holographic imaging.

different rays at a given distance and making them interfere to form a magnified or demagnified replica of the object.

Where lenses do not exist or are hard to make, as is the case at X-ray wavelengths, the best one can do is record the diffraction pattern on a screen. This is a destructive process that throws away half of the necessary information — that contained in the phase of the electromagnetic field. Alternative methods must then be developed to fully recover an object's shape. For example, by measuring the diffraction pattern on the screen with sufficiently high spatial resolution, and making assumptions about the size of the object⁹, trial-and-error numerical methods to invert the Fourier transformation can be applied^{10,11}.

An alternative approach is to add a second, reference light wave to the field scattered from the object, which allows an image to be recovered from scratch — the technique known as holography¹². But holography is only feasible if one has a well-behaved X-ray beam to start with. The quality of an optical beam is usually quantified in terms of coherence, which is a

measure of the volume over which the electromagnetic field oscillates in lock-step with itself. Free-electron lasers, in which coherent light is produced by amplification through a beam of relativistic electrons, are the first sources devised that are both coherent and generate ultrashort pulses in the X-ray regime. This opens up new possibilities for structure determination based on holography, interferometry or coherent diffraction, as well as for studies that investigate the femtosecond dynamics of matter in new ways.

Chapman *et al.*¹ combine an imaginative experimental geometry with cutting-edge multilayer mirror technology and special imaging algorithms to achieve time-resolved holography. They use this to monitor the X-ray-induced explosion of a microscopic object. An X-ray pulse first impinges onto a tiny sphere, diffracting from it and initiating its explosion. The pulse then travels to a multilayer mirror behind the sphere, hitting it almost at a right angle. Next, it is reflected back and diffracts from the sphere again after a given time delay (see Fig. 1 on page 676).

H. N. CHAPMAN ET AL.

Because of the backing mirror's slight tilt, the reflected pulse follows a slightly different path from the beam that originally interacted with the sphere. The two diffraction patterns — one from the unperturbed sphere, one from the exploding sphere — overlap on a screen and interfere (Fig. 1). The first pattern is always the same, whereas the second varies with the time delay, which can be controlled by the distance between the object and the backing mirror. The interference pattern encodes both the shape of the exploding object and the time delay between the two pulses. The pulse thus acts as a reference beam to itself, permitting a true hologram of the evolving object to be constructed.

Owing to the relatively long wavelength used in this experiment (32.5 nm), it was only possible to probe scales of tens of nanometres. But all the conceptual ingredients are in place, and we can afford to dream of what will become possible when the wavelength is reduced. Most straightforwardly, experiments of this type will become the key towards realizing one of the most ambitious *gedanken* applications of X-ray free-electron lasers — the imaging of single molecules with very high photon doses. This technique would beat the disruption of the molecule initiated by the flux of incident X-rays by taking all the structural information in one ultrashort burst^{13,14}.

As X-ray wavelengths are decreased towards the final goal of 1 ångström (10^{-10} m), the size of the objects that can be imaged decreases towards the atomic scale. At the same time, however, structures also become shorter-lived, and the constraints on the pulse duration more stringent. For this reason, the jury is still out on whether single-molecule imaging using free-electron lasers will work for the smallest timescales.

To perform holography of the disruption process with the necessary time resolution, shorter distances between the object and backing reflector will be required — less than 1 µm for the necessary resolution of near 5 femtoseconds. To achieve this, the imaged object will probably have to be deposited directly on the multilayer mirror, and different grazing-incidence angles used to tune the time delay.

Femtosecond holography could also be used in other fields. In condensed-matter physics, more and more experiments have demonstrated static imaging using lensless techniques^{15,16}. The free-electron laser at DESY in Hamburg used by Chapman *et al.*¹ is now operating at a wavelength near 6 nm, and also at a secondary wavelength near 2 nm. These wavelengths are close to some important X-ray absorption edges that are often used for X-ray studies of solids¹⁷.

In experiments probing condensed matter, one will want to use geometries different from the scheme used by Chapman and colleagues¹. Of interest will be a dynamic behaviour that is controlled by different means, such as laser pulses, terahertz radiation or rapid, transient

magnetic fields. Thus, adapted, time-resolved holography might provide a new way to generate images on both microscopic and mesoscopic scales, overcoming the formidable challenges for those who seek to understand the dynamic physics of complex solids. Equally important, time-resolved imaging will offer a new way of looking at problems in biology and soft matter, in which many different scales in space and time are in play. ■

Andrea Cavalleri is in the Department of Physics, Clarendon Laboratory, University of Oxford, Parks Road, Oxford OX1 3PU, UK.

e-mail: a.cavalleri1@physics.ox.ac.uk

1. Chapman, H. N. *et al. Nature* **448**, 676–679 (2007).

2. Ackerman, W. *et al. Nature Phot.* **1**, 336–342 (2007).
3. Rischel, C. *et al. Nature* **390**, 490–492 (1997).
4. Siwick, B. J., Dwyer, J. R., Jordan, R. E. & Dwayne Miller, R. J. *Science* **302**, 1382–1385 (2003).
5. Schoenlein, R. W. *et al. Science* **287**, 2237–2240 (2000).
6. Cavalleri, A. *et al. Phys. Rev. Lett.* **87**, 237401 (2001).
7. Lindenberg, A. M. *et al. Science* **308**, 392–395 (2005).
8. Gedik, N., Yang, D.-S., Logvenov, G., Bozovic, I. & Zewail, A. H. *Science* **316**, 425–429 (2007).
9. Sayre, D. *Acta Cryst.* **5**, 843 (1952).
10. Fienup, J. R. *Appl. Opt.* **21**, 2758–2769 (1982).
11. Miao, J. W., Charalambous, P., Kirz, J. & Sayre, D. *Nature* **400**, 342–344 (1999).
12. Gabor, D. *Nature* **161**, 777–778 (1948).
13. Neutze, R., Wouts, R., van der Spoel, D., Weckert, E. & Hajdu, J. *Nature* **406**, 752–757 (2000).
14. Chapman, H. N. *et al. Nature Phys.* **2**, 839–843 (2006).
15. Eisebitt, S. *et al. Nature* **432**, 885–888 (2004).
16. Pfeiffer, M. A., Williams, G. J., Vartanyants, I. A., Harder, R. & Robinson, I. K. *Nature* **442**, 63–66 (2006).
17. Abbamonte, P. *et al. Nature* **431**, 1078–1081 (2004).

SYSTEMS NEUROSCIENCE

Timing is everything

Phillip Larimer and Ben W. Strowbridge

Interactions among neurons in brain circuits underlie sensory perception and information storage. Work in locusts shows how the timing of different neuronal signals is synchronized to ensure effective communication.

Most biological systems can adapt to different conditions and environments. The nervous system has elaborated on this ability and developed mechanisms that use prior experience to predict future events. Many of these mechanisms could potentially support behavioural prediction. However, little is known about which specific mechanisms are used during common tasks, such as learning how to hit a baseball or remembering to avoid poison ivy. In a seminal study, Cassenaer and Laurent¹ (page 709 of this issue) demonstrate a specific predictive mechanism that operates during olfactory learning in locusts.

In both mammals and insects, olfactory stimuli trigger diffuse, but reproducible, patterns of neural activity in many interconnected brain regions². At the initial processing stage, odors in the environment evoke all-or-none electrical discharges, which are recorded in neurons as spikes (action potentials). As the cells involved in the odorant-to-spiking conversion have only broad selectivity³, the activity of any one neuron is a poor predictor of odorant identity. Instead, odorant identity seems to be encoded by populations of neurons whose activity becomes transiently synchronized in response to sensory stimulation. Individual neurons often respond to several odorants and probably participate in many transient 'cell assemblies'². The insect brain affords excellent accessibility for electrical recordings from several neurons, making it useful for determining how odorant-evoked activity patterns develop.

Network oscillations also have an important role in the processing of olfactory information

by linking together the neurons that collectively represent a specific odorant. The presence or absence of a single spike on a specific oscillation cycle defines cell assemblies that are activated by an odorant. In honeybees⁴ the disruption of network oscillations impairs olfactory discrimination, highlighting the oscillations' relevance to information processing.

Olfactory information is processed sequentially by different brain regions that are linked by network oscillations. In insects, simple olfactory stimuli activate large subsets of projection neurons in the antennal lobe — a region analogous to the olfactory bulb in mammals. The neural representation of sensory information becomes significantly sparser in the second⁵- and third¹-order stages of olfactory processing (Fig. 1a). Sparse coding is advantageous because it facilitates the recall of memories from partial cues and allows for denser, more reliable storage of biological information⁶.

As several stages of the insect olfactory system represent sensory information as sparse cell assemblies that are tightly linked by network oscillations², small perturbations in the timing of single spikes in constituent neurons can potentially disrupt sensory coding. Thus, the olfactory system has the difficult task of maintaining the temporal precision required to generate odorant-linked cell assemblies. Propagation of information through neuronal circuits typically results in a loss of temporal precision due to randomness associated with the mechanisms by which neurons communicate. The decrease in timing precision (increased jitter) is especially large when target cells are activated by relatively few, but

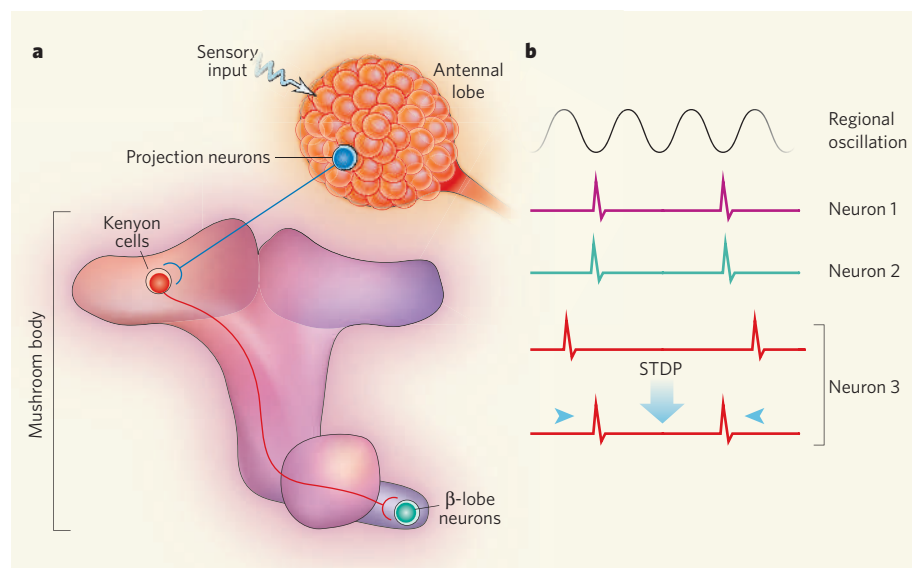


Figure 1 | Representation of information by oscillating networks in the locust brain. **a**, Sensory information is processed by several brain areas in the locust that are linked by network oscillations. Projection neurons in the antennal lobe receive sensory input and transmit it to Kenyon cells in the mushroom body. Kenyon cells, in turn, project to β -lobe neurons. **b**, Sensory information is represented at several stages of processing by transiently activated neuronal subpopulations. Odorant-evoked spiking in individual neurons within a subpopulation is synchronized with an oscillatory rhythm that reflects activity throughout that brain region (regional oscillation). Spike-timing-dependent plasticity (STDP) helps enforce synchrony throughout the subpopulation by adjusting connection strengths in response to inappropriately timed spikes. Here, for example, STDP ensures that the timing of spikes in neuron 3 matches that in neurons 1 and 2.

powerful, inputs. Downstream brain regions must, therefore, maintain temporal precision without the advantage of reducing jitter by averaging over many inputs.

Cassenaer and Laurent¹ found that the insect olfactory system uses information channels comprised of relatively few, but powerful, connections and, surprisingly, that it avoids the temporal-precision penalty normally associated with sparse-coding pathways. In contrast to the weak connections between projection neurons and Kenyon cells⁷, the authors found that Kenyon-cell spiking causes strong activation of β -lobe neurons. The amplitude of the connections from Kenyon cells to β -lobe neurons was almost 20 times larger than that from projection neurons to Kenyon cells. However, inputs from Kenyon cells to β -lobe neurons were relatively rare, occurring 25 times less frequently than weak connections between projection neurons and Kenyon cells. Both the large amplitude and low incidence of these connections are characteristic of sparse-coding pathways⁸. Despite the sparse nature of their main inputs, β -lobe neurons still fired with high temporal precision.

The authors went on to identify a mechanism for circuit modification that explains how infrequent, large inputs from Kenyon cells generate precise timing in the downstream β -lobe neurons (Fig. 1b). In most brain circuits, the strength of connections between neurons is relatively constant. However, dramatic changes in strength can occur after a 'coincident' event in which both the initiating and target cells are active at roughly the same time. The ability of

some neural circuits to modify themselves after detecting coincident activity — termed spike-timing-dependent plasticity (STDP) — is one of the best-understood mechanisms for regulating connection strength⁹.

Cassenaer and Laurent¹ report the first example of STDP in the olfactory system, showing for the first time that STDP facilitates oscillation-linked spike synchronization. Studying the sparse connections between Kenyon cells and β -lobe neurons, the authors find — as shown previously in mammals⁹ — that STDP can bidirectionally regulate connection strength. The strengthening or weakening of connections depends on the sequence in which initiating and target cells are active. If an inappropriately timed input causes a target cell to spike late, this circuit-modification mechanism will strengthen that specific connection so that future spikes occur earlier, thereby preserving spike synchrony across the cell assembly. A parallel mechanism weakens the subset of connections that are active after a premature target-cell spike, thereby altering the aggregate drive to the target cell so that it fires at the appropriate time on subsequent oscillation cycles. The bidirectional nature of STDP provides an elegant means to avoid the expected loss of temporal precision as information propagates through oscillating sparse networks.

Besides providing transient representations of sensory information, cell assemblies may also serve as the initial substrates for long-term memory. An outstanding question is whether the same mechanisms that mushroom-body neurons use to generate precise timing also



50 YEARS AGO

Mental illness is so disturbing and unexpected that it is inevitable that it should arouse an emotional response... The earliest historical reaction seems to have been the view that insanity was due to possession by devils... It may be that the trephining operation in which palaeolithic man removed, with what pain we cannot conceive, sections of a living man's skull, was designed to let out the devils which had somehow become lodged in the head. The next stage in such a belief was that the patient had suffered from a divine intervention. He was 'touched' by God... However, a certain number of mentally ill patients... are definitely dangerous, and many are a nuisance, interfering with the lives and work of ordinary folk... Indeed, in Biblical times, insane people were sometimes chained in caves and dependent on charity for their food, or died if it were not provided. In 1792 Pinel commenced the modern era by removing the patients' shackles in France... From this time, physicians tried to treat their patients.

From *Nature* 10 August 1957.

100 YEARS AGO

The fuels committee of the Motor Union of Great Britain and Ireland has issued a valuable report on motor-car fuels... a famine in petrol appears to be inevitable in the near future, owing to the fact that demand is increasing at a rate much greater than the rate of increase of the supply. In 1904 the consumption of petrol in the United Kingdom was 12,000,000 gallons; in 1907 it had risen to 27,000,000 gallons... the committee discusses in the report other possible fuels. The supply is divided into two parts. The first includes all fuels limited in quantity... The second group contains one item only — alcohol — and it is evident from the whole tone of the report that the committee expects to find in denatured vegetable spirits the fuel of the future.

From *Nature* 8 August 1907.

50 & 100 YEARS AGO

trigger long-term circuit modifications that underlie sensory memory — extending the neuroscience axiom that “neurons that fire together, wire together” to transient cell assemblies. This study¹ will probably also spark a search for STDP in ‘secondary’ olfactory regions of mammals — including many of the relatively unexplored olfactory areas, such as the olfactory tubercle and agranular insula cortex — that may be analogous to assemblies of β -lobe neurons.

As synchronous oscillations can be recorded in many diverse mammalian brain regions that exhibit STDP, the model presented by Cassenaer and Laurent¹ may be broadly applicable. Subsequent studies will probably test whether neuronal assemblies with self-correcting timing underlie predictive memory in other

behavioural contexts, as described by theoretical models^{9,10}.

Phillip Larimer and Ben W. Strowbridge are in the Department of Neurosciences, Case Western Reserve University, Cleveland, Ohio 44106, USA. e-mail: bens@case.edu

1. Cassenaer, S. & Laurent, G. *Nature* **448**, 709–713 (2007).
2. Mazon, O. & Laurent, G. *Neuron* **48**, 661–673 (2005).
3. Laurent, G. *et al. Annu. Rev. Neurosci.* **24**, 263–297 (2001).
4. Stopfer, M., Bhagavan, S., Smith, B. H. & Laurent, G. *Nature* **390**, 70–74 (1997).
5. Perez-Orive, J. *et al. Science* **297**, 359–365 (2002).
6. Olshausen, B. A. & Field, D. J. *Curr. Opin. Neurobiol.* **14**, 481–487 (2004).
7. Jortner, R. A., Farivar, S. S. & Laurent, G. *J. Neurosci.* **27**, 1659–1669 (2007).
8. Henze, D. A., Urban, N. N. & Barrionuevo, G. *Neuroscience* **98**, 407–427 (2000).
9. Abbott, L. F. & Nelson, S. B. *Nature Neurosci.* **3**, 1178–1183 (2000).
10. Suri, R. E. & Sejnowski, T. J. *Biol. Cybern.* **87**, 440–445 (2002).

CHEMICAL BIOLOGY

Ions illuminated

Christopher J. Chang

Calcium ions act as signals between cells, but their exact locations — at the nanometre scale — have been difficult to pinpoint. The latest biosensor promises to reveal these details in dynamic living systems.

Cell signalling is all about location. This concept is best illustrated with calcium signals — cells funnel bursts of calcium ions to specific locations, where the ions selectively activate a wide variety of physiological functions. Calcium signals ebb and flow to cellular hotspots that are confined to regions ranging in size from micrometres down to tens of nanometres. But despite the importance of localization for controlling the effects of calcium signals on cells, it has been a daunting task to study calcium and other transient cellular signals at the nanometre scale.

Reporting in *Nature Chemical Biology*, Tour *et al.*¹ describe a promising approach to this long-standing problem. They have developed a calcium sensor that allows rapid, selective and sensitive tracking of localized calcium signals with high temporal and spatial resolution.

Fluorescence microscopy is a powerful technique for imaging, in real time, many aspects of communication within and between cells. The difficulty with this method for determining the movement of dynamic cell signals such as calcium is detecting the non-uniform variation in signal concentrations within highly localized regions. Being able to detect these signal fluctuations is essential, as they may lead to drastically different biological outcomes. Synthetic, small-molecule (that is, non-protein) fluorescent indicators — such as those in the Fura, Fluo and Calcium Green families of compounds — show very rapid and selective responses to calcium. But these indicators are distributed diffusely in cells and so are

unable to provide resolutions better than one micrometre using conventional light microscopy. Alternatively, protein-based biosensors can be introduced at specific subcellular locations using genetic engineering. This approach provides an easy way to place calcium probes into cells, but such sensors are limited by their slow responses, and their large sizes can perturb the system of interest.

The strategy now presented by Tour *et al.*¹ combines the tunability and small size of synthetic chemical indicators with the spatial resolution and control of genetically targeted proteins. They have developed a prototype small-molecule sensor, known as Calcium Green FAsH (CaGF; Fig. 1a). This molecule comprises a receptor that binds selectively to calcium, a fluorescent reporter that responds to calcium binding, and two arsenic groups that label proteins only at specially incorporated peptide sequences that consist of four cysteine amino acids. This study builds upon previous work from the same group² that showed that small arsenic-containing dyes target tetracycline peptide motifs. The addition of a calcium-reporting group to the dyes introduces an extra dimension that allows calcium's function in cellular systems to be studied using molecular imaging.

With the CaGF tool, Tour *et al.* explored the local dynamics of calcium signals in two cell systems. First, they studied gap junctions — the intersections that allow molecules and ions to pass freely between vertebrate cells. The authors used CaGF in cells expressing a connexin

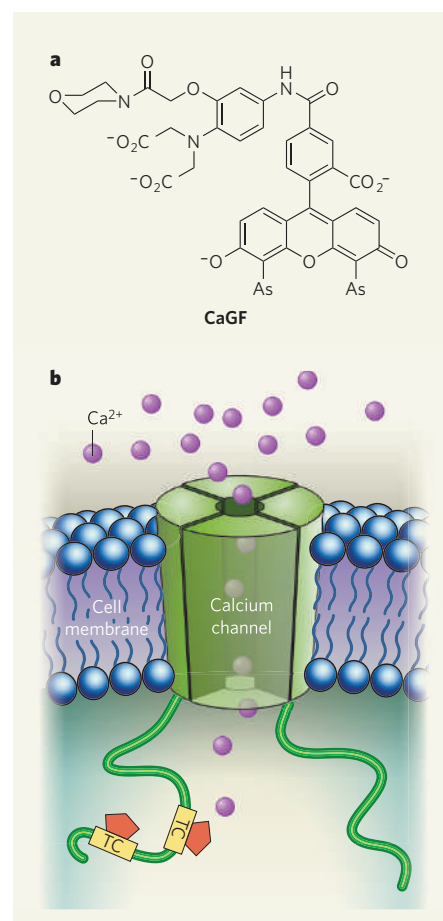


Figure 1 | Detecting calcium in living systems.

a, Tour and colleagues¹ have made a calcium-ion (Ca^{2+}) sensor, known as Calcium Green FAsH (CaGF), that recognizes specific peptide sequences called tetracyclines (TCs). **b**, In the example shown, CaGF molecules (red pentagons) bind to TCs that have been attached to the protein chain of a calcium channel in a cell membrane. When calcium ions enter the cell through the channel, they are trapped by CaGF, which becomes fluorescent and can be detected by fluorescence microscopy. The authors use this method to monitor the fluctuations of calcium ions in living systems in real time.

protein that had been tagged with a tetracycline peptide motif. Connexins are major building-blocks of gap junctions, so the authors were able to use CaGF to monitor waves of calcium passing through the junctions in real time.

In a second set of experiments, Tour and colleagues targeted CaGF to the mouth of $\text{Ca}_v1.2$, which is one of a family of channels that open and close to control the flow of calcium ions into cells (Fig. 1b). In this way, the authors could directly visualize calcium hotspots that colocalize with the clustered $\text{Ca}_v1.2$ channels in the outer cell membrane. Although this technique does not yet allow calcium concentrations to be quantified or kinetic measurements to be made, the authors' results do suggest that bursts of calcium signals exist that are only a few nanometres wide, and that calcium channels cluster together for signalling. More importantly, CaGF offers the tantalizing possibility of

studying non-uniform calcium dynamics in more complex systems, such as brain neurons.

Tour and colleagues' work provides a host of opportunities for the development of further chemical tools. A wish list for next-generation designs might include calcium-responsive groups with brighter fluorescence and more rapid turn-on responses; ratiometric readouts of fluorescence that allow the concentration of ions in nanometre-sized calcium bursts to be measured; and a choice of coloured reporters, so that different kinds of sensor can be used and identified in the same experiment. A range of sensors with different binding affinities for calcium would also be useful, as calcium-ion concentrations vary depending on the cell type.

Furthermore, the discovery and optimization of new peptide motifs that recognize small molecules should lead to sensors that bind with improved selectivity to proteins tagged with those peptides; this will improve the signal-to-noise ratios of sensors in localized cellular regions and allow multiple probes to be used that recognize different tags^{3–7}. The authors' general concept could also be exploited to

visualize protein regions by using methods other than fluorescence, such as electron microscopy, magnetic resonance imaging, positron emission tomography and ultrasound. Different reporters could also be used, so that other metal ions, naturally occurring organic compounds and enzyme-reaction products can be detected. By opening the door to such possibilities, Tour *et al.*¹ have taken a step towards the most ambitious goal of all — developing chemical probes that can visualize specific features of living systems with molecular resolution. ■

Christopher J. Chang is in the Department of Chemistry, University of California, Berkeley, 532A Latimer Hall, Berkeley, California 94720, USA. e-mail: chrischang@berkeley.edu

1. Tour, O. *et al.* *Nature Chem. Biol.* **3**, 423–431 (2007).
2. Griffin, B. A., Adams, S. R. & Tsien, R. Y. *Science* **281**, 269–272 (1998).
3. Hauser, C. T. & Tsien, R. Y. *Proc. Natl Acad. Sci. USA* **104**, 3693–3697 (2007).
4. Ojida, A. *et al.* *J. Am. Chem. Soc.* **128**, 10452–10459 (2006).
5. Prescher, J. A. & Bertozzi, C. R. *Nature Chem. Biol.* **1**, 13–21 (2005).
6. Chen, I. & Ting, A. Y. *Curr. Opin. Biotechnol.* **16**, 35–40 (2005).
7. Guignet, E. G., Hovius, R. & Vogel, H. *Nature Biotechnol.* **22**, 440–444 (2004).

indicate that a rock has spent a long time in an environment with a higher Rb/Sr ratio. High Rb/Sr ratios are characteristic of the continental crust, but can also come about through the melting of mantle rock. Because of its large ionic radius, rubidium fits poorly into the crystal structures of mantle minerals, and so becomes concentrated in melted rock fractions much more effectively than strontium does. This effect is strongest at low melt fractions, so high Rb/Sr ratios could also be the signature of small amounts of melt that formed in one region of the uppermost part of the mantle (the asthenosphere) and migrated into another part (the lithosphere). This process, known as mantle metasomatism, has become increasingly favoured by mantle geochemists⁴. As a result, the burden of coming up with incontrovertible proof has shifted onto those who argue that some volcanic mantle upwellings contain recycled continental material.

Previous assessments have had to rely on extrapolations of isotope-ratio and trace-element trends in various extruded rocks to an endpoint thought to correspond to values found in the continental crust. As the range of ratios covered by the data was small, and their distance from the inferred continental ratio large, this procedure was akin to wagging a large dog with a small tail. One could not know if the ratio of the distant inferred end-point of the trend really did represent the continental crust, or something well short of it — a metasomatized mantle region, for example.

The breakthrough presented by Jackson *et al.*² is an extension of the range of observed ⁸⁷Sr/⁸⁶Sr ratios (and the correlated neodymium isotope ratio ¹⁴³Nd/¹⁴⁴Nd) in volcanic extrusions well into the region of typical old continental rocks (Fig. 1, overleaf). Even so, these isotope ratios might, in principle, be explained by rocks processed through an extreme version of the metasomatic model. But the authors also ascertain values of various other tell-tale trace-element ratios that are a factor of four lower than those found in metasomatized rocks, and are entirely characteristic of an origin in the continental crust⁵.

GEOCHEMISTRY

The lost continents

Albrecht W. Hofmann

Once subducted into the mantle, material from Earth's continental crust seems to disappear. But its distinctive isotopic signature has been found back at the surface — in volcanic rocks on a Pacific island.

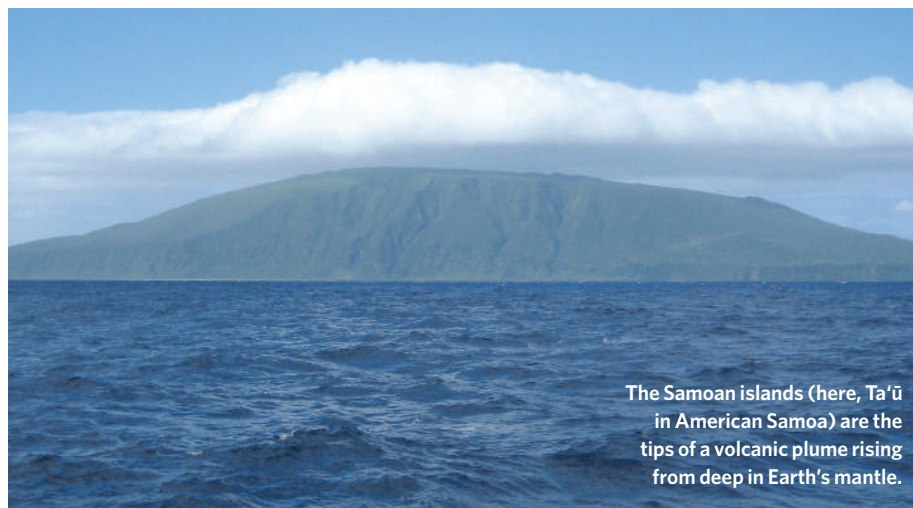
Plate tectonic theory requires that much of Earth's crust returns to the underlying mantle through the process known as subduction. Most of this subducted material is solidified volcanic lava — basalts — from oceanic crust (see, for example, ref. 1). But continents do not completely escape this fate; material eroded from the continental crust is deposited on the ocean floor as a veneer of sediments up to a few hundred metres thick. This layer is subducted, when the time comes, along with the basaltic crust.

But what happens to the continental material after that? Does convection in the mantle stir it around so that it loses its distinctive identity? Or does at least some of it reappear in volcanic rocks formed at ocean ridges or at isolated 'hotspots' of volcanic extrusion under the sea? Jackson *et al.*² (page 684 of this issue) have found what might be a 'smoking gun' for the second option. In unprecedented studies of the isotopic and trace-element compositions of basalts dredged from the flanks of a Samoan island, they find almost unequivocal evidence for traces of recycled ancient continental crust in extruded volcanic rocks.

Samoa, a chain of islands in the South Pacific just east of the International Date Line,

is thought to owe its existence to a plume of volcanic material rising from the deep mantle. It has long been singled out as a possible harbour of traces of recycled continental material because its rocks contain more radiogenic strontium (⁸⁷Sr, produced by β -decay of the very long-lived rubidium isotope ⁸⁷Rb) relative to normal strontium (⁸⁶Sr), than is usual³.

Moderately increased ⁸⁷Sr/⁸⁶Sr ratios



The Samoan islands (here, Ta'u in American Samoa) are the tips of a volcanic plume rising from deep in Earth's mantle.

S. R. HART

One possible loophole in this interpretation is that the continental isotopic and trace-element signature might have been picked up by the basalts in transit from their melting site in the mantle, at depths of 100 km or so, through the original Pacific Ocean floor — which is itself covered with predominantly continent-derived sediment. Jackson *et al.* effectively counter the spectre of such 'crustal contamination' through non-recycled material by analysing actual Pacific sediments near Samoa, finding that the lead isotope ratios of these samples are incompatible with those of Samoan lavas.

If the origin of the Samoan magma source is now settled, one may reasonably infer that other nearby ocean islands of similar isotopic composition (known as enriched-mantle 2, or EM2)⁶, such as the Society Islands (including Tahiti) and the Marquesas, have similar sources. This would be a mixture of mantle rocks and recycled oceanic crust, with a sprinkling of sediment derived from ancient upper continental crust and subducted along with the rest of the package. Similarly, a few other ocean islands, such as Pitcairn, might contain small amounts of recycled pelagic sediment.

The troubling point remains, however, that even if all EM-type volcanoes contain recycled sediments, instances in which this can be recognized are rare. After all, wherever subduction occurs, sediments are likely to enter the mantle. Jackson and colleagues² point out that if the current rate of sediment subduction (0.5–0.7 km³ per year) is representative of the past 4 billion years, the total amount of subducted sediment will make up only about 0.15% of the mass of the mantle. That might

not seem much, but it is about a third of the present-day mass of the continents.

These sediments are also rather highly enriched in incompatible elements (those most likely to be removed by mantle melting), up to a factor of about 100 compared with primitive mantle compositions. They are even more enriched when compared with present-day mantle, which has been depleted in these same elements by the removal of continental crust. Thus, in the present-day mantle, possibly

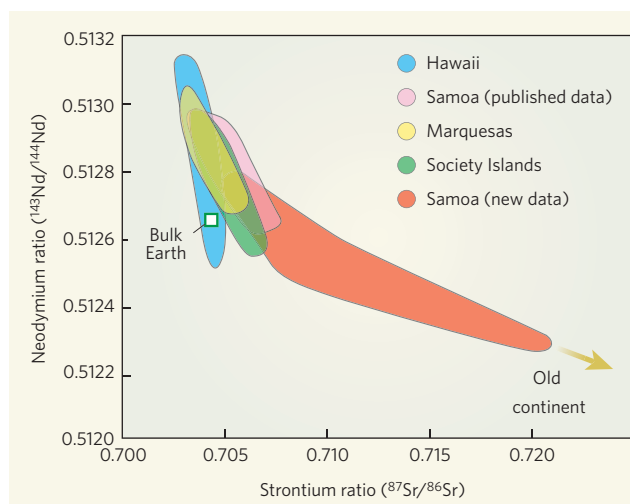


Figure 1 | Adopting continental values. The strontium and neodymium ratios $^{87}\text{Sr}/^{86}\text{Sr}$ versus $^{143}\text{Nd}/^{144}\text{Nd}$ in volcanic rocks from several mantle 'hotspots' or plumes. High strontium and low neodymium ratios are both characteristic of ancient continental rocks, but possibly also of mantle regions enriched by infiltration of small amounts of mantle melt. Data for Hawaiian islands are representative of most ocean island volcanoes, which show isotopic evidence for normal mantle enrichment and depletion processes. Published data from Samoa, the Marquesas and the Society Islands, all island groups in the South Pacific, deviate from the normal mantle trend (which also contains the composition of the total 'bulk' Earth) in the direction of high $^{87}\text{Sr}/^{86}\text{Sr}$ values, indicating that they might contain recycled continental material. Jackson and colleagues' data² (red) greatly extend this trend. Together with other 'continental' geochemical indicators, these data strongly support the continental recycling hypothesis for this (relatively rare) class of volcano. (Isotope data assembled from ref. 7.)

10–20% of the highly incompatible elements rubidium, uranium and thorium might have been reinjected into the mantle from crustal sources by sediment subduction. And the very fact that the mantle is isotopically remarkably heterogeneous demonstrates that convective stirring is not particularly efficient.

Given all these factors, I find it remarkable that so little of the subducted sediments can be recognized in recycled form in both mid-ocean ridges and hotspot volcanoes. Much of the budget of subducted trace elements must therefore either be short-circuited back to the surface during subduction-related volcanism, or be hidden in a relatively stable place such as the subcontinental lithosphere. That is a question for another day. For now at least, such material has at last been identified in one place where it does appear.

Albrecht W. Hofmann is at the Max Planck Institute for Chemistry, Postfach 3060, 55020 Mainz, Germany.
e-mail: hofmann@mpch-mainz.mpg.de

1. Widom, E. *Nature* **443**, 516–517 (2006).
2. Jackson, M. G. *et al.* *Nature* **448**, 684–687 (2007).
3. White, W. M. & Hofmann, A. W. *Nature* **296**, 821–825 (1982).
4. Workman, R. K. *et al.* *Geochim. Geophys. Geosyst.* **5**, doi:10.1029/2003GC000623 (2004).
5. Hofmann, A. W., Jochum, K. P., Seufert, M. & White, W. M. *Earth Planet. Sci. Lett.* **79**, 33–45 (1986).
6. Zindler, A. & Hart, S. R. *Annu. Rev. Earth Planet. Sci.* **14**, 493–571 (1986).
7. <http://geocor.mpch-mainz.gwdg.de>

ELECTROSTATICS

Colour discrimination

Like charges repel, unlike charges attract. The simplest way to show this is to charge up different pieces of insulating plastic by rubbing them on your shirt and watching what they do when brought up close to one another. Amit Mehrotra and colleagues use a similar idea to separate a mixture of red and blue sand grains falling into a hollow acrylic cylinder, purely through the different amount of charge each is carrying (A. Mehrotra *et al.* *Phys. Rev. Lett.* **99**, 058001; 2007).

The red and blue grains were all of the same size and positively

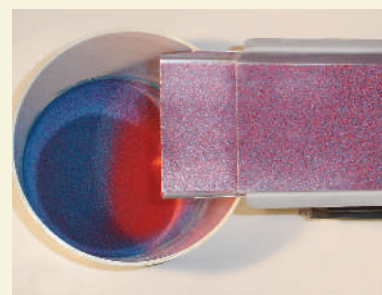
charged, with the charge density of the blue grains being about six times that of the red. The authors also made the cylinder positively charged by rubbing it lightly with nitrile gloves. The grains were mixed up on a vibratory feeder, and then discharged into the cylinder from a metal chute.

On entering the cylinder, the charged grains separated spontaneously into red and blue components (pictured). Oddly, however, it was the more positively charged blue grains that moved towards the positively charged

cylinder walls — rather than being more strongly repelled, as basic electrostatics would seem to demand.

The authors show through simulations that the sand particles are not, in fact, going against the grain. The effect is caused by negative charges induced on the underside of the metal chute, whose concentrated attraction causes a 'beard' of falling sand grains to grow on the lip of the chute. This beard is sufficiently repulsive that the more highly charged blue grains levitate more strongly off the end of the chute, resulting in two falling streams separated according to colour.

Pretty as it is, the experiment also



has a practical aspect. The ability to separate grains by how much charge they carry, rather than by charge sign, could have applications in technologies that exploit electrostatic charging — aerosol drug delivery, xerography and filtration, for example.

Richard Webb

BIODIVERSITY

World of insects

Nigel E. Stork

When it comes to understanding patterns of biodiversity, ours is a little-known planet. Large-scale sampling projects, as carried out in two investigations of insect diversity, show a way forward.

To a first approximation, all multicellular species on Earth are insects¹, and yet explanations for terrestrial biodiversity are largely based on birds, large mammals and plants. Studies of insect diversity by Novotny *et al.*² and Dyer *et al.*³ (pages 692 and 696 of this issue) help to redress this imbalance, and provide an improved understanding of the distribution of global diversity.

Some 80–95% of insect species have yet to be collected, named and described, most of them living in the tropics. Even for the 850,000-plus species that have been named, we know little about how they are distributed or what they feed on⁴. Yet this information is essential for understanding the relationship between biodiversity and the functioning of global ecosystems. One reason is that a massive effort would be required to provide the field-based data for an analysis of patterns that might be applied generally at the global scale.

With the help of a team of locally trained parataxonomists, Novotny *et al.*² have compiled such a database of records for three groups of rainforest insects: those that feed on foliage (Fig. 1), wood and fruit. They show that there is a low rate of change in species composition, or 'β diversity', across 75,000 km² (an area equivalent to that of South Carolina or Ireland) of continuous lowland rainforest in Papua New Guinea. This contrasts with the previous evidence, as discussed by Novotny *et al.*, of high β diversity for insects in the forest canopy and with changes in β diversity with latitude, altitude and climatic gradients.

Novotny *et al.*² also show that insect species on host trees of the same genus, but separated by as much as 500 km, are remarkably similar, and that there do not seem to be barriers to their dispersal. The authors conclude that large, lowland areas of tropical forest, such as the Amazon and Congo, where there is low β diversity of vegetation, should also have low β diversity of insect herbivores.

In a previous paper, Novotny and colleagues⁵ had compared their Papua New Guinea database of feeding records for the caterpillars of moths and butterflies, adult beetles and adult grasshoppers with similar records for taxa in temperate regions of Europe. They controlled for the relatedness of host trees, and concluded that the insect herbivores show similar levels of host specificity in both climatic regions.

In the second new paper discussed here, Dyer *et al.*³ describe how they carried out an equivalent analysis in the New World and

have come to a different conclusion. Their approach required examination of hundreds of thousands of host-specificity feeding records for butterfly and moth caterpillars, from as far back as 1936 and from areas ranging from Canada to Brazil. In contrast to Novotny and colleagues⁵, they find that, on average, the number of tree species on which an insect species feeds is fewer in the tropics than in temperate parts of the New World. They suggest that higher specialization in the tropics might be because of more intense interactions between an insect and its food source, as might be caused by more distinct secondary chemicals in tropical plants than in temperate plants.

Dyer *et al.*³ suggest that the difference between their results and those of Novotny *et al.*⁵ may be due to true biological differences between the continents, or because Novotny *et al.* used only 8–14 focal host-tree species in the study as opposed to the large number of host trees in the Dyer *et al.* study. Other reasons may be in the way Dyer and colleagues' data sets were compiled, particularly differences between the older and much larger Canadian data set and the smaller,

more recent data sets, and in the considerable differences in the sample sizes in the temperate and tropical data sets. Dyer and colleagues also suggest that there may be real differences in host specificity between the Americas, Europe and tropical Asia, but this seems unlikely. The question of which of these contrasting conclusions is correct will remain unresolved until further comparative studies take these sampling and geographical issues into account.

There has been an understandable bias towards the herbivorous insects in ecological studies⁶, because insects have coevolved with the plants and trees on which they feed. Indeed, tree species richness may serve as the best proxy for overall biodiversity in tropical forests, as Terry Erwin inferred in his famous calculation⁷ that raised estimates of tropical insect species tenfold to 30 million. Crucial suppositions he made were that each of the 50,000 tree species or groups of species in the world would have 165 host-specific beetle species, that beetles represent 40% of all insect species, and that the canopy is twice as rich in insect species as the ground, with the inference that species are stratum specific. His calculation implied that 84% of tropical insects are herbivores. The number of insect species that are specific to a particular tree species has since been carefully re-examined, however, and reduced by a factor of four or five⁸.

But what of the insects that have less glamorous and obvious lifestyles than the herbivores: those that feed on dead and decaying material, or on the bacteria and fungi that break down organic material; or the predators and parasites



M. JANDA

Figure 1 | Foliage feeder. This magnificent caterpillar, the aptly named Hercules moth caterpillar, is one of some 500 species of insect herbivore investigated by Novotny *et al.*². The authors conclude that there is a low rate of change of species composition (low β diversity) in the extensive lowland forests of the Sepik-Ramu basin in Papua New Guinea.

that feed on living plants and animals? The proportion of insect biodiversity that these 'feeding guilds' comprise is uncertain, but could be as high as 50–70%, and not 16% as Erwin proposed.

Looking beyond insects and setting aside microorganisms, what about fungi, other invertebrates and most marine life? These groups, too, are often poorly understood because of their taxonomic intractability or because they are so infrequently collected. The apparent rarity of many species in most samples of invertebrates and fungi is probably due to our low level of sampling rather than representing biological rarity. Making sense of such communities is almost impossible without the scale of sampling shown by Novotny and Dyer and their teams. Answers to such fundamental questions as how many species there are, how they are distributed, and how many are being lost through extinction will remain elusive without similar collaborative and large-scale enterprises. Of course, documenting how communities of organisms and their interactions change along ecological gradients is fundamentally more important than merely counting species.

So how much nearer are we to a model or group of models that might predict and explain the distribution of biodiversity on a global or

even a regional scale? Roger Kitching⁹ talked about "crafting the pieces of the diversity jigsaw puzzle", and these two new papers^{2,3} help to identify a few more pieces of this puzzle. But we are still a long way from being able to explain the distribution of global biodiversity. Perhaps the nearest functional model is the mid-domain theory^{10,11}, which attempts to model the distribution of species and shows that species richness is greatest at the centre of a spatial, temporal or functional domain. But whether that theory can be expanded and modified remains to be seen. ■

Nigel E. Stork is in the School of Resource Management, University of Melbourne, Burnley Campus, 500 Yarra Boulevard, Victoria 3121, Australia.
e-mail: nstork@unimelb.edu.au

1. May, R. M. *Nature* **324**, 514–515 (1986).
2. Novotny, V. *et al.* *Nature* **448**, 692–695 (2007).
3. Dyer, L. A. *et al.* *Nature* **448**, 696–699 (2007).
4. Stork, N. E. in *The Living Planet in Crisis: Biodiversity Science and Policy* (eds Cracraft, J. & Grief, F. T.) 3–32 (Columbia Univ. Press, New York, 1999).
5. Novotny, V. *et al.* *Science* **313**, 1115–1118 (2006).
6. Strong, D. R., Lawton, J. H. & Southwood, T. R. E. *Insects on Plants* (Blackwell Scientific, Oxford, 1984).
7. Erwin, T. L. *Coleopt. Bull.* **36**, 74–75 (1982).
8. Novotny, V. *et al.* *Nature* **416**, 841–844 (2002).
9. Kitching, R. L. *Science* **313**, 1055–1056 (2006).
10. Colwell, R. K. & Hurtt, G. C. *Am. Nat.* **144**, 570–595 (1994).
11. <http://viceroy.eeb.uconn.edu/RangeModel>

CRYSTALLOGRAPHY

A down-to-Earth approach

John R. Helliwell and Naomi E. Chayen

In seeking out ideal conditions for growing protein crystals, solutions have increasingly been found in the low-gravity conditions of space. But answers might be lurking in fields closer to home.

Culturing high-quality protein crystals has, in the past decade, undergone a steady transformation from an art to science. That process has been assisted by exploiting the 'microgravity' conditions of space missions to lessen the fluid flows that disturb crystal growth on Earth's surface. As they describe in *Applied Physics Letters*, Heijna *et al.*¹ use an alternative approach: very strong, but inhomogeneous magnetic fields with which they establish a tunable gravity environment that, for crystal growth, recreates space on Earth.

Protein crystals are highly sought-after commodities for many basic studies in biochemistry and structural biology, and for structure-based drug design. The better the quality of a crystal, the better the structural information it yields. Microgravity conditions reduce buoyancy-driven turbulent flows in the 'mother liquor' from which a crystal emerges, and so are thought to promote crystal nucleation and ideal growth. In addition, such conditions remove the sedimentation effect of

crystals heavier than the mother liquor. These near-perfect conditions have indeed been used to deliver bigger and better-formed protein crystals, to perform fundamental studies of crystal quality, and to produce homogeneous distributions of crystal sizes².

But experimentation in space has its disadvantages: restricted access, high costs (albeit mitigated by the small weight of the apparatus required) and political pressures, to name a few³. In addition, creating true microgravity conditions is difficult. Astronaut activity, for example, causes periods of gravity-like disturbance ('g-jitter')⁴. Although space has produced benchmark results, methods that are solely Earth-based have obvious attractions.

The inhomogeneous field (IHF) method harnessed by Heijna *et al.*¹ exploits a vertical magnetic-field gradient to create a force that counterbalances gravity. This approach is the basis of magnetic levitation techniques that have been used, among other things, to make frogs hover⁵. The precise values to which the

field and its gradient must be tuned to negate gravity depend on the nature of the crystals' mother liquor and its density. By creating effective gravity conditions from *g* (normal gravity) down to $-0.15g$ (inverted gravity), the authors were able to slow down, halt and even reverse convection in the mother liquor (Fig. 1). An ingenious optical viewing set-up within the 32-mm-diameter borehole containing their magnetic field allowed them to view and monitor the growing crystal and its surrounding fluid directly.

This control of crystal-growth conditions is different from that brought about by microgravity: because the crystal and mother liquor respond to the magnetic field to different extents, convection (a property of the fluid) and sedimentation (a property of the crystals) are not eliminated simultaneously. This can be viewed in two ways. First, it is a limitation of the magnetic-field method. But second, it allows the experimental conditions 'convection-free' and 'sedimentation-free' to be separated out, and their relative importance in the growth of protein crystals to be evaluated. A caveat here is that, in an experiment to explore the accuracy of the settings in an IHF chamber used to grow inorganic crystals, residual fluid flows equivalent to around $0.5 \mu\text{m s}^{-1}$ — about the same level as g-jitter in space — are found even when gravity is perfectly balanced out⁶.

Besides the IHF approach, other methods, for example those using gels⁷ and microfluidics, can provide the advantages of microgravity on Earth. Microfluidics, when combined with robotics for accurate and systematic screening of growth conditions, allows crystal-growth droplets as small as 10^{-11} m^3 (a hundredth of a cubic millimetre) to be accurately manipulated. In these small volumes, the problems of convection-driven fluid flows and sedimentation are scarcely relevant.

Of course, a crystal growing in such a small drop is also limited in size, but this presents little problem: modern synchrotron radiation facilities can analyse sample volumes of side just $20 \mu\text{m}$ (equivalent to about 10^{-14} m^3). An upgrade programme under way at the European Synchrotron Radiation Facility in Grenoble, France, to narrow the focus of its probing X-ray beam will lower this limit still further. In the upcoming new world of crystals numbering just a few thousand unit cells — 1,000 cells being 10 by 10 by 10 units — beams focused to $0.1 \mu\text{m}$ or less, equivalent to a probed volume of 10^{-21} m^3 , will be required. Indeed, a challenge to the ingenuity of the engineers will be to incorporate the microfluidic and robotic stages necessary for the manipulation of such small volumes within the constrained volume of an IHF apparatus.

Protein crystallography with neutrons, which has the big advantage over X-rays of finding the positions of hydrogens (as deuterium atoms) even at relatively modest diffraction resolutions⁸, uses larger protein crystals. But even here, improvements in

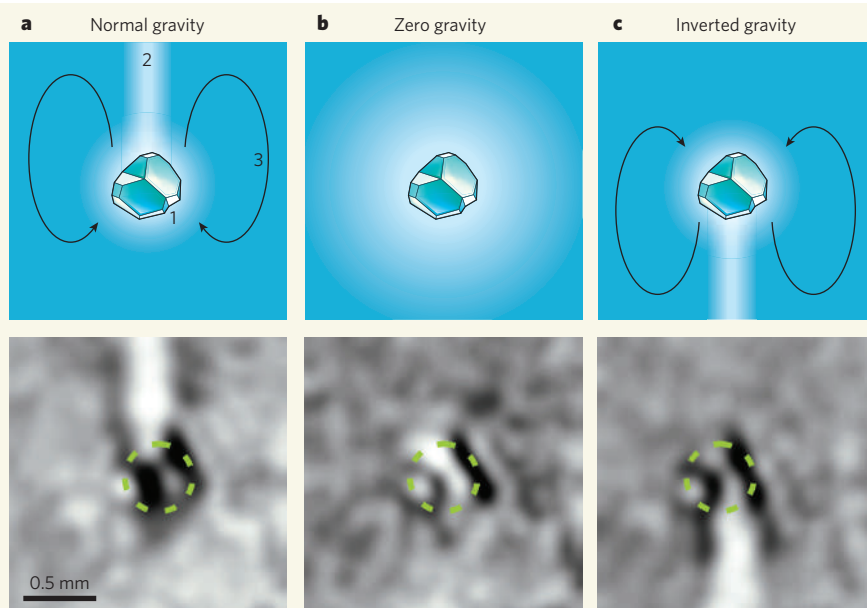


Figure 1 | Suspended animation. **a**, In normal gravity conditions, a growing crystal (1) depletes its surrounding solution, causing density differences in the surrounding fluid, a vertical growth plume (2) and convection (3). **b**, Tuning the strength and gradient of an inhomogeneous magnetic field can be used to eliminate convection and to create ideal, quiescent conditions for crystal growth. **c**, The effective direction of gravity can even be reversed, inverting the fluid flows and growth plume. The bottom panels show equivalent 'shadowgraphy' images from Heijna and colleagues' work¹, at gravity strengths $0g$ and $-0.15g$. (Figure adapted from ref. 1.)

neutron apparatus and new protein deuteration facilities at the Laue Langevin Institute in Grenoble, and from 'megawatt spallation' neutron sources, will allow the reduction of sample sizes to just a fraction of a millimetre.

It is important to mention that it is not just inhomogeneous magnetic fields that can play their part in protein-crystallization techniques — the use of homogeneous magnetic fields was pioneered earlier by Sasaki and Ataka^{9,10}.

When crystals of the protein lysozyme are grown in a homogeneous magnetic field of 10 tesla, charged amino-acid residues in the structure showed increased order through the restraining effect of the magnetic 'Lorentz' force on moving electric charges¹¹. These crystals remained stable when removed from the magnetic field for X-ray synchrotron analysis. Most recently, the use of combined magnetic and electric fields has permitted a quite

remarkable homogeneity of protein-crystal size and shape¹². The use of electric fields on their own in protein-crystal growth is well established¹³. A recent innovation here is an apparatus with multiple wells for crystal growth¹⁴.

The variety of these methods for optimizing crystal growth, as well as new synchrotron X-ray and neutron sources and the attractions of microfluidics and robotics, all add up to an exciting time in the analysis of biological crystal structures. Earth-based techniques such as those explored by Heijna *et al.*¹ will ensure that researchers will keep, if not their imagination, then their equipment on the ground. ■

John R. Helliwell is in the School of Chemistry, University of Manchester, Manchester M13 9PL, UK, and at the Science and Technology Facilities Council Daresbury Laboratory, Daresbury, Cheshire WA4 4AD, UK. Naomi E. Chayen is in the Department of Biomolecular Medicine, Division of Surgery, Oncology, Reproductive Biology and Anaesthetics, Imperial College London, London SW7 2AZ, UK.

e-mails: john.helliwell@manchester.ac.uk; n.chayen@imperial.ac.uk

1. Heijna, M. C. R. *et al. Appl. Phys. Lett.* **90**, 264105 (2007).
2. Snell, E. H. & Helliwell, J. R. *Rep. Prog. Phys.* **68**, 799–853 (2005).
3. Chayen, N. E. & Helliwell, J. R. *Nature* **398**, 20 (1999).
4. Boggon, T. J. *et al. Phil. Trans. R. Soc. Lond. A* **356**, 1045–1061 (1998).
5. Berry, M. V. & Geim, A. K. *Eur. J. Phys.* **18**, 307–313 (1997).
6. Poodt, P. W. G. *et al. Cryst. Growth Des.* **6**, 2275–2280 (2006).
7. Garcia-Ruiz, J. M. & Moreno, A. *Acta Cryst. D* **50**, 484–490 (1994).
8. Blakeley, M. P. *et al. Chem. Soc. Rev.* **33**, 548–557 (2004).
9. Sasaki, G. *et al. J. Cryst. Growth* **173**, 231–234 (1997).
10. Ataka, M. *et al. J. Cryst. Growth* **173**, 592–596 (1997).
11. Saijo, S. *et al. Acta Cryst. D* **61**, 207–217 (2005).
12. Sasaki, G., Moreno, A. & Nakajima, K. *J. Cryst. Growth* **262**, 499–502 (2004).
13. Al-Haq, M. I. *et al. Crystallogr. Rev.* **13**, 29–64 (2007).
14. Al-Haq, M. I. *et al. J. Appl. Cryst.* **40**, 199–201 (2007).

PLANT BIOLOGY

Jasmonate perception machines

Edward E. Farmer

How do plant cells respond so vigorously to organisms that damage their cells? Following on from progress made in understanding hormonal control of growth and development comes news of how a plant's security system operates.

The breaking and entering of plant cells sets off alarms by stimulating the formation of jasmonic acid and its jasmonate derivatives. Papers by Thines *et al.*¹ and Chini *et al.*², published on pages 661 and 666 of this issue, reveal beautifully dynamic mechanisms of jasmonate perception and downstream molecular signalling.

Jasmonic acid is a small lipid that acts as a precursor for the production of jasmonate hormones. Almost all of its natural workings relate, directly or indirectly, to how plants

manage events resulting from penetration of their cells. These include wounding inflicted by herbivores, pathogen invasion, certain symbiotic events, and reproduction. Indeed, plants lacking the ability to perceive jasmonate grow well during the vegetative stage of their life cycle if protected in a laboratory setting. From the considerable body of published work^{3,4}, we know that the protein CORONATINE INSENSITIVE 1 (COI1) is required for the perception of jasmonate. This protein forms part of an enzyme complex called SCF^{COI1}

that was predicted to tag unknown regulators of jasmonate signalling with the polypeptide ubiquitin, leading to their destruction³. The characterization of these regulators, and their mode of action^{1,2}, now paves the way to a new level of understanding of how jasmonates act as signals.

Working largely with the model plant *Arabidopsis thaliana*, the two groups took different routes to get at the genes involved. Thines *et al.*¹ analysed eight related gene transcripts of unknown function that were rapidly upregulated in developing *Arabidopsis* stamens treated with jasmonate. By contrast, Chini *et al.*² characterized a mutant called *jasmonate-insensitive3-1* (*jai3-1*). Working with different genes, both groups found that overexpressing the full-length transcripts had little or no effect on jasmonate perception. But overexpression of shortened forms, encoding proteins truncated at the carboxyl terminus, reduced the plants' sensitivity to jasmonate. Additionally, whereas full-length

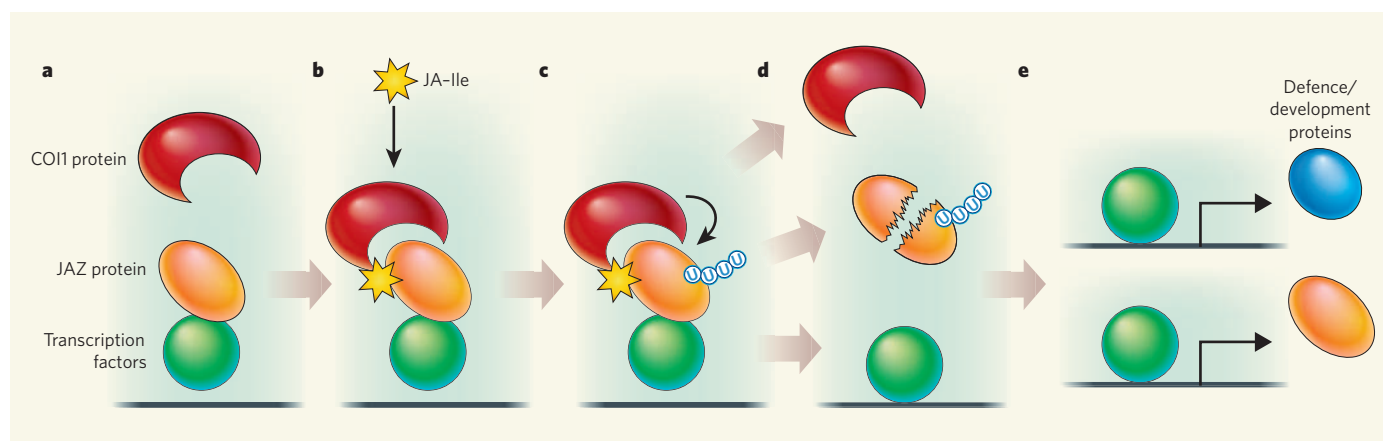


Figure 1 | Five steps in jasmonate signalling^{1,2}. **a**, JAZ proteins are normally bound to transcription factors and inhibit their activity. **b**, In response to attack, jasmonoyl-isoleucine (JA-Ile, marked with a star) stabilizes the interaction between COI1 and JAZ. **c**, The JAZ protein is probably then modified by ubiquitin (U), so marking it for destruction.

d, JAZ is destroyed, liberating the transcription factors; **e**, this allows transcription of genes that produce proteins involved in defence and development, as well as of JAZ genes to restrain the jasmonate response. (Only the COI1 component of the SCF^{COI1} enzyme complex of which it is a part is shown.)

proteins were unstable *in vivo* when treated with jasmonate, proteins with a truncated carboxyl terminus resisted degradation in response to such treatment.

All of this fits in well with a role for these proteins as repressors that might be destroyed upon perception of jasmonate. The proteins are called JAZ proteins, and they are encoded by approximately 12 genes in *Arabidopsis*. We will know the exact number only when all of them are tested for their roles in jasmonate signalling. Additionally, some of these genes encode multiple proteins that have different abilities to repress jasmonate responses⁵. Why so many JAZ proteins? Perhaps, for one thing, they offer enormous regulatory potential — especially if other hormone-signalling pathways impinge on JAZ gene expression.

Now, at last, we know that the site of jasmonate perception consists of two proteins — COI1 (in the SCF^{COI1} complex) together with one of several JAZ proteins (Fig. 1). In a first regulatory step, a small amount of the jasmonic acid precursor hormone that accumulates is attached enzymatically to molecules such as L-isoleucine, producing an active ligand, jasmonoyl-isoleucine (JA-Ile)⁶. Using an elegant yeast two-hybrid strategy, Thines *et al.*¹ showed that JA-Ile interacts with and stabilizes the COI1-JAZ complex. Then, SCF^{COI1} probably tags the captive JAZ proteins with ubiquitin, condemning them to rapid destruction.

Extending the story, Chini *et al.*² found that the carboxyl terminus of their JAZ protein bound to MYC2, a gene transcription factor involved in jasmonate signalling in *Arabidopsis*. So, after destruction of JAZ proteins, MYC2 can set to work regulating jasmonate-dependent gene expression that activates the plant's defences.

Some fascinating questions remain. Where does JA-Ile bind on the JAZ-COI1 complex? The possibility that COI1 acts as a receptor has already been suggested⁷. How many ligands

derived from jasmonic acid (or introduced into plant cells by pathogens) can bring COI1 and JAZ proteins together? In the scheme of jasmonate signalling, we already know that there is a positive feedback loop where jasmonic acid activates its own synthesis⁴. But it's not good to be in a permanent state of alarm: what puts the brakes on jasmonate signalling? The new data reveal a second type of regulatory loop based

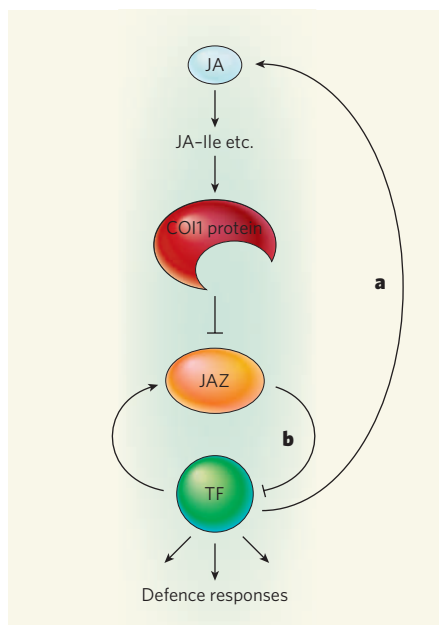


Figure 2 | Primary regulatory cycles in jasmonate signalling. Synthesis of jasmonic acid (JA) is self-promoting (feed-forward loop **a**). Loop **b** is the newly discovered² negative feedback loop involving JAZ proteins and transcription factors (TF) such as MYC2. These two regulatory cycles may be interlocked, but we can expect to find further complexity in the mechanism if, for example, some JAZ proteins bind to transcriptional repressors. Indeed, evidence for secondary regulatory loops already exists. In a regulatory circuit that is not shown here, MYC2 can repress the synthesis of its own transcripts⁹.

on JAZ protein action, whereby jasmonate signalling activates JAZ gene transcription, leading to the downregulation of jasmonate action (Fig. 2). As a thought game, one can imagine similar cycles for each combination of JAZ protein and transcription factor. The importance of these regulatory loops is clear. They bring us to a new level of understanding of how jasmonic acid, the 'cell ingress pro-hormone', activates plant defences in response to cell intrusion.

At this point, researchers working on the developmental hormone auxin must be acknowledged for providing a paradigm for hormone signalling through proteins closely related to COI1 (ref. 7). And it is also intriguing that several JAZ-like genes participate in developmental processes as well as in defence⁸. The new work^{1,2} and a related paper⁵ open possibilities for studying how the fundamental processes of growth control and defence have coevolved, and how they are appropriately managed in complex organisms. In any case, a dynamic yet robust biological security system, tested and shaped over millions of years, has been revealed to us.

Edward E. Farmer is in the Department of Plant Molecular Biology, University of Lausanne, 1015 Lausanne, Switzerland.
e-mail: edward.farmer@unil.ch

1. Thines, B. *et al.* *Nature* **448**, 661–665 (2007).
2. Chini, A. *et al.* *Nature* **448**, 666–671 (2007).
3. Turner, J. G., Ellis, C. & Devoto, A. *Plant Cell* **14**, S153–S164 (2002).
4. Wasternack, C. *Ann. Bot.* (in the press).
5. Yan, Y. *et al.* *Plant Cell* (in the press).
6. Staswick, P. E. & Tiryaki, I. *Plant Cell* **16**, 2117–2127 (2004).
7. Parry, G. & Estelle, M. *Curr. Opin. Cell Biol.* **18**, 152–156 (2006).
8. Vanholme, B. *et al.* *Trends Plant Sci.* **12**, 239–244 (2007).
9. Dombrecht, B. *et al.* *Plant Cell* (in the press).

Correction

In "Microbiology: The inside story" by Laurie E. Comstock (*Nature* **448**, 542–544; 2007), methanogenic archaea should have been cited as consumers not of methane but of hydrogen.

CRYSTALLOGRAPHY

Crystallographic evidence for deviating C3b structure?

Arising from: A. A. Ajees *et al.* *Nature* **444**, 221–225 (2006)

Activation of the protein C3 into C3b in the complement pathway is a crucial step in the complement immune response against pathogenic, immunogenic and apoptotic particles. Ajees *et al.*¹ describe a crystal structure for C3b that deviates from the one reported by Janssen *et al.*² and by Wiesmann *et al.*³. We have reanalysed the data deposited by Ajees *et al.*¹ and have discovered features that are inconsistent with the known physical properties of macromolecular structures and their diffraction data. Our findings therefore call into question the crystal structure for C3b reported by Ajees *et al.*¹.

Three structures of the 12-domain protein C3b have been reported^{1–3}. In the structure of C3b reported by Ajees *et al.*¹, the complement C1r/C1s, Uegf, Bmp1 (CUB) domain adopts an unfolded conformation, and the thioester (TED)

domain has a C3-like conformation, rather than an activated, C3d-like shape, and is positioned away from the main body of the molecule. The structure of the remaining ten domains is similar between the three structures^{1–3} and resembles the C3c structure⁴. The conformation and location of the CUB and TED domains are of specific interest because they are crucial to the biological functions of this molecule that are central to the complement system.

In an analysis of the structural differences between the three structures^{1–3} reported for C3b, we noticed that the coordinates deposited by Ajees *et al.* (Protein Data Bank entry 2HR0) do not form a connected network of molecules in the crystal lattice. The crystal structure forms layers that are separated by a large void in the *c*-direction (a slab of about 30–40 Å thick that spans the entire unit cell). To investigate this highly unusual, and unreported, feature, we used two computer programs (REFMAC⁵ and CNS 1.2 (ref. 6)) to reproduce the reported refinement statistics from the diffraction data¹ deposited in the Protein Data Bank. We found that the published statistics, the deposited coordinate model and diffraction data were consistent with each other.

We then tested whether the gap could be explained by a missing protein molecule. Redetermination by molecular replacement with the program PHASER⁷ resulted in the same overall molecular arrangement as that seen by Ajees *et al.*¹. We found no evidence for potentially absent protein molecules, either from features in the electron-density map or from increased scores in the log-likelihood function when searching for additional components.

In addition to the absence of crystal contacts in the *c*-direction, we noticed other physically implausible features. The diffraction data do not show the features that should arise from the presence of bulk solvent (Fig. 1), whereas the molecular arrangement indicates that large regions are not occupied by protein molecules. In other words, the diffraction data are consistent with protein molecules in a vacuum but not with those surrounded by disordered solvent, as is always seen for macromolecular crystals⁸.

The *B*-factors of the model (both the deposited *B*-factors and those obtained by rerefinement) do not vary significantly throughout the molecule, even though long segments of the chain are almost completely exposed to solvent (Fig. 2). *B*-factors describe the size of displacements available to the atoms, so they are correlated with disorder for surface-exposed residues and rigid-body-like motion of domains⁹. The *R*_{free} (ref. 10) and *R* distributions are exceptionally low at low resolution, and the difference between *R*_{free} and *R* is unusually small for a structure refined at 2.3 Å resolution with

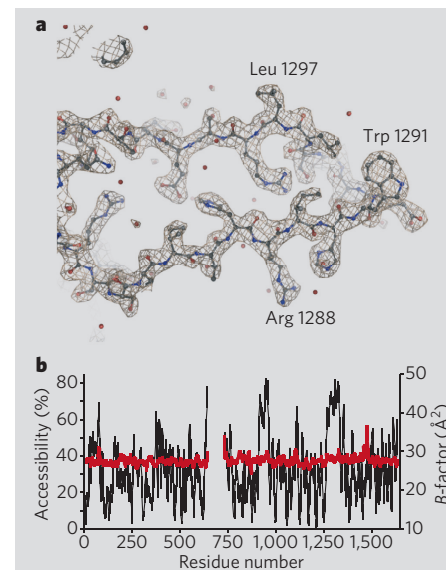


Figure 2 | Lack of correlation between surface exposure and disorder of residues in the C3b crystal structure of Ajees *et al.*¹ **a**, The electron density (calculated with coefficients $2mF_{\text{obs}} - DF_{\text{calc}}$; ref. 12) of a region in the unfolded CUB domain is contoured at 2.5σ ($0.55 \text{ e} \text{ \AA}^{-3}$). It is very unusual to see such a well defined electron density at a high contour level for an unfolded domain that has no stabilizing contacts with other parts of the molecule or neighbouring symmetry-related molecules. **b**, Plot of surface accessibility (black, computed with NACCESS¹³) and atomic *B* factors after rerefinement (red), both averaged over a window of nine residues. Normally, the two measures would be highly correlated.

an amplitude-based target function (Fig. 1b).

We think that these physically implausible features undermine the validity of the model presented by Ajees *et al.*¹ and the deposited diffraction data from which it derives. Only when the experimental diffraction images are made available can the deviating C3b model be either verified or falsified.

Bert J. C. Janssen*, Randy J. Read†, Axel T. Brünger‡, Piet Gros*

*Crystal and Structural Chemistry, Bijvoet Center for Biomolecular Research, Faculty of Sciences, Utrecht University, 3584 CH Utrecht, The Netherlands

e-mail: p.gros@chem.uu.nl

†Department of Haematology, University of Cambridge, Cambridge Institute for Medical Research, Wellcome Trust/Medical Research Council Building, Cambridge CB2 0XY, UK

‡Howard Hughes Medical Institute, and Departments of Molecular and Cellular Physiology, Neurology and Neurological Sciences, Structural Biology, and Stanford Synchrotron Radiation Laboratory, Stanford University, Stanford, California 94305-5432, USA

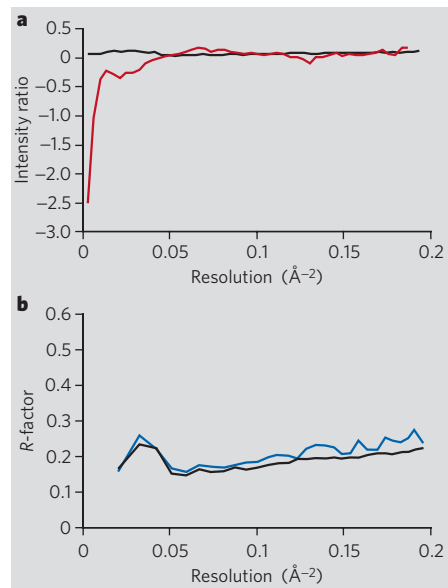


Figure 1 | Absence of bulk solvent in the deposited diffraction data of Ajees *et al.*¹ **a**, Plot, as a function of resolution, of the logarithm of the ratio between the average observed intensities and those calculated from a model without a bulk-solvent contribution. Black line shows the results for the structure of Ajees *et al.* (Protein Data Bank entry 2HR0); red line shows results for a control using data from Protein Data Bank entry 1H18 (ref. 11), which has a similar size and resolution limits. The plot is expected to fall off at low resolution, as seen for 1H18, because the presence of disordered solvent reduces the contrast and hence the average diffraction intensity. **b**, *R* (black line) and *R*_{free} (blue line) plotted as a function of resolution, calculated with computer program CNS 1.2 (ref. 6) using the data and the 2HR0 structure of Ajees *et al.* without a bulk-solvent model. In the absence of a bulk-solvent model, a large *R* factor (beyond 0.5) is expected at low resolution because the model does not account for the contribution of the bulk solvent in the crystal to the diffraction data⁸.

1. Ajees, A. A. *et al.* The structure of complement C3b provides insights into complement activation and regulation. *Nature* **444**, 221–225 (2006).
2. Janssen, B. J., Christodoulidou, A., McCarthy, A., Lambris, J. D. & Gros, P. Structure of C3b reveals conformational changes that underlie complement activity. *Nature* **444**, 213–216 (2006).
3. Wiesmann, C. *et al.* Structure of C3b in complex with CRLg gives insights into regulation of complement activation. *Nature* **444**, 217–220 (2006).
4. Janssen, B. J. *et al.* Structures of complement component C3 provide insights into the function and evolution of immunity. *Nature* **437**, 505–511 (2005).
5. Murshudov, G. N., Vagin, A. A. & Dodson, E. J. Refinement of macromolecular structures by the maximum-likelihood method. *Acta Crystallogr. D Biol. Crystallogr.* **53**, 240–255 (1997).
6. Brünger, A. T. *et al.* Crystallography and NMR system: A new software suite for macromolecular structure determination. *Acta Crystallogr. D Biol. Crystallogr.* **54**, 905–921 (1998).
7. McCoy, A. J., Grosse-Kunstleve, R. W., Storoni, L. C. & Read, R. J. Likelihood-enhanced fast translation functions. *Acta Crystallogr. D Biol. Crystallogr.* **61**, 458–464 (2005).
8. Jiang, J. S. & Brünger, A. T. Protein hydration observed by X-ray diffraction. Solvation properties of penicillopepsin and neuraminidase crystal structures. *J. Mol. Biol.* **243**, 100–115 (1994).
9. Kuriyan, J. & Weiss, W. I. Rigid protein motion as a model for crystallographic temperature factors. *Proc. Natl Acad. Sci. USA* **88**, 2773–2777 (1991).
10. Brünger, A. T. The free R value: a novel statistical quantity for assessing the accuracy of crystal structures. *Nature* **355**, 472–475 (1992).
11. Becker, A. & Kabsch, W. X-Ray structure of pyruvate formate-lyase in complex with pyruvate and CoA: how the enzyme uses the Cys-418 thiol radical for pyruvate cleavage. *J. Biol. Chem.* **277**, 40036–40042 (2002).
12. Read, R. J. Improved Fourier coefficients for maps using phases from partial structures with errors. *Acta Crystallogr. A* **42**, 140–149 (1986).
13. Hubbard, S. J. & Thornton, J. M. 'NACCESS' Computer Program, Department of Biochemistry and Molecular Biology, University College London, UK (1993).

Received 22 December 2006; accepted 21 June 2007.
Competing financial interests: declared none.
doi: 10.1038/nature06102

CRYSTALLOGRAPHY

Ajees *et al.* reply

Replying to: B. J. C. Janssen, R. J. Read, A. T. Brünger & P. Gros *Nature* **448**, doi: 10.1038/nature06102 (2007)

We concur with Janssen *et al.*¹ that the structure of C3b that we reported (Protein Data Bank entry 2HR0)² differs from the other two (2ICF (ref. 3) and 2I07 (ref. 4) in the conformation of the CUB and TED domains. The deviation of 2HR0 from 2I07 is probably relevant physiologically, considering that CUB eventually unfolds.

An electron microscopy study⁵ reports a movement of about 75–100 Å for TED in C3b, which is closer to that found in 2HR0 (about 84 Å) than in 2I07 (about 65 Å). Additionally, the only domain not seen in the electron micrographs is CUB; nine other domains of similar size and structure are all visible, indicating that C3b adopts conformations in which CUB is less compact than in 2I07. Furthermore, in 2I07 TED is not optimally positioned for interaction with some ligands⁶, whereas it is in 2HR0. The 2.3 Å-resolution structure of 2HR0 positions all C3b domains more accurately than is possible at 4 Å in 2I07. The unfolded, but well ordered, CUB has *B* factors comparable to the rest of the structure, indicating that we are observing a different, but physiologically interesting, conformation of C3b.

Statistical disorder⁷ resulting in apparent 'gaps' in the lattice has been observed for other proteins (W. A. Hendrickson, personal communication). In the gap along the *c*-direction, PHASER⁸ locates, with reasonable *Z*-scores (Table 1), fragments that are apparently from a protein of the RCA (for regulators of complement activation) family⁹, which specifically bind C3d and C3dg (ref. 10). These fragments, which are probably contaminants, bridge two C3b molecules to form the lattice (Fig. 1a). Putative fragments here interact non-specifically with several domains of C3b (Fig. 1b). They are statistically disordered and are present in different orientations in different sets of unit cells, which would prevent construction of an atomic model for these regions. Stabilization of the protein lattice by adventitious entities is not unprecedented¹¹. Figure 2a of Janssen *et al.*¹ seems not to be contoured at a level needed

to display disordered entities, as shown in our Fig. 1. These observations unambiguously indicate the existence of a crystal lattice.

We have also determined and refined a structure of C3b in another crystal form, with a shorter *c*-axis, which reveals direct crystal contacts between C3b molecules. Notably, the rest of the structure is nearly identical to 2HR0 except for an unmodified glutamine residue at position 991. Changes in the length of the axis, accompanied by hydration adjustments, leaving the molecular conformation mostly unaltered, have been seen in other structures¹².

Figure 2b of Janssen *et al.*¹ ignores the fact that

B-factors are much higher in 2I07 ($B = \langle 174 \rangle$), within the model errors and uncertainties at 4 Å, than in 2HR0 ($B = \langle 27 \rangle$), at 2.3 Å. When normalized for this difference, variation in *B*-factors as a function of solvent exposure is comparable for 2I07 and 2HR0 (Fig. 1 c, d). *R* and *R*_{free} values, and the difference between them, which are similar to those reported by us, are widespread (for example, see Protein Data Bank entries 1Q0D, 2BL2, 2BS3). Bulk-solvent modelling is contentious, making many refinements necessary to constrain parameters to obtain acceptable values¹³. Analysis of the few deposited values reveals no correlation of either parameter with

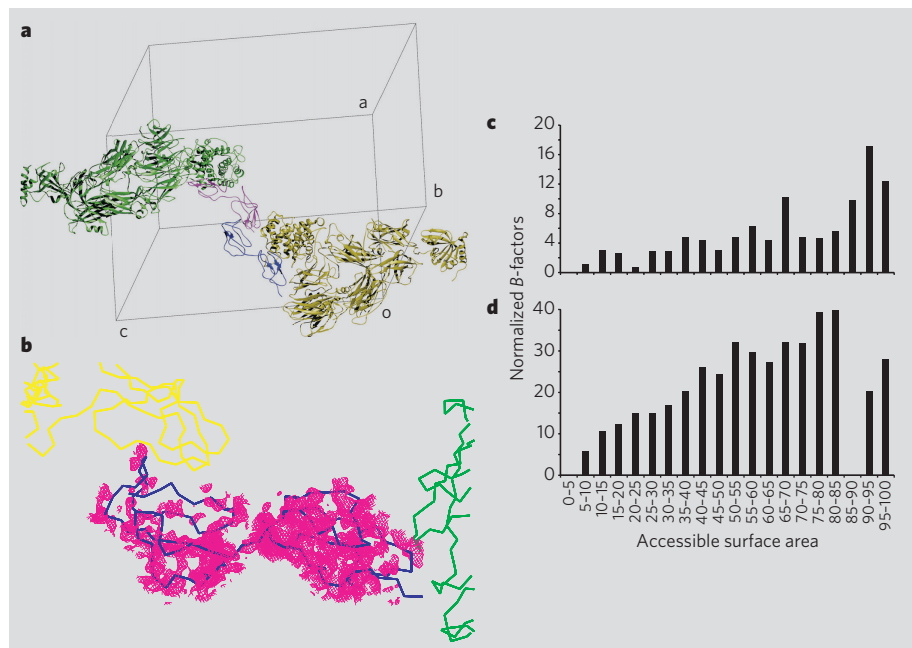


Figure 1 | Crystal lattice and normalized *B* factors. **a**, Packing diagram of C3b with the vaccinia virus complement-control protein VCP1-2, showing one symmetry-related molecule. The Ca 'worm' of C3b in the asymmetrical unit is coloured yellow and VCP1-2 is blue. Symmetry equivalents are green (C3b) and magenta (VCP1-2). **b**, A section of the 2Fo-Fc map (magenta), calculated using the published data from PDB entry 2HR0, contoured at 0.7σ around solution 6 (Table 1). C3b is shown in green and VCP1-2 in blue; the symmetry-related molecule is in yellow. **c**, **d**, Plots of normalized *B* factor versus accessible solvent area for **c**, 2HR0, and **d**, 2I07. Normalized *B*-factor calculated as $((B_{\text{group}} - B_{\text{ref}}) / B_{\text{group}}) \times 100$, in which *B*_{ref} is the reference *B*-factor for residues in the 0–5% accessibility range, and *B*_{group} is the average *B*-factor for residues with other accessibility ranges.

solvent content or composition¹³. If our data had really represented a structure in a vacuum, we would not have been able to locate the RCA protein fragments.

Hence we rebut the arguments of Janssen *et al.*¹ and stand by our model, the underlying diffraction data and the functional implications we derive from the model.

A. Abdul Ajees*, Krishnasamy Gunasekaran*, Sthanam V. L. Narayana*, H. M. Krishna Murthy*

*Center for Biophysical Sciences and Engineering, University of Alabama at Birmingham, Birmingham, Alabama 35294, USA
e-mail: murthy@cbse.uab.edu

- Janssen, B. J., Read, R. J., Brünger, A. T. & Gros, P. Crystallographic evidence for deviating C3b structure. *Nature* **448**, doi: 10.1038/nature06102 (2007).
- Ajees, A. A. *et al.* The structure of complement C3b provides insights into complement activation and regulation. *Nature* **444**, 221–225 (2006).
- Wiesmann, C. *et al.* Structure of C3b in complex with CR1g gives insights into regulation of complement activation. *Nature* **444**, 217–220 (2006).
- Janssen, B. J., Christodoulidou, A., McCarthy, A., Lambris, J. D. & Gros, P. Structure of C3b reveals conformational changes that underlie complement activity. *Nature* **444**, 213–216 (2006).
- Nishida, N., Walz, T. & Springer, T. A. Structural transitions of complement component C3 and its activation products. *Proc. Natl Acad. Sci. USA* **103**, 19737–19742 (2006).
- Hammel, M. *et al.* A structural basis for complement inhibition by *Staphylococcus aureus*. *Nature Immunol.* **8**, 430–437 (2007).
- Trame, C. B. & McKay, D. B. Structure of *Haemophilus influenzae* HslU protein in crystals with one-dimensional disorder twinning. *Acta Crystallogr. D Biol. Crystallogr.* **57**, 1079–1090 (2001).
- McCoy, A. J., Grosse-Kunstleve, R. W., Storoni, L. C. & Read, R. J. Likelihood-enhanced fast translation functions. *Acta Crystallogr. D Biol. Crystallogr.* **61**, 458–464 (2005).
- Liszewski, M. K., Farries, T. C., Lublin, D. M., Rooney, I. A. & Atkinson, J. P. Control of the complement system. *Adv. Immunol.* **61**, 201–283 (1996).
- Pangburn, M. K. in *The Complement System* (eds Rother, K. & Till, G. O.) 93–117 (Springer, New York, 1998).
- Chang, G., Spencer, R. H., Lee, A. T., Barclay, M. T. & Rees, D. C. Structure of the MscL homolog from *Mycobacterium tuberculosis*: a gated mechanosensitive ion channel. *Science* **282**, 2220–2226 (1998).
- Esnouf, R. M. *et al.* Continuous and discontinuous changes in the unit cell of HIV-1 reverse transcriptase crystals on dehydration. *Acta Crystallogr. D Biol. Crystallogr.* **54**, 938–953 (1998).
- Glykos, N. M. & Kokkinidis, M. On the distribution of the bulk-solvent correction parameters. *Acta Crystallogr. D Biol. Crystallogr.* **56**, 1070–1072 (2000).

doi:10.1038/nature06103

Table 1 | Crystal lattice gap

Molecule	Z-scores		Closest C3b domain to PHASER solution
	RFZ	TFZ	
C3b (PDB ID: 2HRO)	87.4	92.2	
C3b + VCP SCR 1 and 2 Ajees*			
Fragments bridging two C3b molecules in adjacent unit cells			
Solution 1	3.6	5.0	TED
Solution 3	3.1	5.1	MG5
Solution 5	3.6	4.7	TED
Solution 6	3.6	4.5	TED
Solution 11	3.6	4.2	TED
Solution 12	3.2	4.8	TED
Solution 13	3.1	4.6	TED
Solution 15	3.2	4.6	MG4
Solution 16	3.1	4.5	MG5
Solution 17	3.6	4.4	MG5
Solution 18	3.8	4.5	TED
Solution 19	3.2	4.6	TED
Fragments with symmetry clashes			
Solution 2			CUB
Solution 4			MG1
Solution 10			TED
Solution 20			TED
Other			
Solution 7			TED
Solution 8			MG5
Solution 9			MG8
Solution 14			CUB
Solution 21			MG4
Solution 22			TED
C3b + VCP NMR SCR 1-2 (PDB ID: 1VVC)			
Fragments bridging two C3b molecules in adjacent unit cells			
Solution 3	3.8	4.9	TED
Solution 5	3.2	4.6	TED
Solution 6	3.8	4.7	MG5
Fragments with symmetry clashes			
Solution 1			MG4
Solution 2			TED
Solution 4			TED
C3b + CR2 (PDB ID: 1LY2)			
Fragments bridging two C3b molecules in adjacent unit cells			
Solution 1	4.0	4.2	TED
Solution 2	4.0	4.4	MG5
Solution 5	4.6	4.5	TED
Solution 10	4.0	4.0	TED
Fragments with symmetry clashes			
Solution 4			MG5
Solution 9			MG8
Other			
Solution 3			MG5
Solution 6			MG4
Solution 7			TED
Solution 8			MG1
Solution 11			MG4

Solutions were obtained from PHASER (using search option RMS 1.5) using our deposited F_{obs} fragments from vaccinia virus complement-control protein (VCP), complement receptor-2 (CR2), C3 and C3b domains, as well as haemoglobin. Negative results from PHASER: using Protein Data Bank (PDB) ID code 2G71, 1G40 (SCR1-4), 2A73 (MG1; MG2; MG8; TED and CUB domains) and 2HBF. *A. A. A., unpublished.

JAZ repressor proteins are targets of the SCF^{COI1} complex during jasmonate signalling

Bryan Thines^{1†}, Leron Katsir^{2,3}, Maeli Melotto², Yajie Niu¹, Ajin Mandaokar¹, Guanghui Liu², Kinya Nomura², Sheng Yang He^{2,4}, Gregg A. Howe^{2,3} & John Browse¹

Jasmonate and related signalling compounds have a crucial role in both host immunity and development in plants, but the molecular details of the signalling mechanism are poorly understood. Here we identify members of the jasmonate ZIM-domain (JAZ) protein family as key regulators of jasmonate signalling. JAZ1 protein acts to repress transcription of jasmonate-responsive genes. Jasmonate treatment causes JAZ1 degradation and this degradation is dependent on activities of the SCF^{COI1} ubiquitin ligase and the 26S proteasome. Furthermore, the jasmonoyl-isoleucine (JA-Ile) conjugate, but not other jasmonate-derivatives such as jasmonate, 12-oxo-phytodienoic acid, or methyl-jasmonate, promotes physical interaction between COI1 and JAZ1 proteins in the absence of other plant proteins. Our results suggest a model in which jasmonate ligands promote the binding of the SCF^{COI1} ubiquitin ligase to and subsequent degradation of the JAZ1 repressor protein, and implicate the SCF^{COI1}-JAZ1 protein complex as a site of perception of the plant hormone JA-Ile.

Jasmonate is the prototypical member of a class of related oxylipin signalling molecules (collectively referred to as jasmonates) that have overlapping roles in regulating both stress responses and development in plants^{1–4}. Stress responses that depend on jasmonate signalling not only include defence against insects and pathogens^{2–6} but also responses to ultraviolet radiation, ozone and other abiotic stresses^{7,8}. In healthy, unwounded plant tissue, jasmonate is involved in carbon partitioning, mechanotransduction, senescence, and reproductive development^{1,8–14}. This wide spectrum of action mirrors, to some extent, that for prostaglandins, which are chemically related to jasmonate¹⁵. The jasmonate-dependent responses are associated with large-scale reprogramming of gene expression and hundreds of downstream jasmonate-regulated and co-regulated genes have been identified^{1,6}.

Much of our knowledge about jasmonate action comes from *Arabidopsis* mutants that are deficient in jasmonate synthesis or unable to respond to jasmonate^{1,3,9}. Importantly, the *Arabidopsis* mutant *coi1* is deficient in all jasmonate responses⁹. The discovery that *COI1* encodes an F-box protein led to the suggestion¹⁰ that core jasmonate signalling and responses depend on actions of an Skp/Cullin/F-box complex (SCF^{COI1})—a type of E₃ ubiquitin ligase¹⁶. This hypothesis has been supported by investigations of additional mutants^{17–19}. It is therefore likely that jasmonate signalling involves ubiquitination of specific target proteins by the SCF^{COI1} complex and their subsequent degradation by the 26S proteasome¹³. Unfortunately, extensive genetic screens for positive effectors^{9,12,20,21}, negative effectors^{19,20,22} and components downstream of COI1 (ref. 11), as well as searches for COI1-interacting proteins^{18,23} have so far failed to identify viable candidates for SCF^{COI1} targets. Transcript profiling experiments that have identified jasmonate-responsive⁶ and COI1-dependent genes²⁴ have also failed to provide candidates, or other clues about the precise connection between SCF^{COI1} and the jasmonate-regulated transcriptomes.

Here we report the discovery of a family of jasmonate ZIM-domain proteins (JAZ) that include key components of jasmonate signalling. Molecular and biochemical characterization of *Arabidopsis thaliana* JAZ1 and a tomato orthologue supports a model in which JAZ proteins function as repressors of jasmonate signalling and are degraded through the SCF^{COI1}-dependent 26S proteasome pathway. Protein–protein interaction studies indicate that jasmonoyl-isoleucine (JA-Ile) specifically promotes COI1–JAZ1 interaction in the absence of other plant proteins. Our results therefore implicate the COI1–JAZ complex as a site of perception for JA-Ile, and provide the basis for understanding the multifaceted effects of jasmonates on plant development and immunity.

Discovery of the JAZ genes

We used transcript profiling to follow gene expression changes in stamens of an *Arabidopsis* jasmonate-synthesis mutant, *opr3*, treated with exogenous jasmonate¹. At the earliest sampling time, 0.5 h after jasmonate application, only 31 genes showed significant induction relative to the 0 h control, including 8 that encode proteins of unknown function. Seven of these eight proteins contain a twenty-eight-amino-acid ZIM domain²⁵. One additional gene encoding a ZIM-domain protein was significantly induced at 2 h. We have designated these *JASMONATE ZIM-DOMAIN* (JAZ) genes. JAZ transcripts were induced 6- to 40-fold in stamens following jasmonate treatment (Fig. 1a). Data from the AtGenExpress expression atlas²⁶ indicate that all the JAZ genes are widely expressed throughout plant development. An experimental data set from 7-day-old seedlings treated with 10 μ M jasmonate (see Supplementary Information) shows 8- to 60-fold induction of the same genes within 0.5 h (Fig. 1b). In addition, RNA gel-blot analysis showed jasmonate induction of the JAZ genes in mature rosette leaves (Supplementary Fig. 1a). Database searches identified five additional JAZ genes in *Arabidopsis* (see Supplementary Information).

¹Institute of Biological Chemistry, Washington State University, Pullman, Washington 99164-6340, USA. ²Department of Energy-Plant Research Laboratory, ³Department of Biochemistry and Molecular Biology, ⁴Department of Plant Biology, Michigan State University, East Lansing, Michigan 48824, USA. [†]Present address: USDA Plant Gene Expression Center, 800 Buchanan Street, Albany, California 94710, USA.

On alignment, only 14 residues are identical in these 8 JAZ sequences (Fig. 1c), with an additional 9 positions having conservative substitutions. Homology among the proteins is highly confined to three domains (Fig. 1c). Domain 1 exhibits the weakest sequence similarity; domain 2 is the recognized ZIM motif; and domain 3 is most-strongly conserved, with 11 of 22 residues identical or with conservative substitutions. Unlike the *Arabidopsis* ZIM and ZIM-like proteins, which have zinc-finger DNA-binding domains²⁵, none of the JAZ proteins contains a known DNA-binding domain. Sequence analysis programs did not identify a nuclear localization motif in any of the JAZ proteins (see Supplementary Information), so we used green fluorescent protein (GFP) fusions to investigate subcellular localization of JAZ proteins empirically. In contrast to a GFP control, both the GFP–JAZ1 and GFP–JAZ6 fusion proteins were localized to the nucleus (Fig. 1d).

A modified JAZ protein blocks jasmonate signalling

To investigate the function of JAZ proteins, we first took a reverse-genetics approach by identifying T-DNA insertion lines through the *Arabidopsis* database (<http://www.arabidopsis.org>). We identified T-DNA insertions in six of the genes, with mutations in JAZ2, JAZ5, JAZ7 and JAZ9 being null (Supplementary Fig. 2), but none of these mutants exhibited an obvious jasmonate-related phenotype. These negative results suggest that the JAZ proteins may have overlapping functions, and this may explain the failure of forward-genetic screens to identify recessive mutations in the JAZ genes^{19,20,22}. We next produced transgenic plant lines in which complementary DNAs encoding each JAZ protein were overexpressed under the control of the *CaMV* 35S promoter. Again, no phenotype was observed. In a third approach, we sought to induce a dominant-negative phenotype by targeted deletion of the conserved domains identified in Fig. 1c. A total of seven deletion constructs were produced for the JAZ1 cDNA (Fig. 1c), and expressed in wild-type plants under the control of the 35S promoter. Only one construct produced a

phenotype; expression of a protein lacking domain 3 (residues 202–228; construct 35S–JAZ1Δ3A) yielded T₁ plants that were sterile (Fig. 2a). The sterile plants were similar to wild type in vegetative growth and development, but the flower phenotype corresponded closely to that observed in jasmonate-synthesis mutants^{1,27} and the jasmonate-response mutant *coi1* (ref. 9; Fig. 2b). Jasmonate treatment of sterile plants did not result in any seed set. We successfully fertilized JAZ1Δ3A flowers using wild-type pollen, so the plants are female-fertile; however, pollen from sterile JAZ1Δ3A plants did not fertilize flowers and failed to germinate on artificial media (Fig. 2c). Progeny of JAZ1Δ3A plants (obtained by pollination with wild-type pollen) segregated 1:1 for sterile plants carrying the JAZ1Δ3A transgene to fertile plants lacking the transgene. The JAZ1Δ3A transgenic plants exhibit other phenotypes typical of jasmonate-response mutants, including resistance to jasmonate-inhibition of root growth⁹ (Fig. 2d, e), resistance to infection by *Pseudomonas syringae* pv. *tomato* (Pst) DC3000 (ref. 28) (Fig. 2f, g), and weak induction of jasmonate-responsive genes, *DHS1*, *LEC* (At1g16410) and *VSP1* (refs 6, 29; Fig. 2h). These results indicate that high-level expression of the JAZ1Δ3A transgene blocks jasmonate responsiveness, possibly through the dominant-negative action of the altered JAZ1 protein.

Requirements for JAZ1–GUS degradation

One possible explanation for our results is that the JAZ proteins are repressors preventing transcription of jasmonate-responsive genes and that jasmonate mediates removal of the JAZ proteins to allow signalling responses to proceed via increased expression of specific downstream genes. By analogy with established mechanisms for other plant hormones^{30,31}, the JAZ repressors could be targets of the SCF^{COI1} complex (Fig. 3a). Jasmonate would facilitate or enhance interaction between JAZs and the F-box protein, COI1, leading to degradation of the JAZ proteins through the ubiquitination–26S proteasome pathway.

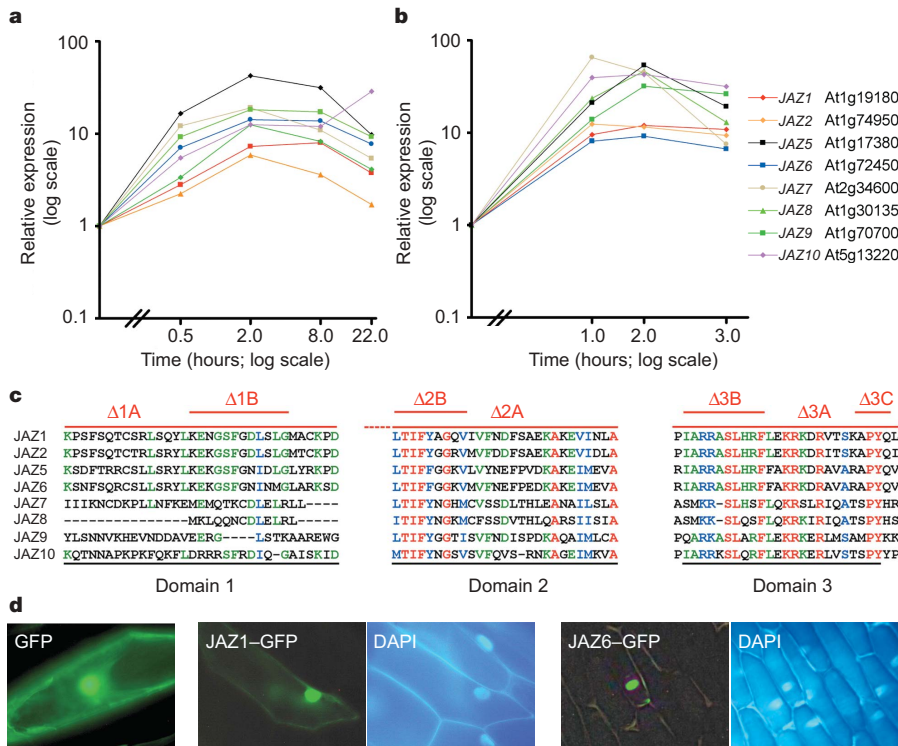


Figure 1 | Identification and analysis of eight JAZ proteins in *Arabidopsis*. **a**, Rapid, strong induction of JAZ genes in stamens of *opr3* by jasmonate. **b**, JAZ genes are also induced in wild-type (WT) seedlings treated with jasmonate. **c**, Deduced amino-acid sequences of conserved domains in *Arabidopsis* JAZ proteins. Red, identical residues; blue, conservative

substitutions; green, identical in 5–7 sequences. Seven deletion constructs used to investigate JAZ1 function are indicated. **d**, GFP–JAZ1 and GFP–JAZ6 are specifically targeted to the nucleus. DAPI (4,6-diamidino-2-phenylindole) staining (right panels) confirms location of the nuclei.

To investigate this hypothesis, we generated transgenic plants expressing a JAZ1–GUS (β -glucuronidase) fusion protein under control of the 35S promoter. Whereas seedlings expressing a 35S–GUS construct consistently exhibited strong blue staining especially in root tissue, lines carrying a 35S–JAZ1–GUS transgene provided weaker signals (Fig. 3b), as did plants transgenic for a 35S–JAZ6–GUS construct (Supplementary Fig. 3a). When seedlings were treated with 100 μ M jasmonate for 1 h before histochemical staining, JAZ1–GUS and JAZ6–GUS plants showed complete loss of GUS activity, whereas control seedlings were unaffected (Fig. 3c, and Supplementary Fig. 3a). Thus, jasmonate treatment specifically induces degradation of the JAZ–GUS fusion proteins. Treatment with 10 μ M MG132, a specific inhibitor of the 26S proteasome, prevented

jasmonate treatment from eliminating GUS staining in roots of JAZ1–GUS and JAZ6–GUS plants (Fig. 3d; Supplementary Fig. 3a).

Next, we generated transgenic lines expressing GUS fused to the JAZ1 Δ 3A deletion protein. Expression of the 35S–JAZ1 Δ 3A–GUS transgene resulted in a dominant, jasmonate-resistant male-sterile phenotype, like the original JAZ1 Δ 3A protein. Transgenic progeny of the male-sterile JAZ1 Δ 3A–GUS plants (derived from crosses to wild type) exhibited strong GUS activity in roots and other tissues, and this activity remained unchanged after jasmonate treatment (Fig. 3e). In contrast, four fertile lines expressing the 35S–JAZ1 Δ 3A–GUS transgene exhibited considerably lower levels of GUS staining (data not shown). We conclude that deletion of domain 3 from JAZ1 produces a protein that remains stable in the presence of jasmonate, and that accumulation of the deletion protein induces the dominant-negative, jasmonate-insensitive phenotypes shown in Fig. 2.

Finally, we transferred the 35S–JAZ1–GUS transgene into a line carrying the *coi1* mutation. Seeds were collected from a heterozygous (*COI1/coi1*) plant homozygous for a single transgene to ensure that segregating progeny would all express the same JAZ1–GUS reporter. In the absence of jasmonate treatment, root tips of wild-type (*COI1*) and homozygous mutant (*coi1*) segregants showed similar levels of GUS activity (Fig. 3d). As expected, the *COI1* roots were devoid of detectable GUS activity after incubation for 1 h in 100 μ M jasmonate. In contrast, roots of *coi1* seedlings retained GUS activity after the same incubation. The JAZ6–GUS reporter gave similar results

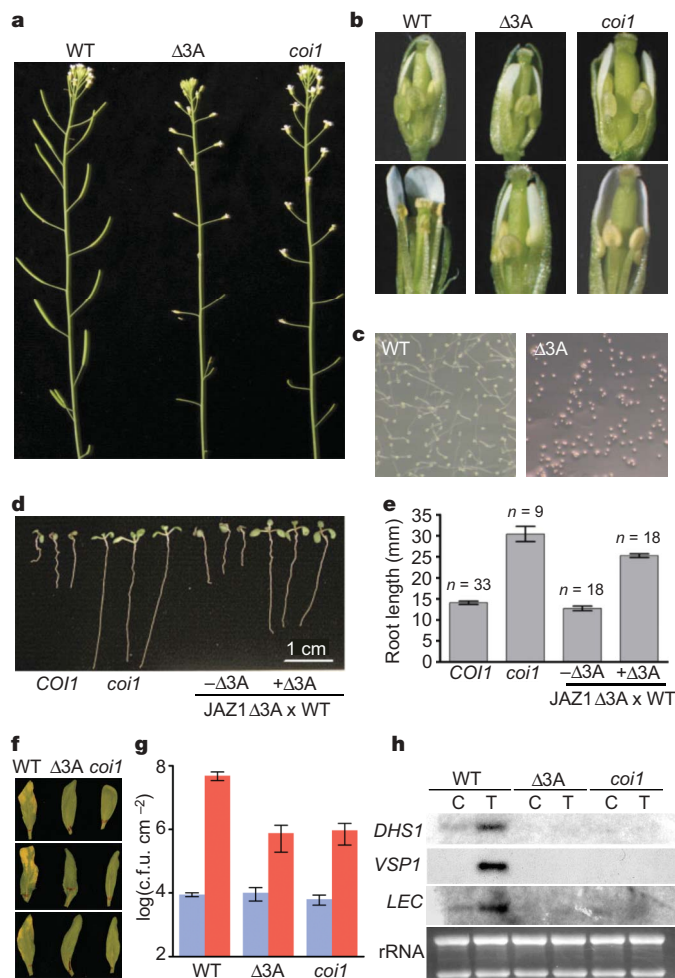


Figure 2 | Deletion of domain 3 of JAZ1 produces a dominant, jasmonate-resistant phenotype. **a**, Plants from line JAZ1 Δ 3A-5 (Δ 3A), like *coi1* mutants, are male-sterile. **b**, Stage 12 flowers (top panels) are similar in JAZ1 Δ 3A-5, *coi1* and wild type (WT); however, at stage 15 (lower panels), JAZ1 Δ 3A-5 and *coi1* flowers have short anther filaments and non-dehiscent anthers. **c**, JAZ1 Δ 3A-5 anthers produce inviable pollen. **d**, **e**, On 25 μ M of jasmonate, progeny of JAZ1 Δ 3A-5 \times WT have either short roots like wild-type progeny from a *COI1/coi1* parent (*COI1*) or elongated roots like *coi1* mutants. Progeny with long roots (20–28 mm) all carried the 35S–JAZ1 Δ 3A transgene, whereas plants with short roots (6–15 mm) lacked the transgene. Data are mean \pm s.e.m. for *n* shown. **f**, Three days after inoculation with *Pst* DC3000 bacteria, wild-type leaves had disease symptoms, whereas JAZ1 Δ 3A-5 and *coi1* did not. **g**, *Pst* DC3000 populations, shown as colony-forming units (c.f.u.) cm⁻² of leaf area, in wild-type, JAZ1 Δ 3A-5 and *coi1* plants at day 0 (blue) and day 3 (red) post inoculation; means \pm s.e.m. (*n* = 3). **h**, Gel-blot analysis of RNA from jasmonate-treated (T) and control (C) plants indicates that genes strongly induced by jasmonate in wild type are induced poorly or not at all in JAZ1 Δ 3A-5 and *coi1* plants. Ribosomal RNA indicates equal loading of RNA.

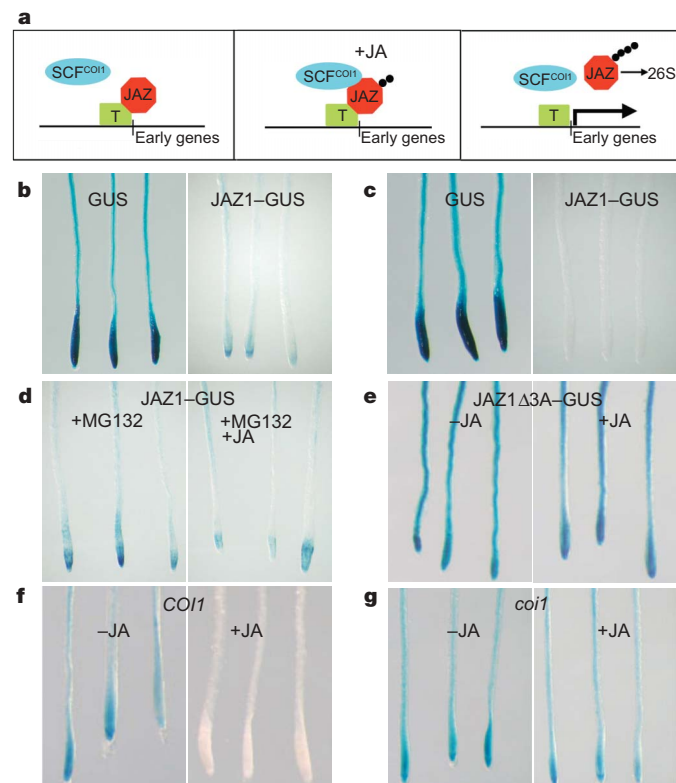


Figure 3 | Analysis of JAZ1–GUS function. **a**, Simplified model of possible SCF^{COI1} action. In response to jasmonate (JA), SCF^{COI1} interacts with JAZ repressors blocking transcription complexes (T) on jasmonate-responsive genes. JAZ ubiquitination (black circles) results in degradation through the 26S proteasome and de-repression of the jasmonate-response pathway. **b**, **c**, Plants expressing a 35S–JAZ1–GUS transgene showed low GUS activity (**b**), which was eliminated by jasmonate treatment (**c**). **d**, The proteasome inhibitor, MG132, increased GUS activity in JAZ1–GUS plants and made it resistant to jasmonate treatment. **e**, Sterile plants expressing a 35S–JAZ1 Δ 3A–GUS transgene had high GUS activity that was resistant to jasmonate. **f**, **g**, GUS activity in JAZ1–GUS transgenics was resistant to jasmonate treatment in *coi1* mutants but not in *COI1* segregants.

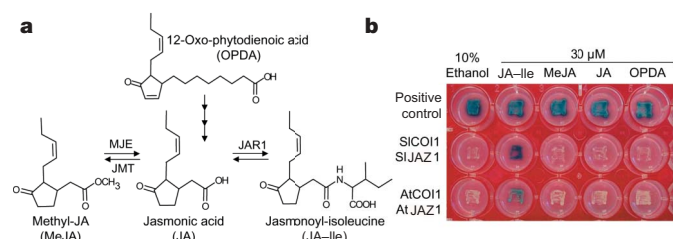


Figure 4 | JA-Ile-dependent interaction between COI1 and JAZ1 in yeast. **a**, The biosynthetic relationship between various jasmonates (OPDA, jasmonate, MeJA and JA-Ile) that have been implicated as bioactive signals. MJE, MeJA esterase; JMT, jasmonate carboxyl methyltransferase; JAR1, jasmonate resistant 1 conjugating enzyme. **b**, Y2H protein-protein interaction assay. Sl, *Solanum lycopersicum*; At, *Arabidopsis thaliana*. Blue colonies indicate interaction, white colonies indicate no interaction. Colonies of a positive-control strain, pLexA-53/pB42AD-T, are shown (top row).

(Supplementary Fig. 3b). We conclude that jasmonate-mediated degradation of JAZ1 and JAZ6 is dependent on COI1 function.

JA-Ile promotes the COI1-JAZ1 interaction

To test further the hypothesis that JAZ1 is a substrate of the SCF^{COI1} ubiquitin ligase, we examined a possible physical interaction between COI1 and JAZ1 using the yeast two-hybrid (Y2H) system. Indeed, COI1 and JAZ1 interacted in this assay, and, remarkably, the interaction was dependent on inclusion of JA-Ile in the growth medium (Fig. 4a, b). Other jasmonate derivatives, including jasmonate, methyl-jasmonate (MeJA), and the precursor, 12-oxo-phytodienoic acid (OPDA), did not promote the interaction at the concentrations tested. To determine whether this result extends to COI1-JAZ interactions in other plants, we studied the interaction between tomato (*Solanum lycopersicum*) COI1 (SlCOI1) and SlJAZ1, the tomato JAZ family member that is most closely related to *Arabidopsis* JAZ1 (Supplementary Fig. 1). Interaction between tomato COI1 and JAZ1 in yeast was also dependent on the presence of JA-Ile, and was not stimulated by jasmonate, MeJA or OPDA (Fig. 4b).

To determine whether COI1 and JAZ proteins interact *in vitro*, we took advantage of a transgenic line of tomato that expresses a functional c-Myc-tagged tomato COI1 (COI1-Myc) (Supplementary Fig. 5). *In vitro* interaction studies using COI1-Myc were performed with tomato JAZ1, which interacts with tomato COI1 in yeast (Fig. 4b). COI1-Myc was recovered from pull-down reactions containing JA-Ile, but not from reactions supplemented with MeJA or mock control (Fig. 5a). JA-Ile promoted the COI1-JAZ1 interaction in a dose-dependent manner (Fig. 5b) with the stimulatory effect apparent at concentrations as low as 50 nM JA-Ile. MeJA, jasmonate and OPDA, as well as the jasmonate-amino-acid conjugates JA-Phe and JA-Trp, failed to stimulate COI1-JAZ1 interaction at concentrations up to 25 μ M (Fig. 5c). JA-Leu exhibited activity that was at least 50-fold lower than that of JA-Ile. Taken together, the Y2H and protein pull-down results demonstrate that COI1 and JAZ1 interact physically, and that the interaction is promoted in a highly specific manner by JA-Ile.

Discussion

We have identified a previously unrecognized family of proteins and present evidence here that some of them act as repressors of jasmonate signalling and are targets of the SCF^{COI1} E₃ ubiquitin ligase. The JAZ genes are widely expressed in *Arabidopsis* plants and at least eight are rapidly induced by jasmonate. This rapid induction suggests that one function of the JAZ repressors is to regulate their own synthesis. In this way, COI1-dependent removal of pre-existing JAZ proteins can provide for rapid activation of defences and other jasmonate-dependent processes, whereas rapid synthesis of new JAZ proteins ensures attenuation of the jasmonate response soon after transmission of the signal. This second function may be important in

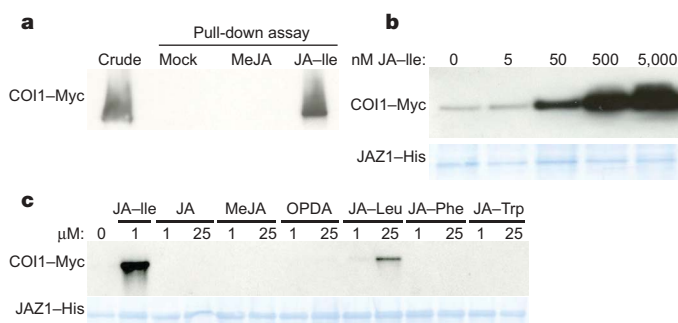


Figure 5 | Specificity of jasmonate action in a cell-free system. Pull-down assays used recombinant SlJAZ1-His and extracts from 35S-COI1-Myc plants. **a**, Assays were supplemented with 5 μ M MeJA, JA-Ile, or a control (mock) and incubated for 30 min at 4 °C. Protein bound to JAZ1-His was analysed by immunoblotting for the presence of COI1-Myc. Leaf extract (crude) shows position of COI1-Myc. **b**, Assays supplemented with various concentrations of JA-Ile, and processed as described above. In **b** and **c**, Coomassie stain shows JAZ1-His. **c**, Control ('0') or various jasmonate derivatives were added to pull-down reactions at the indicated concentrations.

preventing possible cellular damage caused by hyperactive and/or long-term stimulation of defence responses⁵. At least one additional *Arabidopsis* JAZ gene (*JAI3/JAZ3*; Supplementary Fig. 4) has been shown to encode a repressor³². The extent to which other JAZ and JAZ-like proteins have roles in jasmonate signalling remains to be determined.

Y2H and protein pull-down experiments show that, among the jasmonate derivatives tested, JA-Ile is the most active in promoting COI1-JAZ1 interaction; the other compounds had little or no activity (Fig. 5c). There is evidence that jasmonate, MeJA, JA-Phe and OPDA may also be active signals^{1,13,33-35}. It is possible that these compounds mediate interaction of COI1 with other members of the JAZ family, or with SCF^{COI1} substrates that remain to be identified. Alternatively, activity may depend on metabolic conversion to active compounds such as JA-Ile¹². The ability of JA-Ile to promote COI1-JAZ1 interaction in yeast (that is, in the absence of any other plant factors) suggests that the COI1-JAZ1 complex is the site of JA-Ile perception. The closest homologues of COI1 are six F-box proteins that act in auxin signalling through SCF-dependent ubiquitination of Aux/IAA repressor proteins and one of these F-box proteins, TIR1, was recently shown to be an auxin receptor³⁶. It will now be possible to test whether COI1 similarly acts as a receptor for JA-Ile.

Identification of the JAZ family of proteins will facilitate experiments to understand how the many different responses to jasmonate are regulated by the action of a single E₃ enzyme, SCF^{COI1}. It is possible that the specificity of interactions between distinct jasmonate compounds, COI1, JAZ proteins, and the downstream transcription or other complexes that JAZ proteins act on determines the outcome of jasmonate signalling in different tissues. Identification of the JAZ proteins will permit experiments to test this and other hypotheses, and will develop a better mechanistic understanding of jasmonate signalling in plants.

METHODS SUMMARY

DNA constructs and plant transformation. The production of GFP, GUS, JAZ1-deletion and COI1-Myc constructs followed standard molecular biology protocols. *Arabidopsis* plants were transformed using the floral-dip method³.

Phenotypic analysis and GUS assays. Characterization of *JAZ1Δ3A* transgenics used protocols that were based on previous experiments with *coi1* and jasmonate-synthesis mutants^{1,9,10,27,28}. For the gel-blot shown in Fig. 2h, wild-type, *JAZ1Δ3A* and *coi1* plants were treated with 10 μ M jasmonate for 6 h. Roots of plants expressing GUS reporter constructs were treated for 1 h with 100 μ M of MeJA. Pre-treatment with 10 μ M of MG132 as indicated was also for 1 h. Histochemical GUS staining was carried out as described³⁰, and the results observed under a Leica MZ8 dissecting microscope.

Protein–protein interaction. Y2H experiments were conducted using the MatchMaker system (Clontech). Protein–protein interactions in transformed yeast cells were assessed on agar medium containing various jasmonate derivatives at 30 μ M. For protein pull-down experiments, assays contained leaf extract from 35S-COII–Myc tomato plants (~1 mg total protein) and 100 μ g recombinant JAZ1–His (fused to maltose-binding protein at the amino terminus) in 300 μ l. Ni-NTA resin (Qiagen) was used to bind JAZ1–His. After washing and elution with imidazole, proteins were separated by electrophoresis, transferred to PVDF membrane and probed with anti-c-Myc antibody (Roche)³⁷.

Full Methods and any associated references are available in the online version of the paper at www.nature.com/nature.

Received 14 March; accepted 25 May 2007.

Published online 18 July 2007.

- Mandaokar, A. *et al.* Transcriptional regulators of stamen development in *Arabidopsis* identified by transcriptional profiling. *Plant J.* **46**, 984–1008 (2006).
- Farmer, E. E. & Ryan, C. A. Interplant communication: airborne methyl jasmonate induces synthesis of proteinase inhibitors in plant leaves. *Proc. Natl Acad. Sci. USA* **87**, 7713–7716 (1990).
- Vijayan, P., Shockey, J., Lévesque, C. A., Cook, R. J. & Browse, J. A role for jasmonate in pathogen defense of *Arabidopsis*. *Proc. Natl Acad. Sci. USA* **95**, 7209–7214 (1998).
- Kessler, A., Halitschke, R. & Baldwin, I. T. Silencing the jasmonate cascade: induced plant defenses and insect populations. *Science* **305**, 665–668 (2004).
- Farmer, E. E. Surface-to-air signals. *Nature* **411**, 854–856 (2001).
- Reymond, P. *et al.* A conserved transcript pattern in response to a specialist and a generalist herbivore. *Plant Cell* **16**, 3132–3147 (2004).
- Conconi, A., Smerdon, M. J., Howe, G. A. & Ryan, C. A. The octadecanoid signalling pathway in plants mediates a response to ultraviolet radiation. *Nature* **383**, 826–829 (1996).
- Browse, J. in *Vitamins and Hormones* (ed. Litwack, G.) 431–456 (AP-Elsevier, New York, 2005).
- Feys, B., Benedetti, C. E., Penfold, C. N. & Turner, J. G. *Arabidopsis* mutants selected for resistance to the phytotoxin coronatine are male sterile, insensitive to methyl jasmonate, and resistant to a bacterial pathogen. *Plant Cell* **6**, 751–759 (1994).
- Xie, D. X., Feys, B. F., James, S., Nieto-Rostro, M. & Turner, J. G. *COI1*: an *Arabidopsis* gene required for jasmonate-regulated defense and fertility. *Science* **280**, 1091–1094 (1998).
- Xiao, S. *et al.* *COS1*: an *Arabidopsis coronatine insensitive1* suppressor essential for regulation of jasmonate-mediated plant defense and senescence. *Plant Cell* **16**, 1132–1142 (2004).
- Staswick, P. E. & Tiryaki, I. The oxylipin signal jasmonic acid is activated by an enzyme that conjugates it to isoleucine in *Arabidopsis*. *Plant Cell* **16**, 2117–2127 (2004).
- Turner, J. G., Ellis, C. & Devoto, A. The jasmonate signal pathway. *Plant Cell* **14** (Suppl.), S153–S164 (2002).
- Li, L. *et al.* The tomato homolog of CORONATINE INSENSITIVE1 is required for maternal control of seed maturation, jasmonate-signaled defense responses, and glandular trichome development. *Plant Cell* **16**, 126–143 (2004).
- Funk, C. D. Prostaglandins and leukotrienes: advances in eicosanoid biology. *Science* **294**, 1871–1875 (2001).
- Deshais, R. J. SCF and Cullin/Ring H2-based ubiquitin ligases. *Annu. Rev. Cell Dev. Biol.* **15**, 435–467 (1999).
- Moon, J., Parry, G. & Estelle, M. The ubiquitin-proteasome pathway and plant development. *Plant Cell* **16**, 3181–3195 (2004).
- Lorenzo, O. & Solano, R. Molecular players regulating the jasmonate signalling network. *Curr. Opin. Plant Biol.* **8**, 532–540 (2005).
- Xu, L. *et al.* The SCF(CO1) ubiquitin-ligase complexes are required for jasmonate response in *Arabidopsis*. *Plant Cell* **14**, 1919–1935 (2002).
- Jensen, A. B., Raventos, D. & Mundy, J. Fusion genetic analysis of jasmonate-signalling mutants in *Arabidopsis*. *Plant J.* **29**, 595–606 (2002).
- Lorenzo, O., Chico, J. M., Sanchez-Serrano, J. J. & Solano, R. *JASMONATE-INSENSITIVE1* encodes a MYC transcription factor essential to discriminate between different jasmonate-regulated defense responses in *Arabidopsis*. *Plant Cell* **16**, 1938–1950 (2004).
- Ellis, C. & Turner, J. G. The *Arabidopsis* mutant *cev1* has constitutively active jasmonate and ethylene signal pathways and enhanced resistance to pathogens. *Plant Cell* **13**, 1025–1033 (2001).
- Devoto, A. *et al.* CO1 links jasmonate signalling and fertility to the SCF ubiquitin-ligase complex in *Arabidopsis*. *Plant J.* **32**, 457–466 (2002).
- Devoto, A. *et al.* Expression profiling reveals CO1 to be a key regulator of genes involved in wound- and methyl jasmonate-induced secondary metabolism, defence, and hormone interactions. *Plant Mol. Biol.* **58**, 497–513 (2005).
- Shikata, M. *et al.* Characterization of *Arabidopsis* ZIM, a member of a novel plant-specific GATA factor gene family. *J. Exp. Bot.* **55**, 631–639 (2004).
- Schmid, M. *et al.* A gene expression map of *Arabidopsis thaliana* development. *Nature Genet.* **37**, 501–506 (2005).
- Stintzi, A. & Browse, J. The *Arabidopsis* male-sterile mutant, *opr3*, lacks the 12-oxophytodiene acid reductase required for jasmonate synthesis. *Proc. Natl Acad. Sci. USA* **97**, 10625–10630 (2000).
- Katagiri, F., Thilmony, R. & He, S. Y. in *The Arabidopsis Book* (eds Somerville, C. R. & Meyerowitz, E. M.) doi:10.1199-tab.0039 (American Society of Plant Biologists, Rockville, Maryland, 2002).
- McConn, M., Creelman, R. A., Bell, E., Mullet, J. E. & Browse, J. Jasmonate is essential for insect defense in *Arabidopsis*. *Proc. Natl Acad. Sci. USA* **94**, 5473–5477 (1997).
- Gray, W. M., Kepinski, S., Rouse, D., Leyser, O. & Estelle, M. Auxin regulates SCF^{TIR1}-dependent degradation of AUX/IAA proteins. *Nature* **414**, 271–276 (2001).
- Sasaki, A. *et al.* Accumulation of phosphorylated repressor for gibberellin signaling in an F-box mutant. *Science* **299**, 1896–1898 (2003).
- Chini, A. *et al.* The JAZ family of repressors is the missing link in jasmonate signalling. *Nature* doi:10.1038/nature06006 (this issue).
- Kramell, R. *et al.* Amino acid conjugates of jasmonic acid induce jasmonate-responsive gene expression in barley (*Hordeum vulgare* L.). *FEBS Lett.* **414**, 197–202 (1997).
- Seo, H. S. *et al.* Jasmonic acid carboxyl methyltransferase: a key enzyme for jasmonate-regulated plant responses. *Proc. Natl Acad. Sci. USA* **98**, 4788–4793 (2001).
- Stintzi, A., Weber, H., Reymond, P., Browse, J. & Farmer, E. E. Plant defense in the absence of jasmonic acid: the role of cyclopentenones. *Proc. Natl Acad. Sci. USA* **98**, 12837–12842 (2001).
- Tan, X. *et al.* Mechanism of auxin perception by the TIR1 ubiquitin ligase. *Nature* **446**, 640–645 (2007).
- Li, C. *et al.* Role of β -oxidation in jasmonate biosynthesis and systemic wound signaling in tomato. *Plant Cell* **17**, 971–986 (2005).

Supplementary Information is linked to the online version of the paper at www.nature.com/nature.

Acknowledgements We are particularly grateful to Y. Shimada and members of his laboratory for the publicly available data in Fig. 1b, J. Turner for *coi1-1*, R. Kramell and P. Staswick for providing jasmonate–amino-acid conjugates, and M. Garavito for pRMG-nMAL. We thank C. Skidmore for help preparing the figures, B. Ryan and C. Somerville for discussions and critical reading of the manuscript. *Arabidopsis* T-DNA mutants were from the *Arabidopsis* Biological Resource Center, Ohio State University. This work was supported by funding from the US Department of Energy (J.B., S.Y.H., G.A.H.), the National Institutes of Health (S.Y.H., G.A.H.) and the Agricultural Research Center at WSU (J.B.).

Author Contributions B.T., L.K., M.M., S.Y.H., G.A.H. and J.B. planned experiments and analyses. B.T., L.K., M.M., Y.N., A.M., G.L. and K.N. performed experiments and analysed the results. B.T., S.Y.H., G.A.H. and J.B. wrote the manuscript. All authors discussed the results and commented on the manuscript.

Author Information The GenBank accession number for the tomato JAZ1 nucleotide sequence is EF591123. The GEO accession number for microarray data is GDS2133. Reprints and permissions information is available at www.nature.com/reprints. The authors declare no competing financial interests. Correspondence and requests for materials should be addressed to J.B. (j.b@wsu.edu).

METHODS

Plant material and growth conditions. *Arabidopsis thaliana* wild-type, *opr3* (ref. 27), and *coi1-1* (ref. 9) plants were grown on soil under continuous illumination ($100 \mu\text{E m}^{-2} \text{s}^{-1}$) at 22°C . In all experiments, wild type refers to the Columbia (Col-0) ecotype except in Supplementary Fig. 1, for which the Wassilewskija (Ws) ecotype was used. Plants were transformed by the floral dip method¹. In cases where seedlings were used for experiments, surface-sterilized seeds were sown on media containing half-strength Murashige and Skoog (MS) salts (Sigma) and 1% sucrose, solidified with 0.8% agar. Seedlings were grown in Petri dishes held vertically so roots grew along the agar surface, and used for experiments seven days after sowing. For experiments on the effects of jasmonate on root growth, the agar contained $25 \mu\text{M}$ of jasmonate as the methyl ester (Bedoukian Chemical).

Histochemical GUS analysis and pollen germination. Techniques and primers used for the production of GFP-fusion, GUS-fusion and *JAZ1A3A* deletion constructs and the transformation of plants are included in Supplementary Information. Histochemical GUS staining was carried out essentially as described by ref. 30. Seven-day-old seedlings were taken from plates and immersed in cold 90% acetone and kept on ice until all samples were collected. Samples were incubated for at least 20 mins at room temperature, and then washed in solution of 0.05 M sodium phosphate buffer pH7.2, 0.2% Triton X-100, 2 mM potassium ferrocyanide, and 2 mM potassium ferricyanide. Washing solution was removed and staining solution (washing solution plus 2 mM X-Gluc) was added, and samples were incubated overnight at 37°C . Staining solution was removed and the samples were subject to a series of ethanol washes: 20%, 35%, 50% at room temperature for 30 minutes each. Seedlings were fixed in a solution of 50% ethanol, 10% glacial acetic acid and 5% formaldehyde for 30 minutes, and then stored in 70% ethanol. Stained tissue was visualized under a Leica MZ8 dissecting microscope. Techniques used to genotype the transgenic and mutant plants are described under Supplementary Information.

Pollen viability was tested on plates containing 17% (w/v) sucrose, 1 mM CaCl_2 , and 102 mg l^{-1} boric acid, pH 7.0, solidified with 0.6% (w/v) agarose. Pollen was applied to the medium by touching dehiscent or cut anthers to the surface. Plates were incubated in the dark at room temperature for 16–20 h, and then scored for pollen germination.

Chemical treatments of seedlings expressing GUS fusion proteins. Seven-day-old seedlings grown on plates (see above) were placed in half-strength MS salts, pH 5.8. For jasmonate treatments, the medium was supplemented with $100 \mu\text{M}$ jasmonate, as the methyl ester. A broad-spectrum protease inhibitor cocktail (Sigma) did not provide for increased GUS staining, or alter the effect of jasmonate (data not shown). For pretreatment with MG132, the medium was supplemented with $10 \mu\text{M}$ MG132 (Calbiochem). After addition of jasmonate, seedlings were gently shaken for one hour before GUS staining. Seedlings of

the *JAZ1-GUS* line were also treated with indole acetic acid ($20 \mu\text{M}$; 1 h), 2,4-dichlorophenoxyacetic acid ($5 \mu\text{M}$; 1 h) and gibberellic acid ($50 \mu\text{M}$; 1 h), but these hormone treatments did not cause any observable decrease in GUS staining (data not shown).

Protein–protein interaction studies. The *Arabidopsis* COI1 (*AtCOI1*) and tomato COI1 (*SlCOI1*) genes were cloned into the Y2H ‘bait’ vector pGilda (Clontech). The *Arabidopsis* (*AtJAZ1*) and tomato (*SlJAZ1*) JAZ genes were cloned into the Y2H ‘prey’ vector pB42AD (Clontech). Bait and prey gene constructs were co-transformed into yeast (*Saccharomyces cerevisiae*) strain EGY48 (p8opLacZ). Protein–protein interactions in transformed yeast cells were assessed on agar medium containing various jasmonate derivatives at a concentration of $30 \mu\text{M}$ (see Supplementary Information for details).

Construction of the transgenic 35S-COI1-Myc tomato line is described in the Supplementary Information. Leaflets from 2–3-week-old 35S-COI1-Myc tomato plants were ground to a fine powder in liquid N_2 . Protein was extracted in homogenization buffer containing 50 mM Tris-Cl, pH 7.6, 100 mM NaCl, 25 mM imidazole, 10% (v/v) glycerol, 0.1% (v/v) Tween 20, 20 mM 2-mercaptoethanol, $10 \mu\text{M}$ MG132, and the EDTA-free complete miniprotease inhibitor cocktail (Roche). Insoluble debris was removed by centrifugation at $14,000g$ for 10 min at 4°C . Each pull-down assay contained $\sim 1 \text{ mg}$ of total tomato protein and $100 \mu\text{g}$ of recombinant JAZ1-His (see Supplementary Information) in a total volume of $300 \mu\text{l}$. Reactions were incubated, with gentle rocking, for 30 min at 4°C in the absence or presence of various jasmonate derivatives. Following the addition of $80 \mu\text{l}$ of Ni-NTA Resin (Qiagen), the reaction was incubated for an additional 15 min at 4°C . Ni-NTA resin was recovered by centrifugation on a spin column (Biorad) and washed three times with $250 \mu\text{l}$ of homogenization buffer. The affinity resin was eluted with $30 \mu\text{l}$ of a solution containing 250 mM imidazole. The eluted protein was separated by SDS-PAGE on a 12% gel, transferred to PVDF membrane, and probed with an anti-c-Myc antibody (Roche) as previously described²⁷. The amount of COI1-Myc recovered in the absence of JA-Ile varied between experiments, most likely as a result of differences in endogenous levels of JA-Ile or other active compounds in the tomato extract. Control experiments showed that COI1-Myc was not recovered from pull-down reactions containing JA-Ile but lacking recombinant JAZ1-His, or from reactions containing a maltose-binding-protein-His fusion in place of JAZ-His (data not shown). (\pm)-Jasmonic acid (J2500) and MeJA (392707) were purchased from Sigma. 12-OPDA was chemically synthesized as previously described³⁸. Jasmonoyl-amino-acid conjugates were kindly provided by R. Kramell. Conjugates were synthesized by reaction of (\pm)-jasmonate with the corresponding L-amino acid, followed by purification of (–)-jasmonate-L-amino-acid isomers by chiral HPLC³³.

38. Schilmiller, A. L., Koo, A. J. K. & Howe, G. A. Functional diversification of acyl-CoA oxidases in jasmonic acid biosynthesis. *Plant Physiol.* **143**, 812–824 (2007).

ARTICLES

The JAZ family of repressors is the missing link in jasmonate signalling

A. Chini^{1*}, S. Fonseca^{1*}, G. Fernández^{1*}, B. Adie¹, J. M. Chico¹, O. Lorenzo^{1†}, G. García-Casado², I. López-Vidriero², F. M. Lozano³, M. R. Ponce³, J. L. Micol³ & R. Solano^{1,2}

Jasmonates are essential phytohormones for plant development and survival. However, the molecular details of their signalling pathway remain largely unknown. The identification more than a decade ago of COI1 as an F-box protein suggested the existence of a repressor of jasmonate responses that is targeted by the SCF^{COI1} complex for proteasome degradation in response to jasmonate. Here we report the identification of JASMONATE-INSENSITIVE 3 (JAI3) and a family of related proteins named JAZ (jasmonate ZIM-domain), in *Arabidopsis thaliana*. Our results demonstrate that JAI3 and other JAZs are direct targets of the SCF^{COI1} E3 ubiquitin ligase and jasmonate treatment induces their proteasome degradation. Moreover, JAI3 negatively regulates the key transcriptional activator of jasmonate responses, MYC2. The JAZ family therefore represents the molecular link between the two previously known steps in the jasmonate pathway. Furthermore, we demonstrate the existence of a regulatory feed-back loop involving MYC2 and JAZ proteins, which provides a mechanistic explanation for the pulsed response to jasmonate and the subsequent desensitization of the cell.

Life on earth relies on a complex equilibrium of biotic and abiotic interactions. Plant small signalling molecules such as the jasmonates, structurally similar to prostaglandins in metazoans^{1,2}, are essential for plant survival in nature, and thus contribute to modulation of this equilibrium. Jasmonates (jasmonic acid and other oxylipin derivatives) are key regulators of plant responses to environmental stresses and biotic challenges, such as ozone exposure, wounding, water deficit, and pathogen and pest attack^{1–4}. They are also involved in important plant developmental processes, such as root growth, tuberization, fruit ripening, tendril coiling, reproductive development and senescence^{1–4}. Their importance beyond the plant kingdom has been recently highlighted by their suggested anti-cancer activity in humans⁵.

More than four decades after the discovery of methyl jasmonate as a major lipid constituent of the jasmine scent⁶, understanding of the biosynthetic (octadecanoid) pathway of jasmonates from linolenic acid is now well established⁷. In contrast, our current knowledge about the jasmonate signalling pathway lags behind^{3,8}.

Efforts to dissect the signalling pathway have defined two steps. The first one comprises components and regulators of SCF (Skip/Cullin/F-box) E3 ubiquitin ligase complexes (SCF^{COI1})^{9–13}. The second step is defined by transcription factors, such as MYC2 and ERF1, which orchestrate the expression of jasmonate-related effector genes^{14–16}. However, these two steps remain unlinked and major questions about the molecular details of the jasmonate signalling pathway remain unanswered. For example, the jasmonate receptor is unknown, the link between jasmonate perception and SCF^{COI1} is unidentified, and the connection between this SCF complex and the activation of transcription factors remains unresolved.

The existence of these two types of jasmonate-signalling components has led to the hypothesis that activation of jasmonate responses by transcription factors requires ubiquitin-mediated degradation of a repressor that is targeted to the 26S proteasome by the SCF^{COI1} after

jasmonate perception. However, more than a decade after the molecular identification of COI1, the F-box component of the SCF^{COI1} complex, the identity of this hypothetical repressor remains unknown.

Here we report the identification of JASMONATE-INSENSITIVE 3 (JAI3) and show that it belongs to a novel family of jasmonate-regulated nuclear targets of SCF^{COI1}, named JAZ (jasmonate ZIM-domain) proteins. JAI3 and other JAZs physically interact with COI1, and jasmonate treatment induces their SCF^{COI1}-dependent proteasome degradation. The *jai3-1* allele encodes a mutant protein resistant to degradation that also inhibits degradation of the wild-type JAI3 and other JAZs, explaining its dominant jasmonate-insensitive phenotype. Additionally, JAI3 and JAZ1 interact with MYC2, the key transcriptional activator of jasmonate-regulated gene expression, suggesting a model of JAI3/JAZ action as repressors of MYC2. Our results demonstrate that JAZs are direct targets of the SCF^{COI1}, linking ubiquitin-mediated protein degradation to transcriptional activation of jasmonate responses. Moreover, our results show that MYC2 and JAZs are involved in a negative regulatory feed-back loop that provides a mechanistic explanation for the pulsed response to jasmonate and the subsequent desensitization of the cell.

Identification of JAI3

We have previously isolated a jasmonate-insensitive mutant carrying the *jai3-1* dominant mutation¹⁵. In addition to its phenotypic defects in response to jasmonate¹⁵, microarray analyses showed that the *jai3-1* mutant is impaired in the transcriptional activation of jasmonate-responsive genes compared to wild-type plants. Thirty-one genes showed a lower expression in the *jai3-1* mutant after jasmonate treatment compared to jasmonate-treated wild-type plants (Supplementary Table 1). In contrast, only three genes had a higher expression in the mutant. Meta-analysis of downregulated genes showed that most of them were upregulated by jasmonate in wild-type plants

¹Departamento de Genética Molecular de Plantas and ²Unidad de Genómica, Centro Nacional de Biotecnología-CSIC, Campus Universidad Autónoma, 28049 Madrid, Spain. ³División de Genética and Instituto de Bioingeniería, Universidad Miguel Hernández, Campus de Elche, 03202 Elche, Spain. [†]Present address: Dpto. de Fisiología Vegetal. Centro Hispano-Luso de Investigaciones Agrarias (CIALE), Facultad de Biología, Universidad de Salamanca, Plaza de los Doctores de la Reina s/n, 37007 Salamanca, Spain.

*These authors contributed equally to this work.

(Fig. 1a). These results further support the idea that wild-type JAI3 is required for a complete response to jasmonate and that the dominant *jai3-1* mutation represses jasmonate-dependent gene expression.

A positional cloning approach, together with candidate sequencing (based on previous analyses; B. Thines and J. Browse, personal communication; see Methods), allowed us to identify At3g17860 as the mutated gene in the *jai3-1* mutant (Fig. 1b and Supplementary Fig. 1). *JAI3* encodes a member of a previously uncharacterized family of 12 proteins of unknown biochemical function, which we named JAZ (jasmonate ZIM-domain proteins; Supplementary Fig. 1). Homology within this family is confined to two domains, a ZIM motif and a carboxy-terminal domain (Fig. 1c and Supplementary Figs 1, 2). Outside these domains, some members of the family share weak sequence similarity at the amino terminus. Numerous JAZ homologues were identified in several plant species but not in animals, yeast or bacteria, suggesting that JAZs are plant-specific proteins.

JAZ proteins show domain similarity with transcription factors, such as ZIM1 (refs 17,18) and CONSTANS^{19,20} (CO) (Supplementary Fig. 1) that may imply a function as transcriptional regulators. However, none of the JAZs contains any known DNA-binding domain.

Sequencing of At3g17860 genomic DNA in the *jai3-1* mutant identified a G to A transition in the splicing acceptor site of its 5th intron. Sequencing of the corresponding complementary DNA demonstrated that the last two exons of the *JAI3* gene are absent from the mutant *jai3-1* messenger RNA, which translates to an aberrant protein (JAI3-1) lacking the C-terminal domain and including 14 extra amino acids encoded by the fifth intron (now behaving as an exon owing to the *jai3-1* mutation) (Fig. 1b–d).

Constitutive expression of *JAI3ΔC* (amino acids 1 to 298 of JAI3, the same protein as in *jai3-1* without the 14 extra amino acids; see Supplementary Fig. 3) confers jasmonate-insensitivity to *Arabidopsis* transgenic plants, further confirming that this mutation is responsible for the dominant jasmonate-insensitive phenotype of *jai3-1* (Fig. 1e–h). However, defects in jasmonate-related responses could not be observed in transgenic lines overexpressing the wild-type full-length *JAI3* mRNA (Fig. 1g), indicating the importance of the C-terminal domain in the regulation of JAI3 activity.

SCF^{COI1} targets JAI3 for degradation in response to jasmonate

The dominant jasmonate-insensitive phenotype of the *jai3-1* mutant and the molecular nature of the *jai3-1* mutation indicated that JAI3 might be the hypothetical repressor of jasmonate responses, negatively regulated by the proteasome in an SCF^{COI1}-dependent manner.

Consistent with this hypothesis, physical interaction between JAI3 and COI1 proteins was demonstrated by enrichment of [³⁵S]JAI3 in amylose resins containing maltose binding protein (MBP)–COI1 compared to MBP controls (Fig. 2a). Similarly, enrichment of [³⁵S]COI1 was observed in MBP–JAI3-containing resins. Analyses with truncated versions of JAI3 showed that COI1 interacts with the JAI3 N terminus (containing the ZIM domain), but not with its C terminus (containing the C-terminal domain) (Fig. 2b). These results suggest that JAI3 is a direct target of COI1. To confirm further this hypothesis, we monitored proteasome degradation of JAI3 and its dependence on the presence of a functional COI1 protein in transgenic lines expressing JAI3–GFP (green fluorescent protein) both in wild-type and *coi1-1* backgrounds. The JAI3 fusion protein was visible in nuclei of untreated root cells, but disappeared after jasmonate treatment (Fig. 2c, d). The proteasome-specific inhibitor MG132 blocked JAI3 degradation, implicating the 26S proteasome in jasmonate-mediated JAI3 removal (Fig. 2e). Moreover, jasmonate treatment did not promote degradation of JAI3–GFP in the *coi1-1* mutant, further confirming that JAI3 is a target of SCF^{COI1} (Fig. 2f, g). These results indicate that jasmonate treatment induces JAI3 degradation by the 26S proteasome in a COI1-dependent manner. In contrast to JAI3, integrity of the mutant JAI3ΔC protein was unaffected by the jasmonate treatment (Fig. 2h, i), suggesting that the C-terminal domain is required for JAI3 instability in response to jasmonate, and that degradation of JAI3 is required for jasmonate sensitivity.

These results were further confirmed by *in vitro* degradation assays and transient expression by agroinfiltration in *Nicotiana benthamiana* leaves (Supplementary Figs 4 and 5). In agreement with the dominant nature of the *jai3-1* mutation, both types of analyses demonstrated that the presence of JAI3ΔC prevented degradation of the wild-type JAI3 protein in response to jasmonate treatment (Supplementary Figs 4 and 5).

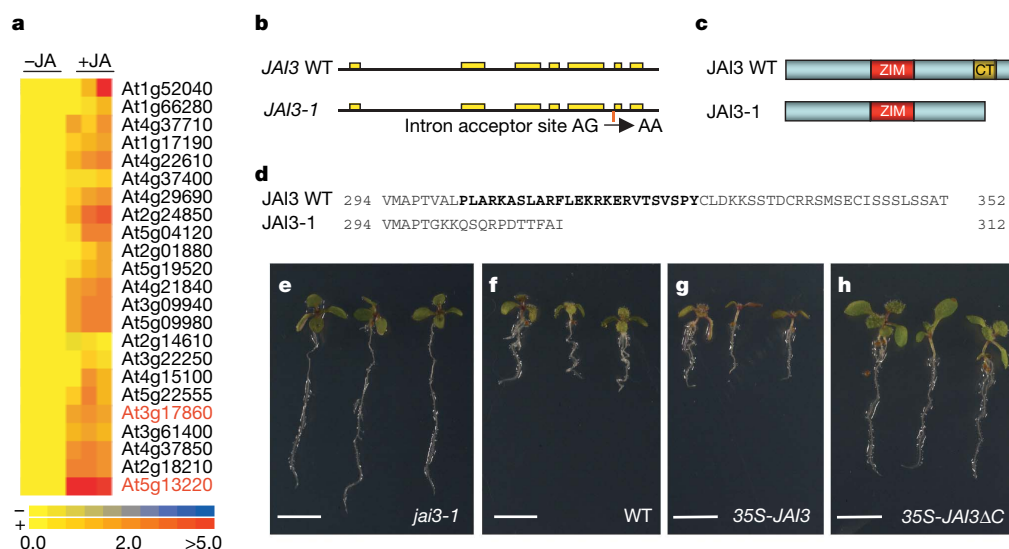


Figure 1 | JAI3-dependent gene expression and identification of JAI3. **a**, Jasmonate (JA) regulation in wild-type plants (0.5, 1 and 3 h) of genes differentially expressed in *jai3-1* (versus Col-0) after jasmonate treatment (see Supplementary Table 1). Data are from http://bbc.botany.utoronto.ca/affydb/cgi-bin/affy_db_express_browser_in.cgi. JAZs are highlighted in red. Scale, log ratio of fold change. **b**, *JAI3* genomic organization showing the

jai3-1 mutation. **c**, JAI3 and JAI3-1 proteins. ZIM and C-terminal domains are shown. **d**, C-terminal sequences of JAI3 and JAI3-1; C-terminal domain is highlighted in bold. **e–h**, Jasmonate sensitivity of *jai3-1* (**e**), wild-type (**f**), and transgenic plants constitutively expressing *JAI3* (**g**) or *JAI3ΔC* (**h**). Scale bars, 5 mm.

It has been previously shown²¹ that JAR1 conjugates jasmonate with amino acids to produce the active jasmonate (JA)-derivative (most likely JA-Ile). In accordance with this hypothesis, degradation of JAI3 in response to jasmonate was greatly impaired in *jar1* mutant extracts (Supplementary Fig. 7). However, JAI3 degradation was not compromised in response to coronatine, a jasmonate analogue structurally similar to JA-Ile. These results support the hypothesis that JA-Ile (or another JAR1-dependent jasmonate-derivative) is the active hormone, rather than jasmonate itself (see ref. 22 for additional results supporting this hypothesis).

JAI3 links SCF^{COI1} with jasmonate transcriptional activation

The lack of an obvious DNA-binding domain in JAI3 suggested that its hypothetical transcriptional repressor function, released by ubiquitin-mediated degradation, would be indirect, and not involve DNA-binding. This raised the hypothesis that JAI3 might act as a repressor of the key transcriptional activator of responses to jasmonate, MYC2 (refs 14, 15). Consistent with this hypothesis, *in vitro* pull-down assays demonstrated a direct MYC2-JAI3 interaction

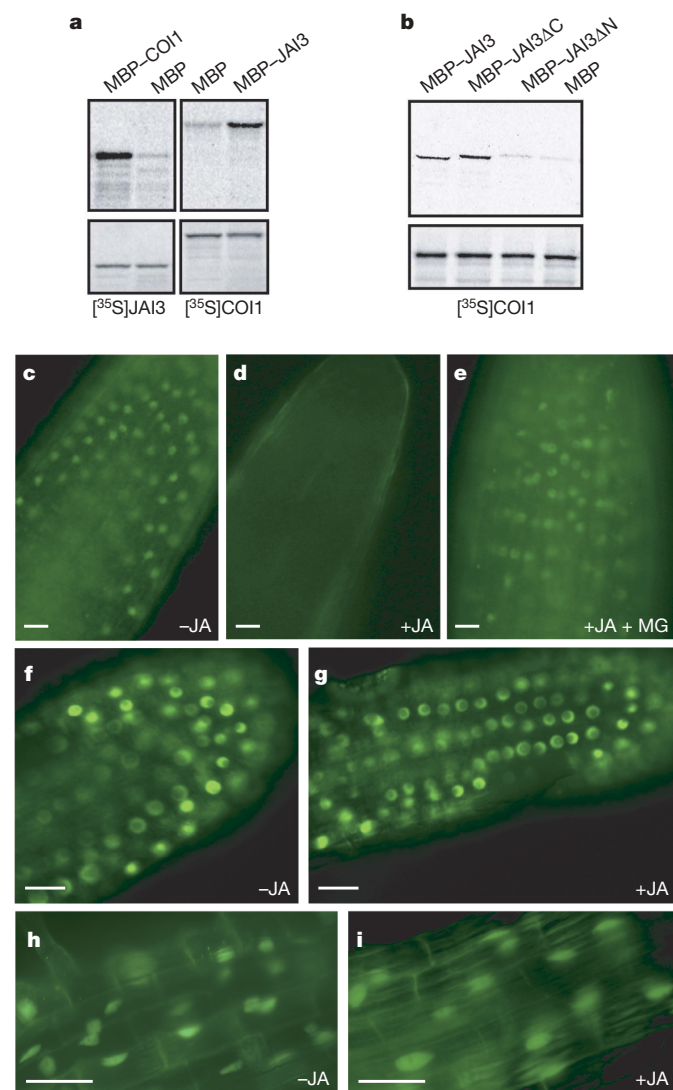


Figure 2 | JAI3-COI1 interaction and COI1-dependent proteasome degradation of JAI3. **a, b,** *In vitro* pull-down of [³⁵S]JAI3 and [³⁵S]COI1 using amylose resins containing MBP-COI1 and MBP-JAI3, respectively (**a**) or MBP-JAI3 derivatives (**b**) (see Supplementary Fig. 3). Lower panels show protein 'input'. **c–i,** JAI3-GFP (**c–g**) or JAI3ΔC-GFP (**h, i**) in nuclei of transgenic root cells in wild-type (**c–e, h, i**) or *coi1-1* (**f, g**) backgrounds. –JA, untreated controls; +JA, treated with 50 µM jasmonate for 1 h; MG, treated with 100 µM of the proteasome inhibitor MG132. Scale bar, 10 µm.

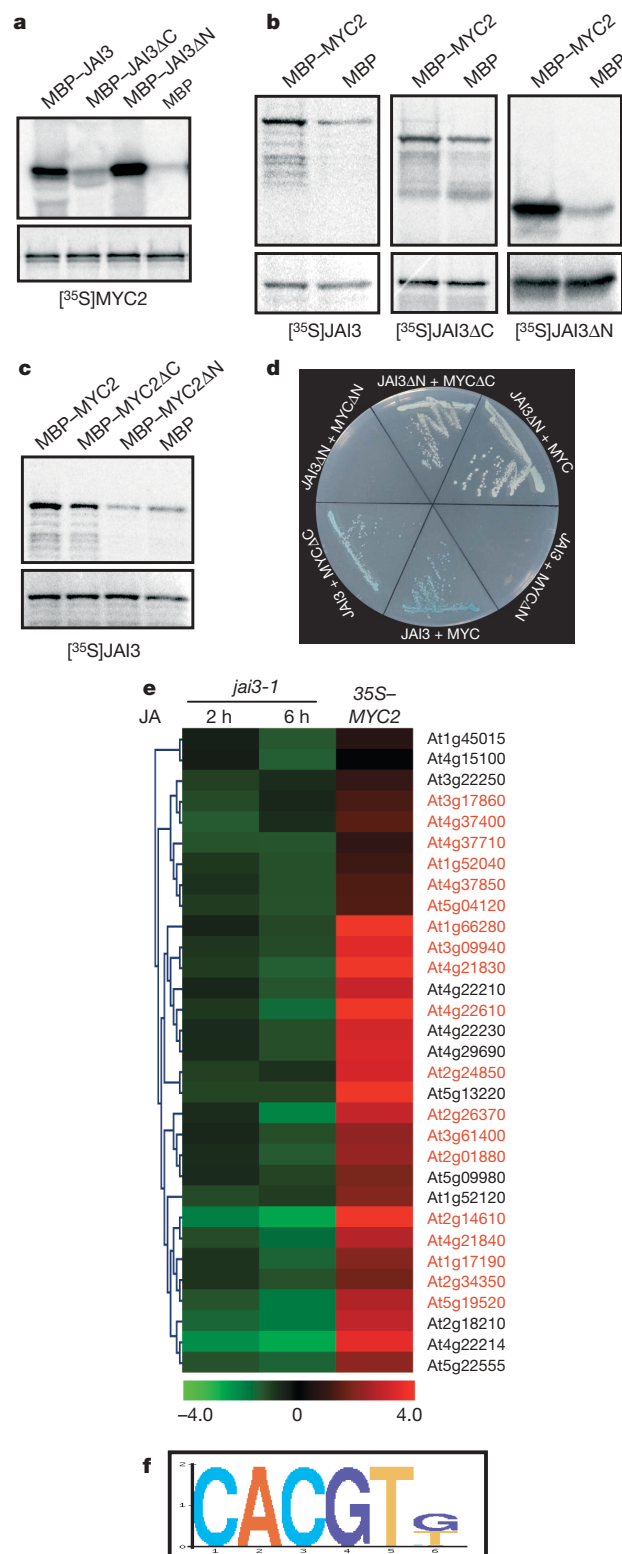


Figure 3 | Regulation of MYC2 by JAI3. **a–c,** *In vitro* pull-down of [³⁵S]MYC2 and [³⁵S]JAI3 (or derivatives; see Supplementary Fig. 3) using amylose resins containing MBP-fused JAI3 (**a**), MYC2 (**b**) or derivatives (**a, c**). Lower panels show protein 'input'. **d,** Yeast two-hybrid interactions between JAI3, MYC2 and derivatives. **e,** Genes differentially expressed in *jai3-1* (versus Col-0) after jasmonate treatment, and expression levels in 35S-MYC2 plants (Supplementary Table 1). **f,** DNA-binding target of MYC2 (T/G-box or G-box) identified as the sequence statistically over-represented in the promoters of genes shown in **e**. Genes with T/G-box or G-box in their promoters are highlighted in red font (**e**).

(Fig. 3a–c). In contrast to COI1, MYC2 interacts with MBP–JAI3ΔN, containing the C-terminal domain (Fig. 3a). Accordingly, enrichment of [³⁵S]JAI3 and [³⁵S]JAI3ΔN proteins (but not [³⁵S]JAI3ΔC) was obtained using MBP–MYC2 (Fig. 3b). Likewise, using MYC2 truncated derivatives we demonstrated that JAI3 interacts with the N terminus of MYC2 (Fig. 3c). Yeast two-hybrid assays further confirmed MYC2–JAI3 interaction (Fig. 3d).

Microarray analysis also supported the result that JAI3 is a negative regulator of MYC2 function. Thus, most of the genes showing a lower expression in *jai3-1* than in wild-type plants after jasmonate treatment are regulated by MYC2 (constitutively expressed in 35S-MYC2 plants; Fig. 3e). Moreover, as shown in Fig. 3f, analysis of the sequences over-represented in the promoters of these genes (*jai3-1* repressed genes) showed the T/G-box (or the G-box, the target binding sites of MYC2; see also below) as the sequence most over-represented (P value 7.19×10^{-7} ; Fig. 3f). These results show that JAI3 represents the missing molecular link between the two well-established steps of the jasmonate signalling pathway, SCF^{COI1} and the transcription factor regulating jasmonate-dependent transcriptional reprogramming.

Redundancy among JAZ proteins

The fact that JAI3ΔC does not interact with MYC2 indicates that the *jai3-1* dominant phenotype might be a consequence of the interaction between the JAI3-1 mutant protein and COI1. The resistance to degradation of the JAI3-1 mutant protein might maintain the SCF^{COI1} complex in an inactive state. Therefore, if JAI3-1 is not repressing MYC2 in *jai3-1*, the lack of MYC2 activity in this mutant is likely explained by redundancy among JAZ proteins that would not be targeted for degradation by the partially inactive SCF^{COI1} and therefore would keep repressing MYC2. Consistent with this hypothesis, defects in jasmonate-related responses could not be detected

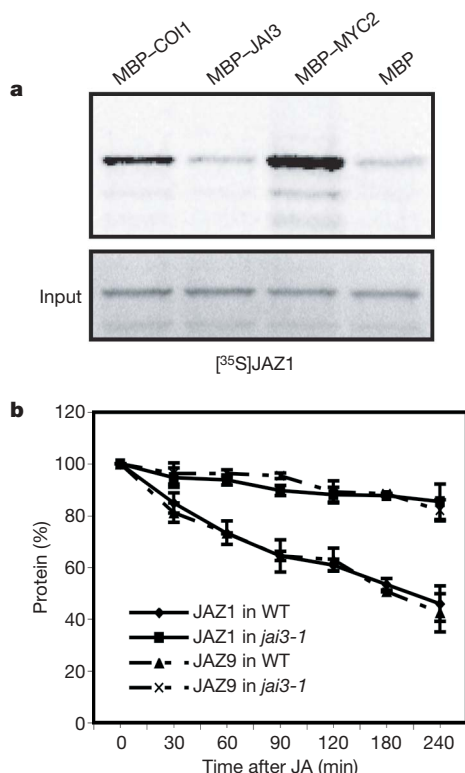


Figure 4 | Functional redundancy among JAZ proteins. **a**, *In vitro* pull-down assays of [³⁵S]-labelled, *in vitro* translated JAZ1 ([³⁵S]JAZ1) using MBP N-terminal fusions of COI1, JAI3 or MYC2. Experimental conditions are as in Figs 2 and 3. **b**, Degradation of [³⁵S]-labelled JAZ1 and JAZ9 proteins after incubation for the indicated times with cellular extracts from wild-type or *jai3-1* plants treated with 50 μM of jasmonate. Values represent the mean ± s.d.; $n = 3$.

in mutants carrying loss-of-function insertional alleles of *JAI3* and other JAZ-encoding genes (not shown). Moreover, other JAZ proteins (for example, JAZ1) also interact with COI1 and MYC2, and are similarly degraded by the proteasome (Fig. 4a, b and data not shown). Likewise, JAZ1 and JAZ9 degradation after jasmonate treatment is greatly impaired in the *jai3-1* mutant (Fig. 4b), further supporting the fact that the dominant effect of JAI3-1 affects not only JAI3 (Supplementary Figs 4 and 5), but also other JAZ proteins.

Feed-back regulation of JAZ genes by MYC2

Microarray analysis of early responses to jasmonate (30 min) showed that expression of 10 members of the JAZ family is quickly and specifically induced by jasmonate treatment (Fig. 5a). Interestingly, MYC2 seems to regulate the expression of most members of this family in response to jasmonate, given that eight of the ten jasmonate-induced JAZ genes are constitutively overexpressed in untreated 35S-MYC2 plants, whereas expression of seven of the ten is reduced in loss-of-function *myc2* mutants treated with jasmonate, as compared to wild-type plants (Fig. 5a). Analysis of the promoter regions of JAZ genes revealed the G-box or its variant T/G-box as the sequences most significantly over-represented (Fig. 5b). It is noteworthy that these two boxes are the target binding sites of MYC2. This transcription factor specifically recognizes the G-box (and T/G-box) sequence in the promoter of *JAI3* (and also present in the promoters of other JAZ genes; Supplementary Table 2), but does not recognize the mutant versions lacking the G- or T/G-boxes (Fig. 5c). Further support for the notion of a regulatory feed-back

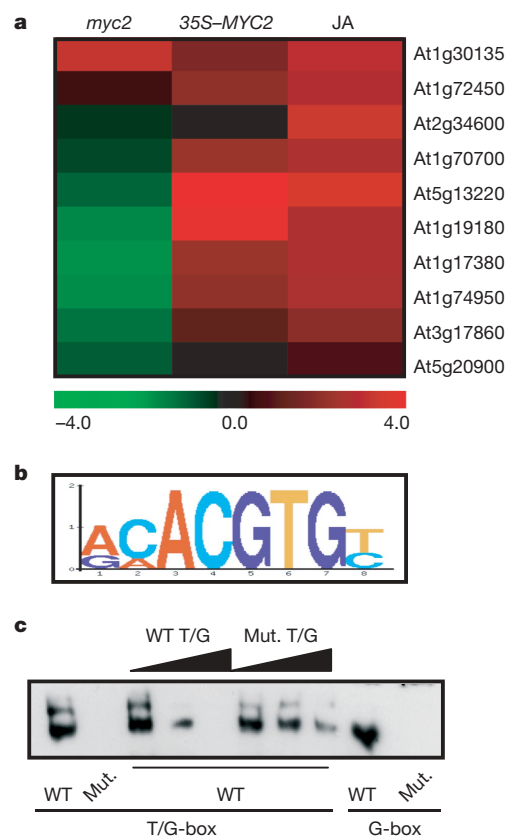


Figure 5 | Feed-back regulation of JAZ expression by MYC2. **a**, JAZ gene expression data in loss-of-function *myc2* versus wild-type (both jasmonate-treated), 35S-MYC2 versus wild-type untreated, and wild-type (jasmonate-treated versus untreated). Colour scale represents fold-change. **b**, Sequence significantly over-represented in the promoters of JAZs using MotifSampler³⁸ (T/G- and G-boxes). **c**, Retarded bands from EMSA of MYC2 binding to promoter fragments of *JAI3* containing the T/G- or G-boxes and mutated versions (Supplementary Table 2). Bottom lettering, biotin-labelled probe. Top lettering, increasing concentrations (1×, 3× and 10×) of unlabelled probes.

loop came from the observation that most of the genes downregulated in the *jai3-1* mutant (as compared to wild-type) following jasmonate treatment seem to be targets of MYC2 (Fig. 3e).

Discussion

Our identification of this new family of COI1 targets solves a major challenge in understanding jasmonate signalling because it demonstrates the existence of a family of repressors that link the SCF^{COI1} E3 ubiquitin ligase to the transcriptional activation of jasmonate responses.

Thus, the activation of jasmonate responses is regulated through a negative feed-back regulatory loop involving MYC2 and JAZ proteins. This provides a mechanistic explanation of the pulsed hormonal response and the subsequent desensitization of the cell to jasmonate²³. Binding of the hormone to its receptor induces SCF^{COI1}-dependent proteasome degradation of JAZ proteins liberating MYC2 and allowing transcriptional activation of jasmonate responses (Supplementary Fig. 6). Because JAZ genes are transcriptional targets of MYC2, their rapid expression induced by this transcription factor contributes to the self-repression of MYC2. In the *jai3-1* mutant, partial sequestration of COI1 by JAI3-1 prevents degradation of the other JAZs after jasmonate perception (Fig. 4b), which keep repressing MYC2 and therefore confer the jasmonate-insensitive phenotype. Consistent with this model, the majority of genes downregulated in the *jai3-1* mutant (as compared with wild-type) following jasmonate treatment seem to be targets of MYC2 (Fig. 3e).

The identification of the JAZ family may also help us to understand jasmonate perception. Since the identification of TIR1 as the auxin receptor^{24–26}, the sequence similarity of COI1 and TIR1 indicated that the SCF^{COI1} might be the jasmonate receptor (see ref. 22 for results supporting this hypothesis). It has been previously proposed that jasmonate is unlikely to be the active hormone²¹. However, several jasmonate analogues, such as JA-Ile and coronatine, displaying an intriguing similarity in their chemical structure^{21,27,28}, show overlapping as well as specific COI1-dependent activities^{29–31}. It is tempting to speculate that different receptor complexes may be formed by the combination of COI1 with different members of the JAZ family. This combinatorial mechanism would provide a molecular explanation for the overlapping and specific activities of these active jasmonate analogues. The identification of JAZ proteins will allow testing of this hypothesis.

Finally, transcriptional reprogramming in response to jasmonate cannot be exclusively attributed to MYC2, because loss-of-function mutations in this gene do not completely impair jasmonate sensitivity^{3,14,15}. The identification of this family of repressors provides a new molecular tool to dissect the transcriptional network regulating jasmonate responses, and to understand how different signalling modules (SCF^{COI1}–JAZ–transcription factors) fine-tune cellular responses to specific challenges.

METHODS SUMMARY

Transgenic lines and *in vivo* degradation assay. Plant growth conditions *in vitro* (in Johnson's media) and in soil were as previously described¹⁵. pDONR201/207 and pGWB5 (ref. 32) were used to generate 35S-JAI3-GFP and 35S-JAI3AC-GFP constructs. Transgenic *Arabidopsis* plants in Col-0 and *coi1-1* backgrounds were obtained by the floral-dip method³³. GFP was visualized by fluorescence microscopy using digital module-R and confocal microscopes.

***In vitro* degradation assay.** JAI3, JAI3AC, JAZ1 and JAZ9 proteins (and proteins used for pull-down assays) were obtained and labelled by *in vitro* translation using TNT wheat germ extract systems in the presence of [³⁵S]methionine. Labelled proteins were incubated at 30 °C with plant extracts (100 µg of total protein extract in 50 mM TrisHCl, pH 7.0, 5 mM MgCl₂, 5 mM ATP and 50 µg µl⁻¹ ubiquitin) with or without proteasome specific inhibitor MG132 or jasmonate, as indicated.

***In vitro* pull-down assays.** Coding sequences for full-length and truncated proteins (Supplementary Fig. 3) were PCR amplified from plasmid templates (Supplementary Table 3), cloned into pDONR201/207 and recombined in pDEST-TH1³⁴ to obtain N-terminal MBP-fusions. Recombinant proteins were

expressed in *Escherichia coli* and purified according to standard protocols. In each pull-down experiment 5 µg of fusion protein was added to 10–20 µl of *in vitro*-translated protein in 300 µl of incubation buffer.

Yeast two-hybrid assays. Yeast strain constructions using the same genes and gene fragments as outlined within the pull-down methods were generated using vectors pDEST 32 and pDEST 22. Vectors containing the appropriate JAI3 or MYC2 fragments (described in Supplementary Fig. 3) were co-transformed into *Saccharomyces cerevisiae* (AH109) following standard heat shock protocols³⁵. Successfully transformed colonies were identified on appropriate selective minimal agar.

Microarray analysis and DNA-binding experiments. Microarray profiles were obtained as described³⁶. Genes were clustered using TIGR multi experiment viewer with Pearson's uncentred distance and complete linkage.

For the electrophoretic mobility shift assay (EMSA), DNA was labelled with biotin using the Pierce's Lightshift Chemiluminescent EMSA Kit. DNA binding and EMSA were performed as previously described³⁷. Sequences of the JAI3 promoter and mutated versions are described in Supplementary Table 2.

Full Methods and any associated references are available in the online version of the paper at www.nature.com/nature.

Received 5 April; accepted 7 June 2007.

Published online 18 July 2007.

- Devoto, A. & Turner, J. G. Regulation of jasmonate-mediated plant responses in *Arabidopsis*. *Ann. Bot. (Lond.)* **92**, 329–337 (2003).
- Farmer, E. E., Almeras, E. & Krishnamurthy, V. Jasmonates and related oxylipins in plant responses to pathogenesis and herbivory. *Curr. Opin. Plant Biol.* **6**, 372–378 (2003).
- Rojas, E., Solano, R. & Sánchez-Serrano, J. J. Interactions between signaling compounds involved in plant defense. *J. Plant Growth Regul.* **22**, 82–98 (2003).
- Lorenzo, O. & Solano, R. Molecular players regulating the jasmonate signalling network. *Curr. Opin. Plant Biol.* **8**, 532–540 (2005).
- Flescher, E. Jasmonates—a new family of anti-cancer agents. *Anticancer Drugs* **16**, 911–916 (2005).
- Demole, E., Lederer, E. & Mercier, D. Isolement et détermination de la structure du jasmonate de méthyle, constituant odorant caractéristique de l'essence de jasmin. *Helv. Chim. Acta* **XLV**, 675–685 (1962).
- Liechti, R. & Farmer, E. E. Jasmonate biochemical pathway. *Sci. STKE* **203**, CM18 (2006).
- Liechti, R., Gfeller, A. & Farmer, E. E. Jasmonate signaling pathway. *Sci. STKE* **322**, CM2 (2006).
- Devoto, A. *et al.* COI1 links jasmonate signalling and fertility to the SCF ubiquitin-ligase complex in *Arabidopsis*. *Plant J.* **32**, 457–466 (2002).
- Feng, S. *et al.* The COP9 signalosome interacts physically with SCF COI1 and modulates jasmonate responses. *Plant Cell* **15**, 1083–1094 (2003).
- Feys, B., Benedetti, C. E., Penfold, C. N. & Turner, J. G. *Arabidopsis* mutants selected for resistance to the phytotoxin coronatine are male sterile, insensitive to methyl jasmonate, and resistant to a bacterial pathogen. *Plant Cell* **6**, 751–759 (1994).
- Xie, D. X., Feys, B. F., James, S., Nieto-Rostro, M. & Turner, J. G. COI1: an *Arabidopsis* gene required for jasmonate-regulated defense and fertility. *Science* **280**, 1091–1094 (1998).
- Xu, L. *et al.* The SCF(COI1) ubiquitin-ligase complexes are required for jasmonate response in *Arabidopsis*. *Plant Cell* **14**, 1919–1935 (2002).
- Boter, M., Ruiz-Rivero, O., Abdeen, A. & Prat, S. Conserved MYC transcription factors play a key role in jasmonate signaling both in tomato and *Arabidopsis*. *Genes Dev.* **18**, 1577–1591 (2004).
- Lorenzo, O., Chico, J. M., Sánchez-Serrano, J. J. & Solano, R. JASMONATE-INSENSITIVE1 encodes a MYC transcription factor essential to discriminate between different jasmonate-regulated defense responses in *Arabidopsis*. *Plant Cell* **16**, 1938–1950 (2004).
- Lorenzo, O., Piqueras, R., Sánchez-Serrano, J. J. & Solano, R. ETHYLENE RESPONSE FACTOR1 integrates signals from ethylene and jasmonate pathways in plant defense. *Plant Cell* **15**, 165–178 (2003).
- Nishii, A. *et al.* Characterization of a novel gene encoding a putative single zinc-finger protein, ZIM, expressed during the reproductive phase in *Arabidopsis thaliana*. *Biosci. Biotechnol. Biochem.* **64**, 1402–1409 (2000).
- Shikata, M. *et al.* Characterization of *Arabidopsis* ZIM, a member of a novel plant-specific GATA factor gene family. *J. Exp. Bot.* **55**, 631–639 (2004).
- Datta, S., Hettiarachchi, G. H. C. M., Deng, X.-W. & Holm, M. *Arabidopsis* CONSTANS-LIKE3 is a positive regulator of red light signaling and root growth. *Plant Cell* **18**, 70–84 (2006).
- Robson, F. *et al.* Functional importance of conserved domains in the flowering-time gene *CONSTANS* demonstrated by analysis of mutant alleles and transgenic plants. *Plant J.* **28**, 619–631 (2001).
- Staswick, P. E. & Tiryaki, I. The oxylipin signal jasmonic acid is activated by an enzyme that conjugates it to isoleucine in *Arabidopsis*. *Plant Cell* **16**, 2117–2127 (2004).
- Thines, B. *et al.* JAZ repressor proteins are targets of the SCF^{COI1} complex during jasmonate signalling. *Nature advance online publication*, doi:10.1038/nature05960 (this issue).

23. Färber, K., Schumann, B., Miersch, O. & Roos, W. Selective desensitization of jasmonate- and pH-dependent signaling in the induction of benzophenanthridine biosynthesis in cells of *Eschscholzia californica*. *Phytochemistry* **62**, 491–500 (2003).
24. Dharmasiri, N., Dharmasiri, S. & Estelle, M. The F-box protein TIR1 is an auxin receptor. *Nature* **435**, 441–445 (2005).
25. Kepinski, S. & Leyser, O. The *Arabidopsis* F-box protein TIR1 is an auxin receptor. *Nature* **435**, 446–451 (2005).
26. Tan, X. *et al.* Mechanism of auxin perception by the TIR1 ubiquitin ligase. *Nature* **446**, 640–645 (2007).
27. Weiler, E. W. *et al.* The *Pseudomonas* phytotoxin coronatine mimics octadecanoid signalling molecules of higher plants. *FEBS Lett.* **345**, 9–13 (1994).
28. Axel, M., Mathias, M. & Wilhelm, B. Structural and biological diversity of cyclic octadecanoids, jasmonates, and mimetics. *J. Plant Growth Regul.* **23**, 170–178 (2004).
29. Stintzi, A., Weber, H., Reymond, P., Browse, J. & Farmer, E. E. Plant defense in the absence of jasmonic acid: the role of cyclopentenones. *Proc. Natl Acad. Sci. USA* **98**, 12837–12842 (2001).
30. Taki, N. *et al.* 12-oxo-phytodienoic acid triggers expression of a distinct set of genes and plays a role in wound-induced gene expression in *Arabidopsis*. *Plant Physiol.* **139**, 1268–1283 (2005).
31. Uppalapati, S. R. *et al.* The phytotoxin coronatine and methyl jasmonate impact multiple phytohormone pathways in tomato. *Plant J.* **42**, 201–217 (2005).
32. Mita, S., Suzuki-Fujii, K. & Nakamura, K. Sugar-inducible expression of a gene for beta-amylase in *Arabidopsis thaliana*. *Plant Physiol.* **107**, 895–904 (1995).
33. Clough, S. J. & Bent, A. F. Floral dip: a simplified method for *Agrobacterium*-mediated transformation of *Arabidopsis thaliana*. *Plant J.* **16**, 735–743 (1998).
34. Hammarstrom, M., Hellgren, N., van Den Berg, S., Berglund, H. & Hard, T. Rapid screening for improved solubility of small human proteins produced as fusion proteins in *Escherichia coli*. *Protein Sci.* **11**, 313–321 (2002).
35. Schiestl, R. H. & Gietz, R. D. High efficiency transformation of intact yeast cells using single stranded nucleic acids as a carrier. *Curr. Genet.* **16**, 339–346 (1989).
36. Adie, B. A. T. *et al.* ABA is an essential signal for plant resistance to pathogens affecting JA biosynthesis and the activation of defenses in *Arabidopsis*. *Plant Cell* **19**, 1665–1681 (2007).
37. Solano, R., Stepanova, A., Chao, Q. & Ecker, J. R. Nuclear events in ethylene signaling: a transcriptional cascade mediated by ETHYLENE-INSENSITIVE3 and ETHYLENE-RESPONSE-FACTOR1. *Genes Dev.* **12**, 3703–3714 (1998).
38. Thijs, G. *et al.* A higher-order background model improves the detection of promoter regulatory elements by Gibbs sampling. *Bioinformatics* **17**, 1113–1122 (2001).

Supplementary Information is linked to the online version of the paper at www.nature.com/nature.

Acknowledgements We thank C. Castresana, J. A. García, J. Paz-Ares and S. Prat for critical reading of the manuscript and V. Rubio, J. C. del Pozo and J. M. Iglesias-Pedraz for advice on pull-down and proteasome degradation experiments. We also thank M. Laos and S. Gutiérrez for technical assistance. We are grateful to B. Thines and J. Browse for sharing results before publication. We also thank J. Turner for providing *coi1-1* seeds, P. Staswick for *jar1* and NASC for T-DNA insertion lines and full-length cDNAs. This work was supported by funding from the Ministerio de Educación y Ciencia of Spain (to R.S., J.L.M. and M.R.P.), and the Comunidad de Madrid and European Commission (to R.S.). A.C. was supported by an EMBO long-term Fellowship, and S.F. by a Portuguese FCT fellowship.

Author Contributions A.C. was responsible for experiments of Fig. 1b–h and Fig. 2c–i. S.F. performed all pull-down experiments, G.F., *in vitro* degradation experiments and EMSA, B.A., two-hybrid assays, J.M.C., G.G.-C. and I.L.-V., microarray analysis and A.C., O.L., F.M.L., J.L.M. and M.R.P. mapped *jai3-1*. R.S. designed experiments, supervised the work and wrote the manuscript. All authors discussed the results and commented on the manuscript.

Author Information MIAMExpress Accession numbers for all microarray experiments are: E-ATMX-15, E-ATMX-16, E-ATMX-17 and E-ATMX-18. Accession numbers for JAZ family members are: JAZ1, At1g19180; JAZ2, At1g74950; JAZ3, At3g17860; JAZ4, At1g48500; JAZ5, At1g17380; JAZ6, At1g72450; JAZ7, At2g34600; JAZ8, At1g30135; JAZ9, At1g70700; JAZ10, At5g13220; JAZ11, At3g43440; and JAZ12, At5g20900. Reprints and permissions information is available at www.nature.com/reprints. The authors declare no competing financial interests. Correspondence and requests for materials should be addressed to R.S. (rsolano@cnb.uam.es).

METHODS

Plant materials. All the *Arabidopsis thaliana* plants used in this work were in a Col-0 genetic background, including *jai3-2* and *jai3-3* knockout lines (SALK_139337 and SALK_067825)³⁹, which were obtained from NASC. Plant growth conditions *in vitro* (in Johnson's media) and in soil were as previously described¹⁵. A concentration of 50 μ M was used in all jasmonate treatments.

Recombinant proteins and *in vivo* protein degradation. The *JAI3* coding sequence was amplified with High-Fidelity Taq-polymerase (Roche) from plasmid templates (Ambion MessageAmp kit), using Gateway-compatible primers (Supplementary Table 3). PCR products were cloned into pDONR201/207 with a Gateway BP II kit (Invitrogen) and sequenced (ABI PRISM 3700; Applied Biosystems). A Gateway LR II kit (Invitrogen) and the destination vector pGWB5 (ref. 32) were used to generate *35S-JAI3-GFP* and *35S-JAI3AC-GFP*. These constructs were then transferred to *Agrobacterium tumefaciens* C58C1 carrying the pGV2260 (ref. 40) by heat shock and *Arabidopsis* Col-0 plants were transformed by floral dipping³³. Transgenic *35S-JAI3-GFP* and *35S-JAI3AC-GFP* plants were treated with 50 μ M jasmonate (Sigma) with or without the specific proteasome inhibitor MG132 (100 μ M) (Sigma). Two hours after treatment, roots were observed and GFP was visualized by fluorescence microscopy using DMR and confocal microscopes (Leica). Photographs of cells expressing the GFP were taken as previously described¹⁵.

***Nicotiana benthamiana* agroinfiltration.** *Nicotiana benthamiana* plants were infiltrated with *Agrobacterium tumefaciens* C58C1 strain carrying the *35S-JAI3* and *35S-JAI3AC* constructs as previously described⁴¹. Briefly, *Agrobacterium* cultures were applied with a syringe to the underside of three leaves of 4-week-old plants. Two days later agroinfiltrated leaves were treated with 50 μ M jasmonate with or without 100 μ M MG132. Leaves were observed 24 h after treatment. GFP was visualized as outlined within the *in vivo* protein degradation method.

Positional cloning of the *JAI3* gene. Low-resolution gene mapping was performed as previously described^{42,43} by using 50 F₂ phenotypically mutant plants derived from a *jai3-1/jai3-1* \times Ler cross. Novel In/Del (http://www.arabidopsis.org/browse/Cereon/index.jsp) and SSLP markers⁴⁴ were used to map a population of 415 F₂ plants, delimiting *JAI3* to a region of 400 kb that encompassed 7 overlapping BAC clones. Seven genes within this region were regulated by jasmonate, with At3g17860 being the most highly induced. On the basis of these data and previous analysis (B. Thines and J. Browse, personal communication) a candidate approach allowed us to identify At3g17860 as the mutated gene in the *jai3-1* mutant (Fig. 1b and Supplementary Fig. 1). Sequencing of this candidate revealed the described mutation.

***In vitro* degradation assay.** *JAI3*, *JAI3AC*, *JAZ1* and *JAZ9* proteins were expressed from a plasmid template under a T3 promoter in the TNT-coupled wheat germ extract system (Promega) or using TNT T7 Quick for PCR DNA (Promega) in the presence of [³⁵S]methionine (GE Healthcare).

For extract preparation, seedlings (pre-treated with jasmonate and/or MG132 during 12 h) were ground in liquid nitrogen, resuspended in buffer (20 mM Tris-HCl, pH 7.0, 25 mM NaCl, 0.01% Nonidet-40 and protease inhibitors (Sigma)), sonicated and clarified by centrifugation. Protein concentration was determined by the Bradford method and 100 μ g of total protein was added to the reaction mix (50 mM Tris-HCl, pH 7.0, 5 mM MgCl₂, 5 mM ATP, 50 μ g μ l⁻¹ ubiquitin and *in vitro* translated [³⁵S] labelled protein). Incubation was performed at 30 °C in the presence of a protease inhibitor cocktail for different times with or without 200 μ M MG132 or 50 μ M jasmonate, as indicated. The reaction was stopped by adding loading buffer at 4 °C, boiled at 95 °C and run on SDS gels. Quantification of the gels and analysis of the images was performed on a Phosphorimager using the ImageJ software (http://rsb.info.nih.gov/ij/index.html).

***In vitro* pull-down assays.** Coding sequences for full-length COI1, *JAI3* and MYC2, and the *JAI3AC* (amino acids 1–298), *JAI3AN* (amino acids 208–352), MYC2AC (amino acids 1–333) and MYC2AN (amino acids 181–624) truncated proteins were PCR amplified from plasmid templates, maintaining the frame and stop codons (see Supplementary Table 3 for primer sequences). Using the Gateway system (Invitrogen) these amplicons were cloned into pDONR201/pDONR207 and recombined in pDEST-TH1 (ref. 34) to obtain N-terminal MBP-fusions. All constructs were verified by sequencing before protein expression.

In vitro synthesis of full-length COI1, *JAI3*, *JAZ1* and MYC2 proteins was achieved using a plasmid template with the TNT Coupled Wheat Germ Extract System (Promega) in the presence of [³⁵S]methionine. *JAI3* and MYC2 truncated proteins (as above) were *in vitro* expressed and radiolabelled using PCR products containing a T7 promoter as template with the TNT T7 Quick for PCR DNA kit (Promega).

Recombinant MBP-fusion proteins were expressed in *Escherichia coli* BL21 cells and purified in amylose resin (New England Biolabs) columns according to

standard protocols although without elution. In each pull-down experiment 10–20 μ l of *in vitro* translated protein in 300 μ l of incubation buffer (50 mM Tris-HCl, pH 7.4, containing 150 mM NaCl, 5 mM MgCl₂, 0.2% Nonidet P40, 1 mM phenylmethylsulphonyl fluoride, protease inhibitor cocktail) were added to 5 μ g of resin-bound fusion protein. After 90 min incubation at room temperature, and under rotation, the samples were washed 6 times for 3 min each in fresh incubation buffer. The washed amylose resin was resuspended in 30 μ l of SDS–PAGE loading buffer containing maltose. Following boiling for 5 min, the samples were loaded on SDS–PAGE. The bound radiolabelled proteins were detected using a Phosphorimager.

Yeast two-hybrid assays. Yeast strain constructs using the same genes and gene fragments as outlined within the pull-down methods were generated using Gateway technology (Invitrogen) (see Supplementary Table 3 for primer sequences). Vectors pDEST 32 (Gal4 DNA-Binding Domain; BD) and pDEST 22 (Gal4 Activation Domain; AD) containing the appropriate *JAI3* or MYC2 fragments (Fig. 3) were co-transformed into *Saccharomyces cerevisiae* AH 109 cells following standard heat shock protocols³⁵. Successfully transformed colonies were identified on appropriate selective minimal agar (Minimal synthetic dropout Agar Base) containing 2% glucose and 5 mM 3AT (predetermined as sufficient to obviate false positives). β -galactosidase indicator plates contained an additional 40 mg l⁻¹ X-gal (4'-bromo-5'-chlor-3'-indolyl- β -D-galactoside) and 70 mM potassium phosphate buffer (pH 7.0).

Microarray analysis. *Arabidopsis thaliana* plants were grown in Johnson's media at 25 °C and a light cycle of 16 h light:8 h dark. Ten-day-old seedlings were treated (or not) with 50 μ M jasmonate as specified below and immediately frozen in liquid nitrogen. Twelve comparisons were made between jasmonate-treated *jai3-1* and wild-type; 8 comparisons after 2 h of jasmonate treatment and 4 comparisons after 6 h. mRNA levels in wild-type and pooled samples of the *jnl1-1* and *jnl1-2* mutants were compared after 6 h of jasmonate treatment (4 replicates). mRNA levels were compared between *35S-MYC2* transgenic lines and wild-type without any treatment (four replicates). Finally, genes differentially expressed in response to jasmonate treatment (30 min) were determined by comparing the transcriptomic profiles of wild-type treated and non-treated plants (14 replicates).

RNA amplification, microarray hybridization and scanning were performed as previously reported³⁶. Briefly, RNA was amplified with the MessageAmp II aRNA kit (Ambion) and 5-(3-aminolallyl)-2'-deoxyuridine-5'-triphosphate (aa-dUTP, Ambion) following the manufacturer's instructions. Microarray slides of synthetic 70mer oligonucleotides were obtained from the University of Arizona (Operon *Arabidopsis* Genome Oligo Set Version 3.0 (Qiagen) spotted on aminosilane-coated slides (Telechem)). For each hybridization, equal amounts of dye of each aRNA labelled with either Cy3 or Cy5, were mixed with 20 μ g of polyA and 20 μ g of yeast transfer RNA (Sigma-Aldrich) and treated with the RNA Fragmentation Reagents (Ambion). Images from Cy3 and Cy5 channels were equilibrated and captured with a GenePix 4000B (Axon) and spots quantified using GenPix Pro 5.1 software (Axon).

Background correction and normalization of expression data were performed as previously reported³⁶. Linear model methods were used for determining differentially expressed genes. To control the false-discovery rate, P values were corrected by using the method of Benjamini and Hochberg⁴⁵. Criteria for selection of differentially expressed genes in Fig. 3 were log ratio < -0.5 and false-discovery rate \leq 10%. The hierarchical cluster was calculated and drawn using the TIGR MeV (Multiarray experiment viewer)⁴⁶ software provided by the TIGR Institute, with Pearson's uncentred distance and complete linkage.

Promoter analysis. Motif Analysis (TAIR) and Motif Sampler³⁸ were used for the identification of sequences statistically over-represented in the promoters. Scores of sequences shown in Fig. 3 are: consensus score, 1.75; information content, 1.97; log likelihood score, 98.13; and in Fig. 5 are: consensus score, 1.59; information content, 1.76; log likelihood score, 73. Motif Analysis (TAIR) also identified the T/G-box (CACGTT / AACGTG) as the sequence most over-represented (P value 7.19×10^{-7}) (Fig. 3).

Protein analysis and phylogenetic tree. Sequence analyses were carried out as previously described⁴⁷. Briefly, alignments of protein sequences were generated using DiAlign (Genomatix) and ClustalW (EBI). Conserved amino acids were then coloured by BoxShade (EMBNet). Phenogram representation of the neighbour-joining tree of the JAZ family was created by Phylodendron (http://iubio.bio.indiana.edu/treeapp/treeprint-form.html).

39. Alonso, J. M. et al. Genome-wide insertional mutagenesis of *Arabidopsis thaliana*. *Science* **301**, 653–657 (2003).

40. Deblaere, R. et al. Efficient octopine Ti plasmid-derived vectors for *Agrobacterium*-mediated gene transfer to plants. *Nucleic Acids Res.* **13**, 4777–4788 (1985).

41. Valli, A., Martin-Hernandez, A. M., Lopez-Moya, J. J. & Garcia, J. A. RNA silencing suppression by a second copy of the P1 serine protease of Cucumber vein

- yellowing ipomovirus, a member of the family Potyviridae that lacks the cysteine protease HCPro. *J. Virol.* **80**, 10055–10063 (2006).
42. Ponce, M. R., Robles, P. & Micol, J. L. High-throughput genetic mapping in *Arabidopsis thaliana*. *Mol. Gen. Genet.* **261**, 408–415 (1999).
 43. Ponce, M. R., Robles, P., Lozano, F. M., Brotons, M. A. & Micol, J. L. Low-resolution mapping of untagged mutations. *Methods Mol. Biol.* **323**, 105–113 (2006).
 44. Bell, C. J. & Ecker, J. R. Assignment of 30 microsatellite loci to the linkage map of *Arabidopsis*. *Genomics* **19**, 137–144 (1994).
 45. Benjamini, Y. & Hochberg, Y. Controlling the false discovery rate. *J. R. Stat. Soc. Ser. C Appl. Stat.* **57**, 289–300 (1995).
 46. Saeed, A. I. *et al.* TM4: a free, open-source system for microarray data management and analysis. *Biotechniques* **34**, 374–378 (2003).
 47. Chini, A. & Loake, G. J. Motifs specific for the ADR1 NBS-LRR protein family in *Arabidopsis* are conserved among NBS-LRR sequences from both dicotyledonous and monocotyledonous plants. *Planta* **4**, 597–601 (2005).

LETTERS

Strong dipolar effects in a quantum ferrofluid

Thierry Lahaye¹, Tobias Koch¹, Bernd Fröhlich¹, Marco Fattori¹, Jonas Metz¹, Axel Griesmaier¹, Stefano Giovanazzi¹ & Tilman Pfau¹

Symmetry-breaking interactions have a crucial role in many areas of physics, ranging from classical ferrofluids to superfluid ³He and *d*-wave superconductivity. For superfluid quantum gases, a variety of new physical phenomena arising from the symmetry-breaking interaction between electric or magnetic dipoles are expected¹. Novel quantum phases in optical lattices, such as checkerboard or supersolid phases, are predicted for dipolar bosons^{2,3}. Dipolar interactions can also enrich considerably the physics of quantum gases with internal degrees of freedom^{4–6}. Arrays of dipolar particles could be used for efficient quantum information processing⁷. Here we report the realization of a chromium Bose–Einstein condensate with strong dipolar interactions. By using a Feshbach resonance, we reduce the usual isotropic contact interaction, such that the anisotropic magnetic dipole–dipole interaction between ⁵²Cr atoms becomes comparable in strength. This induces a change of the aspect ratio of the atom cloud; for strong dipolar interactions, the inversion of ellipticity during expansion (the usual ‘smoking gun’ evidence for a Bose–Einstein condensate) can be suppressed. These effects are accounted for by taking into account the dipolar interaction in the superfluid hydrodynamic equations governing the dynamics of the gas, in the same way as classical ferrofluids can be described by including dipolar terms in the classical hydrodynamic equations. Our results are a first step in the exploration of the unique properties of quantum ferrofluids.

A quantum ferrofluid is a superfluid quantum gas consisting of polarized dipoles, either electric or magnetic. The first option (using polarized electric dipoles) might be achieved for instance with polar molecules in their vibrational ground state, aligned by an electric field. Progress has been made recently in the slowing and trapping of polar molecules (see ref. 8 and references therein), but the densities and temperatures achieved to date are far away from the quantum-degenerate regime. The use of Feshbach resonances to create polar molecules from two ultracold atomic species⁹ is a promising, actively explored alternative¹⁰; however it is a challenging task to bring those heteronuclear molecules to their vibrational ground state¹¹. Alternatively, atomic electric dipoles induced by dc fields¹² or by light¹³ could be used. The second option, chosen here, relies on the magnetic dipole–dipole interaction (MDDI) between atoms with a large magnetic moment, such as chromium, for which a Bose–Einstein condensate (BEC) was achieved recently¹⁴. The relative strength of the MDDI to the contact interaction is conveniently expressed by the dimensionless ratio

$$\varepsilon_{\text{dd}} = \frac{\mu_0 \mu^2 m}{12 \pi \hbar^2 a} \quad (1)$$

where m is the atomic mass, a is the *s*-wave scattering length, μ_0 is the permeability of a vacuum, \hbar is $h/2\pi$, and μ is the magnetic moment (numerical factors in ε_{dd} are such that a homogenous BEC with $\varepsilon_{\text{dd}} > 1$ is unstable against dipolar collapse). Chromium has a large dipole moment, $\mu = 6\mu_B$, and a background scattering length in the

fully polarized case of $a \approx 100 a_0$ (μ_B is the Bohr magneton, and a_0 the Bohr radius), yielding¹⁵ $\varepsilon_{\text{dd}} \approx 0.16$. Although this value is typically 36 times larger than in standard alkali quantum gases, the MDDI is still a small perturbation compared to the contact interaction. A perturbative mechanical effect of the MDDI has been demonstrated by analysing the expansion of a chromium BEC from an anisotropic trap for various orientations of the dipoles¹⁶.

The existence of Feshbach resonances¹⁷ allows us to increase ε_{dd} and go beyond the perturbative limit. Indeed, close to a resonance, the scattering length varies with the applied magnetic field B as

$$a = a_{\text{bg}} \left(1 - \frac{\mathcal{A}}{B - B_0} \right) \quad (2)$$

where a_{bg} is the background scattering length, B_0 the resonance position, and \mathcal{A} the resonance width. For B approaching $B_0 + \mathcal{A}$, the scattering length tends to zero, thus enhancing ε_{dd} . This gives the possibility of reaching an MDDI-dominated quantum gas.

We report here the observation of strong dipolar effects in a chromium BEC in the vicinity of the broadest Feshbach resonance at

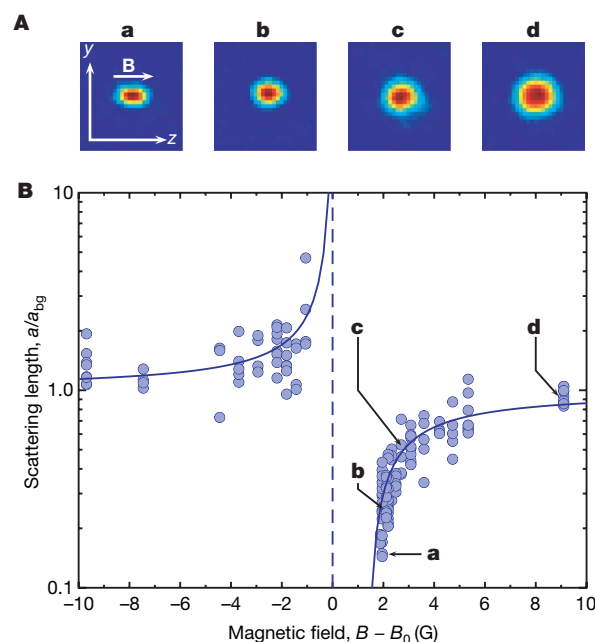


Figure 1 | Tuning the chromium scattering length. **A**, Absorption images (field of view $260 \mu\text{m}$ by $260 \mu\text{m}$) of the condensate after 5 ms of expansion, for different fields B above resonance ($B - B_0$ is 2, 2.2, 2.7 and 9 G for **a**, **b**, **c** and **d**, respectively). Reducing a slows down the mean-field driven expansion. The change in aspect ratio for small a is a direct signature of strong MDDI. **B**, Variation of a across the resonance, inferred from the mean-field energy released during expansion. The line is a fit to equation (2), yielding $\mathcal{A} = 1.4 \pm 0.1$ G.

¹Physikalisches Institut, Universität Stuttgart, Pfaffenwaldring 57, D-70550 Stuttgart, Germany.

$B_0 \approx 589$ G. We measure the dispersive behaviour of the scattering length, and observe that the change in a is accompanied by enhanced inelastic losses. Close to the zero-crossing of a , we observe a large modification of the aspect ratio of the cloud when ε_{dd} increases, which is direct evidence for strong dipolar effects. We finally show that the usual inversion of ellipticity of the condensate during expansion is inhibited for large enough MDDI.

We modified our experimental set-up, which has been described in detail elsewhere¹⁴, in order to be able to produce Cr condensates in high field, close to B_0 (see Methods). Once the condensate is obtained, the magnetic field is ramped close to its final value B in 10 ms, and held there for 2 ms to let it settle down. The trap is then switched off, and the condensate expands freely for 5 ms before being imaged by absorption of resonant light in high field. Figure 1A shows a series of images taken when approaching the resonance from above, and clearly displays a reduction of the cloud size, as well as a change in its aspect ratio.

From the measured optical density profiles, we extract the BEC atom number N , as well as the Thomas–Fermi radii R_z (along the magnetization direction) and R_y (along the vertical axis). Without MDDI, one could easily obtain the scattering length a from these measurements, as the Thomas–Fermi radii after a time of flight would scale as $(Na)^{1/5}$. In our case, we take into account the MDDI using the hydrodynamic formulation of the Gross–Pitaevskii equation, including both contact and dipole–dipole interactions¹⁸ (see Methods for the assumptions underlying our analysis). Figure 1B shows the measured variation of $a(B)$ across the resonance, showing a characteristic dispersive shape¹⁹. A fit according to equation (2) yields $\Delta = 1.4 \pm 0.1$ G, in good agreement with the prediction $\Delta = 1.7$ G of multi-channel calculations¹⁷. The position $B_0 \approx 589$ G of the resonance coincides with the one obtained by observing inelastic losses in a thermal cloud¹⁶. We can tune a by more than one order of magnitude, with a reduction by a factor of five above the resonance.

Close to the resonance, we observe on both sides enhanced inelastic processes resulting in a decay of the condensate. We studied the BEC atom number as a function of the time spent at the final magnetic field B , and fitted the corresponding curves by an exponential decay law (this functional form being chosen for simplicity). The $1/e$ BEC lifetime obtained in this way is shown in Fig. 2 as a function of B (the initial peak atomic density is $3 \times 10^{14} \text{ cm}^{-3}$). Enhanced inelastic losses close to a Feshbach resonance have been observed with other species, for example, sodium²⁰. Here the losses are small enough to

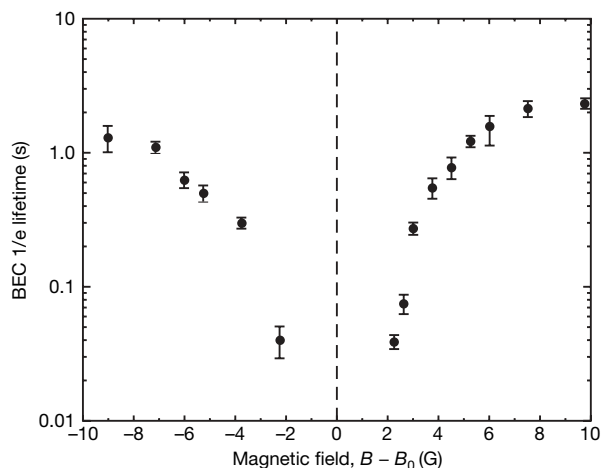


Figure 2 | Inelastic losses close to the resonance. The $1/e$ lifetime of the condensate is plotted as a function of the magnetic field B . Error bars correspond to one standard deviation; the lifetime was determined by fitting the atom number remaining in the BEC after a variable holding time with an exponential decay law. The losses are small enough to allow for the observation of enhanced dipolar interactions (see Methods).

allow us to observe the effect of the enhanced relative strength of the MDDI on the equilibrium shape of the condensate.

Figure 3 shows the aspect ratio R_y/R_z of the cloud as a function of the value of ε_{dd} obtained from the measured a , and constitutes the main result of this Letter. The aspect ratio decreases when ε_{dd} increases: the cloud becomes more elongated along the direction of magnetization z , as can be seen unambiguously in Fig. 1A. This is a clear signature of the MDDI, as for pure contact interaction, the aspect ratio is independent of the scattering length (provided the Thomas–Fermi approximation is valid). The solid line in Fig. 3 shows the aspect ratio after time of flight calculated using the hydrodynamic theory including MDDI¹⁸, without any adjustable parameter. The agreement between our data and the theoretical prediction is excellent, given the dispersion of data points and the uncertainty in the theoretical prediction arising from the measurements of trap frequencies. The highest value of ε_{dd} we could reach reliably is about 0.8, corresponding to a fivefold reduction of the scattering length. For our trap geometry, the condensate is expected to become unstable with respect to dipolar collapse^{21,22} for values of ε_{dd} slightly above one (the exact value depending on the trap anisotropy, but also on the atomic density).

As an application of the tunability of the dipolar parameter, we study the expansion of the condensate for two orthogonal orientations of the dipoles with respect to the trap, as was done in ref. 16, but now as a function of ε_{dd} . In practice, for the large fields required to approach the Feshbach resonance, we cannot change the magnetic field orientation, which is always along z . We therefore use two different trap configurations, with interchanged y and z frequencies, and identical frequencies along x : trap 1 has frequencies $(\omega_x, \omega_y, \omega_z)/2\pi \approx (660, 370, 540)$ Hz, while trap 2 has $(\omega_x, \omega_y, \omega_z)/2\pi \approx (660, 540, 370)$ Hz. We then measure the aspect ratio of the cloud (defined as $A_1 = R_z/R_y$ for trap 1, and $A_2 = R_y/R_z$ for trap 2) as a function of the time of flight, for different values of B (and hence of ε_{dd}). This protocol is equivalent to a mere rotation of the magnetization direction with respect to the trap axes.

Figure 4 presents the results. In order to check that the two trap configurations only differ by an exchange of the y and z frequencies, we first perform the expansion experiment without switching on the

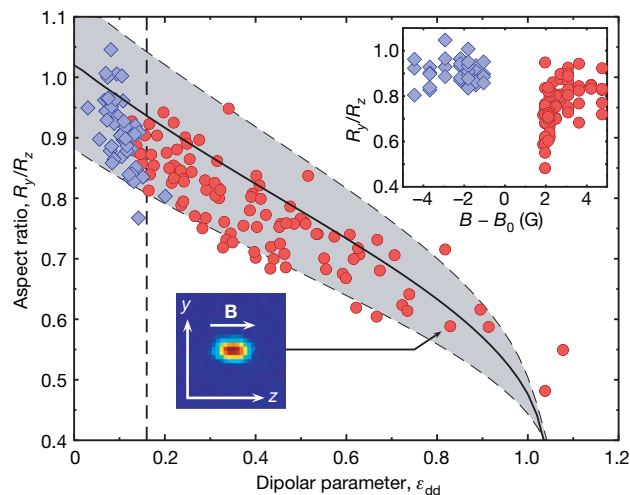


Figure 3 | Increasing the dipolar parameter. Main plot, condensate aspect ratio after 5 ms of expansion plotted against the measured ε_{dd} . Diamonds (circles) correspond to data taken below (above) resonance. The solid line is the prediction of hydrodynamic theory including MDDI, without adjustable parameters (the grey-shaded area corresponds to the uncertainties in the trap frequencies). The dashed line indicates the off-resonant ε_{dd} value. Top right inset, a subset of the same data points plotted against the magnetic field. The condensate elongates appreciably along B only just above resonance, when a approaches zero. Bottom left inset, sample absorption image giving an example of a condensate with strong MDDI.

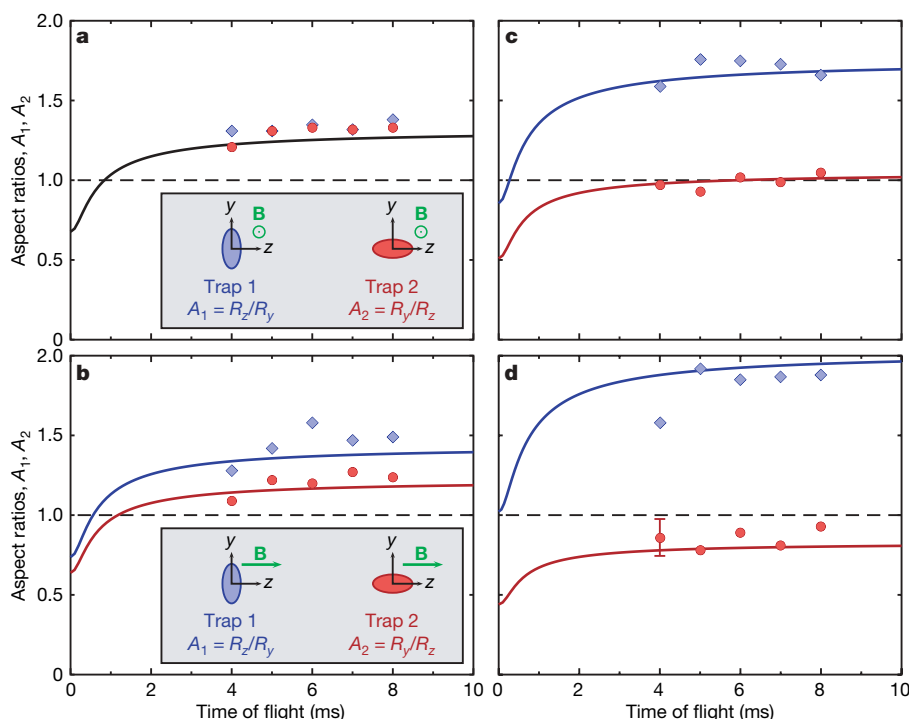


Figure 4 | MDDI-dominated BEC expansion. Aspect ratio of the condensate versus time of flight, for two traps with interchanged y and z frequencies (see text). The solid lines are theoretical predictions without adjustable parameters. The error bar (in **d**) gives the typical dispersion over several runs. **a**, Dipoles perpendicular to the observation plane (see inset sketching

large magnetic field along z , but with a small (11.5 G) field along x (the line of sight of the imaging). The magnetization is therefore perpendicular to the observation plane, and changing the trap configuration does not affect the aspect ratios, as the difference between the two situations is simply a rotation of the trap around the magnetization axis. Figure 4a shows the equality $A_1 = A_2$, confirming the equivalence of the two configurations. We then study the expansion with the large magnetic field B along z . In this case, the MDDI induces a change in the aspect ratios, and $A_1 \neq A_2$. Far from resonance, $\epsilon_{dd} \approx 0.16$ and we recover the perturbative dipolar effect already observed in ref. 16 (see Fig. 4b). However, for values of B approaching $B_0 + \Delta$, ϵ_{dd} increases and, correspondingly, the difference between A_1 and A_2 becomes very large (Fig. 4c and d, where ϵ_{dd} is 0.5 ± 0.1 and 0.75 ± 0.1 , respectively). The lines correspond to the prediction of the hydrodynamic theory without adjustable parameters, and show again a very good agreement with the data. The effect of the dipolar interaction is far beyond the perturbative regime, and induces very strong deviations from what one expects for contact interaction. In particular, for $\epsilon_{dd} \approx 0.75$, the aspect ratio A_2 always remains smaller than unity during the time of flight: the strong anisotropic dipolar interaction inhibits the inversion of ellipticity, the ‘smoking gun’ evidence for BECs with contact interaction.

In conclusion, the use of a Feshbach resonance to reduce the s -wave scattering length of chromium allowed us to realize a BEC with strong dipolar interaction, and to study the hydrodynamics of this novel quantum ferrofluid. This work opens up many avenues towards the study of dipolar quantum gases beyond the perturbative regime. Structured density profiles are predicted for dipolar condensates in anisotropic traps²³, including biconcave density distributions in pancake-shaped traps²⁴. A clear direction for future work is thus to use a one-dimensional optical lattice, creating a stack of pancake-shaped traps. A condensate with dipoles perpendicular to the trap plane is then stable with respect to dipolar collapse, which should allow entry to the regime $\epsilon_{dd} \gg 1$. In particular, the investigation of the unusual, roton-like excitation spectrum predicted in this system²⁵

the in-trap BEC shape); both configurations yield the same aspect ratio.

b–d, Dipoles along z (see inset in **b**); ϵ_{dd} takes the values 0.16 (**b**), 0.5 (**c**) and 0.75 (**d**). The MDDI induces larger and larger effects, even inhibiting (**d**) the inversion of ellipticity.

is a fascinating possibility. The creation of Cr_2 molecules by ramping over the Feshbach resonance is another appealing experiment. In a two-dimensional trap, the repulsive interaction between the molecules, due to their large magnetic moment, might stabilize them against inelastic losses. Another possible extension of this work is the study of degenerate fermions with strong dipolar interactions, which may display new types of pairing mechanisms (ref. 1, and references therein). Finally, the behaviour of strongly correlated dipolar quantum gases in three-dimensional optical lattices is an interesting open field, with many connections to fundamental questions in condensed-matter physics—such as the study of supersolid phases, whose experimental observation in helium is still debated (see, for example, ref. 26).

METHODS SUMMARY

We modified our experimental sequence¹⁴ to produce chromium condensates in high field. For this, we switch on quickly (in less than 5 ms) a large field (~ 600 G) during forced evaporation in the dipole trap. The low atomic density at this stage of evaporation allows for small losses. The current in the coils used to produce the field is actively stabilized; care is taken to ensure a high homogeneity of the field. Evaporation is then resumed until an almost pure condensate of 3×10^4 atoms is obtained. The trap is then adjusted to obtain frequencies ($\omega_x, \omega_y, \omega_z/2\pi \approx (840, 600, 580)$ Hz (measured by exciting the centre of mass motion of the cloud, with an accuracy of 5%)).

In our data analysis to extract the scattering length a (Fig. 1), we assumed that no external forces act on the atoms during the time of flight, that the condensate stays in equilibrium during the magnetic field ramp, and finally that the hydrodynamic (Thomas–Fermi) approximation is valid even for small a . These assumptions are largely fulfilled for all our parameters.

Full Methods and any associated references are available in the online version of the paper at www.nature.com/nature.

Received 4 May; accepted 15 June 2007.

- Baranov, M., Dobrek, Ł., Góral, K., Santos, L. & Lewenstein, M. Ultracold dipolar gases — a challenge for experiments and theory. *Phys. Scr.* **T102**, 74–81 (2002).

2. Góral, K., Santos, L. & Lewenstein, M. Quantum phases of dipolar bosons in optical lattices. *Phys. Rev. Lett.* **88**, 170406 (2002).
3. Menotti, C., Trefzger, C. & Lewenstein, M. Metastable states of a gas of dipolar bosons in a 2D optical lattice. *Phys. Rev. Lett.* **98**, 235301 (2007).
4. Kawaguchi, Y., Saito, H. & Ueda, M. Einstein–de Haas effect in dipolar Bose–Einstein condensates. *Phys. Rev. Lett.* **96**, 080405 (2006).
5. Santos, L. & Pfau, T. Spin-3 chromium Bose–Einstein condensates. *Phys. Rev. Lett.* **96**, 190404 (2006).
6. Yi, S. & Pu, H. Spontaneous spin textures in dipolar spinor condensates. *Phys. Rev. Lett.* **97**, 020401 (2006).
7. DeMille, D. Quantum computation with trapped polar molecules. *Phys. Rev. Lett.* **88**, 067901 (2002).
8. Doyle, J., Friedrich, B., Krems, R. V. & Masnou-Seeuws, F. (eds) Special issue on ultracold molecules. *Eur. Phys. J. D* **31**, 149–445 (2004).
9. Köhler, T., Góral, K. & Julienne, P. S. Production of cold molecules via magnetically tunable Feshbach resonances. *Rev. Mod. Phys.* **78**, 1311–1361 (2006).
10. Ospelkaus, C. *et al.* Ultracold heteronuclear molecules in a 3D optical lattice. *Phys. Rev. Lett.* **97**, 120402 (2006).
11. Sage, J., Sainis, S., Bergeman, T. & DeMille, D. Optical production of ultracold polar molecules. *Phys. Rev. Lett.* **94**, 203001 (2005).
12. Marinescu, M. & You, L. Controlling atom–atom interaction at ultralow temperatures by dc electric fields. *Phys. Rev. Lett.* **81**, 4596–4599 (1998).
13. Giovanazzi, S., O'Dell, D. & Kurizki, G. Density modulations of Bose–Einstein condensates via laser-induced interactions. *Phys. Rev. Lett.* **88**, 130402 (2002).
14. Griesmaier, A., Werner, J., Hensler, S., Stuhler, J. & Pfau, T. Bose–Einstein condensation of chromium. *Phys. Rev. Lett.* **94**, 160401 (2005).
15. Griesmaier, A. *et al.* Comparing contact and dipolar interactions in a Bose–Einstein condensate. *Phys. Rev. Lett.* **97**, 250402 (2006).
16. Stuhler, J. *et al.* Observation of dipole–dipole interaction in a degenerate quantum gas. *Phys. Rev. Lett.* **95**, 150406 (2005).
17. Werner, J., Griesmaier, A., Hensler, S., Stuhler, J. & Pfau, T. Observation of Feshbach resonances in an ultracold gas of ^{52}Cr . *Phys. Rev. Lett.* **94**, 183201 (2005).
18. Giovanazzi, S. *et al.* Expansion dynamics of a dipolar Bose–Einstein condensate. *Phys. Rev. A* **74**, 013621 (2006).
19. Inouye, S. *et al.* Observation of Feshbach resonances in a Bose–Einstein condensate. *Nature* **392**, 151–154 (1998).
20. Stenger, J. *et al.* Strongly enhanced inelastic collisions in a Bose–Einstein condensate near Feshbach resonances. *Phys. Rev. Lett.* **82**, 2422–2425 (1999).
21. Santos, L., Shlyapnikov, G. V., Zoller, P. & Lewenstein, M. Bose–Einstein condensation in trapped dipolar gases. *Phys. Rev. Lett.* **85**, 1791–1794 (2000).
22. Góral, K., Rzążewski, K. & Pfau, T. Bose–Einstein condensation with magnetic dipole–dipole forces. *Phys. Rev. A* **61**, 051601(R) (2000).
23. Dutta, O. & Meystre, P. Ground-state structure and stability of dipolar condensates in anisotropic traps. *Phys. Rev. A* **75**, 053604 (2007).
24. Ronen, S., Bortolotti, D. C. E. & Bohn, J. L. Radial and angular rotons in trapped dipolar gases. *Phys. Rev. Lett.* **98**, 030406 (2007).
25. Santos, L., Shlyapnikov, G. V. & Lewenstein, M. Roton–maxon spectrum and stability of trapped dipolar Bose–Einstein condensates. *Phys. Rev. Lett.* **90**, 250403 (2003).
26. Sasaki, S., Ishiguro, R., Caupin, F., Maris, H. J. & Balibar, S. Superfluidity of grain boundaries and supersolid behavior. *Science* **313**, 1098–1100 (2006).

Acknowledgements We thank L. Santos for discussions and J. Stuhler for contributions in the initial phases of the experiment. We acknowledge financial support by the German Science Foundation (SFB/TRR21) and the EU (Marie–Curie fellowship to T.L.).

Author Information Reprints and permissions information is available at www.nature.com/reprints. The authors declare no competing financial interests. Correspondence and requests for materials should be addressed to T.L. (t.lahaye@physik.uni-stuttgart.de) or T.P. (t.pfau@physik.uni-stuttgart.de).

METHODS

Production of Cr condensates in a high magnetic field. We load chromium atoms in the $|^7S_3, m_S = 3\rangle$ state into a Ioffe magnetic trap for 10 s, and subsequently cool them by r.f.-induced evaporation down to 20 μ K. We capture 10^6 of these atoms in an optical trap consisting of a horizontal laser beam at 1,076 nm with a power of 16 W and a $1/e^2$ radius of 30 μ m, and optically pump them in the high-field seeking state $|m_S = -3\rangle$. A 11.5 G magnetic field prevents losses due to dipolar relaxation. At this stage, a vertical beam (power 9 W, $1/e^2$ radius 50 μ m) is ramped up over 5 s, creating a 'dimple' in the trap. We then ramp the horizontal beam power down to 30% of its initial value in 5 s, and switch on rapidly (less than 5 ms) a magnetic field B_{evap} along z . The field is provided by the offset and pinch coils of the Ioffe trap, in which we run currents of around 400 A and 15 A, respectively. This combination ensures that the field is as homogenous as possible. The remaining inhomogeneities correspond to trapping (anti-trapping) frequencies below 5 Hz (7 Hz) radially (longitudinally). The current in the offset coils is stabilized at the 3×10^{-5} level (r.m.s.), giving in principle a control of the field better than 100 mG. B_{evap} is 600 G (575 G) for the data taken above (below) resonance. The fast magnetic ramp and the low atomic density (about 10^{13} cm^{-3}) at this stage of the evaporation are required to cross the resonances below B_{evap} without appreciable losses. Forced evaporation is resumed in high field until an almost pure condensate of 3×10^4 atoms is obtained. The powers of the beams are finally adjusted adiabatically to reach the desired trap frequencies.

Data analysis for the measurement of a . The assumptions in our analysis are: (1) no external forces act on the atoms during the expansion; (2) the condensate stays in equilibrium during the magnetic field ramp; and (3) the hydrodynamic (Thomas–Fermi) approximation is valid. We therefore checked (1) that the effect of the inhomogeneities of the magnetic field during expansion is completely negligible for our parameters, and (2) that the magnetic field ramp is slow enough to fulfil the adiabaticity criterion $\dot{a}/a \ll \omega_{\text{min}}$, where ω_{min} is the smallest trap frequency. We checked that no collective oscillations were excited in the condensate when varying a . For this, we varied the time spent at the final magnetic field B before expansion, and observed no change in the condensate shape, even for the data taken close to $B_0 + \Delta$. Note that the occurrence of losses makes the adiabaticity criterion more difficult to fulfil, as one must stay far enough from resonance in order to satisfy $\dot{N}/N \ll \omega_{\text{min}}$. This criterion is largely fulfilled for our data. Finally, we checked (3) that the hydrodynamic description of the condensate is valid: the Thomas–Fermi parameter, defined as Na/a_{ho} , where $a_{\text{ho}} = \sqrt{\hbar/(m\bar{\omega})}$ is the trap harmonic oscillator length and $\bar{\omega} = (\omega_x\omega_y\omega_z)^{1/3}$, is always higher than ~ 60 (a value achieved for the lowest values of a and N). The Thomas–Fermi condition $Na/a_{\text{ho}} \gg 1$ is therefore fulfilled.

LETTERS

Femtosecond time-delay X-ray holography

Henry N. Chapman^{1,2}, Stefan P. Hau-Riege¹, Michael J. Bogan¹, Saša Bajt¹, Anton Barty¹, Sébastien Boutet^{1,3,4}, Stefano Marchesini^{1,†}, Matthias Frank¹, Bruce W. Woods¹, W. Henry Benner¹, Richard A. London¹, Urs Rohner¹, Abraham Szöke¹, Eberhard Spiller¹, Thomas Möller⁵, Christoph Bostedt⁵, David A. Shapiro^{2,†}, Marion Kuhlmann⁶, Rolf Treusch⁶, Elke Plönjes⁶, Florian Burmeister⁴, Magnus Bergh⁴, Carl Caleman⁴, Gösta Hult⁴, M. Marvin Seibert⁴ & Janos Hajdu^{3,4}

Extremely intense and ultrafast X-ray pulses from free-electron lasers offer unique opportunities to study fundamental aspects of complex transient phenomena in materials. Ultrafast time-resolved methods usually require highly synchronized pulses to initiate a transition and then probe it after a precisely defined time delay. In the X-ray regime, these methods are challenging because they require complex optical systems and diagnostics. Here we propose and apply a simple holographic measurement scheme, inspired by Newton's 'dusty mirror' experiment¹, to monitor the X-ray-induced explosion of microscopic objects. The sample is placed near an X-ray mirror; after the pulse traverses the sample, triggering the reaction, it is reflected back onto the sample by the mirror to probe this reaction. The delay is encoded in the resulting diffraction pattern to an accuracy of one femtosecond, and the structural change is holographically recorded with high resolution. We apply the technique to monitor the dynamics of polystyrene spheres in intense free-electron-laser pulses, and observe an explosion occurring well after the initial pulse. Our results support the notion that X-ray flash imaging^{2,3} can be used to achieve high resolution, beyond radiation damage limits for biological samples⁴. With upcoming ultrafast X-ray sources we will be able to explore the three-dimensional dynamics of materials at the time-scale of atomic motion.

One of the earliest recorded observations of interference was made by Newton¹ in his 'dusty mirror' experiment. In a darkened room, Newton used a prism and a small hole in a screen to form a quasi-monochromatic beam from sunlight, which he shone onto a back-quicksilvered mirror. The mirror was angled to return the beam back through the hole, and on the screen Newton observed dark and light rings of light, which he found "strange and surprising". Newton determined that the squares of the diameters of the bright rings followed an integer progression, and that the diameters depended on the thickness of the glass; a front-surface metal mirror did not produce these rings. The ring phenomenon was later explained by Young (page 41 of ref. 5) as being caused by the interference at the screen between two paths of light scattering from dust particles on the mirror's front surface: on one path the light scatters from a particle on its way in towards the mirror, after which it reflects from the silvered surface, and on the other, the light is first reflected from the silvered surface before scattering from this same particle only after emerging from the glass. Such 'diffusion rings', as they were known, can be seen with white light and were a common bane of optical instruments well into the twentieth century, until the use of vacuum coatings⁶.

Our experiment makes use of Newton's geometry to follow the X-ray-induced explosion of uniform polystyrene spheres in a free-electron laser (FEL) pulse, using a focused 25-fs pulse of 32.5-nm-wavelength light from the FLASH soft-X-ray laser⁷. We placed 140-nm-diameter spherical polystyrene particles on a 20-nm-thick silicon nitride membrane that was mounted with a thin spacer in front of a multilayer mirror; this assembly resembles Newton's dusty mirror. Instead of a screen, we used another plane mirror angled at 45° to reflect the interference pattern onto a back-illuminated CCD detector, as shown in Fig. 1. Some interference patterns, recorded with single pulses of about 1.6×10^{12} photons (or 10 μ J) are shown in Fig. 2. Unlike the static conditions of Newton's experiment, in our case the object is ultimately vaporized by the X-ray pulse and the object size changes in the brief interval that the pulse takes to reflect back to the particle, as depicted in Fig. 3. (The normal-incidence mirror is also locally destroyed by the pulse energy, but not before reflecting the pulse⁸.) We can describe our interference pattern as an X-ray hologram, caused by the interference of a reference beam scattered from the 'known' sphere on the first pass, and then scattered

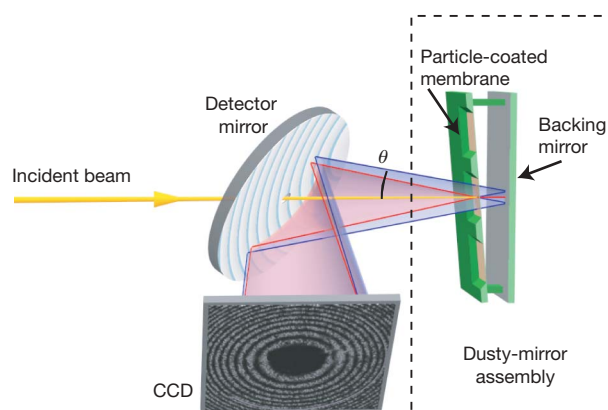


Figure 1 | Diagram of the apparatus, similar to Newton's dusty-mirror experiment. The incident FEL pulse from the left passes through a hole in a multilayer-coated detector mirror. The 'dusty mirror' consists of particles on a 20-nm-thick silicon nitride membrane backed by a multilayer-coated plane mirror. This returns the direct beam back through the hole in the detector mirror, which reflects the diffracted light onto a CCD detector. The prompt diffraction (blue, the reference wave) and delayed diffraction (red, the object wave) interfere to generate the hologram on the CCD detector.

¹University of California, Lawrence Livermore National Laboratory, 7000 East Avenue, Livermore, California 94550, USA. ²Center for Biophotonics Science and Technology, University of California, Davis, 2700 Stockton Boulevard, Suite 1400, Sacramento, California 95817, USA. ³Stanford Synchrotron Radiation Laboratory, Stanford Linear Accelerator Center, 2575 Sand Hill Road, Menlo Park, California 94305, USA. ⁴Laboratory of Molecular Biophysics, Department of Cell and Molecular Biology, Uppsala University, Husargatan 3, Box 596, SE-75124 Uppsala, Sweden. ⁵Institut für Optik und Atomare Physik, Technische Universität Berlin, Hardenbergstraße 36, PN 3-1, 10623 Berlin, Germany. ⁶Deutsches Elektronen-Synchrotron, DESY, Notkestraße 85, D-22607 Hamburg, Germany. [†]Present address: Advanced Light Source, Lawrence Berkeley National Laboratory, Berkeley, California 94720, USA (S.M., D.A.S.).

again from the ‘unknown object’ (the exploding sphere) on the second pass. This hologram encodes both the time delay and the structural change.

The delay time between the pumping and probing of the sphere by the FEL pulse depends on the distance l from the particles to the backing mirror, given simply as $\Delta t = 2l/c$, where c is the speed of light in a vacuum. We used both a wedge-shaped spacing between the particle-coated membrane and the backing multilayer X-ray mirror, and a stair-stepped mirror, producing values of l varying between 30 μm and 1,200 μm , corresponding to delays between 200 fs and 8 ps.

There is no need to precisely measure the distance l , as this distance is encoded directly in the hologram. The geometry of the dusty-mirror hologram can be easily understood by unfolding the optical train and considering path lengths of rays scattering from two particles separated longitudinally by $2l$. For a scattering angle θ , the path difference of these scattered rays (for the approximation of a detector at infinity) is $2l(1 - \cos \theta) \approx l\theta^2$. In the forward direction ($\theta = 0$), rays will add constructively if the object does not change during the delay. Otherwise, if the optical path through the object does change during this interval, there will be a phase shift ϕ applied to the fringe pattern. Each bright ring of the hologram counts another wavelength (λ) of path difference, so at the N th bright ring we have $l\theta^2 + \phi\lambda/(2\pi) \approx N\lambda$, in agreement with Newton’s observation when the object does not change ($\phi = 0$). From a measurement of the angles of the bright rings, we can derive l and hence the delay $2l/c$ to an accuracy of about 1 fs, and we can determine ϕ to an accuracy of 3° for delays less than 1 ps (see Methods).

We used this holographic set-up to investigate the explosion of spherical particles caused by a focused X-ray FEL pulse. We wish to study the dynamics of material in the extreme conditions of intense FEL pulses, both during the pulse and as it turns into a plasma. Models have been developed^{8,9} to predict the effects of intense X-ray pulses on materials and particles, and to understand the resolution limitations of flash imaging³, the technological limitations of X-ray optics⁸, and the fundamental physics of light–matter interactions¹⁰. However, there has been no experimental validation of these models. Indeed, there have been no structural methods to follow early steps in plasma formation. Spherical particles are the simplest shape to consider for modelling the interaction dynamics and scattering of X-ray pulses, and they can be size-selected to a very homogeneous distribution¹¹ to give accurate scattering measurements. In these experiments, we focused 32.5-nm-wavelength pulses of

energies between 2 μJ and 18 μJ to about a 20- μm gaussian-profiled spot on the sample¹². The highest peak intensity was $10^{14} \text{ W cm}^{-2}$, more than 5,000 times the damage threshold of the polystyrene particles¹³.

Each hologram shown in Fig. 2 is the superposition of the time-delay holographic patterns of about 1,000 quasi-identical polystyrene spheres of diameter 140 nm, illuminated by the focused pulse. As the FEL pulse is almost completely transversely coherent, the superposition from the many spheres occurs coherently, and we observe speckle across the hologram. Phase retrieval techniques^{14–16} could be used to reconstruct the positions of all the spheres. To examine the dynamics, we compare our holographic measurements at different delay times to simulations based on the propagation of the pulse through the object and subsequent hydrodynamic explosion from the absorbed energy, as shown in Fig. 4a–c (Methods). As shown in Fig. 4d, we observe that the hologram intensity envelope is unchanged for delays shorter than 1 ps (only the 0.5-ps curve is shown for these short delays) and becomes narrower with longer delays, indicating that the particle diameter begins to increase. This narrowing of the structure factor is observed for delays longer than 3.8 ps, in agreement with our simulations that predict the transverse particle diameter has increased by 40% (60 nm) at 3.8 ps.

At a delay of 500 fs, there is no observable change in the hologram intensity envelope, and we estimate that the spheres have not expanded by more than 20% of their transverse diameter, or 30 nm. We have, however, a more sensitive measure of the structural change of the particle: the holographically determined phase shift, ϕ . We observe an increase in ϕ with delay, for all but the lowest pulse fluences. This is shown in Fig. 4e, indicating a larger optical path length through the exploding object compared to the reference. Because at this wavelength the refractive index of polystyrene is less than unity (equal to 0.87 at room temperature), this increase in optical path corresponds to a decrease in refracting material along the path as time progresses (or a change in refractive index towards unity). We can simulate the phase shift of the exploding spheres from our hydrodynamic model. This also shows an increase of ϕ with delay, primarily due to ball material expanding away in a transverse direction to the beam path (that is, the projected mass is decreasing). A 6-nm expansion in diameter gives a calculated 5° phase shift, as observed at a 350-fs delay.

A further factor is a change in refractive index following the cooling of electrons that were ionized from the atoms during the initial (holographic reference) pulse. Our hydrodynamic model predicts

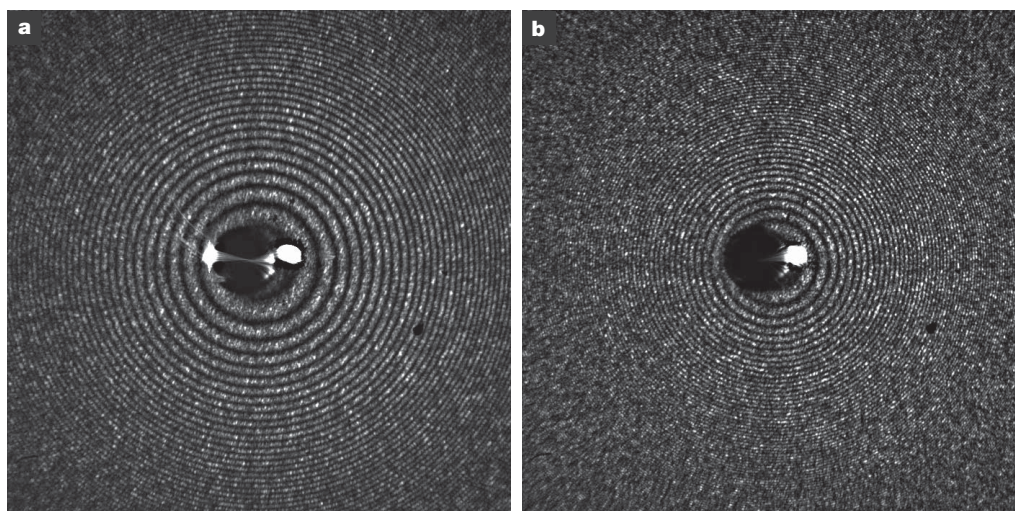


Figure 2 | Time-delay X-ray holograms of 140-nm-diameter polystyrene spheres. The time delays were 348 ± 1 fs (a) and 733 ± 2 fs (b). The pulses were 32-nm wavelength, 25-fs duration with intensities $(0.5 \pm 0.2) \times 10^{14} \text{ W cm}^{-2}$. The intensities of the holograms are shown on a

linear greyscale, to a half-width of $4.5 \mu\text{m}^{-1}$. We derive the time delays and the change in optical path through the exploding particles from the fringe pattern. The particle sizes are determined from the envelope of the intensity.

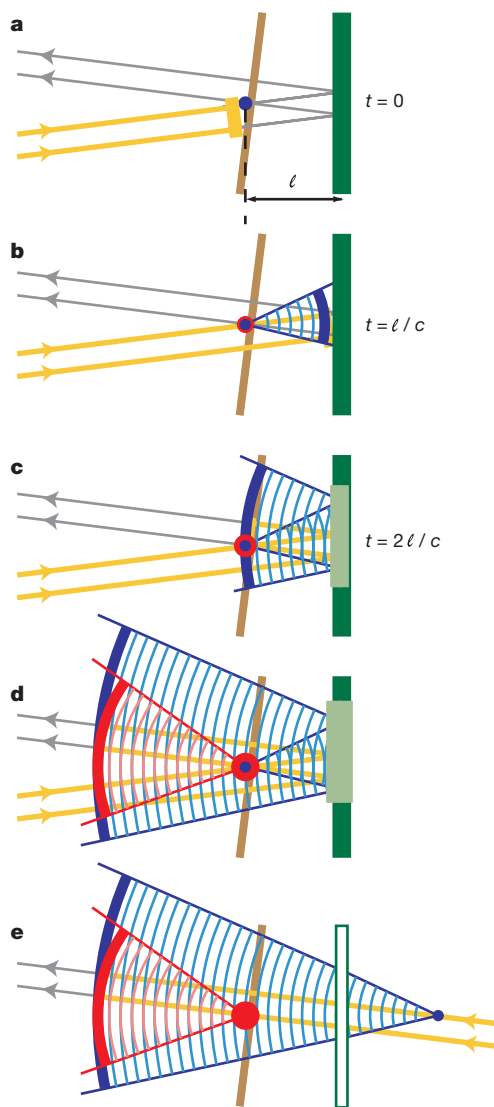


Figure 3 | Geometry for time-delay holography. A pulse is incident (at an angle, for clarity) on a particle located a distance l from a mirror. **a**, Time $t = 0$. **b**, At time $t = l/c$, the pulse and prompt diffraction have reached the mirror. The pulse length is much less than l . **c**, At time $t = 2l/c$, the pulse returns to the particle. By this time the particle has undergone changes due to the initial interaction. The mirror also explodes after it reflects the pulse, but this has no effect on the reflected pulse. **d**, The delayed diffraction (red) co-propagates with the prompt diffraction (blue), and these waves interfere at the detector (not shown). **e**, The geometry can be conceptually unfolded for easier analysis.

that the peak electron temperature of the spheres reaches 10^5 K during the 10^{14} W cm $^{-2}$ pulse. Accurate calculations of refractive index for this degenerate ‘warm dense matter’ regime¹⁰ are not available, and the observed phase shift could be due to a 1.5% increase in refractive index caused by the electron heating (the available models of high-temperature plasmas predict less than a 0.3% increase). The expansion of 6 ± 3 nm at 350 fs delay is thus considered an upper bound of the explosion. Extrapolating to the end of the pulse duration, we predict an expansion of no more than 0.4 nm during the pulse. Thus, it appears feasible to overcome conventional radiation damage limits⁴ in soft-X-ray microscopy of cells^{17,18} with sufficiently short and intense X-ray FEL pulses².

Time-delay holography, inspired by Newton’s experiment, provides a simple method to achieve extremely high spatial and temporal resolution in a single image. The method is well suited to a wide range of short-pulse X-ray sources^{19–21}, and could be extended to hard-X-ray pulsed sources using a grazing-incidence geometry as well as to

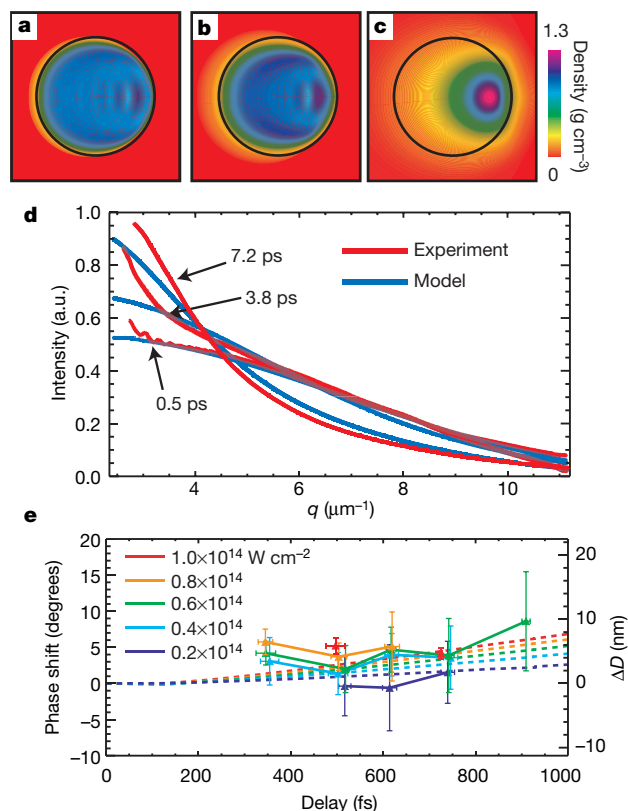


Figure 4 | Determination of the explosion of polystyrene spheres.

a–c, Simulated density profile of an initially uniform 140-nm-diameter polystyrene ball (black circle) irradiated by a 25-fs, 10^{14} W cm $^{-2}$ soft-X-ray FEL pulse from the left, after 0.5 ps (**a**), 0.9 ps (**b**) and 3.2 ps (**c**). **d**, Measured (red) and simulated (blue) envelope of the hologram intensity as a function of momentum transfer $q = (2/\lambda) \sin(\theta/2)$, for three pulse delays and pulse intensities of $(0.8 \pm 0.3) \times 10^{14}$ W cm $^{-2}$. The narrowing of the envelope with time indicates a larger particle diameter, in agreement with the simulations. **e**, Average phase shifts, determined from 129 separate holograms measured at various delays and pulse intensities, as a function of delay. The phase shifts were averaged over ranges of time delay (denoted by the horizontal error bars) and ranges of pulse intensity (indicated by the symbol colour). Vertical error bars give one standard deviation in the phase shift. Solid lines guide the eye. Dashed lines are the phase shifts calculated from hydrodynamic simulations. The approximate change in the ball diameter (ΔD) as obtained from the model is shown on the right-hand axis.

high-resolution experiments using ultrafast optical pump pulses^{22,23}. In particular, time-delay holography can be extended to measure the evolution of clusters, macromolecules and particles irradiated by X-ray FEL pulses, to explore dynamics and imaging^{24–26} at inter-atomic length scales. The coherence demands of the experiment are relatively modest, as Newton’s success attests. The advantage of the almost complete spatial coherence of the X-ray FEL pulses is that holographic reconstructions over large fields of view will be possible, allowing us to examine the time evolution of complex geometries, to study shocks and crack formation, ablation, melting, plasma formation, ultrafast phase transitions, and nonlinear optical effects.

METHODS SUMMARY

Experiments were conducted at FLASH, the soft-X-ray FEL at DESY in Hamburg. The FEL pulses were focused to a 20- μ m-diameter beam on the dusty-mirror sample. The converging beam first passes through a hole in a flat mirror substrate that later reflects the scattered waves to interferometrically combine on a CCD detector. The dusty mirrors consisted of size-selected polystyrene spheres placed onto silicon wafers arrayed with openings supporting thin silicon nitride membranes. These were sandwiched against normal-incidence multilayer mirrors. We obtained a range of time delay distances for various positions across the wafer by either setting the wafer at a small wedge angle to the mirror or by stacking a ‘staircase’ of mirrors. Single-pulse holograms were

recorded at many positions across the wafer. Holograms were sorted according to the measured pulse fluence (which has a large pulse-to-pulse variation owing to the FEL self amplification of spontaneous emission process⁷). From the fringe positions in the hologram we extracted the time delay to an accuracy of about 1 fs, and the change in forward-scattered particle phase shift to an accuracy of about 3° for delays shorter than 1 ps. We compared the phase shift and hologram intensity envelope, defined as the mean of curves fitted through the maximum and minimum fringe intensities, to calculations obtained from a radiation hydrodynamics model. The width of the intensity envelope of the hologram depends inversely on the sphere width, so a narrowing of the envelope function indicates the sphere explosion.

Full Methods and any associated references are available in the online version of the paper at www.nature.com/nature.

Received 1 March; accepted 22 June 2007.

- Newton, I. *Opticks* Book 2, part IV (Dover Publications, New York 1952) (originally published by the Royal Society, London, 1704).
- Solem, J. C. & Baldwin, G. C. Microholography of living organisms. *Science* **218**, 229–235 (1982).
- Chapman, H. N. *et al.* Femtosecond diffractive imaging with a soft-X-ray free-electron laser. *Nature Phys.* **2**, 839–843 (2006).
- Howells, M. R. *et al.* An assessment of the resolution limitation due to radiation-damage in x-ray diffraction microscopy. *J. Electron. Spectrosc. Relat. Phenom.* (in the press); preprint at (<http://arxiv.org/abs/physics/0502059>) (2005).
- Young, T. The Bakerian Lecture: On the theory of light and colours. *Phil. Trans. R. Soc.* **92**, 12–48 (1802).
- de Witte, A. J. Interference in scattered light. *Am. J. Phys.* **35**, 301–313 (1967).
- Ayvazyan, V. *et al.* First operation of a free-electron laser generating GW power radiation at 32 nm wavelength. *Eur. Phys. J. D* **37**, 297–303 (2006).
- Hau-Riege, S. *et al.* Interaction of nanometer-scale multilayer structures with x-ray free-electron laser pulses. *Phys. Rev. Lett.* **98**, 145502 (2007).
- Jurek, Z., Faigel, G. & Tegze, M. Dynamics in a cluster under the influence of intense femtosecond hard X-ray pulses. *Eur. Phys. J. D* **29**, 217–229 (2004).
- Lee, R. *et al.* Finite temperature dense matter studies on next-generation light sources. *J. Opt. Soc. Am. B* **20**, 770–778 (2003).
- Bogan, M. J., Benner, W. H., Hau-Riege, S. P., Chapman, H. N. & Frank, M. Aerosol methods for x-ray diffractive imaging: Size-selected nanoparticles on silicon nitride foils. *J. Aerosol Sci.* (submitted).
- Sorokin, A. A. *et al.* Method based on atomic photoionization for spot-size measurement on focused soft x-ray free-electron laser beams. *Appl. Phys. Lett.* **89**, 221114 (2006).
- Gaur, U. & Wunderlich, B. Heat capacity and other thermodynamic properties of linear macromolecules. V. Polystyrene. *J. Phys. Chem. Ref. Data* **11**, 313–325 (1982).
- Fienup, J. R. Reconstruction of a complex-valued object from the modulus of its Fourier transform using a support constraint. *J. Opt. Soc. Am. A* **4**, 118–123 (1987).
- Miao, J., Charalambous, P., Kirz, J. & Sayre, D. Extending the methodology of x-ray crystallography to allow imaging of micrometre-sized non-crystalline specimens. *Nature* **400**, 342–344 (1999).
- Marchesini, S. *et al.* X-ray image reconstruction from a diffraction pattern alone. *Phys. Rev. B* **68**, 140101R (2003).
- Larabell, C. A. & Le Gros, M. A. X-ray tomography generates 3-D reconstructions of the yeast, *Saccharomyces cerevisiae*, at 60-nm resolution. *Mol. Biol. Cell* **115**, 957–962 (2004).
- Shapiro, D. *et al.* Biological imaging by soft x-ray diffraction microscopy. *Proc. Natl Acad. Sci. USA* **102**, 15343–15346 (2005).
- Bartels, R. A. *et al.* Generation of spatially coherent light at extreme ultraviolet wavelengths. *Science* **297**, 376–378 (2002).
- Schoenlein, R. W. *et al.* Femtosecond X-ray pulses at 0.4 Å generated by 90° Thomson scattering: A tool for probing the structural dynamics of materials. *Science* **274**, 236–238 (1996).
- Schoenlein, R. W. *et al.* Generation of femtosecond pulses of synchrotron radiation. *Science* **287**, 2237–2240 (2000).
- Temnov, V. V., Sokolowski-Tinten, K., Zhou, P. & von der Linde, D. Ultrafast imaging interferometry at femtosecond-laser-excited surfaces. *J. Opt. Soc. Am. B* **23**, 1954–1964 (2006).
- Cavalleri, A. *et al.* Femtosecond structural dynamics in VO₂ during an ultrafast solid-solid phase transition. *Phys. Rev. Lett.* **87**, 237401 (2001).
- Hau-Riege, S. P., London, R. A. & Szöke, A. Dynamics of biological molecules irradiated by short x-ray pulses. *Phys. Rev. E* **69**, 051906 (2004).
- Bergh, M., Timneanu, N. & van der Spoel, D. A model for the dynamics of a water cluster in a X-ray FEL beam. *Phys. Rev. E* **70**, 051904 (2004).
- Neutze, R., Wouts, R., van der Spoel, D., Weckert, E. & Hajdu, J. Potential for biomolecular imaging with femtosecond X-ray pulses. *Nature* **406**, 752–757 (2000).

Acknowledgements Special thanks are due to the scientific and technical staff of FLASH at DESY, Hamburg, in particular to T. Tschentscher, S. Dusterer, J. Schneider, J. Feldhaus, R. L. Johnson, U. Hahn, T. Nuñez, K. Tiedtke, S. Toleikis, E. L. Saldin, E. A. Schneidmiller and M. V. Yurkov. We also thank R. Lee, R. Falcone, M. Ahmed and T. Allison for discussions, and J. Alameda, E. Gullikson, F. Dollar, T. McCarville, F. Weber, J. Crawford, C. Stockton, M. Haro, J. Robinson, H. Thomas, M. Hoener and E. Eremina for technical help with these experiments. This work was supported by the following agencies: the US Department of Energy (DOE) under contract to the University of California, Lawrence Livermore National Laboratory; the National Science Foundation Center for Biophotonics, University of California, Davis; the Advanced Light Source, Lawrence Berkeley Laboratory, under DOE contract; the Natural Sciences and Engineering Research Council of Canada (postdoctoral fellowship to M.J.B.); the Swiss National Science Foundation (fellowship to U.R.); the Sven and Lilly Lawskis Foundation (doctoral fellowship to M.M.S.); the US DOE Office of Science to the Stanford Linear Accelerator Center; the European Union (TUIXS); the Swedish Research Council; the Swedish Foundation for International Cooperation in Research and Higher Education; and The Swedish Foundation for Strategic Research.

Author Contributions H.N.C. conceived the experiment, and H.N.C., S.P.H., A.B., S.M., B.W.W., S. Boutet, M.F., R.A.L. and A.S. contributed to its design. S. Bajt, E.S. and H.N.C. designed the camera and designed and characterized the dusty-mirror optics. Samples were prepared by M.J.B., W.H.B. and M.F., and characterized by M.J.B., S.M., S. Boutet and D.A.S.; H.N.C., M.J.B., A.B., S. Boutet, S.M., M.F., B.W.W., W.H.B., U.R., T.M., C.B., D.A.S., F.B., M.B., C.C., G.H., M.M.S. and J.H. carried out the experiment. M.K., R.T. and E.P. interfaced the experiment to FLASH and developed diagnostics. H.N.C., S.P.H., M.J.B. and M.B. carried out data analysis. All authors discussed the results and contributed to the final manuscript.

Author Information Reprints and permissions information is available at www.nature.com/reprints. The authors declare no competing financial interests. Correspondence and requests for materials should be addressed to H.N.C. (henry.chapman@llnl.gov).

METHODS

Diffraction set-up. Experiments were carried out at FLASH, the soft-X-ray FEL at DESY in Hamburg, under conditions previously reported³. Compared with previous work, the diffraction camera was rotated by 180° to admit the focused incident beam onto the sample through the detector mirror hole. The detector accepts $\pm 15^\circ$, allowing a hologram resolution of 62 nm at 32.5 nm wavelength. **'Dusty mirror' samples.** Polystyrene spheres (PostNova) were aerosolized by charge-reduction electrospray (TSI, model 3480), and selected with a differential mobility analyser (TSI, model 3936) to reduce the size distribution from 16% to less than 4% (as measured by soft-X-ray diffraction at the Advanced Light Source), before deposition onto the membrane¹¹. The substrate, which had several etched openings or 'windows' that were 1.5 mm square and which supported the free-standing 20-nm-thick silicon nitride membrane, was manufactured at the Microfabrication Center at LLNL. This was then wedged against a single multilayer mirror or a stack of stepped mirrors, with the substrate's nitride side facing the mirror. The mirror assemblies gave a range of distances l between the spheres and the mirror, and we selected different delay times by exposing different windows in the substrate. We made assemblies for distances l from 30 μm to 1,200 μm . The largest wedge angle of the nitride substrate was 0.6° , which gives a spread of 0.7 fs in delay over the 20 μm width of the beam. The sample backing multilayer mirror consisted of 50 Si/Mo/B₄C trilayers, and was designed for a peak reflectivity of 50% under normal incidence at a wavelength of 32.5 nm. The peak reflectivity varied by less than 10% for an angle of incidence up to 15° . The pulse fluence was up to 50 times higher than the damage threshold of the backing mirror, and caused it to ablate, but not before the pulse was reflected⁸.

Holograms. Holograms encode the delay time in the fringe pattern caused by the interference of the reference and object waves. Constructive interference occurs at scattering angles θ according to $2l(1 - \cos \theta) - 2l(1 - \cos \alpha) + \phi \lambda / (2\pi) = N\lambda$, for path differences $N\lambda$ shorter than the coherence length, where ϕ is the phase shift of the object relative to the reference, α is the angle between the incident beam and mirror normal, and θ is the angle between the scattered beam and mirror normal. The above equation is fitted to the measured θ values of the bright rings to determine the quantities l and ϕ . The angle α is determined from measurements with attenuated pulses (where damage to the sample does not occur and ϕ is zero), and was less than 0.8° for all mirror assemblies. The accuracy to which we determine l is limited by the precision to which we can measure θ , given by $\Delta l/l \approx 2\Delta\theta/\theta$. Through fitting, we determine the radius of the interference maxima to better than one-tenth the width of a pixel at angles corresponding to 500 pixels on the CCD. This contribution to the error in l is therefore about 1 part in 2,500, or 0.2 fs for a 500-fs delay. However, the sample to CCD distance is only known to 1 part in 500, which places a systematic error in the estimation of the angle θ , corresponding to a 1-fs temporal resolution on the 500-fs delay. This compares with an accuracy of less than 60 fs for state-of-the-art timing diagnostics to synchronize an X-ray beam to a laser beam²⁷.

The determination of the phase shift is independent of the CCD distance. The accuracy for measuring ϕ depends on the number of pixels spanning an entire fringe, which is greatest at the centre of the pattern. However, the hole in our mirror prevents us from measuring the centre, so we determine the fringe shift

for the observed fringes at $q < 5 \mu\text{m}^{-1}$ to estimate the phase shift at $q = 0$. We observe no dependence of phase shift on fringe number in this range, implying that the explosion is spherical over lengthscales larger than 200 nm. We determined ϕ to an accuracy of about 3° for delays shorter than 1 ps. At longer delays the error in ϕ increased in proportion to the delay, owing to the decreasing fringe spacing with increasing delay. As in interferometry, higher accuracy of the phase measurement could be obtained by measuring the fringes in smaller intervals.

There will be no interference for path differences $N\lambda$ greater than the coherence length, which can be no longer than the 7.5- μm FEL pulse length (or a maximum of 230 fringes). The measured fringe visibility also depends on the CCD pixel width. The fringe spacing decreases with N and intensity modulation is not observed when this spacing spans only a single pixel. In our measurements we have observed a maximum of about 150 fringes, limited by the pixel width. We define the hologram intensity envelope as the mean of curves fitted through the maximum and minimum fringe intensities, which is not dependent on the fringe visibility.

Hydrodynamic simulations. The light intensity distribution inside the polystyrene spheres was calculated using Mie theory²⁸; this time-independent model is applicable because the time for the light to propagate through the sphere (approximately 2 fs) is much shorter than the pulse length (25 fs). We based our estimate of the complex index of refraction on published room-temperature solid-density values²⁹, and corrected for changes with temperature and density using an average ion model employing screened hydrogen potentials³⁰. We calculated the temperature and density of the sphere using the HYDRA radiation hydrodynamics code³¹. This model accounts for radiation transport and electron thermal conduction. The change in transverse sphere diameter, ΔD , projected along the ray direction z , is quantified as $\Delta D/2 = (2\pi/m) \int_{-\infty}^{\infty} \int_0^{\infty} r_{\perp}^2 \rho(r_{\perp}, z) dr_{\perp} dz$, where ρ is the sphere density, m its mass, and r_{\perp} is the radial coordinate perpendicular to z . Finally, the superposition of the far-field diffraction patterns of the undamaged sphere and of the exploded sphere was calculated using the Fresnel–Kirchhoff diffraction integral³². This hologram is the product of the structure factors of the undamaged and damaged balls, modulated by the delay-encoding ring pattern. The width of the intensity envelope of the hologram depends inversely on the sphere width, so a narrowing of the envelope function indicates the sphere explosion.

27. Cavalieri, A. L. *et al.* Clocking femtosecond x-rays. *Phys. Rev. Lett.* **94**, 114801 (2005).
28. Bohren, C. F. & Huffman, D. R. *Absorption and Scattering of Light by Small Particles* (Wiley-Interscience, New York, 1983).
29. Henke, B. L., Gullikson, E. M. & Davis, J. C. X-ray interactions: photoabsorption, scattering, transmission, and reflection at $E=50\text{--}30000$ eV, $Z=1\text{--}92$. *Atom. Nucl. Data Tables.* **54**, 181–342 (1993).
30. Zimmerman, G. B. & More, R. M. Pressure ionization in laser-fusion target simulation. *J. Quant. Spectrosc. Radiat. Transf.* **23**, 517–522 (1980).
31. Marinak, M. M. *et al.* Three-dimensional HYDRA simulations of National Ignition Facility targets. *Phys. Plasmas* **8**, 2275–2280 (2001).
32. Goodman, J. W. *Introduction to Fourier Optics* (McGraw-Hill, Boston, 1996).

LETTERS

Intense mixing of lower thermocline water on the crest of the Mid-Atlantic Ridge

Louis C. St Laurent¹ & Andreas M. Thurnherr²

Buoyancy exchange between the deep and the upper ocean, which is essential for maintaining global ocean circulation, mainly occurs through turbulent mixing^{1,2}. This mixing is thought to result primarily from instability of the oceanic internal wave field³, but internal waves tend to radiate energy away from the regions in which they are generated rather than dissipate it locally as turbulence⁴ and the resulting distribution of turbulent mixing remains unknown. Another, more direct, mixing mechanism involves the generation of turbulence as strong flows pass through narrow passages in topography, but the amount of turbulence generated at such locations remains poorly quantified owing to a lack of direct measurements. Here we present observations from the crest of the Mid-Atlantic Ridge in the subtropical North Atlantic Ocean that suggest that passages in rift valleys and ridge-flank canyons provide the most energetic sites for oceanic turbulence. Our measurements show that diffusivities as large as $0.03 \text{ m}^2 \text{ s}^{-1}$ characterize the mixing downstream of a sill in a well-stratified boundary layer, with mixing levels remaining of the order of $10^{-4} \text{ m}^2 \text{ s}^{-1}$ at the base of the main thermocline. These mixing rates are significantly higher than the diffusivities of the order of $10^{-5} \text{ m}^2 \text{ s}^{-1}$ that characterize much of the global thermocline and the abyssal ocean⁵. Our estimates suggest that overflows associated with narrow passages on the Mid-Atlantic Ridge in the North Atlantic Ocean produce as much buoyancy flux as has previously been estimated for the entire Romanche fracture zone^{6,7}, a large strait in the Mid-Atlantic Ridge that connects the North and South Atlantic basins. This flux is equivalent to the interior mixing that occurs in the entire North Atlantic basin at the depth of the passages, suggesting that turbulence generated in narrow passages on mid-ocean ridges may be important for buoyancy flux at the global scale.

We focused on the upper layer of North Atlantic Deep Water, originating in the Greenland, Iceland and Norwegian seas. While some North Atlantic Deep Water flows south in a deep western boundary current along Labrador, much of the water mass flows southward in a diffuse interior circulation south of the Denmark Strait⁸, where it encounters the dramatic topography of the Mid-Atlantic Ridge. There, a complex network of fracture zones emanates from the rift valley where the North American and Eurasian/African tectonic plates diverge. Within the network of fracture zones and rift-valley segments, flows passing through constrictions and across sills accelerate to speeds much greater than the tidal or overlying geostrophic flows. The resulting overflows are often hydraulically controlled, with rapid conversion of potential to kinetic energy downstream of the controlling topography, and extremely large levels of turbulent mixing. While most past work has focused on overflows of prominent straits separating major basins (Denmark Strait⁸; Strait of Gibraltar⁹) and major deep fracture zones (Vema Passage¹⁰,

Romanche⁶), more recent work has indicated significant overflow processes acting in the smaller passages along the Mid-Atlantic Ridge^{11–14}. Aside from the Romanche passage⁶, and several turbulence profiles unintentionally collected downstream of sills in a deep fracture zone canyon¹⁴, no direct measurements of mixing are available.

Motivated by the lack of direct measurements, we conducted a survey in the rift valley of the 'Lucky Strike' segment on the Mid-Atlantic Ridge (LS in Fig. 1). The geology of the site is being studied in the context of the French MoMAR (Monitoring the Mid-Atlantic Ridge) programme¹⁵. The GRAVILUCK cruise, carried out in August 2006 primarily to investigate details of the gravity field at Lucky Strike, provided a cruise opportunity for physical oceanographic measurements at a novel site. The survey focused on the narrow passage to the east of the Lucky Strike volcano (Fig. 1). The axial depth of the 7 km long eastern passage ranges from 2,200 m to 2,050 m at a sill. Below 1,800 m the passage is laterally constricted by the rift-valley wall in the east and by the eastern flank of the Lucky Strike volcano in the west; at 1,800 m its width at the latitude of the sill is roughly 3 km, and the mean steepness of the sidewalls is 0.3 (rise over run). We are unaware of any previous deep-ocean turbulence survey accomplished in such a narrow and steep passage.

The field survey used two instrument systems to characterize the hydrography, flow and turbulence. A deep microstructure profiler system (DMP), and a lowered acoustic Doppler current profiler system (ADCP) were used. Both incorporate conventional conductivity, temperature and depth (CTD) systems for hydrographic measurements. All DMP and lowered ADCP deployments were carried out simultaneously, allowing for concurrent measurements of turbulence and velocity in the passage. In addition to the lowered systems, a bottom-mounted ADCP was deployed by the submersible *Nautille* in close proximity to the sill. This additional unit recorded velocity for two weeks in the 100-m depth interval above the sill, giving an unambiguous record of the time-varying flow.

A combined hydrography and flow section showing cluster-averaged fields along the eastern passage is presented in Fig. 2. Profiles were made in clusters of two to five profiles each, at eight locations within the passage, corresponding to three upstream sites (U1 to U3), one at the sill, and four downstream (D1 to D4). The data show a mean northward flow, with strong shear below 1,800 m separating the flow through the passage from the circulation above. The velocity data indicate a marked acceleration at the sill, leading to mean downstream velocities exceeding 10 cm s^{-1} . The density structure across the passage has features typical of hydraulically controlled flows. Along the passage, isopycnals (neutral density contours; γ_n) slope significantly across the sill. Froude numbers, $Fr = V/(NH)$, were calculated along the passage from depth-averaged meridional velocities V , mean buoyancy frequencies N , and layer thicknesses H below 1,800 m.

¹Department of Oceanography, Florida State University, Tallahassee, Florida 32306, USA. ²Division of Ocean and Climate Physics, Lamont-Doherty Earth Observatory, Palisades, New York 10964, USA.

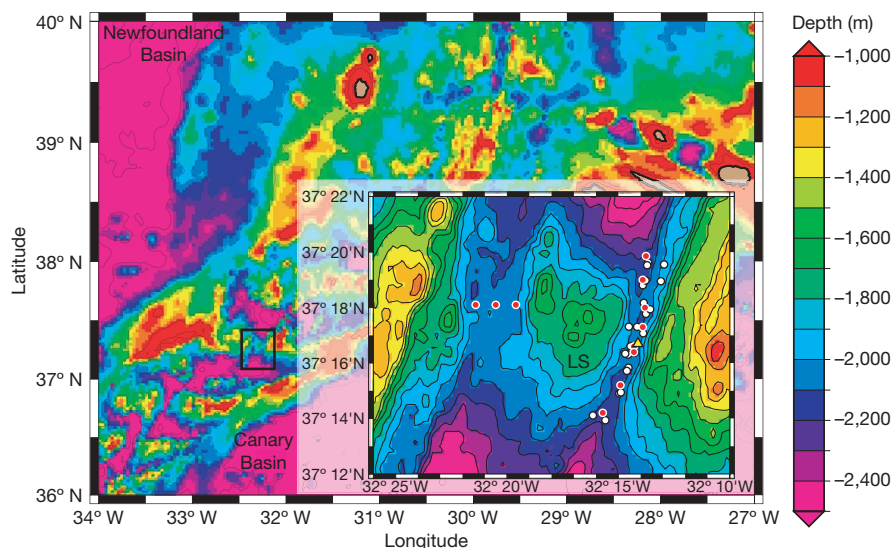


Figure 1 | Regional setting (box) and topography (inset) of the Lucky Strike segment. The main figure shows basin-scale bathymetric data²¹, and the inset shows local survey bathymetric data²⁸. The colour scheme is chosen to

maximize contrast for the Mid-Atlantic Ridge axis. Measurement locations show lowered ADCP stations (white circles), DMP stations (red circles), and a bottom-mounted ADCP (yellow triangle).

Froude numbers reported in Fig. 2 show an abrupt increase to values near 1 at the sill and a similarly abrupt decrease between D2 and D3. This is suggestive of hydraulic control and, possibly, of a hydraulic jump downstream of the sill.

Density contours incrop along the passage floor, suggesting strong mixing, which was clearly indicated in the measurements of turbulent dissipation rate (Fig. 3). Dissipation rates reaching $\varepsilon \geq 10^{-8} \text{ W kg}^{-1}$ were observed throughout the depth interval of the passage, in contrast to typical thermocline levels of $\varepsilon = (1-3) \times 10^{-10} \text{ W kg}^{-1}$. Both upstream and downstream of the sill, dissipation levels are largest near the seabed, indicating the presence of an active bottom boundary layer. Upstream of the sill, elevated dissipation levels occur between 2,000 m and the sea bed, but they are generally below $10^{-8} \text{ W kg}^{-1}$. Just downstream of the sill, dissipation levels reach nearly $10^{-6} \text{ W kg}^{-1}$, as large as any observed in the abyssal ocean⁶.

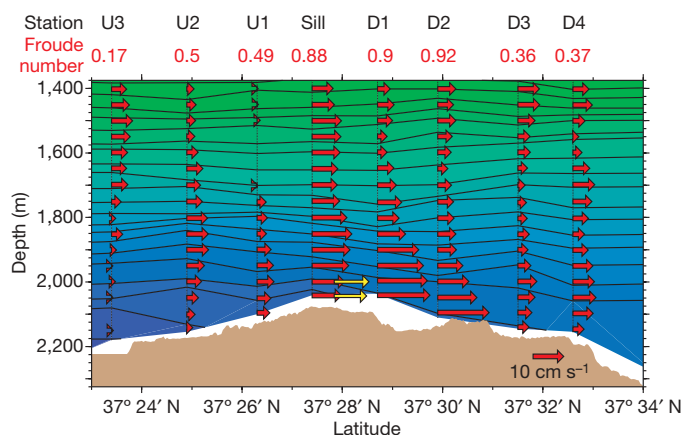


Figure 2 | Velocity and neutral-density contours along the deep passage east of the Lucky Strike volcano. Between U2 and D2, the passage is laterally closed below 1,800 m (Fig. 1). Average station locations upstream (U1 to U3), at the sill, and downstream (D1 to D4) are indicated along the upper edge of the figure; red numbers indicate the maximum Froude numbers below 1,800 m (see text for details). Red arrows, 50-m-averaged lowered ADCP data; yellow arrows, the two-week-averaged velocities recorded by a bottom-mounted ADCP. Irregularly spaced neutral density contours ranging from 27.852 to 27.952 kg m^{-3} were selected for approximately uniform spacing in depth.

Turbulent diffusivities were also calculated by averaging downstream, sill, and upstream DMP measurements. A model¹⁶ assuming a constant mixing efficiency parameter of $\Gamma = 0.2$ was used to relate the diffusivity k_p to the dissipation rate and buoyancy gradient: $k_p = \Gamma \langle \varepsilon \rangle / \langle N^2 \rangle$. Figure 4 shows these ensemble-averaged profiles. In all profiles diffusivities of $k_p \geq 1 \times 10^{-4} \text{ m}^2 \text{ s}^{-1}$ ($1 \text{ cm}^2 \text{ s}^{-1}$) reach to levels 600 m above the passage bottom, that is, to the base of the main thermocline. Mixing is greatly enhanced within the passage, with diffusivities exceeding $k_p = 3 \times 10^{-3} \text{ m}^2 \text{ s}^{-1}$ ($30 \text{ cm}^2 \text{ s}^{-1}$) within the bottom boundary layer. In particular, diffusivities just downstream of the sill reach $k_p \approx 3 \times 10^{-2} \text{ m}^2 \text{ s}^{-1}$ ($300 \text{ cm}^2 \text{ s}^{-1}$) with a vertical density gradient of $N > 1 \times 10^{-3} \text{ s}^{-1}$, an order of magnitude greater than stratifications in abyssal fracture zones⁶.

We are unaware of any previous observation of such large turbulence levels in significantly stratified deep water (below 1,000 m). A similar section of flow and turbulence was observed in the Romanche fracture zone⁶, but that passage is the major connection between the North and South Atlantic basins, whereas the Lucky Strike passage connects two minor sub-basins in the rift valley of the Mid-Atlantic Ridge. Furthermore, the effects of overflow mixing in the Romanche fracture zone are limited to Antarctic Bottom Water, and thus do not directly affect the buoyancy of the main

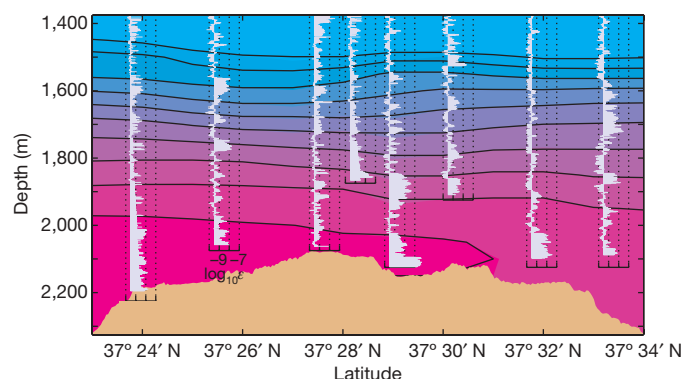


Figure 3 | Turbulence dissipation-rate profiles along the eastern passage at the Lucky Strike site. In all cases, a logarithmic axis is used, as indicated by the labelled example. Data are plotted about a reference level of $3 \times 10^{-10} \text{ W kg}^{-1}$, roughly corresponding to a background level of dissipation in the main thermocline. Contours show potential temperatures (relative to the sea surface) from 4.0 to 5.0 $^{\circ}\text{C}$ at 0.1 $^{\circ}\text{C}$ intervals.

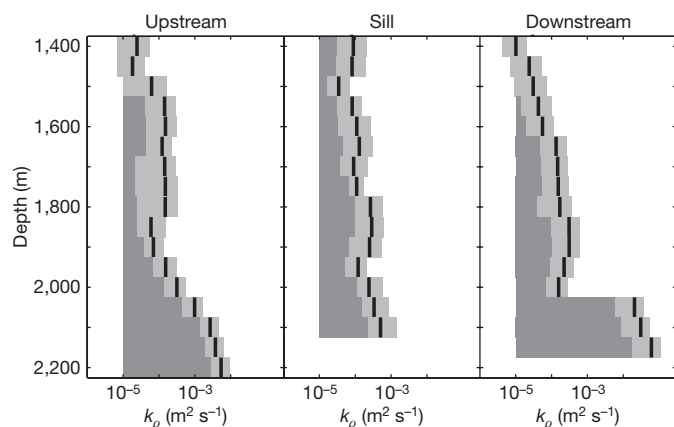


Figure 4 | Turbulent diffusivity estimates for station groups at the upstream, sill and downstream passage locations. Estimates were made in 50-m depth intervals, and mean values (dark line segments) and 95% confidence intervals (light-shaded band) are shown relative to a reference of $1 \times 10^{-5} \text{ m}^2 \text{ s}^{-1}$, which is a typical thermocline mixing rate.

thermocline, which mostly involves North Atlantic Deep Water^{17,18}. The processes acting at Lucky Strike are in contrast to those acting in abyssal fracture zones because, first, the site is shallow enough to allow enhanced mixing to extend into the well-stratified waters at the base of the thermocline, and second, although it is small in spatial extent, the Lucky Strike passage is typical of many thousands of similar sites through the global mid-ocean ridge canyon network¹⁴.

Water mass conversion at Lucky Strike can be assessed by estimating the buoyancy flux occurring in the passage, $F = Q\Delta\rho \approx 2 \times 10^3 \text{ kg s}^{-1}$, where Q is the along-valley volume flux and $\Delta\rho$ is the deep cross-sill density difference⁷. Persistent northward flow in the continuous rift valley between 35.5° N and 37.5° N has been observed at several latitudes^{12,13,19} and the monotonically decreasing rift-valley density in the same region²⁰ suggests that this northward flow is continuous. Topographic data indicate that, within this 250 km of rift valley, the water must flow through at least nine passages. Unambiguous evidence for overflows is available from four of those locations^{12,13,19}, and overflows probably occur in all. Taken together, the buoyancy flux associated with overflows in this short 2° stretch of the Mid-Atlantic Ridge rift valley equals a tenth of that occurring at the Romanche fracture zone⁷. Scaled over the greater North Atlantic Mid-Atlantic Ridge, this result suggests that overflows in the rift valley alone account for as much water mass conversion as is occurring at Romanche.

The large-scale effects of water mass conversion at Lucky Strike can also be assessed by examining the influence of rift-valley and ridge-flank mixing on the North Atlantic basin as a whole. From an analysis of bathymetric data²¹ for the region between 20° N and 60° N , we find that just over 3% of the basin area bounded by the 2,000-m isobath on the continental slopes contains ridge topography shallower than 2,000 m. Treating this ridge topography as similar to the Lucky Strike region, we assume that diffusivities of $k_p = 3 \times 10^{-4} \text{ m}^2 \text{ s}^{-1}$ ($3 \text{ cm}^2 \text{ s}^{-1}$) characterize the mixing in and above the narrow passages constricting the flow. If the regions away from mid-ocean ridge locations are assumed to have a diffusivity of $k_p \approx 1 \times 10^{-5} \text{ m}^2 \text{ s}^{-1}$ ($0.1 \text{ cm}^2 \text{ s}^{-1}$) (ref. 5), then the 3% of the deep basin area occupied by ridges and their associated passages contributes the same area-integrated diapycnal buoyancy flux as the rest of the basin.

METHODS

Lowered acoustic Doppler profile data for velocity, and CTD hydrographic data were analysed using methods now common in the oceanographic community^{22,23}. The DMP is a specialized free-falling, autonomous, vertical microstructure system made by Rockland Scientific International. Specifications for the system can be found online²⁴. Of specific interest is the measurement of

microstructure shear used in the quantification of turbulent kinetic energy ε . This is the rate of energy removal by the molecular viscosity of sea water ν acting on the mean-square turbulent shear $\langle u_z^2 \rangle$, and is used in the relation $\varepsilon = (15/2)\nu\langle u_z^2 \rangle$ (ref. 25). Analysis of the shear signal is done using spectral analysis²⁶ over 1-m depth intervals of the microstructure record. For each ε estimate, shear variance $\langle u_z^2 \rangle$ is computed using a spectral integration. Estimates of diffusivity were made for 50-m profile segments, as reported in Fig. 4. Confidence intervals were computed using a bootstrap method applied to each 50-m segment²⁷.

Lowered ADCP and CTD data. A Teledyne RD Instruments 300 kHz Workhorse ADCP was used in conjunction with a Seabird 911 CTD on a 24-bottle rosette frame. Bottle samples were used to verify the accuracy of this CTD's salinity calibration, which is better than 0.002. In addition to the lowered ADCP profiles done in conjunction with the DMP, 18 additional full-depth profiles were collected in the eastern passage (Fig. 1). Resampling of the eastern passage was done roughly every four days, with the full observational record extending over three weeks. These were timed to sample the semidiurnal tidal cycle as completely as possible. The excellent correspondence between the time-averaged velocities recorded by the bottom-mounted ADCP (also a Teledyne RD Instruments 300 kHz Workhorse) near the sill (yellow arrows) and the nearby cluster-averaged lowered ADCP profile suggests that Fig. 2 closely approximates a temporal average. Thus, the available hydrographic and velocity measurements capture the tidal variability associated with the spring-neap cycle.

Dissipation data. The DMP instrument system was designed to match the general specifications of the several other full-depth capable microstructure systems in use by the ocean turbulence community. In addition to a Seabird CTD system, the DMP uses up to six microstructure sensors to determine the turbulent mixing rates. The profiler samples turbulent shear at 512 Hz as it descends at roughly 0.6 m s^{-1} , achieving a vertical full-wavelength resolution of 3 mm. The raw shear signal is processed using well-documented techniques²⁵. Electronic noise, instrument vibration, and small amounts of turbulence generated at the leading edge of the guard assembly apply a shear dissipation rate noise level of $1 \times 10^{-10} \text{ W kg}^{-1}$ to our measurements. Ensemble averages over non-overlapping 50-m profile segments are used in the estimates for diffusivities. Dissipation statistics in each 50-m segment are treated as containing five degrees of freedom, based on taking 10 m as the average turbulence patch scale. It follows that each Monte Carlo bootstrap sampling of the 50-m segment data contains five ε values, drawn with replacement²⁷.

Received 9 February; accepted 21 June 2007.

1. Munk, W. H. Abyssal recipes. *Deep-Sea Res.* **13**, 207–230 (1966).
2. Munk, W. & Wunsch, C. Abyssal recipes. II: Energetics of tidal and wind mixing. *Deep-Sea Res.* **45**, 1977–2010 (1998).
3. Munk, W. in *Evolution of Physical Oceanography* 264–291 (The MIT Press, Cambridge, 1981).
4. St Laurent, L. C. & Garrett, C. The role of internal tides in mixing the deep ocean. *J. Phys. Oceanogr.* **32**, 2882–2899 (2002).
5. Kunze, E. & Sanford, T. B. Abyssal mixing: where it is not. *J. Phys. Oceanogr.* **26**, 2286–2296 (1996).
6. Polzin, K. L., Speer, K. G., Toole, J. M. & Schmitt, R. W. Intense mixing of Antarctic Bottom Water in the equatorial Atlantic Ocean. *Nature* **380**, 54–57 (1996).
7. Bryden, H. L. & Nurser, A. J. G. Effects of strait mixing on ocean stratification. *J. Phys. Oceanogr.* **33**, 1870–1872 (2003).
8. Girton, J. B. & Sanford, T. B. Descent and modification of the overflow plume in the Denmark Strait. *J. Phys. Oceanogr.* **33**, 1351–1364 (2003).
9. Farmer, D. & Armi, L. The flow of Mediterranean water through the Strait of Gibraltar. *Prog. Oceanogr.* **21**, 1–105 (1988).
10. Hogg, N. G., Biscaye, P., Gardner, E. & Schmitz, W. J. On the transport of Antarctic Bottom Water in the Vema Channel. *J. Mar. Res.* **40** (Suppl.), 231–263 (1982).
11. Thurnherr, A. M. Diapycnal mixing associated with an overflow in a deep submarine canyon. *Deep-Sea Res.* **53**, 194–206 (2006).
12. Thurnherr, A. M. & Richards, K. R. Hydrography and high-temperature heat flux of the rainbow hydrothermal site (36°14N, Mid-Atlantic Ridge). *J. Geophys. Res.* **106**, 9411–9426 (2001).
13. Thurnherr, A. M., Richards, K. J., German, C. R., Lane-Serff, G. F. & Speer, K. G. Flow and mixing in the rift valley of the Mid-Atlantic Ridge. *J. Phys. Oceanogr.* **32**, 1763–1778 (2002).
14. Thurnherr, A. M., St Laurent, L. C., Speer, K. G., Toole, J. M. & Ledwell, J. R. Mixing associated with sills in a canyon on the mid-ocean ridge flank. *J. Phys. Oceanogr.* **35**, 1370–1381 (2005).
15. Escartin, J. *Monitoring the Mid-Atlantic Ridge (MoMAR)* (<http://www.ipgp.jussieu.fr/rech/lgm/MoMAR/>) (2006).
16. Osborn, T. R. Estimates of the local rate of vertical diffusion from dissipation measurements. *J. Phys. Oceanogr.* **10**, 83–89 (1980).
17. Webb, D. J. & Suginohara, N. Vertical mixing in the ocean. *Nature* **409**, 37 (2001).

18. St Laurent, L. & Simmons, H. L. Estimates of power consumed by mixing in the ocean interior. *J. Clim.* **19**, 4877–4890 (2006).
19. Keller, G. H., Anderson, S. H. & Lavelle, J. W. Near-bottom currents in the Mid-Atlantic Ridge rift valley. *Can. J. Earth Sci.* **12**, 703–710 (1975).
20. Wilson, C., Speer, K., Charlou, J.-L., Bougault, H. & Klinkhammer, G. Hydrography above the Mid-Atlantic Ridge (33°–40°N) and within the Lucky Strike segment. *J. Geophys. Res.* **100**, 20555–20564 (1995).
21. Smith, D. K. & Sandwell, D. Global sea floor topography from satellite altimetry and ship depth soundings. *Science* **277**, 1956–1962 (1997).
22. Joyce, C. & Corry, C. *WHP 90-1: Requirements for WOCE Hydrographic Program Data Reporting* (<http://cchdo.ucsd.edu/manuals.htm>) (1994).
23. Visbeck, M. Deep velocity profiling using lowered acoustic Doppler current profiler: bottom track and inverse solutions. *J. Atmos. Ocean. Technol.* **19**, 794–807 (2002).
24. Rockland Scientific International. *Microstructure Instruments—VMP 5500* (http://www.rocklandscientific.com/products_vmp5500.php) (2006).
25. Lueck, R. G., Wolk, F. & Yamazaki, H. Oceanic velocity microstructure measurements in the 20th century. *J. Oceanogr.* **58**, 153–174 (2002).
26. Gregg, M. C. Uncertainties and limitations in measuring ϵ and χ . *J. Atmos. Ocean. Technol.* **16**, 1483–1490 (1999).
27. Emery, W. J. & Thomson, R. E. *Data Analysis Methods in Physical Oceanography* (Elsevier Science, Amsterdam, 2001).
28. Cannat, M. *et al.* Mid-Atlantic Ridge-Azores hotspot interactions: Along-axis migration of a hotspot-derived event of enhanced magmatism 10 to 4 Ma ago. *Earth Planet. Sci. Lett.* **173**, 257–269 (1999).

Acknowledgements We thank V. Ballu for inviting us to join the GRAVILUCK cruise. We also thank P. Bouruet-Aubertot, G. Reverdin, and the scientific staff and crew of the N/O *Atalante* for their assistance during the field programme. Technical support of the DMP by R. Lueck, F. Wolk, and P. Stern of Rockland Scientific, and by E. Howarth of FSU, was invaluable. E. Kunze provided comments on the early draft of the manuscript. The FSU turbulence instrumentation programme is supported by the US Office of Naval Research. The LDEO lowered ADCP programme, and our participation in GRAVILUCK, was sponsored by the US National Science Foundation.

Author Contributions L.C.StL. and A.M.T. contributed equally to this work. L.C.StL. led the microstructure sampling programme, and analysed the turbulence data. A.M.T. led the lowered ADCP measurement programme, and analysed the velocity data.

Author Information Reprints and permissions information is available at www.nature.com/reprints. The authors declare no competing financial interests. Correspondence and requests for materials should be addressed to L.C.StL. (stlaurent@ocean.fsu.edu).

LETTERS

The return of subducted continental crust in Samoan lavas

Matthew G. Jackson¹, Stanley R. Hart², Anthony A. P. Koppers^{3,4}, Hubert Staudigel³, Jasper Konter³, Jerzy Blusztajn², Mark Kurz² & Jamie A. Russell³

Substantial quantities of terrigenous sediments are known to enter the mantle at subduction zones, but little is known about their fate in the mantle¹. Subducted sediment may be entrained in buoyantly upwelling plumes and returned to the Earth's surface at hotspots^{2–5}, but the proportion of recycled sediment in the mantle is small, and clear examples of recycled sediment in hotspot lavas are rare^{6,7}. Here we report remarkably enriched ⁸⁷Sr/⁸⁶Sr and ¹⁴³Nd/¹⁴⁴Nd isotope signatures in Samoan lavas from three dredge locations on the underwater flanks of Savai'i island, Western Samoa. The submarine Savai'i lavas represent the most extreme ⁸⁷Sr/⁸⁶Sr isotope compositions reported for ocean island basalts to date. The data are consistent with the presence of a recycled sediment component (with a composition similar to the upper continental crust) in the Samoan mantle. Trace-element data show affinities similar to those of the upper continental crust—including exceptionally low Ce/Pb and Nb/U ratios⁸—that complement the enriched ⁸⁷Sr/⁸⁶Sr and ¹⁴³Nd/¹⁴⁴Nd isotope signatures. The geochemical evidence from these Samoan lavas significantly redefines the composition of the EM2 (enriched mantle 2; ref. 9) mantle endmember, and points to the presence of an ancient recycled upper continental crust component in the Samoan mantle plume.

The Earth's mantle, as sampled by ocean island basalts erupted at hotspots, is chemically and isotopically heterogeneous. However, the origin of the geochemical heterogeneity of the mantle is not well understood. One model for the geochemical evolution of the mantle assumes that much of the chemical diversity is a result of subduction, a tectonic process that introduces enriched oceanic crust and compositionally heterogeneous sediment into a largely primitive (or slightly depleted) mantle^{5,10,11}. Following subduction, these surface materials mix with a peridotitic mantle, thus imprinting their enriched chemical and isotopic signatures on its various domains. A number of isotopically distinct geochemical reservoirs, as sampled by ocean island basalts, have resulted from this process. The isotopic endmembers are often referred to as HIMU (high $\mu = {}^{238}\text{U}/{}^{204}\text{Pb}$), EM1 (enriched mantle 1) and EM2 (enriched mantle 2) and DMM (depleted mid-ocean-ridge basalt mantle)⁹. Although the most radiogenic Pb isotope ratios observed in the HIMU component have been proposed to result from a contribution of recycled oceanic crust^{9,12}, most models for the creation of the EM1 and EM2 mantle reservoirs invoke a small portion of lithologically distinct sediments that have been recycled into the mantle^{9,13}.

The volcanically active Samoan islands and seamounts define a hotspot track with a classical EM2 pedigree^{7,14,15}. The first high-precision ⁸⁷Sr/⁸⁶Sr and ¹⁴³Nd/¹⁴⁴Nd measurements from Samoan lavas were interpreted as evidence of sediment recycling⁵. Recently,

however, the proposed recycled sediment origin of the enriched Samoan basalts has been questioned (see Supplementary Discussion), and an alternative model favouring source enrichment by metasomatic processes was proposed⁷. The extreme isotopic and chemical enrichment in the new Samoan EM2 lavas exhibit distinctly continental fingerprints, and argue for a role for a component similar to ancient recycled upper continental crust (UCC) in the Samoan plume (see Supplementary Discussion for the ALIA 2005 cruise dredge locations and geochemical data).

The most isotopically enriched Samoan whole-rock ⁸⁷Sr/⁸⁶Sr signature (0.720469, Mg# = 57.2) is recorded in a trachyandesite, dredge sample D115-21, which was taken from the southwestern flank of Savai'i. Clinopyroxene mineral separates from the same sample yielded an even higher ⁸⁷Sr/⁸⁶Sr ratio (0.721630). A trachybasalt (D115-18) hosts the second-most-enriched ⁸⁷Sr/⁸⁶Sr (0.718592, Mg# = 58.7), and clinopyroxene mineral separates from the sample also gave more enriched ratios (0.720232–0.720830). Six other lavas recovered in the same dredge also exhibit enriched ⁸⁷Sr/⁸⁶Sr ratios (0.708175–0.716394, Mg# = 52.0–65.1). Dredge D118, located on the far western end of the Savai'i lineament, contained an alkali basalt with enriched ⁸⁷Sr/⁸⁶Sr (0.710337, measured on fresh clinopyroxene). Dredge D128, taken on the northeastern flanks of Savai'i, yielded a transitional basalt with a high ⁸⁷Sr/⁸⁶Sr ratio (0.712500, Mg# = 70.5) and several other basalts with less enriched ⁸⁷Sr/⁸⁶Sr (0.706397–0.708170, Mg# = 61.2–63.9). Dredge D114, taken on the southwestern flanks of Savai'i, provided younger shield basalts of transitional chemistry and normal ⁸⁷Sr/⁸⁶Sr (0.705422–0.705435, Mg# = 67.2 and 76.3).

The ⁸⁷Sr/⁸⁶Sr isotopes in the basalts from all three ultra-enriched sampling localities are complemented by enriched (low) ¹⁴³Nd/¹⁴⁴Nd and the lowest ³He/⁴He ratios (4.31–4.93 Ra, or ratio to atmosphere) observed in Samoan basalts. Together, the new data extend the Samoan isotope array to a region outside the global ocean island basalt field (Fig. 1). Highly enriched EM2 signatures have previously been observed only in metasomatized xenoliths from Savai'i (⁸⁷Sr/⁸⁶Sr up to 0.712838; ref. 16), and the Samoan EM2 basalts provide the first evidence that the enriched component hosted in these xenoliths also occurs as erupted basalts. The enriched ⁸⁷Sr/⁸⁶Sr and ¹⁴³Nd/¹⁴⁴Nd isotope ratios, coupled with the low ³He/⁴He, are consistent with a recycled UCC component in the mantle source of the Samoan EM2 basalts.

The UCC reservoir exhibits several diagnostic trace-element characteristics that can be useful for detecting its presence in Samoan EM2 lavas. Compared to ocean island basalt and mid-ocean-ridge basalt lavas, UCC displays exceptional depletion in Nb (and Ta), Ti and Eu, and enrichment in Pb (Fig. 2). Samoan basalts have

¹Massachusetts Institute of Technology, Woods Hole Oceanographic Institution Joint Program, ²Woods Hole Oceanographic Institution, Woods Hole, Massachusetts 02543-1525, USA. ³Scripps Institution of Oceanography, University of California, San Diego, La Jolla, California 92093-0225, USA. ⁴College of Oceanic and Atmospheric Sciences, Oregon State University, Corvallis, Oregon 97331-5503, USA.

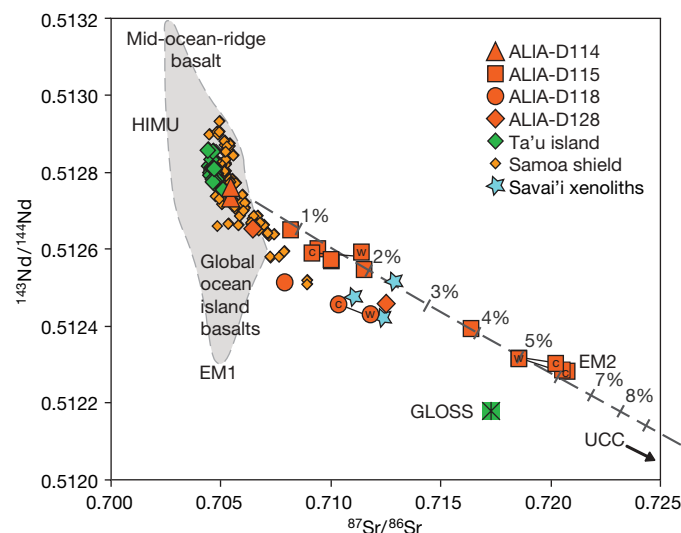


Figure 1 | $^{87}\text{Sr}/^{86}\text{Sr}$ and $^{143}\text{Nd}/^{144}\text{Nd}$ isotope ratios of new enriched Samoan lavas. The values are compared with other Samoan shield basalts⁷, global ocean island basalt compositions and GLOSS (global subducting sediment)¹. Analyses in which whole-rock (w) powders and clinopyroxene (c) analyses are performed on the same sample are connected by a tie-line. A model mixing line between depleted Ta'u peridotite and UCC is marked at 1% intervals, with increasing contribution from the latter component. The hypothetical UCC mixing endmember lies outside the figure. Approximately 5% UCC is required to produce the spidergram of sample D115-18 (see Supplementary Discussion), and ~6% is required to generate the $^{87}\text{Sr}/^{86}\text{Sr}$ and $^{143}\text{Nd}/^{144}\text{Nd}$ in D115-21.

trace-element characteristics that are increasingly similar to UCC with more enriched $^{87}\text{Sr}/^{86}\text{Sr}$ and $^{143}\text{Nd}/^{144}\text{Nd}$ values (Fig. 3). Although the most isotopically depleted basalts from Samoa show slight positive anomalies in Nb and Ti, the magnitude of these anomalies decreases monotonically towards the most enriched Samoan EM2 basalts. Similarly, a correlation exists between greater

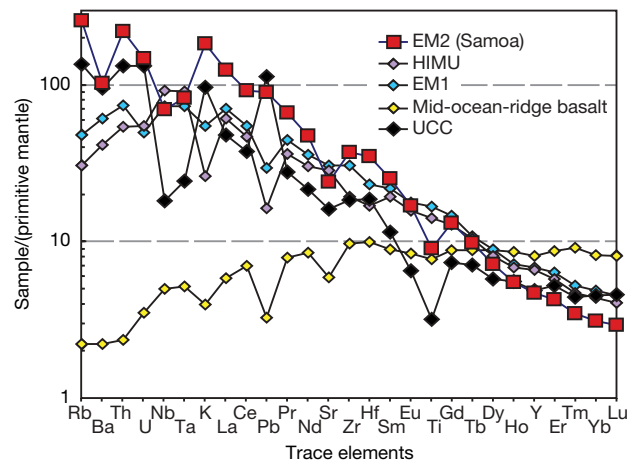


Figure 2 | Primitive-mantle-normalized²⁷ trace-element patterns for the Samoan EM2 endmember. The EM2 spidergram is the most isotopically enriched Samoan lava, sample D115-21 ($^{87}\text{Sr}/^{86}\text{Sr} = 0.720469$, $\text{Mg}\# = 57$). The other mantle endmembers (corrected to $\text{Mg}\#$ numbers of 60–62) and UCC¹⁷ are plotted for comparison. Similar to UCC, the Samoan EM2 lava exhibits large negative Ti and Nb (and Ta) anomalies and an excess of Pb (and K).

Pb enrichment and increasing isotopic enrichment in Samoan basalts. Importantly, the Eu anomaly is increasingly negative in the most isotopically enriched Samoan EM2 lavas (excluding basalts with $\text{MgO} < 6.5$ wt%), and the Rb/Sr and U/Pb are too low in the lower (or middle) continental crust¹⁷ to be consistent with the new Samoan Sr and Pb isotope data; these observations rule out the involvement of lower (or middle) continental crust. Furthermore, rare xenoliths with enriched $^{87}\text{Sr}/^{86}\text{Sr}$ and $^{143}\text{Nd}/^{144}\text{Nd}$ from the subcontinental lithospheric mantle⁹ suggest that this mantle domain can be isotopically enriched. However, the subcontinental lithospheric mantle does not appear to exhibit the trace-element anomalies observed in the most isotopically enriched Samoan lavas¹⁸. Instead, isotope ratios

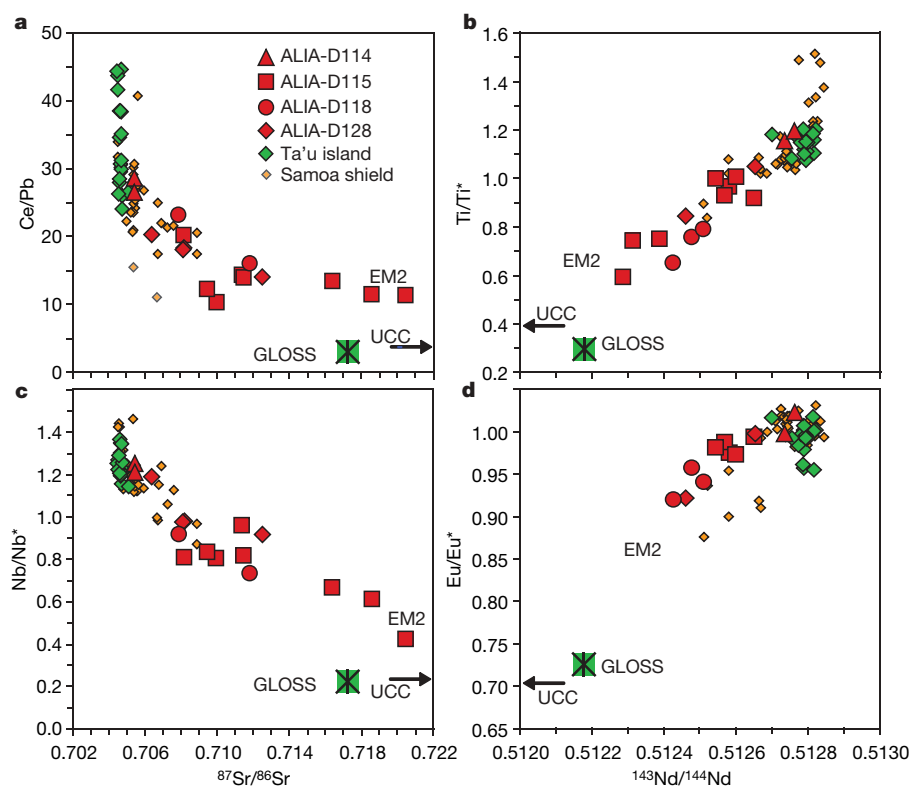


Figure 3 | $^{87}\text{Sr}/^{86}\text{Sr}$ and $^{143}\text{Nd}/^{144}\text{Nd}$ ratios suggest the presence of a UCC component in Samoan EM2 lavas. The $^{87}\text{Sr}/^{86}\text{Sr}$ and $^{143}\text{Nd}/^{144}\text{Nd}$ ratios are plotted against diagnostic UCC trace-element indicators in Samoan basalts: the more isotopically enriched Samoan basalts exhibit trace-element characteristics that are increasingly similar to UCC. UCC¹⁷ plots outside the panels, and its trace-element and isotopic composition is indicated by the level (and direction) of the arrows. **a–c**, All submarine Savai'i samples are plotted, as are other Samoan shield lavas with $\text{MgO} > 6.5$ wt%. **d**, Submarine Savai'i samples with $\text{MgO} < 6.5$ are excluded (avoiding possible effects of plagioclase fractionation). All trace-element data shown are by ICP-MS (inductively coupled plasma mass spectrometry). Element anomalies are calculated as follows (where subscript N means normalized to primitive mantle²⁷): $\text{Ti}/\text{Ti}^* = \text{Ti}_N / (\text{Nd}_N^{-0.0555} \times \text{Sm}_N^{0.333} \times \text{Gd}_N^{0.722})$; $\text{Nb}/\text{Nb}^* = \text{Nb}_N / \sqrt{(\text{Th}_N \times \text{La}_N)}$; $\text{Eu}/\text{Eu}^* = \text{Eu}_N / \sqrt{(\text{Sm}_N \times \text{Gd}_N)}$.

and trace-element anomalies (Nb, Ti, Eu and Pb) in Samoan basalts generate arrays that trend towards a composition similar to UCC.

We can exclude a shallow origin for the anomalous enrichment observed in the Samoan EM2 lavas. Owing to the close proximity of the Tonga trench, located only 120 km south of Savai'i, rapid cycling of sediment from the subduction zone into the Samoan plume was proposed as a mechanism for generating the extreme isotopic enrichment in Samoan lavas¹⁴. However, at the time that the submarine Savai'i lavas were erupted 5 Myr ago³¹, plate reconstructions indicate that the northern terminus of the Tonga trench was located 1,300 km to the west of Savai'i (ref. 19), and sediment input from the Tonga trench can be ruled out as a source of enrichment in these lavas.

Evidence from Pb isotopes suggests that it is unlikely that shallow-level contamination by modern marine sediments is responsible for the isotopic enrichment in the Samoan EM2 basalts. In $\Delta^{207}\text{Pb}/^{204}\text{Pb}$ – $\Delta^{208}\text{Pb}/^{204}\text{Pb}$ isotope space, Samoan basalts and global marine sediments¹ exhibit non-overlapping fields with diverging trends (Fig. 4). Moreover, three composite cores taken from the Samoan region, and a single ferromanganese crust from the flanks of Savai'i, plot in the global marine sediment field and exhibit no geochemical relationship with the extremely enriched Samoan lavas. It is also unlikely that the Samoan plume has been contaminated by stranded continental crust, such as was found beneath the Kerguelen plateau²⁰ and the southern Mid-Atlantic Ridge²¹, or by ancient limestone blocks like those discovered in the Romanche fracture zone²². The tectonic history of the Samoan region places it neither at the locus of continental rifting, which was responsible for the marooned Kerguelen and southern Atlantic continental blocks, nor in proximity to any Pacific fracture zones²³.

Large quantities of sediment derived from UCC have entered the mantle at subduction zones over geologic time¹, and such a reservoir is ideally suited as an enriched source for the Samoan plume. The array formed by the Samoan EM2 basalts in $^{143}\text{Nd}/^{144}\text{Nd}$ – $^{87}\text{Sr}/^{86}\text{Sr}$ isotope space is anchored on the depleted end by basalts from

Ta'u, one of the youngest, easternmost Samoan islands. The $^{143}\text{Nd}/^{144}\text{Nd}$ – $^{87}\text{Sr}/^{86}\text{Sr}$ array suggests mixing between this dominant, slightly depleted Ta'u component and a rare, enriched component that exhibits isotope and trace-element characteristics similar to UCC. The proportion of the enriched component in the Samoan EM2 lavas can be estimated by calculating trace-element concentrations in the depleted Ta'u mantle and mixing this composition with UCC (see Supplementary Discussion). A contribution of 5% UCC to the depleted Ta'u mantle generates a composition that, after mixing and melting, produces a trace-element pattern similar to that observed in Samoan EM2 sample D115-18 (with $^{87}\text{Sr}/^{86}\text{Sr}$ of 0.718592). Fixing the proportions of the depleted and UCC components in the Samoan EM2 source in this way then defines the $^{87}\text{Sr}/^{86}\text{Sr}$ and $^{143}\text{Nd}/^{144}\text{Nd}$ isotopic composition of this material as 0.7421 and 0.5117, respectively. The most isotopically enriched Samoan lavas have higher $^{87}\text{Sr}/^{86}\text{Sr}$ than the average continental crust inferred from suspended river sediments ($^{87}\text{Sr}/^{86}\text{Sr} \approx 0.716$; ref. 24) and global marine sediments (~ 0.717 ; ref. 1), values that are biased towards younger continental crust. However, composites of directly sampled ancient continental shield rocks show isotopically enriched compositions²⁵ that bracket the calculated composition of the recycled UCC sediment in the Samoan mantle. The new ultra-enriched EM2 lavas suggest an unusually enriched recycled protolith in the Samoan mantle.

Despite the large volumes of sediment entering the mantle at subduction zones (estimated at 0.5 – $0.7 \text{ km}^3 \text{ yr}^{-1}$; ref. 1), isotopic signatures associated with recycled UCC are rare in ocean island basalts²⁶. This enriched component is also uncommon in the Samoan plume, where the highly enriched Samoan EM2 lava D115-18 is calculated to have only 5% recycled UCC (and 95% depleted Ta'u source), and 90% of the remaining Samoan basalts exhibit depleted $^{143}\text{Nd}/^{144}\text{Nd}$ ratios (>0.512638). In addition to being rare in other ocean island basalts, recycled UCC may exist in low abundance in the Samoan plume. The reason for this may be that most subducted sediment melts and is rapidly returned to the surface in subduction zone volcanoes, or is simply scraped off onto the forearc and is never subducted. Alternatively, if a significant portion of UCC has been subducted over the past 4 Gyr (0.5 – $0.7 \text{ km}^3 \text{ yr}^{-1}$) and has survived subduction zone melting, the resulting accumulated reservoir in the mantle will constitute only $\sim 0.15\%$ of its mass. Such a small reservoir may be diluted by the ambient mantle after convective stirring, a mechanism that efficiently attenuates mantle heterogeneities. Therefore, recycled crustal signatures can be greatly diluted and difficult to detect. By contrast, the recycled UCC component in the Samoan plume is an anomalous survivor in a chaotic mantle.

Received 26 January; accepted 22 June 2007.

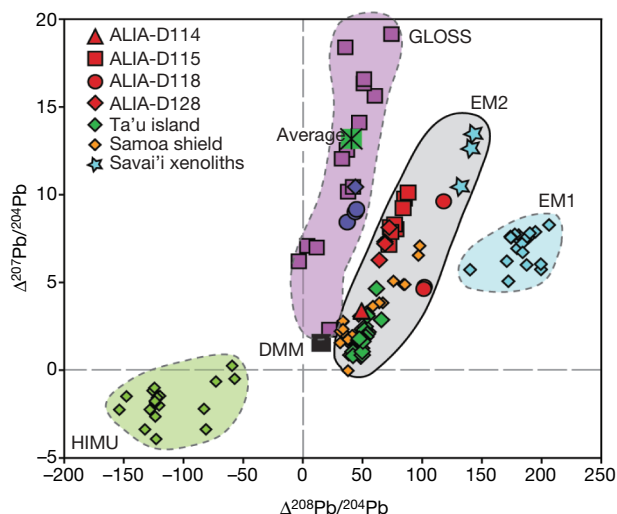


Figure 4 | ΔPb isotope compositions of Samoan lavas and marine sediment samples indicate that the Samoan EM2 lavas are not contaminated with modern marine sediment. Samoan basalts show no overlap with oceanic sediments contributing to GLOSS¹ (purple squares, where the GLOSS average composition is represented by a green crossed 'average' square), composite sections from three sediment cores taken in the Samoan region (blue circles), and a Samoan ferromanganese rind (blue diamond). Pb-isotope data for mantle endmembers DMM (using data from mid-ocean ridge basalt normal segments, as defined and catalogued by ref. 28), EM1 (Pitcairn), and HIMU (Mangaia and Tubuai) are from the literature (see Supplementary Information for reference citations). The use of ΔPb isotope notation²⁹ to identify sediment components in ocean island basalts is discussed elsewhere³⁰. All Samoan data shown are determined using a high-precision Tl-spike protocol⁷.

1. Plank, T. & Langmuir, C. H. The chemical composition of subducting sediments and its consequences for the crust and mantle. *Chem. Geol.* **145**, 325–394 (1998).
2. Allegre, C. J. & Turcotte, D. L. Geodynamic mixing in the mesosphere boundary layer and the origin of oceanic islands. *Geophys. Res. Lett.* **12**, 207–210 (1985).
3. Cohen, R. S. & O'Nions, R. K. Identification of recycled continental material in the mantle from Sr, Nd and Pb isotope investigations. *Earth Planet. Sci. Lett.* **61**, 73–84 (1982).
4. Hawkesworth, C. J., Norry, M. J., Roddick, J. C. & Vollmer, R. $^{143}\text{Nd}/^{144}\text{Nd}$ and $^{87}\text{Sr}/^{86}\text{Sr}$ ratios from the Azores and their significance in LIL-element enriched mantle. *Nature* **280**, 28–31 (1979).
5. White, W. M. & Hofmann, A. W. Sr and Nd isotope geochemistry of oceanic basalts and mantle evolution. *Nature* **296**, 821–825 (1982).
6. White, W. M. & Duncan, R. A. in *Earth Processes: Reading the Isotopic Code* (eds Basu, A. & Hart, S. R.) 183–206 (Geophys. Monogr. 95, AGU, Washington DC, 1996).
7. Workman, R. K. *et al.* Recycled metasomatized lithosphere as the origin of the Enriched Mantle II (EM2) endmember: evidence from the Samoan volcanic chain. *Geochim. Geophys. Geosyst.* **5**, doi:10.1029/2003GC000623 (2004).
8. Hofmann, A. W., Jochum, K. P., Seufert, M. & White, W. M. Nb and Pb in oceanic basalts: new constraints on mantle evolution. *Earth Planet. Sci. Lett.* **79**, 33–45 (1986).
9. Zindler, A. & Hart, S. R. Chemical geodynamics. *Annu. Rev. Earth Planet. Sci.* **14**, 493–571 (1986).

10. Hofmann, A. W. & White, W. M. Mantle plumes from ancient oceanic crust. *Earth Planet. Sci. Lett.* **57**, 421–436 (1982).
11. Chase, C. G. Oceanic island Pb: two-stage histories and mantle evolution. *Earth Planet. Sci. Lett.* **52**, 277–284 (1981).
12. Zindler, A., Jagoutz, E. & Goldstein, S. Nd, Sr and Pb isotopic systematics in a three-component mantle: a new perspective. *Nature* **298**, 519–523 (1982).
13. Weaver, B. L. The origin of ocean island basalt end-member compositions: Trace element and isotopic constraints. *Earth Planet. Sci. Lett.* **104**, 381–397 (1991).
14. Farley, K. A., Natland, J. H. & Craig, H. Binary mixing of enriched and undegassed (primitive?) mantle components (He, Sr, Nd, Pb) in Samoan lavas. *Earth Planet. Sci. Lett.* **111**, 183–199 (1992).
15. Wright, E. & White, W. M. The origin of Samoa: new evidence from Sr, Nd and Pb isotopes. *Earth Planet. Sci. Lett.* **82**, 151–162 (1987).
16. Hauri, E. H., Shimizu, N., Dieu, J. & Hart, S. R. Evidence for hotspot-related carbonatite metasomatism in the oceanic upper mantle. *Nature* **365**, 221–227 (1993).
17. Rudnick, R. L. & Gao, S. in *The Crust* (ed. Rudnick, R. L.) 1–64, Vol. 3 of *Treatise in Geochemistry* (Elsevier, Amsterdam, 2003).
18. McDonough, W. F. Constraints on the composition of the continental lithospheric mantle. *Earth Planet. Sci. Lett.* **101**, 1–18 (1990).
19. Hart, S. R. *et al.* Genesis of the Western Samoa seamount province: age, geochemical fingerprint and tectonics. *Earth Planet. Sci. Lett.* **227**, 37–56 (2004).
20. Frey, F. A., Weis, D., Borisova, A. Y. & Xu, G. Involvement of continental crust in the formation of the Cretaceous Kerguelen plateau: new perspectives from ODP Leg 201 sites. *J. Petrol.* **43**, 1207–1239 (2002).
21. Kamenetsky, V. S. *et al.* Remnants of Gondwanan continental lithosphere in oceanic upper mantle: evidence from the South Atlantic Ridge. *Geology* **29**, 243–246 (2001).
22. Bonatti, E. *et al.* Lower Cretaceous deposits trapped near the equatorial Mid-Atlantic Ridge. *Nature* **380**, 518–520 (1996).
23. Taylor, B. The single largest oceanic plateau: Ontong Java-Manihiki-Hikurangi. *Earth Planet. Sci. Lett.* **241**, 372–380 (2006).
24. Goldstein, S. J. & Jacobsen, S. B. Nd and Sr isotopic systematics of river water suspended material: implications for crustal evolution. *Earth Planet. Sci. Lett.* **87**, 249–265 (1988).
25. McCulloch, M. T. & Wasserburg, G. J. Sm–Nd and Rb–Sr chronology of continental crust formation. *Science* **200**, 1003–1011 (1978).
26. Hofmann, A. W. Mantle geochemistry: The message from oceanic volcanism. *Nature* **385**, 219–229 (1997).
27. McDonough, W. F. & Sun, S. S. The composition of the Earth. *Chem. Geol.* **120**, 223–253 (1995).
28. Su, Y. *Global MORB Chemistry Compilation at the Segment Scale*. Thesis, Columbia Univ. (2003).
29. Hart, S. R. A large-scale isotope anomaly in the Southern Hemisphere mantle. *Nature* **309**, 753–757 (1984).
30. Hart, S. R. Heterogeneous mantle domains: signatures, genesis and mixing chronologies. *Earth Planet. Sci. Lett.* **90**, 273–296 (1988).
31. Koppers, A. A. P., Russell, J. A., Jackson, M. G., Konter, J., Staudigel, H. & Hart, S. R. Samoa reinstated as a primary hotspot trail. *Geology* (submitted).

Supplementary Information is linked to the online version of the paper at www.nature.com/nature.

Acknowledgements We thank A. Hofmann and W. White for reviews. We thank N. Shimizu, R. Workman and R. Rudnick for discussions, and J. Natland for sharing unpublished data. This study was supported by National Science Foundation grants. We are grateful to the scientific party and ships crew of the R/V *Kilo Moana* for the success of the ALIA 2005 expedition (<http://earthref.org/ERESE/projects/ALIA/>).

Author Contributions M.G.J. performed most of the experimental work, developed the model and wrote the paper. S.R.H. and H.S. conceived the project, and were co-chiefs of the ALIA expedition. A.A.P.K. and J.K. were responsible for the cruise bathymetry, and A.A.P.K. greatly improved the figures. J.B. and M.K. provided analytical assistance and access to facilities. A.A.P.K., J.B., J.K. and J.A.R. helped with sample preparation. All authors participated in the discussion and interpretation of results, and commented on the manuscript.

Author Information Reprints and permissions information is available at www.nature.com/reprints. The authors declare no competing financial interests. Correspondence and requests for materials should be addressed to M.G.J. (mjackson@whoi.edu).

LETTERS

Implications of new early *Homo* fossils from Ileret, east of Lake Turkana, Kenya

F. Spoor¹, M. G. Leakey^{2,3}, P. N. Gathogo⁵, F. H. Brown⁵, S. C. Antón⁶, I. McDougall⁷, C. Kiarie⁸, F. K. Manthi⁸ & L. N. Leakey^{2,4}

Sites in eastern Africa have shed light on the emergence and early evolution of the genus *Homo*^{1–6}. The best known early hominin species, *H. habilis* and *H. erectus*, have often been interpreted as time-successive segments of a single anagenetic evolutionary lineage^{3,7–10}. The case for this was strengthened by the discovery of small early Pleistocene hominin crania from Dmanisi in Georgia that apparently provide evidence of morphological continuity between the two taxa^{11,12}. Here we describe two new cranial fossils from the Koobi Fora Formation, east of Lake Turkana in Kenya, that have bearing on the relationship between species of early *Homo*. A partial maxilla assigned to *H. habilis* reliably demonstrates that this species survived until later than previously recognized, making an anagenetic relationship with *H. erectus* unlikely. The discovery of a particularly small calvaria of *H. erectus* indicates that this taxon overlapped in size with *H. habilis*, and may have shown marked sexual dimorphism. The new fossils confirm the distinctiveness of *H. habilis* and *H. erectus*, independently of overall cranial size, and suggest that these two early taxa were living broadly sympatrically in the same lake basin for almost half a million years.

KNM-ER 42700 is a small, well preserved calvaria with an estimated geological age of 1.55 million years (Myr) (Fig. 1a–e; metrics in Supplementary Note 1.1). It is largely intact and suffered only minor postmortem damage and deformation, mainly to the frontal squama. Endocranial capacity, measured from computed tomography (CT) scans and corrected for deformation, is estimated at 691 cm³. The sphenoccipital synchondrosis is two-thirds fused. Thus, KNM-ER 42700 is a young adult or a late subadult, and full vault size had been attained, although growth in the supraorbital, mastoid and nuchal areas may not have fully ceased. In lateral view, the calvaria is ovoid rather than round in outline as a result of a sloping frontal, flattened parietal, and moderately angled occipital contour. In posterior view it is heptangular, with greatest breadth measured between the supra-mastoid crests. In superior view it is teardrop-shaped, with its greatest width posteriorly and a substantially smaller postorbital breadth anteriorly. The frontal bone exhibits a projecting glabella, uniformly thin supraorbital tori, shallow supratrochlear sulci divided by a flatter supraglabellar area, and a well developed frontal keel that continues as a sagittal keel onto the parietals. The occipital bone lacks an occipital torus. The temporal squama is low and gently convex. Near its mastoid angle, the parietal bone shows a slight longitudinal swelling in association with the faint superior temporal line, which can be interpreted as an incipient angular torus. The mandibular fossa is deep but small, with well developed postglenoid and entoglenoid processes, the latter formed by the temporal bone, not the sphenoid. The tympanic is coronally oriented (tympanomedian angle², 100°),

whereas the petrous portion of the temporal is more sagittally oriented (petromedian angle², 34°). The tympanic shows a faint petrous crest, which is well anterior (8 mm) to the short, slender mastoid process. CT imaging reveals a relatively thin cranial vault, a small frontal sinus, a well developed sphenoid sinus, and a flexed cranial base (basion–sella–foramen caecum angle, 138°).

Although it is closer in overall size to *H. habilis* (Supplementary Note 1.1), we assign KNM-ER 42700 to *H. erectus*. Features suggesting this attribution include frontal and parietal keeling, the medio-laterally narrow temporomandibular joint, the distinct coronal and sagittal orientation of the tympanic and petrous elements, respectively, and a posterior midsagittal profile with a low occipital upper scale and opisthocranium positioned close to lambda (Supplementary Note 1.3). A multivariate analysis of calvarial dimension confirms the affinities of KNM-ER 42700 with *H. erectus* (Fig. 2a and Supplementary Note 2.1.1). Some characters often considered diagnostic of this species (for example, a thick cranial vault and supraorbital torus, and strong occipital angulation) are lacking in KNM-ER 42700, but scaling analyses of *H. erectus* and *H. habilis* crania suggest that these features scale allometrically with cranial size¹³, and in any event do not clearly differentiate the two taxa (Supplementary Note 2.1.2). In external dimensions, KNM-ER 42700 is the smallest known adult cranial vault attributed to *H. erectus*. In overall appearance it is similar to, but slightly smaller than, the juvenile D2700 cranium from Dmanisi¹⁴ (Supplementary Note 1.1). Its relatively high vault and divided supraorbital tori are features shared with specimen Sm3 from Sambungmacan (Indonesia), which is geologically much younger¹⁵.

KNM-ER 42703 is a right maxilla, with an estimated age of 1.44 Myr. It includes parts of the palatine and zygomatic processes and most of the alveolar process, with teeth C to M³ (Fig. 1f–h). The nasal sill and the anterior alveolar wall of the incisors and canine are largely missing, but anterior parts of the alveolar and palatine processes are sufficiently preserved to indicate the midline. Dimensions estimated by mirror-imaging the right side indicate a relatively wide and shallow palate (Supplementary Note 1.2). The zygomatic process is robust, with its anterior and posterior surfaces 25 mm apart, positioned between P⁴/M¹ and M²/M³, respectively. In anterior view, the process has a high, gently curved inferior margin, which becomes horizontal above the level of the canine root apex and the inferred nasal floor. The dental crowns exhibit heavy occlusal and interproximal wear as well as postmortem weathering. Little or no cusp morphology is present, and preserved crown diameters are therefore minimum values only (Supplementary Note 1.2). The canine has a large root (cervix 8.0 mm mesiodistally, 10.0 mm labiolingually, length labially 29 mm). Both premolars have a buccal and a mesial root. The molar shape is rectangular, rather than the derived

¹Department of Anatomy and Developmental Biology, University College London, Gower Street, London WC1E 6BT, UK. ²Koobi Fora Research Project, PO Box 24926 Nairobi 00502, Kenya. ³Department of Anatomical Sciences, ⁴Department of Anthropology, Stony Brook University, Stony Brook, New York 11794, USA. ⁵Department of Geology and Geophysics, University of Utah, Salt Lake City, Utah 84112, USA. ⁶Department of Anthropology, New York University, New York, New York 10003, USA. ⁷Research School of Earth Sciences, Australian National University, Canberra, ACT 0200, Australia. ⁸Division of Palaeontology, National Museums of Kenya, Nairobi 00100, Kenya.

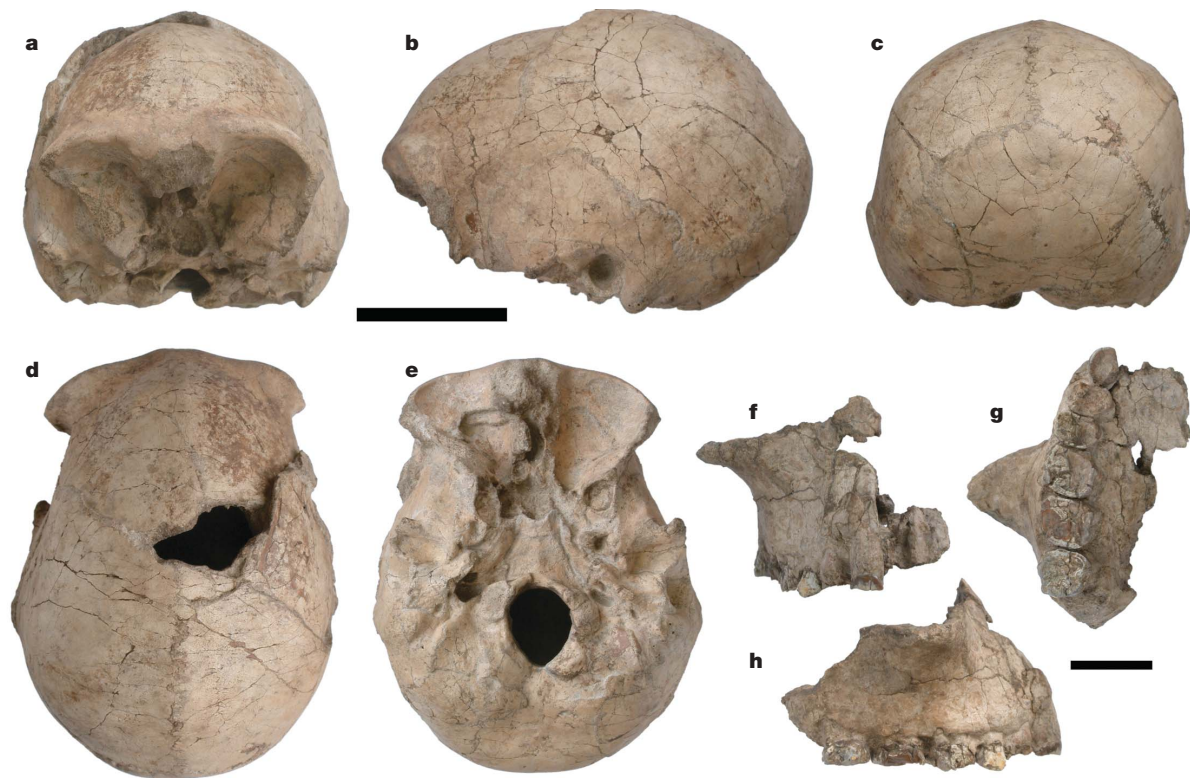


Figure 1 | The KNM-ER 42700 calvaria and KNM-ER 42703 partial maxilla. **a**, Anterior, **b**, left lateral, **c**, posterior, **d**, superior and **e**, inferior views of

KNM-ER 42700 (scale bar, 5 cm). **f**, Anterior, **g**, occlusal and **h**, right lateral views of KNM-ER 42703 (scale bar, 2 cm).

asymmetrical rhomboidal crown outline seen in some specimens of early *Homo* and in the M^2 and M^3 of *H. erectus*, in particular.

A multivariate analysis of maxillary molar dimensions clearly separates *H. erectus* and *H. habilis* specimens, with the former having smaller molars overall, as well as a mesiodistally shorter M^3 (Fig. 2b, Supplementary Note 2.2). Given this distinction, the affinities of KNM-ER 42703 are with *H. habilis*, and overall morphology is closest to the larger specimens attributed to this species that are dated to over 1.8 Myr ago (KNM-ER 1805, OH 65)^{6,16}. KNM-ER 42703 and the other *H. habilis* (*sensu stricto*) maxillae lack the derived morphology of the *H. rudolfensis* lectotype KNM-ER 1470, which has anteriorly placed and forwardly sloping zygomatic processes.

The small size of KNM-ER 42700 indicates that *H. erectus* showed substantial size variation throughout the early Pleistocene. Thus, the *H. erectus* crania from Dmanisi cannot be argued to be primitive, or transitional between *H. habilis* and *H. erectus*, on the basis of their small size or of size-dependent characters alone. The intraspecific variation of vault size in *H. erectus*, including KNM-ER 42700, is larger than in extant humans and chimpanzees, but smaller than in gorillas (Supplementary Note 2.1.3). This degree of variation may well imply that *H. erectus* showed marked sexual dimorphism, rather than the reduced levels that characterize the derived condition in *H. sapiens* (*contra ref. 17*).

The presence of supposedly distinctive 'Asian' characters¹⁸, such as cranial vault keeling and a well separated petrous crest and mastoid process in KNM-ER 42700, underscores the difficulty in separating the African and Asian hypodigms of *H. erectus*¹⁹. This difficulty is further accentuated by the observation that the more angulated occipitals and the thicker vaults and supraorbital tori seen in Asian *H. erectus* are allometric consequences of an increase in cranial size, rather than independent characters (Supplementary Note 2.1.2).

With the discovery of the new, well dated specimens from Ileret, *H. habilis* and *H. erectus* can now be shown to have co-occurred in eastern Africa for nearly half a million years. Previously, the most recent occurrence of *H. habilis* was at 1.65 Myr ago or older (OH 13, Supplementary Note 3)^{20–22}. KNM-ER 42703 now provides a reliable and substantially younger age of 1.44 Myr. The earliest occurrence of specimens with affinities to *H. habilis* is at approximately 2.33 Myr ago at Hadar (A.L. 666)⁴, but *H. habilis* (*sensu stricto*) first appears in eastern Africa at about 1.9 Myr ago (for example, OH 24)^{21,23}. Diagnostic evidence of *H. erectus* appears in the African record at about the same time (that is, KNM-ER 2598)^{2,16}, and the youngest African fossils attributed to that taxon are dated to circa 1.0 Myr ago (for example, OH 12, Daka, KNM-OG 45500)^{19,24,25}.

Although some characters previously regarded as diagnostic of *H. erectus* differ from *H. habilis* simply on the basis of overall cranial size (Supplementary Note 2.1.2), the two taxa are nonetheless

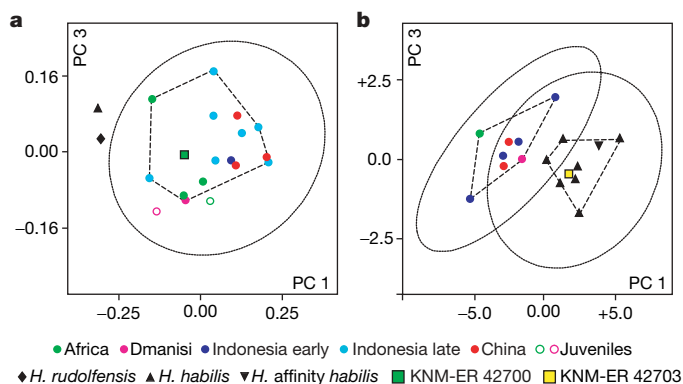


Figure 2 | Comparisons of early *Homo* calvariae and upper molars. Principal component analyses showing plots of principal components (PC) 3 against 1. **a**, Using ten size-corrected calvarial dimensions. KNM-ER 42700 falls within the convex hull (dashed line) and 95% confidence ellipse of *H. erectus*, but falls away from the *H. habilis* and *H. rudolfensis* specimens. **b**, Using mesiodistal and buccolingual size of M^1 to M^3 . KNM-ER 42703 falls within the convex hull (dashed line) and 95% confidence ellipse of *H. habilis*, but falls outside those of *H. erectus*. Details can be found in Supplementary Notes 2.1.1 and 2.2.

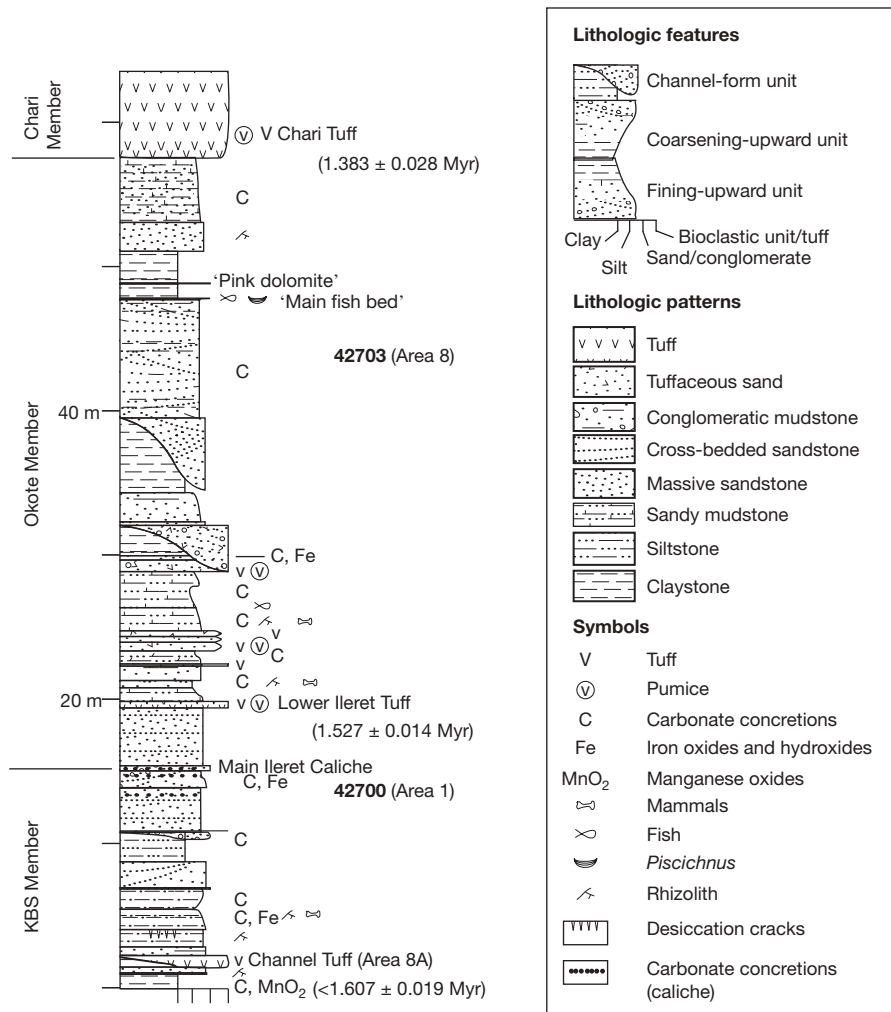


Figure 3 | A composite stratigraphic section of strata in the Ileret area. Components are taken from sections PNG-06A and PNG-08A of ref. 27, adding only the Chari Tuff to section PNG-06A. $^{40}\text{Ar}/^{39}\text{Ar}$ ages are from ref.

metrically and nonmetrically distinguishable throughout their lengthy co-occurrence through time. Moreover, during this period of nearly half a million years the dento-gnathic morphology of *H. habilis* shows relatively little change. The long period of sympatry suggests the existence of some form of niche differentiation between *H. erectus* and *H. habilis*, one that may have included foraging or dietary differences. Taken together, these new fossil data highlight that an anagenetic relationship between the two taxa is implausible⁹. As the earliest secure evidence of *Homo* is found outside the known region of overlap⁴, it is nonetheless possible that *H. erectus* evolved from *H. habilis* elsewhere, and that the Turkana basin was a region of secondary contact between the two hominin taxa.

METHODS

Both hominins were found during fieldwork in 2000 at Ileret (north-eastern Kenya). They lie between the KBS Tuff (1.869 ± 0.021 Myr)²⁶ and the Chari Tuff (1.383 ± 0.028 Myr)²⁶; the age of the Lower Ileret Tuff (1.527 ± 0.014 Myr)²⁶ provides additional chronological control. We estimate an age of 1.54 Myr for the Main Ileret Caliche (Fig. 3), and 1.60 Myr for tuff IL02-043, assuming a linear sediment accumulation rate between the KBS Tuff and the Lower Ileret Tuff²⁷. IL02-043 correlates with a tuff in Submember J-5 of the Shungura Formation²⁸, so it must be slightly younger than the Morutot Tuff, which has an arithmetic mean age of 1.607 ± 0.019 Myr (ref. 26).

KNM-ER 42700 was found *in situ* in 'Area 1' by F.K.M. Almost fully embedded in a matrix of coarse sandstone and carbonates, only

26. The placement of calvaria KNM-ER 42700 and partial maxilla KNM-ER 42703 are shown. Section in meters (m).

a small area of the right temporal bone and of the right supraorbital torus was exposed. This specimen was recovered from strata above IL02-043, and 1.5 m below the Main Ileret Caliche. Therefore its age is between 1.53 and 1.61 Myr, probably within the interval 1.55 ± 0.01 Myr, assuming constant sedimentation rates between IL02-043 and the Main Ileret Caliche.

KNM-ER 42703 was found by John E. Kaatho in Area 8. It was *ex situ*, coated in carbonate matrix, on the brown mudstone and sandstone sequences between the Lower Ileret Tuff and the Chari Tuff. Assuming constant sedimentation rates between these dated levels, the probable age is 1.44 ± 0.01 Myr. This is consistent with the age of the 'Main fish bed', estimated to have formed at about 1.42 Myr ago (ref. 28), and also with the youngest measured ages (1.476 ± 0.013 Myr) of materials from the Okote Tuff Complex at Koobi Fora²⁶.

Received 12 March; accepted 5 June 2007.

1. Leakey, M. G. & Leakey, R. E. *Koobi Fora Research Project Vol. 1 The Fossil Hominids and an Introduction to their Context 1968–1974* (Clarendon, Oxford, 1978).
2. Wood, B. *Koobi Fora Research Project Vol. 4 Hominid Cranial Remains* (Clarendon, Oxford, 1991).
3. Tobias, P. V. *Olduvai Gorge Vol. 4 The Skulls and Endocasts of Homo habilis* (Cambridge Univ. Press, Cambridge, 1991).
4. Kimbel, W. H., Johanson, D. C. & Rak, Y. Systematic assessment of a maxilla of *Homo* from Hadar, Ethiopia. *Am. J. Phys. Anthropol.* **103**, 235–262 (1997).
5. Bromage, T. G., Schrenk, F. & Zonneveld, F. W. Paleanthropology of the Malawi Rift: an early hominid mandible from the Chiwondo Beds, northern Malawi. *J. Hum. Evol.* **28**, 71–108 (1995).

6. Blumenschine, R. J. *et al.* Late Pliocene *Homo* and hominid land use from western Olduvai Gorge, Tanzania. *Science* **299**, 1217–1221 (2003).
7. Howell, F. C. in *The Cambridge History of Africa* Vol. 1 *From the earliest times to c. 500 BC* (ed. Clark, J. D.) 70–156 (Cambridge Univ. Press, Cambridge, 1982).
8. Tobias, P. V. in *Hominidae* (ed. Giacobini, G.) 141–149 (Jaca Books, Milan, 1989).
9. Kimbel, W. H. Species, species concepts and hominid evolution. *J. Hum. Evol.* **20**, 355–371 (1991).
10. Tattersall, I. Paleoanthropology: the last half-century. *Evol. Anthropol.* **9**, 2–16 (2000).
11. Vekua, A. *et al.* A new skull of early *Homo* from Dmanisi, Georgia. *Science* **297**, 85–89 (2002).
12. de Lumley, M. A., Gabounia, L., Vekua, A. & Lordkipanidze, D. Human remains from the Upper Pliocene–Early Pleistocene Dmanissi site, Georgia (1991–2000). Part I. The fossil skulls (D 2280, D 2282 and D 2700). *L'Anthropol.* **110**, 1–110 (2006).
13. Antón, S. C., Spoor, F., Fellmann, C. D. & Swisher, C. C. III. in *Handbook of Paleoanthropology* Vol. 3 (eds Henke, W. & Tattersall, I.) 1655–1693 (Springer, Heidelberg, 2007).
14. Rightmire, G. P., Lordkipanidze, D. & Vekua, A. Anatomical descriptions, comparative studies and evolutionary significance of the hominin skulls from Dmanisi, Republic of Georgia. *J. Hum. Evol.* **50**, 115–141 (2006).
15. Márquez, S., Mowbray, K., Sawyer, G. J., Jacob, T. & Silvers, A. New fossil hominid calvaria from Indonesia—Sambungmacan 3. *Anat. Rec.* **262**, 344–368 (2001).
16. Feibel, C. S., Brown, F. H. & McDougall, I. Stratigraphic context of fossil hominids from the Omo groups deposits: northern Turkana Basin, Kenya and Ethiopia. *Am. J. Phys. Anthropol.* **78**, 595–622 (1989).
17. Aiello, L. C. & Key, C. Energetic consequences of being a *Homo erectus* female. *Am. J. Hum. Biol.* **14**, 551–565 (2002).
18. Andrews, P. An alternative interpretation of the characters used to define *Homo erectus*. *Cour. Forsch. Inst. Senckenberg* **69**, 167–175 (1984).
19. Asfaw, B. *et al.* Remains of *Homo erectus* from Bouri, Middle Awash, Ethiopia. *Nature* **416**, 317–320 (2002).
20. Leakey, M. D. *Olduvai Gorge* Vol. 3 *Excavations in Beds I and II* 1960–1963 (Cambridge Univ. Press, Cambridge, 1971).
21. Hay, R. L. *Geology of Olduvai Gorge* (Univ. California Press, Berkeley, 1976).
22. Manega, P. C. *Geochronology, Geochemistry, and Isotopic Study of Plio-Pleistocene Hominid Sites and the Ngorongoro Volcanic Highlands in Northern Tanzania*. PhD thesis, Univ. Colorado (1993).
23. Walter, R. C., Manega, P. C., Hay, R. L., Drake, R. E. & Curtis, G. H. Laser-fusion $^{40}\text{Ar}/^{39}\text{Ar}$ dating of Bed I, Olduvai Gorge, Tanzania. *Nature* **354**, 145–149 (1991).
24. Antón, S. C. The face of Olduvai Hominid 12. *J. Hum. Evol.* **46**, 337–347 (2004).
25. Potts, R., Behrensmeyer, A. K., Deino, A., Ditchfield, P. & Clark, J. Small Mid-Pleistocene hominin associated with East African Acheulean technology. *Science* **305**, 75–78 (2004).
26. McDougall, I. & Brown, F. H. Precise $^{40}\text{Ar}/^{39}\text{Ar}$ geochronology for the upper Koobi Fora Formation, Turkana Basin, northern Kenya. *J. Geol. Soc. Lond.* **163**, 205–220 (2006).
27. Gathogo, P. N. & Brown, F. H. Stratigraphy of the Koobi Fora Formation (Pliocene and Pleistocene) in the Ileret region of northern Kenya. *J. Afr. Earth Sci.* **45**, 369–390 (2006).
28. Brown, F. H., Haileab, B. & McDougall, I. Sequence of tuffs between the KBS Tuff and the Chari Tuff in the Turkana Basin, Kenya and Ethiopia. *J. Geol. Soc. Lond.* **163**, 185–204 (2006).

Supplementary Information is linked to the online version of the paper at www.nature.com/nature.

Acknowledgements We thank the government of Kenya for permission to carry out this research, and the National Museums of Kenya and E. Mbua for support. The National Geographic Society funded the field work. We thank R. Blumenschine, R. Clarke, C. Dean, A. Deino, C. Feibel, Ø. Hammer, J. Harris, L. Humphrey, N. Jeffery, W. Kimbel, R. Kruszynski, K. Kupczik, D. Lieberman, C. Lockwood, D. Lordkipanidze, J. Moggi-Cecchi, S. Muteti, Ph. Rightmire, B. Sokhi, C. Swisher, A. Walker and B. Wood for their help. Caltex (Kenya) provided fuel for the field expeditions, and R. Leakey allowed us to use his aeroplane. The field expedition members included R. Bobe, G. Ekalale, C. Epaat, M. Eregei, J. Erus, J. Kaatho, S. Labun, R. Lorinyok, B. Malika, S. Muge, S. Muteti, D. Mutinda and N. Mutiwa.

Author Information Reprints and permissions information is available at www.nature.com/reprints. The authors declare no competing financial interests. Correspondence and requests for materials should be addressed to F.S. (f.spoor@ucl.ac.uk) or M.G.L. (meaveleakey@uuplus.com).

LETTERS

Low beta diversity of herbivorous insects in tropical forests

Vojtech Novotny¹, Scott E. Miller², Jiri Hulcr^{1,3}, Richard A. I. Drew⁴, Yves Basset⁵, Milan Janda¹, Gregory P. Setliff⁶, Karolyn Darrow², Alan J. A. Stewart⁷, John Auga⁸, Brus Isua⁸, Kenneth Molem⁸, Markus Manumbor⁸, Elvis Tamtiai⁸, Martin Mogia⁸ & George D. Weiblen⁹

Recent advances in understanding insect communities in tropical forests^{1,2} have contributed little to our knowledge of large-scale patterns of insect diversity, because incomplete taxonomic knowledge of many tropical species hinders the mapping of their distribution records³. This impedes an understanding of global biodiversity patterns and explains why tropical insects are under-represented in conservation biology. Our study of approximately 500 species from three herbivorous guilds feeding on foliage (caterpillars, Lepidoptera), wood (ambrosia beetles, Coleoptera) and fruit (fruitflies, Diptera) found a low rate of change in species composition (beta diversity) across 75,000 square kilometres of contiguous lowland rainforest in Papua New Guinea, as most species were widely distributed. For caterpillars feeding on large plant genera, most species fed on multiple host species, so that even locally restricted plant species did not support endemic herbivores. Large plant genera represented a continuously distributed resource easily colonized by moths and butterflies over hundreds of kilometres. Low beta diversity was also documented in groups with differing host specificity (fruitflies and ambrosia beetles), suggesting that dispersal limitation does not have a substantial role in shaping the distribution of insect species in New Guinea lowland rainforests. Similar patterns of low beta diversity can be expected in other tropical lowland rainforests, as they are typically situated in the extensive low basins of major tropical rivers similar to the Sepik–Ramu region of New Guinea studied here.

Locally coexisting species (alpha diversity) represent a large proportion of the regional species pool (gamma diversity) for many of the few tropical insect taxa for which distributions are known^{4–6}. For instance, a single lowland rainforest site hosted 37% of all butterfly species of Borneo⁶; another hosted 40% of all taxonomically described fruitfly species of Papua New Guinea⁴. This pattern, implying a low rate of spatial change in species composition (beta diversity), is at variance with the high beta diversity of samples obtained from tropical forest canopies where a majority of species occur at single sites⁷. Overestimates of beta diversity can result from inadequate sampling of numerous rare species. On the other hand, relying on the taxonomically known species might underestimate the extent of beta diversity, as widespread species tend to be described first⁸. Quantitative studies of insect communities replicated on a regional scale are needed to resolve the debate.

Beta diversity of tropical herbivores has been examined in relation to latitudinal, altitudinal, disturbance and climatic gradients^{3,9,10}. Not surprisingly, these studies confirmed high species turnover among

sites as they comprised very different vegetation types. Even so, the relative influence of plant species composition, herbivore host specificity, or herbivore dispersal on the large-scale distribution of tropical insects remains unknown. Such knowledge is needed to understand the roles of historical and contemporary ecological processes in maintaining tropical diversity¹¹, to predict species extinction after habitat fragmentation, and to design systems of protected natural areas¹².

We sampled ~75,000 caterpillars (Lepidoptera) from 370 species feeding on plant species from four diverse genera (*Ficus*, *Psychotria*, *Syzygium* and *Macaranga*) across eight sites situated within a 500 × 150 km matrix of contiguous, largely undisturbed lowland rainforest in Papua New Guinea (Fig. 1). Study sites were evenly distributed across the Ramu and Sepik river basins and are characterized by relatively uniform altitude, climate, soil and vegetation. The comparison of caterpillar communities across a matrix of host plant species and sites represents the first attempt to assess insect beta diversity while controlling for the effects of host plant availability, altitude, rainfall, and habitat type and fragmentation. This survey was partially replicated using ambrosia beetles (Coleoptera: Scolytinae and Platypodinae) collected from four tree species at three sites, and fruitflies (Diptera: Tephritidae) attracted to lure traps from diverse rainforest vegetation at four sites.

The four plant genera were represented by 175 species across the study area (Supplementary Appendix 1). Similarity in species composition between the study sites was very high for *Ficus* and low for *Psychotria* and *Syzygium*, but in neither case did similarity decline significantly with distance between the sites. Decay of similarity in species composition was significant only for *Macaranga* (Fig. 2a and Supplementary Table 1). Similarity of caterpillar communities feeding on a particular plant species declined significantly with distance between sites in nine of the eighteen plant species sampled for herbivores. Similarity decreased gradually with geographical distance so that the proportion of species shared between sites remained >50% for distances up to 500 km (Fig. 2b and Supplementary Table 1). Likewise, samples of ambrosia beetles reared from particular plant species shared >60% of species (Fig. 2c) and fruitfly communities remained virtually constant (Fig. 2d) for distances up to 950 km.

The insect species collected at each study site were compared with the species pool known to occur in a 20 × 30 km area also including the town of Madang (Fig. 1). This is a relatively well-known regional fauna at the eastern boundary of our study area, intensely studied for >10 yr^{4,13,14}. The proportion of caterpillar species recorded from

¹Biology Center of the Czech Academy of Sciences and School of Biological Sciences, University of South Bohemia, Branisovska 31, 370 05 Ceske Budejovice, Czech Republic. ²National Museum of Natural History, Smithsonian Institution, Washington DC 20013-7012, USA. ³Department of Entomology, Michigan State University, 243 Natural Science, East Lansing, Michigan 48824, USA. ⁴Australian School of Environmental Studies, Griffith University, Nathan Campus, Brisbane, Queensland 4111, Australia. ⁵Smithsonian Tropical Research Institute, Apartado 0843-03092, Balboa, Ancon, Panama. ⁶Department of Entomology, University of Minnesota, 219 Hodson Hall, 1980 Folwell Avenue, Saint Paul, Minnesota 55108, USA. ⁷School of Life Sciences, University of Sussex, Brighton BN1 9QG, UK. ⁸New Guinea Binatang Research Center, PO Box 604 Madang, Papua New Guinea. ⁹Bell Museum of Natural History and Department of Plant Biology, University of Minnesota, 250 Biological Sciences Center, 1445 Gortner Avenue, Saint Paul, Minnesota 55108-1095, USA.

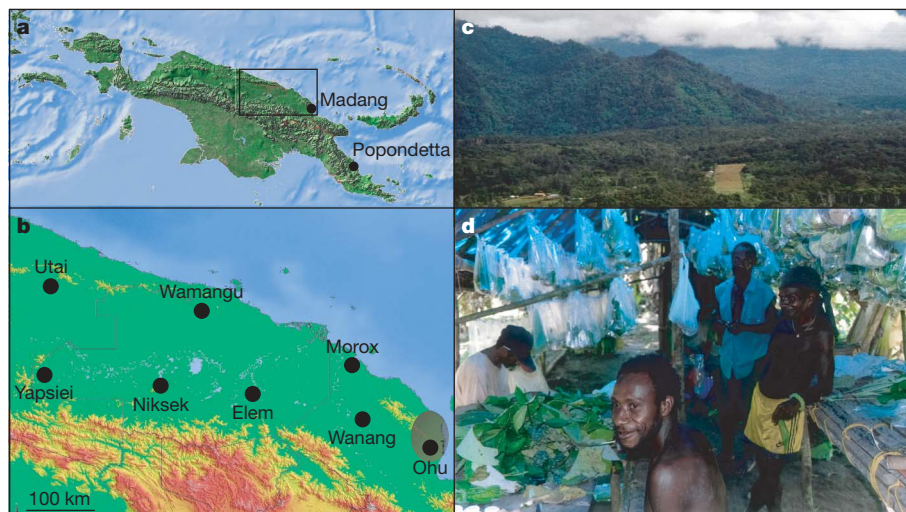


Figure 1 | Study sites and field techniques of insect rearing. **a**, The study is located in the basins of the Sepik and Ramu rivers within a 75,000 km² area of lowland terrain with continuous rainforest and wetland vegetation, and at an additional site (Popondetta) in the Papuan Peninsula. **b**, The location of eight lowland (<500 m above sea level) rainforest study sites with pair-wise

distances ranging from 59 to 513 km. Madang area, including also the Ohu site, is marked by an ellipse. **c**, A typical study site (Yapsiei) including a village with an airstrip surrounded by large tracts of rainforest. **d**, A field laboratory rearing caterpillars at one of the study sites.

each site also known from Madang decreased linearly with distance from Madang. However, the slope of the relationship was low so that even the samples 500 km from Madang included >60% of Madang species. All samples of ambrosia beetles and fruitflies comprised >75% of species known also from the Madang area, irrespective of their distance from that area (Fig. 3).

The probability $C(d)$ of two caterpillars drawn at random from the same host species d kilometres apart belonging to the same species (Supplementary Fig. 1) is strongly influenced by common species and, as such, measures the turnover of dominant species between communities, a different aspect of beta diversity than the proportion of shared species. There was no decline in $C(d)$ with distance for $d = 59\text{--}513$ km. The values reported here (>0.1) are remarkably high, particularly when compared with neotropical rainforest tree communities where $C(d) < 0.01$ (ref. 15).

Hubbell's neutral model¹⁶, where only dispersal and speciation affect species distribution, predicts that $C(d)$ declines linearly with log-distance over a wide range of distances. This relationship was shown for rainforest tree communities¹⁵. The lack of a distance effect on $C(d)$ suggests that dispersal limitation may not be important in structuring caterpillar communities at this spatial resolution. The weak effect of distance on community similarity is consistent with the broad distribution of species across the study area. Most of the species sufficiently abundant for analysis were collected at the majority of study sites not only for caterpillars but also for ambrosia beetles and fruitflies (Fig. 4 and Supplementary Fig. 2).

The Sepik, a major tropical river representing the only large discontinuity in the rainforest ecosystem of the study area, is probably not a barrier to lepidopteran dispersal as there was no difference in similarity between caterpillar samples taken on either side of the river

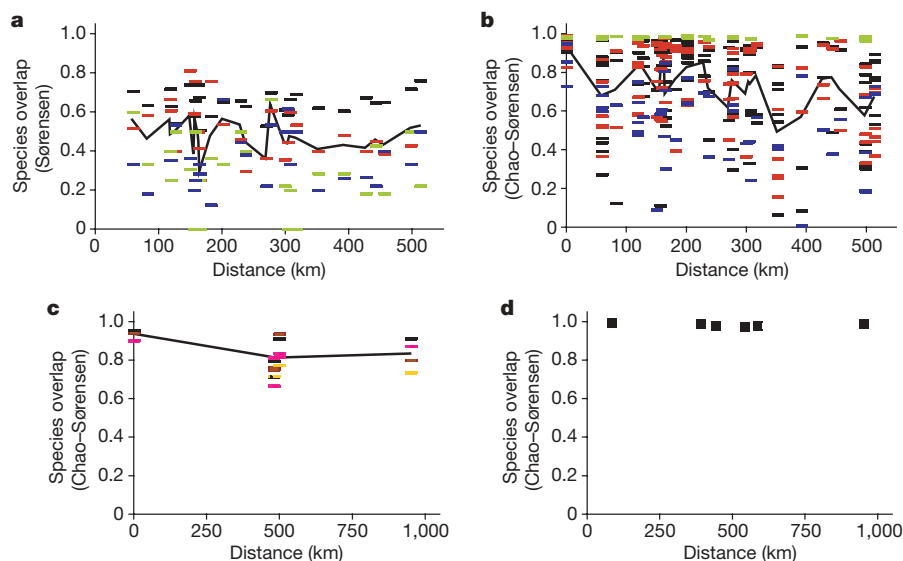


Figure 2 | Similarity of plant, caterpillar, ambrosia beetle and fruitfly assemblages as a function of geographical distance. **a**, Sørensen similarity of species composition in each of four plant genera among all possible pairs of study sites is shown. **b**, **c**, Chao-Sørensen similarity for caterpillar (**b**) and ambrosia beetle (**c**) assemblages feeding on particular plant species is shown for all plant species at all possible pairs of sites where they were sampled.

d, Chao-Sørensen similarity for fruitflies from diverse forest vegetation is shown for all possible pairs of study sites. Markers denote host species of *Ficus* (black), *Macaranga* (red), *Psychotria* (green), *Syzygium* (blue), *Artocarpus* (brown), *Leea* (yellow), *Nauclea* (violet) and mixed forest vegetation (solid squares). Lines connect average values in different distance categories. Methods and Supplementary Table 2 list the plant species.

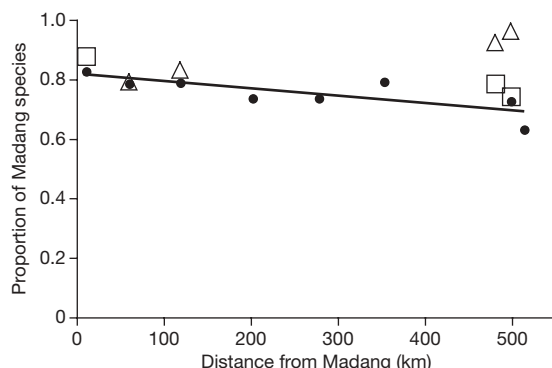


Figure 3 | Overlap in species composition between the Madang regional species pool and insect assemblages at each of the study sites as a function of their distance from Madang. The proportion of species known to occur also in the Madang area is reported for the caterpillar communities feeding on four plant genera (filled circles), ambrosia beetles feeding on four plant species (open squares) and fruitfly species sampled from diverse forest vegetation (open triangles) at each of the study sites. The regression line was fitted to data on caterpillars only (Pearson $r = 0.78$, $P < 0.01$, $n = 8$ sites).

(Chao–Sørensen index 0.79 ± 0.05) when compared to equidistant sites on the same side of the river (0.78 ± 0.04 , paired t -test, $P > 0.8$, $N = 19$). The importance of large rivers as barriers to dispersal in lowland rainforests continues to be debated, as the evidence is equivocal at least in the Amazon Basin^{17,18}.

Contemporary estimates of beta diversity can be placed in the context of historical changes in climate, topography and vegetation. Our study area is characterized by complex geological history, sea incursions and vegetation change (see Methods). The broad geographical distribution of insect herbivores suggests that herbivorous insects effectively track their plant resources even across such a very dynamic landscape.

Host specificity was not correlated with geographical distribution in Lepidoptera (Fig. 4). This is probably because most Lepidoptera were clade specialists feeding on multiple congeneric plant species as opposed to feeding on only a single host species. The maximum possible geographical span for a particular herbivore species is a function of the combined distributions of all recorded hosts. It amounted to the entire 500-km span for all common lepidopteran species analysed, so that the potential distribution of Lepidoptera was not limited by the distribution of particular host plant species (Supplementary Results).

Plant species with limited geographical distribution did not support many specialized herbivores. Although four out of five *Psychotria* species sampled for caterpillars had restricted distributions (Supplementary Table 2), all were dominated by one or more of only three crambid species together representing 66–99% of all caterpillars feeding on *Psychotria* at each site. This is illustrative of a general pattern, as there was no correlation between the geographical

distribution of particular host species and the average geographical distribution of their lepidopteran herbivores (Supplementary Fig. 3).

The number of lepidopteran species (S) increases as a power function of the number of hosts and the number of sites: $\log S = a + b \log(\text{host species}) + c \log(\text{sites})$ (Supplementary Fig. 4). This simple model combines a power function describing species–area relationships¹⁹ and another describing the accumulation of herbivore species with increasing host plant diversity¹⁴, enabling the prediction of herbivore species richness on diverse vegetation across geographical areas.

This report of low insect beta diversity across a large area of tropical forest points to the need for comparative data from other major forest ecosystems. Species range sizes are known to decrease with latitude in various taxa, implying higher beta diversity in the tropics (Rapoport's rule), but this trend has yet to be documented in insects²⁰.

Large plant genera represent a continuous resource for caterpillars that is readily colonized across large areas of lowland rainforests. Ambrosia beetles and fruitflies also exhibited low beta diversity, such that dispersal limitation seems to be unimportant for at least three herbivore guilds up to distances of 500–1,000 km. Insect species were broadly distributed across habitat discontinuities such as large rivers, and across historically disjunct geological terranes. A complete description of beta diversity need be supplemented by data on specialized herbivores from species-poor plant genera with limited geographical distribution, as these might produce higher estimates of beta diversity. For instance, most of the >700 monotypic genera in the flora of New Guinea²¹ have poorly known geographical distributions and herbivore communities. Furthermore, we only studied relatively common species of trees. This bias may not be serious, because at least host specificity, one of the potential determinants of beta diversity, showed no relationship with the local abundance of host plants²². Rare insect species and their contribution to beta diversity are also a concern, but prove difficult to study.

Our beta diversity estimates obtained from samples of communities in different locations are in general agreement with low beta diversity estimates based on regional species pools^{4–6}. This lends further support to relatively low global estimates of insect diversity at <10 million species^{23–25}. Previous estimates of global insect species richness derived from the number of plant species and local species richness of herbivore communities were approximately doubled to account for beta diversity²³ or failed to consider geographical turnover among herbivore communities on conspecific trees²⁴. Expanding the scope of sampling from a single location to distances up to 500 km between sites approximately doubled the number of unique lepidopteran species per plant species (Supplementary Figs 4 and 5).

Steep environmental gradients can show high turnover in herbivore communities even on the same plant species. For instance, *Ficus* trees at our lowland sites shared very few lepidopteran species with conspecific trees at 1,800 m above sea level in the New Guinea central

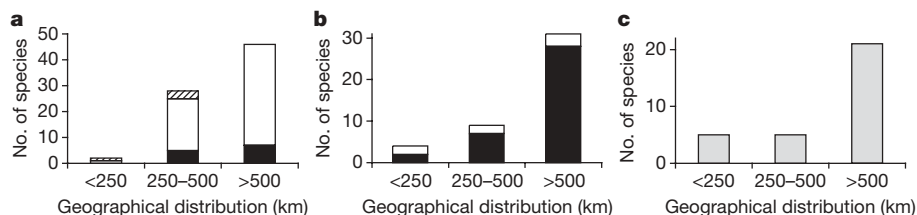


Figure 4 | Geographical distribution of caterpillar (a), ambrosia beetle (b) and fruitfly (c) species in Papua New Guinea lowland rainforests. Geographical distribution was quantified as the distance between the two most distant occurrences of the species. Species were classified as generalists, feeding on >1 genus (black); clade specialists, feeding on >1 species from a single genus (white); and monophagous, feeding on a single plant species (hatched). Host specificity of fruitfly species (grey) is unknown. Note that

monophagous species could be recognized only in the Lepidoptera, as the ambrosia beetles were not reared from multiple congeneric plant species. Host specificity was not correlated with geographical distribution (caterpillars: Spearman r , $P > 0.25$; ambrosia beetles: Mann–Whitney U -test, $P > 0.20$). Only common herbivore species, listed in Supplementary Appendices 2–4, were analysed.

cordillera²⁶. Tropical altitudinal gradients coincide with global maxima of plant species diversity²⁷ and the same is probably true for herbivorous insects. However, a large proportion of the world's tropical rainforest is situated in the more homogeneous lowland basins of major tropical rivers. For instance, the Sepik–Ramu and Fly–Strickland river systems comprise more than half of the lowland rainforest area in Papua New Guinea, and the two largest tropical forest areas, the Amazon and Congo basins, are also situated around large river systems²⁸. Where relatively uniform altitude, climate and soil support a low beta diversity of vegetation^{15,29}, we argue that low beta diversity characterizes insect herbivores as well.

METHODS SUMMARY

The study included eight sites within a 500 × 150 km lowland area with continuous rainforest in the basin of the Sepik and Ramu rivers, and an additional site in the Papuan Peninsula (Fig. 1). Four large genera—*Ficus* (Moraceae), *Macaranga* (Euphorbiaceae), *Psychotria* (Rubiaceae) and *Syzygium* (Myrtaceae)—were the focus of the plant study. Each site hosted a floristic survey in a 5 × 5 km area and quantitative surveys in 50 plots, 20 × 20 m each.

The herbivore study included guilds feeding on leaves (caterpillars, Lepidoptera), wood (ambrosia beetles, Coleoptera) and fruit (fruitflies, Diptera). Caterpillars were sampled on 11–12 plant species from the four focal genera at each of eight study sites, surveying 1,500 m² of foliage per plant species^{13,14}. Ambrosia beetles (Curculionidae: Scolytinae and Platypodinae) were sampled from four tree species—*Artocarpus altilis* (Moraceae), *Ficus nodosa* (Moraceae), *Leea indica* (Leeaceae) and *Nauclea orientalis* (Rubiaceae)—at three sites. Three individual trees from each study species were killed *in situ* at each site and after 20 days, standardized timber samples were hand-dissected for colonizing beetles. Dacine fruitflies (Tephritidae) were attracted to Steiner traps baited with lures (cuelure and methyl eugenol)⁴. Eight traps located in primary forest vegetation were operated for 6 weeks at each of four sites.

The similarity of plant and insect assemblages was quantified as the average proportion of species shared between sites, using the Sørensen index and its modification, the Chao–Sørensen index, which corrects for bias owing to incomplete sampling of rare species³⁰. The probability $C(d)$ that two randomly selected individuals from different sites were conspecific was used as another measure of similarity¹⁵. Geographic distribution, measured as distance between the two most distant occurrences, was estimated only for common species of insects. The effect of the Sepik River as a dispersal barrier was tested by comparing approximately equidistant assemblages of caterpillars feeding on the same and opposite sides of the river.

Full Methods and any associated references are available in the online version of the paper at www.nature.com/nature.

Received 20 April; accepted 14 June 2007.

- Novotny, V. & Basset, Y. Host specificity of insect herbivores in tropical forests. *Proc. R. Soc. B* **272**, 1083–1090 (2005).
- Lewinsohn, T. M., Novotny, V. & Basset, Y. Insects on plants: diversity of herbivore assemblages revisited. *Annu. Rev. Ecol. Syst.* **36**, 597–620 (2005).
- Novotny, V. & Weiblen, G. D. From communities to continents: beta-diversity of herbivorous insects. *Annal. Zool. Fenn.* **42**, 463–475 (2005).
- Novotny, V., Clarke, A. R., Drew, R. A. I., Balagawi, S. & Clifford, B. Host specialization and species richness of fruit flies (Diptera: Tephritidae) in a New Guinea rain forest. *J. Trop. Ecol.* **21**, 67–77 (2005).
- Gaston, K. J. & Gauld, I. D. How many species of pimplines (Hymenoptera: Ichneumonidae) are there in Costa Rica? *J. Trop. Ecol.* **9**, 491–499 (1993).
- Orr, A. G. & Haeuser, C. L. Temporal and spatial patterns of butterfly diversity in a lowland tropical rainforest. In *Tropical Rainforest Research — Current Issues* (eds Edwards, D. S., Booth, W. E. & Choy, S.) 125–138 (Kluwer, Dordrecht, 1996).
- Erwin, T. L. The biodiversity question: How many species of terrestrial arthropods are there? In *Forest Canopies* 2nd edn (eds Lowman, M. D. & Rinker, H. B.) 259–269 (Elsevier, Burlington, 2004).
- Ruokolainen, K., Tuomisto, H., Vormisto, J. & Pitman, N. Two biases in estimating range sizes of Amazonian plant species. *J. Trop. Ecol.* **18**, 935–942 (2002).

- Ødegaard, F. Host specificity, alpha- and beta-diversity of phytophagous beetles in two tropical forests in Panama. *Biodivers. Conserv.* **15**, 83–105 (2006).
- Beck, J. & Chey, V. K. Beta-diversity of geometrid moths from northern Borneo: effects of habitat, time and space. *J. Anim. Ecol.* **76**, 230–237 (2007).
- Brown, K. S. Jr. Geologic, evolutionary, and ecological bases of the diversification of Neotropical butterflies. In *Tropical Rainforests. Past, Present, and Future* (eds Birmingham, E., Dick, C. W. & Moritz, C.) 166–201 (Univ. Chicago Press, Chicago, 2005).
- Howard, P. C. *et al.* Complementarity and the use of indicator groups for reserve selection in Uganda. *Nature* **394**, 472–474 (1998).
- Miller, S. E., Novotny, V. & Basset, Y. Studies on New Guinea moths. 1. Introduction (Lepidoptera). *Proc. Entomol. Soc. Wash.* **105**, 1035–1043 (2003).
- Novotny, V. *et al.* Local species richness of leaf-chewing insects feeding on woody plants from one hectare of a lowland rainforest. *Cons. Biol.* **18**, 227–237 (2004).
- Condit, R. *et al.* Beta-diversity in tropical forest trees. *Science* **295**, 666–669 (2002).
- Hubbell, S. P. *The Unified Neutral Theory of Biodiversity and Biogeography* (Princeton Univ. Press, Princeton, New Jersey, 2001).
- Gascon, C. *et al.* Riverine barriers and the geographic distribution of Amazonian species. *Proc. Natl Acad. Sci. USA* **97**, 13672–13677 (2000).
- Hall, J. P. W. & Harvey, D. J. The phylogeography of Amazonia revisited: New evidence from riodinid butterflies. *Evolution* **56**, 1489–1497 (2002).
- Rosenzweig, M. L. *Species Diversity in Space and Time* (Cambridge Univ. Press, Cambridge, 1995).
- Koleff, P., Lennon, J. J. & Gaston, K. J. Are there latitudinal gradients in species turnover? *Glob. Ecol. Biogeogr.* **12**, 483–498 (2003).
- Höft, R. *Plants of New Guinea and the Solomon Islands. Dictionary of the Genera and Families of Flowering Plants and Ferns, Handbook no. 13.* (Wau Ecology Institute, Wau, 1992).
- Novotny, V. *et al.* Response to comment on “Why are there so many species of herbivorous insects in tropical rainforests?”. *Science* **315**, 1666 (2007).
- Ødegaard, F. How many species of arthropods? Erwin's estimate revised. *Biol. J. Linn. Soc.* **71**, 583–597 (2000).
- Novotny, V. *et al.* Low host specificity of herbivorous insects in a tropical forest. *Nature* **416**, 841–844 (2002).
- Stork, N. E. How many species are there? *Biodiv. Cons.* **2**, 215–232 (1993).
- Novotny, V. *et al.* An altitudinal comparison of caterpillar (Lepidoptera) assemblages on *Ficus* trees in Papua New Guinea. *J. Biogeogr.* **32**, 1303–1314 (2005).
- Barthlott, W., Lauer, W. & Placke, A. Global distribution of species diversity in vascular plants: towards a world map of phytodiversity. *Erkunde* **50**, 317–327 (1996).
- Mittermeier, R. A. *et al.* Wilderness and biodiversity conservation. *Proc. Natl Acad. Sci. USA* **100**, 10309–10313 (2003).
- Pitman, N. C. A., Terborgh, J., Silman, M. R. & Nuñez, V. P. Tree species distributions in an upper Amazonian forest. *Ecology* **80**, 2651–2661 (1999).
- Chao, A., Chazdon, R. L., Colwell, R. K. & Shen, T. J. A new statistical approach for assessing similarity of species composition with incidence and abundance data. *Ecol. Lett.* **8**, 148–159 (2005).

Supplementary Information is linked to the online version of the paper at www.nature.com/nature.

Acknowledgements We thank D. Bito, W. Boen, A. Borney, L. Cizek, G. Damag, A. Krasa, J. Kua, R. Kutil, R. Lilip, M. Manaono, M. Rimandai, S. Sau, G. Sosanika, D. Stancik, V. Iwam and D. Wal for technical assistance, and V. O. Becker, J. Brown, A. Cognato, L. Craven, K. Damas, C. Drew, J. D. Holloway, M. Horak, K. Maes, J. Miller, E. G. Munroe, M. Shaffer, A. M. Solis, D. Stancik, W. Takeuchi and K. Tuck for taxonomic assistance. More than 150 insect collectors contributed to the study. P. Herbert provided DNA barcodes; J. Leps advised on statistical analysis; R. Condit, H. L. Davies, O. Diserud, J. Chave, M. Heads, J. Hrcsek, D. H. Janzen, O. T. Lewis, F. Ødegaard, D. Storch and C. O. Webb commented on the manuscript. This work was supported by the National Science Foundation (USA), Grant Agencies of the Czech Republic, Czech Academy of Sciences and Czech Ministry of Education, Darwin Initiative for the Survival of Species (UK), David and Lucile Packard Fellowship in Science and Engineering, the National Geographic Society (USA), and The International Centre for the Management of Pest Fruit Flies (Griffith University). We thank Papua New Guinea customary landowners for allowing us to work in their forests. We dedicate this work to the late Richard Kutil.

Author Information Reprints and permissions information is available at www.nature.com/reprints. The authors declare no competing financial interests. Correspondence and requests for materials should be addressed to V.N. (novotny@entu.cas.cz).

METHODS

Study sites. The study was located in the basin of the Sepik and Ramu rivers in northern New Guinea (Fig. 1a), within a 500 × 150 km area of lowland terrain with continuous rainforest and wetland vegetation. The area is populated by <10 people per km², has <1 km of roads per 100 km², and is bisected by a major tropical river, the Sepik. The river is up to 1 km wide while the accompanying belt of floodplain swamps, lakes and grasslands is up to 70 km wide³¹ and represents the only large discontinuity in the rainforest ecosystem of the study area. The area is also among the most culturally diverse regions in the world, inhabited by populations speaking >200 different languages with even the most widespread ones only spoken across <5% of the region^{32,33}. The study area is representative of lowland rainforests in Papua New Guinea as the Sepik–Ramu and Fly–Strickland river systems encompass the majority of these forests in this country.

We outlined an approximately equidistant grid of eight sites with an average distance of 160 km between neighbouring sites, and pair-wise distances ranging from 59 to 513 km (Fig. 1b). We also included one site in the Papuan Peninsula (Fig. 1a) to extend the range of between-site distances to 950 km. All sites were located in lowland rainforest <500 m above sea level with vegetation classified as mixed evergreen hill forest³⁴. The climate at these sites is humid with a mean annual rainfall of 2,000–4,000 mm, with a moderate dry season from July to September (monthly mean rainfall ≤100 mm), and mean monthly air temperature ~26 °C. Soils are latosols³⁵. The Madang area, approximately 20 × 30 km at the eastern boundary of our study area, including the Ohu study site and the town of Madang (Fig. 1a, b), was the focus of comparison with other study sites as it has a relatively well known insect fauna resulting from intensive study for >10 yr^{4,13,14,36}.

Each site consisted of a small village practicing subsistence agriculture in a matrix of primary and secondary rainforest (Fig. 1c). Four sites could be accessed by four-wheel-drive vehicle, others only by light aircraft. Each site was surveyed by a team including one researcher, four paratonomists and ten locally hired assistants³⁷. The surveys were conducted from December 2001 to July 2006 and included ~34 person-years under remote and challenging field conditions. Different sites were surveyed at different times of the year, avoiding the dry season and, in any case, insect seasonality in the area is low³⁸.

The study area was situated in a complex tectonic region at the convergence of two major plates: the Australian and Pacific. The northern New Guinea lowlands are a product of the gradual accretion of volcanic arc terranes to the central cordillera. The foothills of the central range that demarcate our study area in the south, and the Bewani and Torricelli ranges in the north, accreted to the existing landmass of New Guinea approximately 30–35 million years ago^{39,40}. Furthermore, several terranes amalgamated to a single block, now forming the Papuan peninsula, which accreted about 15 million years ago. The last accretion event so far, involving the Adelbert and Finisterre blocks, was completed about 2 million years ago⁴¹. Most of the study area between the central and northern ranges was submerged from the Early Miocene until the Pliocene epoch^{39,40}. Oceanic incursions across the northern lowlands during periods of elevated sea level continued until very recently, including a sea that stretched ~100 km inland and separated our Elem and Wamangu sites only 6,000 yr ago⁴². Alterations of climate and vegetation also occurred during the Holocene epoch. In particular, a mosaic of broadleaf open and closed forests covered the study area during a cooler and drier period about 17,000 yr ago⁴³.

Plants and insects. Large genera representing four plant families—*Ficus* (Moraceae), *Macaranga* (Euphorbiaceae), *Psychotria* (Rubiaceae) and *Syzygium* (Myrtaceae)—were the focus of the plant study. They are well represented in all stages of lowland rainforest succession⁴⁴ and together total at least 475 species in New Guinea²¹. Each site hosted a floristic survey of genera in a 5 × 5 km area and quantitative surveys of target plant species in 50 plots, 20 × 20 m each. Plots were divided evenly between primary and secondary forest types.

The study of herbivorous insects included guilds feeding on leaves (caterpillars, Lepidoptera), wood (ambrosia beetles, Coleoptera) and fruit (fruitflies, Diptera). Caterpillars (Lepidoptera) represent the most species-rich group of leaf-chewing insects in the study area¹⁴. Caterpillars were sampled during a 3 month survey staged at each study site from December 2001 to October 2005, except Popondetta where only ambrosia beetles and fruitflies were collected. Ohu hosted two consecutive surveys to assess the effect of sample size on our results. At each site, we collected caterpillars from 11–12 locally common plant species (4–5 *Ficus*, 3–5 *Macaranga*, 1–2 *Psychotria* and 1–2 *Syzygium* species per site) except at Ohu where we included 20 species that were sampled at one or more other sites (Supplementary Table 2). The selected species represented on average 40–86% of the basal area of each genus per site. These species are shrubs or small trees and represented <5% of the total basal area of the local

woody vegetation (Supplementary Table 3). Target species included, as far as possible, a mix of those with widespread and limited geographical distribution across the study area.

Caterpillars were hand collected from approximately 1,500 m² of foliage per plant species per site. Each caterpillar was tested in a makeshift laboratory for feeding on the plant species from which it was collected and reared to an adult whenever possible (Fig. 1d). Only caterpillars that fed were retained for study. Species identifications were verified by dissection of genitalia, and when possible by reference to type specimens or in consultation with experts. Comparisons of mitochondrial cytochrome oxidase I (COI) DNA sequence divergence with morphology were used to identify polymorphic species including cases of sexual dimorphism^{45,46}. Lepidopteran species are illustrated at <http://www.entu.cas.cz/png/caterpillars>. We recorded 74,184 caterpillars and 370 species feeding on the target plant species, including 25,437 individuals and 346 species reared to adults. Only information on reared adults was used in the analysis. We further characterized the Lepidoptera of the Madang area using additional data sets from Ohu and two nearby (<20 km) forest sites. These data comprised 56,002 caterpillars, including 19,011 reared to adults, from 580 species feeding on 94 plant species in 32 families, and 10,498 adults from 1,537 species collected at light (our own unpublished data and refs 13, 14).

Ambrosia beetles (Curculionidae: Scolytinae and Platypodinae) excavate tunnels in xylem of dead or moribund woody hosts, which they inoculate with symbiotic xylosaprophagous fungi, their sole source of food^{47,48}. This feeding habit has evolved multiple times and allows ambrosia beetles to expand markedly their host ranges^{49,50}. We sampled ambrosia beetles from four tree species: *Artocarpus altilis* (Park.) Fosb. (Moraceae), *Ficus nodosa* Teysm. & Binn. (Moraceae), *Leea indica* Merrill (Leeaceae) and *Nauclea orientalis* (L.) L. (Rubiaceae) at Ohu, Utai and Popondetta (Fig. 1). Three individual trees from each study species with diameters at breast height of 20–25 cm were killed at each site by ringing the bark and burning the base of the trunk at ground level. Trees were left standing for 20 days to attract ambrosia beetles. Standardized 1-m-long sections of trunk, 2 m of sections of branches 2–10 cm in diameter, and 2 m of sections of twigs <2 cm in diameter, were hand-dissected for colonizing beetles. Sampling was completed between February and July 2006. We obtained 12,751 beetles from 86 species. The ambrosia beetle fauna of the Madang area was further characterized by additional observations of ~70,000 individuals from at least 77 species reared from 15 tree species in 13 families (J.H., unpublished).

Dacine fruitflies (Tephritidae) feed as larvae on soft fleshy fruit. They are the most host-specific of the three guilds we studied, as most of the species are limited to a single plant genus or species⁴. They are endemic to subtropical and tropical rainforests from the Indian subcontinent across to Oceania, reaching their greatest diversity in New Guinea⁵¹. The adult fruitflies were attracted to Steiner traps baited with lures (cuelure and methyl eugenol) known to attract males of ~70% of the fruitfly species in Papua New Guinea⁵¹. Eight traps located in primary forest vegetation were operated for 6 weeks at each of four sites (Utai, Morox, Wanang and Popondetta, Fig. 1) from February to July 2006. We obtained 36,811 fruitflies from 46 species. The fruitfly fauna of the Madang area was further characterized by additional data from ~165,000 individuals and 69 species collected in traps^{4,36,52} and from 168 species of plants supporting at least 29 fruitfly species⁴.

Statistics. The geographical distribution of each species was measured by the number of sites, n , where it occurred and kilometres between the two most distant occurrences (5 km for species restricted to a single site). The sensitivity of these parameters to sample size was examined by randomization of species abundance among sites. It is necessary to compare our sampling effort to predictions of a null model because insufficient sampling may overestimate beta diversity⁵³.

The probability of observing a rare species ($N < 3$, 4 ... individuals) at n sites was estimated under the extreme case where beta diversity is zero. The probability that a particular site is occupied when N individuals are randomly distributed among n sites is $P = 1 - (1 - 1/n)^N$. We adhered to a threshold minimum abundance such that $P > 0.95$ for a randomly distributed species to be observed at all sites. The condition was satisfied by $N \geq 23$ individuals at eight sites sampled for caterpillars, $N \geq 8$ individuals at three sites sampled for ambrosia beetles, and $N \geq 11$ individuals at four sites sampled for fruitflies. We regarded these values of N as the minimum abundance for accurate detection of a species distribution in a particular herbivore guild. Only common species exceeding this minimum abundance were used to estimate geographical distribution and host specificity of insect herbivores. Seventy six of 370 Lepidoptera species, 31 of 46 fruitfly species, and 44 of 86 ambrosia beetle species met this threshold. The probability that N individuals are distributed so that any two particular sites, including the two most distant sites, are occupied is p^2 assuming no spatial autocorrelation of occurrences. The maximum possible geographical

span is of special interest because it was recorded for a surprisingly large number of herbivore species.

Host specificity of caterpillars and ambrosia beetles was assessed from feeding records combining all sites. Records of only a single individual feeding on a particular host species were excluded on the grounds that it is difficult to distinguish dubious records from genuine rarity. Monophagous species were defined as those feeding on a single plant species, clade specialists as those feeding on >1 species from a single genus, and generalists as those feeding on >1 genus. Monophagous species could not be separated from clade specialists in ambrosia beetles where only one plant species per genus was studied. No host information was available for fruitflies.

The Sørensen index, or the average proportion of species shared between two communities, was selected from a range of community similarity measures⁵³ because its modification, the Chao–Sørensen index, corrects for possible bias owing to incomplete sampling of rare species⁵⁰. The original Sørensen index was applied to the plant records because abundance data were unavailable. Insect sampling included measures of species abundance, thus permitting calculation of the Chao–Sørensen index using EstimateS⁵⁴. The mean Chao–Sørensen similarity between pairs of insect samples obtained from the same plant species during two successive surveys at Ohu approached unity as expected for identical assemblages (0.94 ± 0.015 for caterpillars sampled from 20 plant species and 0.94 ± 0.017 for ambrosia beetles sampled from three plant species), indicating that sample size was sufficient for inference of beta diversity. The significance of the correlation between geographical distance and community similarity was tested for caterpillars by the Mantel procedure. Only caterpillar assemblages from the 18 plant species studied at >3 surveys were included in this analysis. The similarity between lepidopteran communities was estimated from complete data on reared individuals, that is, including both rare and abundant species.

The effect of the Sepik River as a dispersal barrier was tested by comparing approximately equidistant assemblages of caterpillars feeding on the same and opposite sides of the river. The composition of the assemblage feeding on a particular plant species at a particular site (for example, Niksek, Fig. 1b) was compared with assemblages from nearly equidistant sites, one located on the same side of the river and the other on the opposite side (for example, Elem and Wamangu). Each insect sample from a particular plant species and a particular site was used only once in the analysis to preserve the independence of all comparisons. Nineteen matched pairs of samples from particular plant species were analysed, comparing sites 160 ± 12 km apart and separated by the river to sites 148 ± 6 km apart on the same side of the river.

The probability $C(d)$ that two randomly selected individuals from sites A and B were conspecific was calculated as $C(d) = \Sigma(n_{iA}/N_A)(n_{iB}/N_B)$ where n_i is the number of individuals from species i and N the total number of all individuals at a particular site. d denotes the distance between sites A and B.

31. Reiner, E. J. & Robbins, R. G. The Middle Sepik Plains, New Guinea: A physiographic study. *Geogr. Rev.* **54**, 20–44 (1964).
32. Wurm, S. A. & Hattori, S. *Language Atlas of the Pacific Area* (Australian Academy of the Humanities, Canberra, 1981).
33. Novotny, V. & Drozd, P. Size distribution of conspecific populations: peoples of New Guinea. *Proc. R. Soc. Lond. B* **267**, 947–952 (2000).
34. Pajmians, K. (ed.) *New Guinea Vegetation* (Australian National Univ. Press, Canberra, 1976).
35. Wood, A. W. The soils of New Guinea. In *Biogeography and Ecology of New Guinea* (ed. Gressitt, J. L.) 73–86 (W. Junk, The Hague, 1982).
36. Fletcher, B. S. Dacine fruit flies collected during the dry season in the lowland rainforest of Madang Province, Papua New Guinea (Diptera: Tephritidae). *Aust. J. Entomol.* **37**, 315–318 (1998).
37. Basset, Y. *et al.* Conservation and biological monitoring of tropical forests: the role of parataxonomists. *J. Appl. Ecol.* **41**, 163–174 (2004).
38. Novotny, V. *et al.* Predictably simple: communities of caterpillars (Lepidoptera) feeding on rainforest trees in Papua New Guinea. *Proc. R. Soc. Lond. B* **269**, 2337–2344 (2002).
39. Pigram, C. J. & Davies, H. L. Terranes and the accretion history of the New Guinea orogen. *J. Austral. Geol. Geophys.* **10**, 193–211 (1987).
40. Davies, H. L., Perembo, R. C. B., Winn, R. D. & KenGemar, P. Terranes of the New Guinea orogen. In *Proceedings of the Geology Exploration and Mining Conference, Madang* (ed. Hancock, G.) 61–66 (Australasian Institute of Mining and Metallurgy, Melbourne, 1997).
41. Abbott, L. D. Neogene tectonic reconstruction of the Adelbert–Finisterre–New Britain collision, northern Papua New Guinea. *J. S. E. Asian Earth Sci.* **11**, 33–51 (1995).
42. Swadling, P. Changing shorelines and cultural orientations in the Sepik–Ramu, Papua New Guinea: implications for Pacific prehistory. *World Archaeol.* **29**, 1–14 (1997).
43. Nix, H. A. & Kalma, J. D. Climate as a dominant control in the biogeography of northern Australia and New Guinea. In *Bridge and Barrier: the Natural and Cultural History of Torres Strait* (ed. Walker, D.) 61–92 (Australian National University, Canberra, 1972).
44. Leps, J., Novotny, V. & Basset, Y. Habitat and successional status of plants in relation to the communities of their leaf-chewing herbivores in Papua New Guinea. *J. Ecol.* **89**, 186–199 (2001).
45. Hebert, P. D., Penton, N. E. H., Burns, J. M., Janzen, D. H. & Hallwachs, W. Ten species in one: DNA barcoding reveals cryptic species in the neotropical skipper butterfly *Astrartes fulgerator*. *Proc. Natl Acad. Sci. USA* **101**, 14812–14817 (2004).
46. Hulcr, J. *et al.* DNA barcoding confirms polyphagy in a generalist moth, *Homona mermerodes* (Lepidoptera: Tortricidae). *Mol. Ecol. Notes* **7**, 549–557 (2007).
47. Beaver, R. A. Insect–fungus relationship in the bark and ambrosia beetles. In *Insect–Fungus Interactions* (eds Wilding, N., Collins, N. M., Hammond, P. M. & Webber, J. F.) 121–143 (Academic, London, 1989).
48. Mueller, U. G., Gerardo, N. M., Aanen, D. K., Six, D. L. & Schultz, T. R. The evolution of agriculture in insects. *Annu. Rev. Ecol. Syst.* **36**, 563–595 (2005).
49. Beaver, R. A. Host specificity of temperate and tropical animals. *Nature* **281**, 139–141 (1979).
50. Farrell, B. D. *et al.* The evolution of agriculture in beetles (Curculionidae: Scolytinae and Platypodinae). *Evolution* **55**, 2011–2027 (2001).
51. Drew, R. A. I. The tropical fruit flies (Diptera: Tephritidae: Dacinae) of the Australasian and Oceanian regions. *Mem. Queensl. Mus.* **26**, 1–521 (1989).
52. Clarke, A. R. *et al.* Distribution and biogeography of *Bactrocera* and *Dacus* species (Diptera: Tephritidae) in Papua New Guinea. *Aust. J. Entomol.* **43**, 148–156 (2004).
53. Koleff, P., Gaston, K. J. & Lennon, J. J. Measuring beta diversity for presence and absence data. *J. Anim. Ecol.* **72**, 367–382 (2003).
54. Colwell, R. K. EstimateS: Statistical Estimation of Species Richness and Shared Species from Samples. Version 7.5 <<http://purl.oclc.org/estimates>> (2005).

LETTERS

Host specificity of Lepidoptera in tropical and temperate forests

L. A. Dyer¹, M. S. Singer², J. T. Lill³, J. O. Stireman⁴, G. L. Gentry¹, R. J. Marquis⁵, R. E. Ricklefs⁵, H. F. Greeney⁶, D. L. Wagner⁷, H. C. Morais⁸, I. R. Diniz⁸, T. A. Kursar^{9,10} & P. D. Coley^{9,10}

For numerous taxa, species richness is much higher in tropical than in temperate zone habitats¹. A major challenge in community ecology and evolutionary biogeography is to reveal the mechanisms underlying these differences. For herbivorous insects, one such mechanism leading to an increased number of species in a given locale could be increased ecological specialization, resulting in a greater proportion of insect species occupying narrow niches within a community. We tested this hypothesis by comparing host specialization in larval Lepidoptera (moths and butterflies) at eight different New World forest sites ranging in latitude from 15° S to 55° N. Here we show that larval diets of tropical Lepidoptera are more specialized than those of their temperate forest counterparts: tropical species on average feed on fewer plant species, genera and families than do temperate caterpillars. This result holds true whether calculated per lepidopteran family or for a caterpillar assemblage as a whole. As a result, there is greater turnover in caterpillar species composition (greater β diversity) between tree species in tropical faunas than in temperate faunas. We suggest that greater specialization in tropical faunas is the result of differences in trophic interactions; for example, there are more distinct plant secondary chemical profiles from one tree species to the next in tropical forests than in temperate forests as well as more diverse and chronic pressures from natural enemy communities.

Ecological theory requires that organisms differ in their use of shared, limiting resources if they are to coexist. The role of resource specialization in fostering biodiversity is thus a central issue in ecology and evolutionary biology. A longstanding hypothesis predicts a direct relationship between ecological specialization and species richness in communities². Specialization reduces interspecific competition and facilitates species coexistence by partitioning niche space^{3,4}. Character divergence across generations in response to trophic interactions or competition⁵ provides an evolutionary mechanism by which species richness and specialization can increase together^{6–8}. Beginning with observations recounted by Darwin⁹ and Wallace¹⁰, examples of ecological specialization in tropical organisms have fostered a widespread perception that specificity of interactions is a hallmark of the high-diversity tropics.

Although biotic inventories often confirm the higher species richness of tropical communities than those at higher latitudes¹, few studies have quantified increased ecological specialization along a latitudinal gradient¹¹. Novotny *et al.*¹² recently challenged the notion that herbivorous insects are more specialized in the tropics by the use of a quantitative comparison of host specificity of herbivorous insects

in tropical forests of Papua New Guinea and those in temperate forests of central Europe. They reported a similar host specificity among temperate and tropical herbivorous insects and concluded that the greater species richness of tropical herbivores is a direct consequence of greater tropical plant diversity rather than increased host plant specialization. The large contribution that herbivorous insects make to global biodiversity¹³ as well as the centrality of ecological specialization in theories of biodiversity warrant further comparison of host specificity of tropical and temperate herbivorous insects.

Here we demonstrate a latitudinal gradient in host specificity for the most ecologically dominant group of externally feeding herbivores, larval Lepidoptera, using extensive caterpillar–host–plant data sets from the Americas (Table 1). Any such data set, regardless of size, is incomplete: the most specialized herbivores might not be sampled, cryptic specialist species might not be distinguished, the host plant range of generalist herbivores might be underestimated, and herbivore diets can shift from one community to another¹⁴. Thus, although thorough collecting efforts involved in generating these data sets are crucial¹², smaller data sets in particular present practical problems for traditional calculations of diet breadth. We address this issue explicitly by analysing the host specificity of herbivores with two measures: first, a direct comparison of taxonomic diet breadth calculated for each herbivore species, which depends heavily on sampling effort, and second, beta diversity (turnover) of herbivores among focal tree species¹⁵, which gives an indirect but more accurate representation of host specificity with limited sampling effort.

We compiled rearing data of field-collected caterpillars from eight sites in North, Central, and South America (Table 1) spanning temperate (southern Canada and Connecticut, USA), subtropical (southern Arizona and southern Louisiana, USA) and tropical forests or woodlands (wet forest in Costa Rica, moist forest in Panama, cloud forest in Ecuador, and cerrado in Brazil). Lists of host plants and caterpillar species used for analyses are provided in Supplementary Information. Externally feeding caterpillars (mostly macrolepidopterans, but including Zygaenoidea and in some cases Pyraloidea) were collected in the field by scanning visually or by beating foliage.

The host plant specificity of forest caterpillars decreased significantly with increasing latitude as measured for plant families ($F_{1,5} = 47.2$, $P = 0.001$, $R^2 = 0.90$), genera ($F_{1,5} = 20.8$, $P = 0.006$, $R^2 = 0.81$; Fig. 1) and species ($F_{1,5} = 14.7$, $P = 0.01$, $R^2 = 0.75$). The latitude–specialization relationship as measured by the number of host plant species per caterpillar species was strengthened slightly

¹Department of Ecology and Evolutionary Biology, Tulane University, New Orleans, Louisiana 70118, USA. ²Department of Biology, Wesleyan University, Middletown, Connecticut 06459, USA. ³Department of Biological Sciences, George Washington University, Washington, DC 20052, USA. ⁴Department of Biological Sciences, Wright State University, Dayton, Ohio 45435, USA. ⁵Department of Biology, University of Missouri–St Louis, St Louis, Missouri 63121, USA. ⁶Yanayacu Biological Station and Center for Creative Studies, Cosanga, Napo, Ecuador c/o Foch 721 y Juan Leon Mera, Quito, Ecuador. ⁷Department of Ecology and Evolutionary Biology, University of Connecticut, Storrs, Connecticut 06269, USA. ⁸Department of Ecology/Zoology, University of Brasília, 70910-900, Brasília, DF, Brazil. ⁹Department of Biology, University of Utah, Salt Lake City, Utah 84112-0840, USA. ¹⁰Smithsonian Tropical Research Institute, Panama City, Panama.

Table 1 | Caterpillar rearing databases

Study site	Median latitude	Sampling area (ha)	Rearings	Caterpillars	Host plants	Effort (h)	Years
Canada	47° 15' N	80,000,000	131,431	28, 280, 653	27, 59, 155	Unknown	20
Connecticut	41° 30' N	1,437,100	3,158	19, 166, 252	12, 13, 14	Unknown	5
Arizona	32° 13' N	1,000,000	7,601	20, 136, 184	50, 104, 161	9,000	10
Louisiana	31° 00' N	500,000	2,300	19, 98, 127	48, 77, 106	5,000	6
Brazil	15° 56' S	10,000	5,614	43, 264, 565	44, 80, 109	8,000	12
Costa Rica	10° 25' N	2,400	22,348	29, 223, 509	72, 176, 281	52,000	15
Panama	9° 10' N	1,600	4,536	30, 384, 401	57, 139, 209	8,000	9
Ecuador	0° 25' S	30,000,000	24,413	13, 65, 192	53, 110, 177	72,000	6

Rearings include only those portions of the databases used for analyses in this study. Sampling area was estimated for Canada, Louisiana, Arizona and Ecuador, where multiple sites were sampled. Hours of search effort were estimated for Panama but were not estimable for Canada and Connecticut. Number of rearings per host plant species varied from 1 to over 100 for all sites. Numbers of caterpillar or host plant taxa are listed as families, genera and species, respectively. Vascular plants, including ferns, of all life forms were sampled for all sites except Canada, where only trees were sampled.

when heterogeneity in the data from different sites (Table 1) was corrected by weighting the regressions by sampling area ($F_{1,5} = 47.2$, $P = 0.001$, $R^2 = 0.90$), the reciprocal of sampling area ($F_{1,5} = 22.7$, $P = 0.005$, $R^2 = 0.82$) and years of sampling ($F_{1,5} = 29.4$, $P = 0.003$, $R^2 = 0.85$). Similarly, because the sampling effort per caterpillar species was variable, nonparametric techniques were used to estimate the total richness of host plants for each caterpillar species, which slightly strengthened the latitude–specialization relationship (using the Chao2 estimator, $F_{1,5} = 16.1$, $P = 0.01$, $R^2 = 0.76$).

Within a region (temperate or tropical), the ranges of many caterpillar species encompass multiple sites¹⁴, enabling us to compile estimates of region-wide patterns of host plant use for these species. As a whole, temperate caterpillars fed on significantly higher numbers of plant species, genera, and families (multivariate analysis of variance (MANOVA), Wilks's lambda $F_{1,2637} = 311$; $P < 0.0001$; Fig. 2a). This pattern was significantly stronger for measures using host plant species versus genera and families (profile analysis, for both comparisons, $P < 0.0001$). The difference in diet breadth between tropical and temperate herbivores was not as marked when sampling was restricted to caterpillars feeding on eight randomly selected tree species (Fig. 2a), one of the sample sizes used by Novotny *et al.*¹². These direct measures of diet breadth reveal that the host specificities of particular herbivore lineages (taxonomic families or superfamilies) were always significantly greater in tropical than in temperate sites, but varied by taxon (Fig. 2b). Larval Papilionoidea (all butterflies), for example, had relatively high host specificity in both temperate and tropical sites, whereas larval Geometridae, Noctuidae and Arctiidae (the most diverse families in the combined data set) had much higher host specificity at tropical sites than at temperate sites. In the most comprehensive tropical (Costa Rica) and temperate

(Canada) data sets, the mean proportion of monophagous (that is, eating only one genus) herbivore species found on a given plant species was 0.64 (95% confidence interval (CI) 0.58–0.70) for Costa Rica ($n = 281$ plant species) and 0.11 (95% CI 0.08–0.18) for Canada ($n = 155$ plant species).

The analysis of β (beta diversity) as a proxy for specialization showed that turnover of herbivore species among host tree species was highest in tropical forests, intermediate in subtropical forests, and lowest in temperate forests (on the basis of non-overlapping 95% CIs; Fig. 3). This variable, computed with data from only eight host tree species per site, yielded the same site specialization rankings as the traditional taxonomic measures based on much more extensive sampling (Fig. 1). Similar results were obtained with 14 host tree species (Supplementary Information). Although thorough characterization of herbivore–plant affiliations for entire forests is ideal, many ecological studies focus on a subset of species for practical reasons. Using beta diversity as an indirect measure of herbivore specificity has the dual advantage of simplicity and robustness in the face of a limited sampling effort typical of most ecological studies, permitting more frequent tests of hypotheses about gradients in ecological specialization.

To circumvent problems arising from phylogenetic non-independence¹², we restricted our selection of host species to those from different genera in our analyses of herbivore β diversity. Additionally, in our analyses of herbivore diet breadth, we have included data from hundreds of host plant species representing a wide phylogenetic range of plant taxa in both tropical and temperate zones. By including a large proportion of the entire community we minimize potential bias in phylogenetic disparity (because both tropical and temperate data sets each contain many closely and distantly related taxa). Even if a bias in phylogenetic disparity among tropical and temperate plant

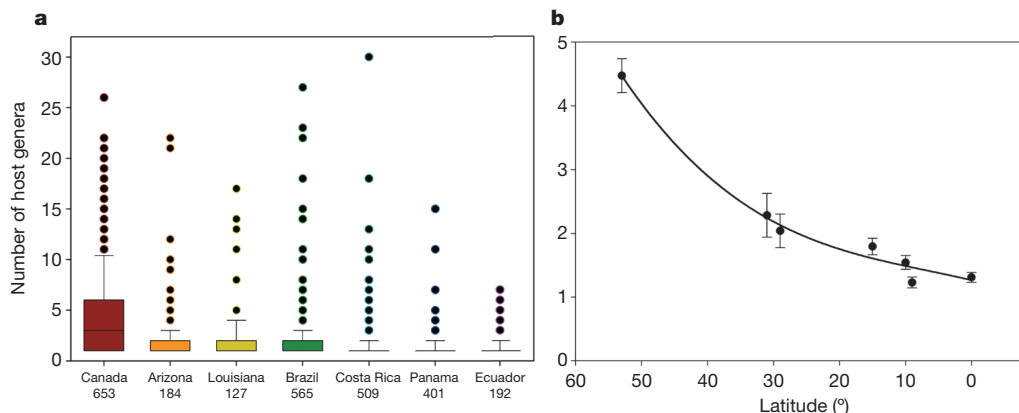


Figure 1 | Caterpillar diet breadth for one temperate site, two subtropical sites and four tropical sites. a, Box plots of number of host plant genera per caterpillar species at seven sites across a latitudinal gradient. Boxes are bounded by the first quartile, median, and third quartile; whiskers are 1.5 times the interquartile range; points outside the whiskers are outliers. Numbers of caterpillar species collected are listed beneath each site name.

Measures based on number of species or families yielded similar distributions. All distributions are skewed towards specialists (feeding on one or two host genera), and outliers represent extreme generalist caterpillars. **b**, An illustrative quadratic regression (diet breadth = $1.4 - 0.007 \times (\text{latitude}) + 0.0012 \times (\text{latitude})^2$; $R^2 = 0.98$, $F_{2,4} = 103.1$, $P = 0.0004$); error bars indicate s.e.m.

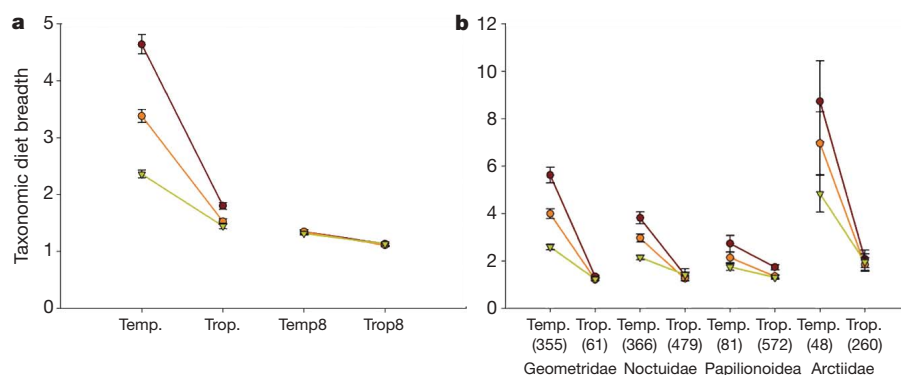


Figure 2 | Mean diet breadth of 1,585 tropical versus 1,052 temperate caterpillar species. **a**, Diet breadth was measured as the number of taxa of host plants per caterpillar species. Temp., temperate; trop., tropical. When eight focal host plant species were chosen randomly from each site, the difference between temperate (Temp8) and tropical (Trop8) diet breadths was greatly reduced (but was still significantly different; $F_{1,606} = 22.5$,

$P < 0.0001$). **b**, Latitudinal differences in diet breadths were consistent for the best-sampled families of Lepidoptera (Geometridae, Noctuidae and Arctiidae), but the difference was modest for the butterflies (Papilionoidea). Numbers of species collected are shown in parentheses in **b**. Purple circles, host species; orange circles, host genera; yellow triangles, host families. Error bars indicate 95% CI.

taxa exists, our comparisons of host breadth at generic and family levels (where the relationship between phylogenetic distance and herbivore similarity breaks down¹²) confirm the higher specificity of tropical taxa. Although the most appropriate phylogenetic correction for analysing herbivore host specificity would be to correct for phylogeny of the herbivores themselves, no such phylogeny currently exists. Our temperate–tropical host range comparisons of the most diverse caterpillar families/superfamilies in our data set demonstrate that the greater specialization of tropical caterpillars is a common feature of all four clades (Fig. 2b).

It is clear that the approach outlined here should be accompanied by similar studies that correct for phylogeny, as argued by other authors^{12,16,17}. Both approaches are necessary¹⁶, because correcting for phylogeny limits the data to a subset of focal species, which can markedly alter ecologically relevant measures of diet breadth (Fig. 2a). Thus, the contrast between the results of our study and those of Novotny *et al.*¹² may be due to true biological differences

between the Americas on the one hand and Europe and tropical Asia on the other, or it might just be a consequence of limiting the comparisons between Europe and Papua New Guinea to 8–14 focal host species.

The accuracy of delineating reproductively isolated units (that is, species) can markedly influence perceptions of the ecological specificity of organisms. Recent analyses of cytochrome *c* oxidase I (COI) haplotypes reveal that many tropical herbivore species with diets broadly distributed among available host plants may in fact be complexes of specialized cryptic species¹⁸. Although it has not been investigated whether such cryptic species complexes are more common in the tropics than in the temperate zone, temperate taxa are likely to be better resolved taxonomically, given the much greater attention they have received from systematists, forest managers and ecologists.

We conclude that host plant specificity of herbivorous insects is, on average, greater in the neotropics than at higher latitudes, and that a latitudinal gradient of dietary specialization is evident from our data. The evidence from this study is consistent with the hypothesis that ecological specialization is a factor in the origin and maintenance of high diversity of tropical herbivorous insects. Broad-scale empirical studies indicate that this increased specialization in tropical herbivore communities may be due to more intense trophic interactions with both host plants and enemies¹⁹. For example, comparisons of tropical and temperate forests indicate that tropical plants are chemically ‘nastier’²⁰ and that selective pressures due to natural enemies are stronger in the tropics^{12,21}, both of which should select for narrower host ranges in herbivores. Additionally, there is some evidence that tropical tree species may be more chemically distinct than temperate tree species^{21,22}, selecting for narrower diet breadths. The underlying mechanisms for differences in specialization by latitude, and perhaps by longitude, should be the focus of future research. Although it is clear that a significant proportion of tropical insect diversity is a product of species richness in higher plants¹², our data also imply that greater ecological specialization contributes to the great α and β diversity of herbivores in low-latitude forests. Recent palaeontological studies of insect-feeding damage²³ and regional analyses of extant phytophagous insects²⁴ provide clear examples of decoupled plant and herbivore diversity. Such examples show that insect diversity cannot be assumed to result only from plant diversity, whatever the specific mechanism invoked. Moreover, these results provide support for ecological^{25,26} and evolutionary theory^{7,8}, highlighting the key role of ecological specialization in the coexistence and diversification of species.

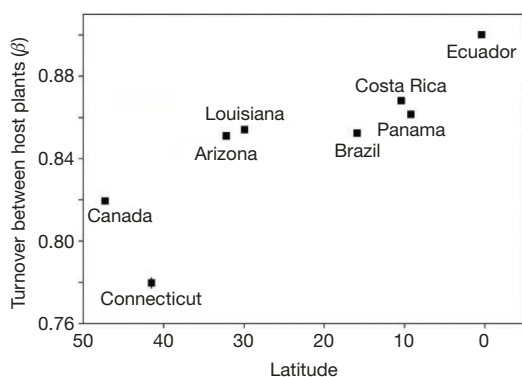


Figure 3 | Caterpillar species turnover among host plant species for eight forest and woodland sites across a latitudinal gradient. Modified Whittaker’s β is shown for two temperate (Canada and Connecticut), two subtropical (Arizona and Louisiana) and four tropical (Brazil, Costa Rica, Panama and Ecuador) sites, ordered by an approximate modal latitude for each site. With this measure, insect species turnover across host plants is used as an index of host plant specialization, with higher values of β indicating higher levels of specialization. Symbol size was greater than the 95% CI for all sites except Connecticut (see the text for details on the computation of β).

METHODS SUMMARY

Caterpillars were reared individually, at ambient temperature and humidity, on leaves of the plant species from which they were collected. To assess the degree of host specialization in each community we calculated the average number of host plant taxa per caterpillar species—the approach used in most other studies of diet breadth. We used linear regression to examine the relationship between median latitude and mean number of host plant families, genera and species (Fig. 1 shows a quadratic regression of genera on latitude for illustrative purposes). Regressions were then weighted by the size of the study areas and years of study to correct for variation between study sites. The reciprocal of area was also used in weighted regressions to decrease influence of very large collecting sites (namely Canada and Ecuador). To correct for unequal sampling per caterpillar species, we computed the Chao2 estimator²⁷ of the number of host plant species per caterpillar and examined its association with latitude by means of linear regression.

We used MANOVA followed by profile analysis to compare the number of plant species, genera and families fed on by each of the caterpillar species in tropical and in temperate latitudes. To compare diet breadths on the basis of focal plant taxa, eight plant species in different families were randomly selected from each site, and the diet breadth of the subset of caterpillars feeding on these hosts was calculated using only those focal plants. We also used modifications²⁸ of Whittaker's²⁹ index of beta (β) diversity as an alternative measure of specialization. For each site, eight host plants from different genera were used to calculate β . This process was repeated for 1,000 random combinations of host plant species per site, generating an estimate of β for each site, along with 95% confidence intervals. Sites for which 95% CIs did not overlap were considered to be statistically different.

Full Methods and any associated references are available in the online version of the paper at www.nature.com/nature.

Received 14 March; accepted 27 April 2007.

- Hillebrand, H. On the generality of the latitudinal diversity gradient. *Am. Nat.* **163**, 192–211 (2004).
- Hutchinson, G. E. Homage to Santa Rosalia, or Why are there so many kinds of animals? *Am. Nat.* **93**, 145–159 (1959).
- MacArthur, R. H. & Levins, R. The limiting similarity, convergence, and divergence of coexisting species. *Am. Nat.* **101**, 377–385 (1967).
- Connell, J. H. Diversity in tropical rain forests and coral reefs. *Science* **199**, 1302–1310 (1978).
- Grant, P. R. & Grant, B. R. Evolution of character displacement in Darwin's finches. *Science* **313**, 224–226 (2006).
- Farrell, B. D. 'Inordinate fondness' explained: why are there so many beetles? *Science* **281**, 555–559 (1998).
- Schluter, D. *The Ecology of Adaptive Radiation* (Oxford Univ. Press, Oxford, 2000).
- Thompson, J. N. *The Geographic Mosaic of Coevolution* (Univ. of Chicago Press, Chicago, 2005).
- Darwin, C. *On the Origin of Species by Means of Natural Selection, or the Preservation of Favoured Races in the Struggle for Life* (John Murray, London, 1859).
- Wallace, A. *Tropical Nature and Other Essays* (MacMillan, London, 1878).
- Armbruster, S. W. in *Plant–Pollinator Interactions* (eds Wasser, N. M. & Ollerton, J.) 260–282 (Chicago Univ. Press, Chicago, 2006).
- Novotny, V. et al. Why are there so many species of herbivorous insects in tropical rainforests? *Science* **313**, 1115–1118 (2006).

- Price, P. W. in *Plant–Animal Interactions* (eds Herrera, C. M. & Pellmyr, O.) 3–26 (Blackwell, Oxford, 2002).
- Thomas, C. D. Fewer species. *Nature* **347**, 237 (1990).
- Lewinsohn, T. M., Novotny, V. & Basset, Y. Insects on plants: Diversity of herbivore assemblages revisited. *Annu. Rev. Ecol. Syst.* **36**, 597–620 (2005).
- Irschick, D., Dyer, L. A. & Sherry, T. Phylogenetic methods for studying specialization. *Oikos* **110**, 404–408 (2005).
- Ødegaard, F., Diserud, O. H. & Østbye, K. The importance of plant relatedness for host utilization among phytophagous insects. *Ecol. Lett.* **8**, 612–617 (2005).
- Hajibabaei, M., Janzen, D. H., Burns, J. M., Hallwachs, W. & Hebert, P. D. N. DNA barcodes distinguish species of tropical Lepidoptera. *Proc. Natl Acad. Sci. USA* **103**, 968–971 (2006).
- Janzen, D. H. Coevolution of mutualism between ants and acacias in Central America. *Evolution Int. J. Org. Evolution* **20**, 249–275 (1966).
- Coley, P. D. & Barone, J. A. Herbivory and plant defenses in tropical forests. *Annu. Rev. Ecol. Syst.* **27**, 305–335 (1996).
- Dyer, L. A. & Coley, P. D. in *Multitrophic Level Interactions* (eds Tscharntke, T. & Hawkins, B.) 67–88 (Cambridge Univ. Press, Cambridge, 2002).
- Marquis, R. J. & Braker, H. E. in *La Selva; Ecology and Natural History of a Tropical Rain Forest* (eds McDade, L., Bawa K. L., Hespeneheide, H. A. & Hartshorn, G. S.) 261–281 (Univ. of Chicago Press, Chicago, 1994).
- Wilf, P., Labandeira, C. C., Johnson, K. R. & Ellis, B. Decoupled plant and insect diversity after the end-Cretaceous extinction. *Science* **313**, 1112–1115 (2006).
- Hawkins, B. A. & Porter, E. E. Does herbivore diversity depend on plant diversity? The case of California butterflies. *Am. Nat.* **161**, 40–49 (2003).
- Tilman, D. *Resource Competition and Community Structure* (Princeton Univ. Press, Princeton, 1982).
- Chase, J. M. & Leibold, M. A. *Ecological Niches: Linking Classical and Contemporary Approaches* (Univ. of Chicago Press, Chicago, 2003).
- Colwell, R. K. & Coddington, J. A. Estimating terrestrial biodiversity through extrapolation. *Phil. Trans. R. Soc. Lond. B* **345**, 101–118 (1994).
- Kiflawi, M. & Spencer, M. Confidence intervals and hypothesis testing for beta diversity. *Ecology* **85**, 2895–2900 (2004).
- Whittaker, R. Vegetation of the Siskiyou Mountains, Oregon and California. *Ecol. Monogr.* **30**, 279–338 (1960).

Supplementary Information is linked to the online version of the paper at www.nature.com/nature.

Acknowledgements We thank D. Janzen, D. Gruner, G. Rodriguez, J. Landosky and R. Forkner for helpful suggestions for improving the manuscript; G. Howse for making available the CFIS data; E. Selig, A. Frevert, J. McGrath and M. Walker for their efforts in constructing the Canadian database; and a large number of taxonomists, field assistants and students for their help in generating all data. Funding came from the US National Science Foundation, Earthwatch Institute, National Geographic, Tulane University, University of Missouri Research Award, Wesleyan University's Hughes Summer Research Program, and the National Institute for Climate Change Research.

Author Contributions All authors designed and performed data collection protocols and contributed substantially to writing the paper; M.S.S. proposed the original idea for the paper; M.S.S. and L.A.D. designed the analyses and wrote the first full draft of the paper; J.O.S., R. J. Marquis, J. T. Lill and R. E. Ricklefs contributed extensive revisions; L.A.D. performed statistical analyses and created figures.

Author Information Reprints and permissions information is available at www.nature.com/reprints. The authors declare no competing financial interests. Correspondence and requests for materials should be addressed to L.A.D. (ldyer@tulane.edu).

METHODS

Methods of rearing the caterpillars used in this study are described in detail in refs 30–35. The Connecticut data included only 13 host plant genera; diet breadth is therefore underestimated for this site; these data were only used in the β diversity measure of diet breadth. Voucher specimens of adults were deposited at appropriate museums (Supplementary Information). Tropical plant species were identified by knowledgeable taxonomists (Supplementary Information).

We used MANOVA to compare the number of plant species, genera, and families fed on by each of the caterpillar species in tropical versus temperate latitudes. Profile analysis was used to compare the response of these different taxonomic measures of diet breadth between the two latitude classes. To compare diet breadths on the basis of focal plant taxa, eight plant species in different families were randomly selected from each site, and the diet breadth of the subset of caterpillars feeding on these hosts was calculated using only those focal plants. We also examined herbivore species turnover across focal host plant species as an alternative measure of specialization. We used modifications²⁸ of Whittaker's²⁹ index of beta (β) diversity across eight host plants as an index of specialization. Mathematically, β represents the probability that a lepidopteran species with an average diet breadth on the eight plant species will be missing from a host plant randomly picked from the eight species. Thus, $\beta = 0$ when all lepidopteran species occur on all host plants, and β approaches 1 when all Lepidoptera are restricted to a single host plant. Higher values of β indicate greater host specialization. For each site, eight host plants, each from a different genus, were selected from the plant species sampled at each site to calculate β . This process was repeated for 1,000 random combinations of host plant species per site. The number of focal plant species (8) in each combination was chosen to mimic one approach used by Novotny *et al.*¹²; subsets of randomly selected plant species of other sizes (6, 14) yielded similar results (Supplementary Information). The number of host plants from which the subsets were randomly drawn varied between sites (see Supplementary Information), but only host plants with at least 50 rearing records are included in the general pool. This process generated an estimate of β for each site, along with 95% CIs. Sites for which 95% CIs did not overlap were considered to be statistically different.

30. McGugan, B. M. (ed) *Forest Lepidoptera of Canada Recorded by the Forest Insect Survey* Vol. 1, *Papilionidae to Arctiidae* (Department of Forestry of Canada, Ottawa, 1958).
31. Gentry, G. & Dyer, L. A. On the conditional nature of neotropical caterpillar defenses against their natural enemies. *Ecology* **83**, 3108–3119 (2002).
32. Stireman, J. O. & Singer, M. S. Determinants of parasitoid–host associations: insights from a natural tachinid–lepidopteran community. *Ecology* **84**, 296–310 (2003).
33. Stireman, J. O. *et al.* Climatic unpredictability and caterpillar parasitism: implications of global warming. *Proc. Natl Acad. Sci. USA* **102**, 17384–17387 (2005).
34. Coley, P. D., Bateman, M. L. & Kursar, T. A. The effects of plant quality on caterpillar growth and defense against natural enemies. *Oikos* **115**, 219–228 (2006).
35. Diniz, I. R. & Morais, H. C. Lepidopteran caterpillar fauna of cerrado host plants. *Biodiv. Conserv.* **6**, 817–836 (1997).

LETTERS

A gastrin-releasing peptide receptor mediates the itch sensation in the spinal cord

Yan-Gang Sun¹ & Zhou-Feng Chen^{1,2,3}

Itching, or pruritus, is defined as an unpleasant cutaneous sensation that serves as a physiological self-protective mechanism to prevent the body from being hurt by harmful external agents. Chronic itch represents a significant clinical problem resulting from renal diseases and liver diseases, as well as several serious skin diseases such as atopic dermatitis^{1–3}. The identity of the itch-specific mediator in the central nervous system, however, remains elusive. Here we describe that the gastrin-releasing peptide receptor (GRPR) plays an important part in mediating itch sensation in the dorsal spinal cord. We found that gastrin-releasing peptide is specifically expressed in a small subset of peptidergic dorsal root ganglion neurons, whereas expression of its receptor GRPR is restricted to lamina I of the dorsal spinal cord. GRPR mutant mice showed comparable thermal, mechanical, inflammatory and neuropathic pain responses relative to wild-type mice. In contrast, induction of scratching behaviour was significantly reduced in GRPR mutant mice in response to pruritogenic stimuli, whereas normal responses were evoked by painful stimuli. Moreover, direct spinal cerebrospinal fluid injection of a GRPR antagonist significantly inhibited scratching behaviour in three independent itch models. These data demonstrate that GRPR is required for mediating the itch sensation rather than pain, at the spinal level. Our results thus indicate that GRPR may represent the first molecule that is dedicated to mediating the itch sensation in the dorsal horn of the spinal cord, and thus may provide a central therapeutic target for antipruritic drug development.

GRPR, a G-protein coupled receptor, is a mammalian homologue of the amphibian bombesin-like peptide receptor that has been implicated in a variety of physiological processes and behaviours, including food intake and fear memory^{4,5}. Intracerebral administration of bombesin in rodents elicited grooming behaviour^{6,7}, which is relevant to the hypothesis that bombesin is a mediator of pruritus⁸. There is, however, little evidence in support of this hypothesis. Indeed, bombesin-evoked grooming behaviour has been generally regarded as a manifestation of stress response and thermoregulation^{9,10}.

We first found that gastrin-releasing peptide (GRP) is expressed in a subset of small and medium-sized dorsal root ganglion (DRG) neurons (Fig. 1a), and that it is colocalized with peripherin, a marker for unmyelinated fibres (Fig. 1b). GRP is also colocalized with peptidergic markers CGRP and substance P, but it neither co-stained with IB4, a nonpeptidergic marker, nor with myelinated marker NF200 (Fig. 1c, d, e, and data not shown). Furthermore, an approximate 80% of GRP⁺ neurons express TRPV1, a vanilloid receptor important for detecting thermal and chemical stimuli, in the DRGs (Supplementary Fig. 1). In the spinal cord, GRP⁺ fibres are restricted to the lamina I and II outer layer (IIo) (Fig. 1f). GRP⁺ fibres in the dorsal horn largely diminished after dorsal rhizotomy (Supplementary Fig. 2), indicating that GRP arises from primary afferents. We

found no GRP mRNA expression in the superficial dorsal horn in adult mice (data not shown). In contrast, we found GRPR⁺ neurons in lamina I of the dorsal horn (Fig. 1g, h) but none in the deep dorsal

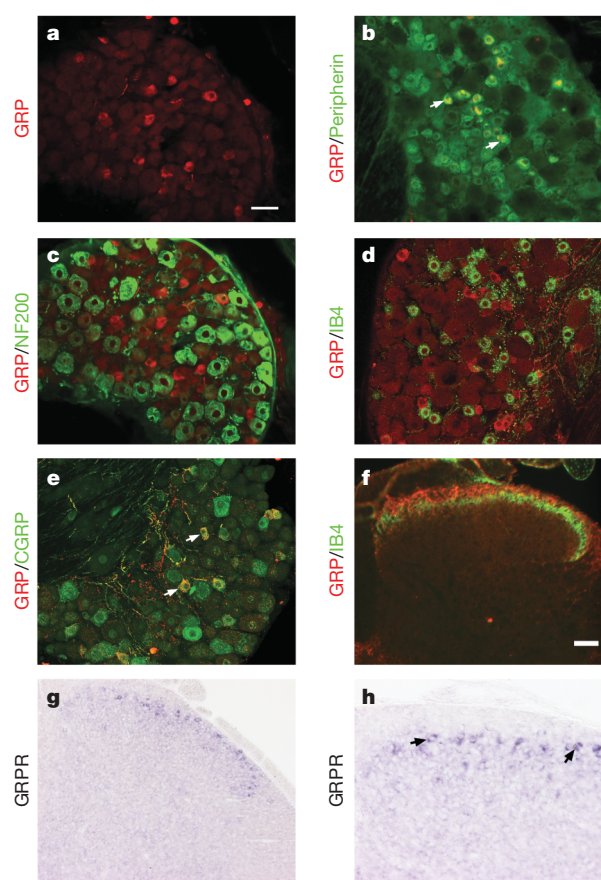


Figure 1 | Expression pattern of GRP and GRPR in adult DRG and dorsal horn of the spinal cord. **a**, GRP is detected in small to medium-sized DRG neurons by immunocytochemistry. **b–e**, Double-staining of GRP with peripherin (**b**), NF200 (**c**), IB4 (**d**) and CGRP (**e**) in DRGs. GRP (red) is localized in peripherin⁺ (green) DRG neurons (**b**). Double-staining of GRP (red) and NF200 (green) in adult mouse DRGs indicates that GRP and NF200 expression do not overlap (**c**). GRP is present in adult DRG neurons labelled with a CGRP antibody (green in **e**), but not with IB4 (green in **d**). Arrows indicate double-labelled neurons (**b**, **e**). **f**, GRP⁺ fibres (red) are located in the superficial dorsal horn; IB4 (green) marks lamina II inner layer (IIi) of the dorsal spinal cord. **g**, **h**, *In situ* hybridization (purple) showed that GRPR is present in the superficial dorsal horn of the spinal cord. Higher magnification of the dorsal horn is shown in **h**. Arrows indicate the GRPR⁺ neurons (**h**). Scale bars, 50 μm (**a**, **b**, **c**, **d**, **e**, **h**); 100 μm (**f** and **g**).

¹Department of Anesthesiology, ²Department of Molecular Biology and Pharmacology, ³Department of Psychiatry, Washington University School of Medicine Pain Center, St Louis, Missouri 63110, USA.

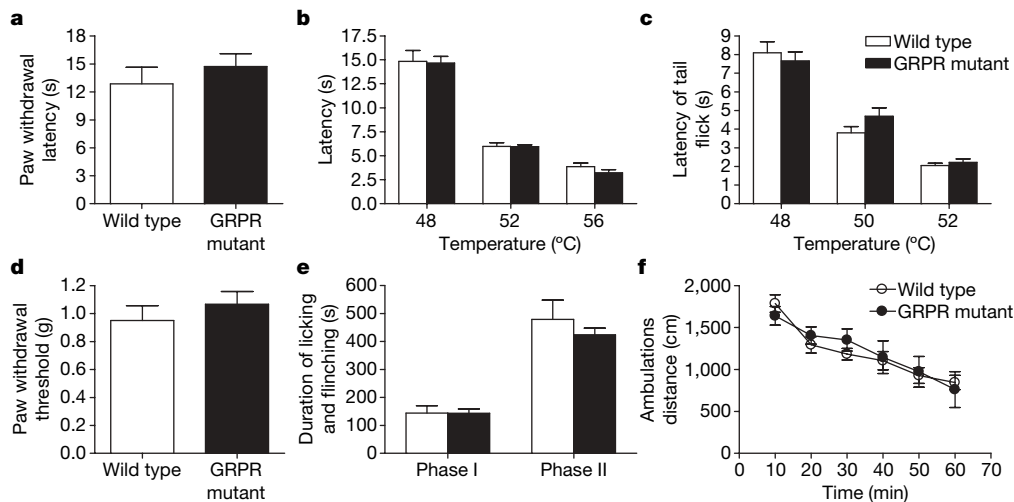


Figure 2 | Pain behaviours and locomotor activity are normal in GRPR mutant mice. **a–c**, Responses to noxious thermal stimulation were measured by paw withdrawal latency (Hargreaves test; **a**), hotplate (**b**) and water immersion tail-flick latency (**c**). There were no significant differences in thermal pain responses between wild-type ($n = 8$; white bars) and GRPR mutant mice ($n = 7$; black bars); Student's t -test; $P > 0.05$. **d**, Sensitivity to mechanical stimuli of GRPR mutant mice ($n = 7$; black bars) as measured by paw withdrawal threshold on exposure to von Frey filaments was

comparable to wild-type mice ($n = 8$; white bars); Student's t -test; $P > 0.05$. **e**, Spontaneous pain responses in the first (0–10 min) and second phase (10–60 min) of the formalin test are comparable between wild-type ($n = 8$; white bars) and GRPR mutant mice ($n = 9$; black bars); Student's t -test; $P > 0.05$. **f**, Locomotor activity measured by ambulations distance is comparable between wild-type ($n = 8$; open circles) and GRPR mutant mice ($n = 7$; filled circles); repeated measures ANOVA (ANOVA); $P > 0.05$. All data are presented as means \pm s.e.m. Error bars represent s.e.m.

horn or the ventral horn of the spinal cord (Fig. 1g, and data not shown). Several studies have suggested an itch-dedicated pathway in the peripheral and central nervous system that involves a group of itch-specific unmyelinated C-fibres and spinothalamic lamina I neurons in the spinal cord^{11,12}. Thus, our results indicate that the GRP/GRPR signalling pathway may be involved in perception of pain and/or itch sensation at the spinal level.

To assess whether GRPR may contribute to pain sensation, we examined thermal, mechanical, inflammatory and neuropathic pain responses of GRPR mutant mice. GRPR mutant mice and wild-type mice did not differ in the Hargreave's paw withdrawal test of thermal nociception (Fig. 2a). And in the hotplate and tail-flick tests, GRPR mutant mice showed comparable thermal sensitivity to the wild-type control across a range of temperatures (48 °C, 52 °C and 56 °C for hotplate, and 48 °C, 50 °C and 52 °C for tail-flick tests; Fig. 2b, c). Mechanical pain sensitivity was measured using graded von Frey filaments. The mechanical threshold in GRPR mutant mice was similar to that in wild-type mice (Fig. 2d). These results indicate that GRPR signalling is not required for the transmission of acute pain messages. To measure the response of GRPR mutant mice to inflammatory pain, flinching and licking behaviours of GRPR mutant mice were compared with their control littermates after injection of 5% formalin (10 μ l) into the right hindpaw of the animals. No

statistically significant differences in the first phase (0–10 min) or in the second phase (10–60 min) between GRPR mutant and wild-type mice were found (Fig. 2e). In addition, mechanical hypersensitivity produced by hindpaw injection of complete Freund's adjuvant was indistinguishable between GRPR mutant mice and wild-type mice (Supplementary Fig. 3). GRPR mutant and wild-type mice also showed comparable mechanical hyperalgesia in a neuropathic pain model (Supplementary Fig. 4). Finally, examination of a pain-related gene expression profile did not reveal significant changes in the dorsal spinal cord of GRPR mutant mice (Supplementary Fig. 5). Taken together, these data suggest that GRPR is not essential for transmission of noxious information.

To ascertain whether GRPR is required for itch sensation, we studied the effects of several pruritogenic agents in GRPR mutant mice and wild-type mice. Intradermal injection of compound 48/80 (100 μ g per 50 μ l), which degranulates mast cells to release histamine¹³, induced vigorous scratching behaviour within 30 min (Fig. 3a). In contrast, although compound 48/80 also initiated scratching behaviour in GRPR mutant mice, the number of scratches was significantly smaller compared with that of wild-type mice ($P < 0.05$, Fig. 3a). We next used a protease-activated receptor 2 (PAR2) agonist as a pruritogenic agent. PAR2, a G-protein coupled receptor, is expressed in primary sensory neurons and is activated by proteinases

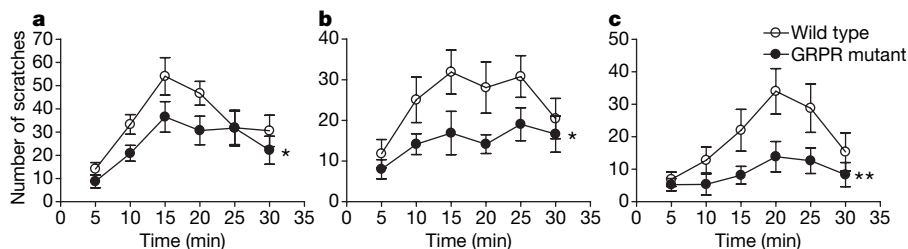


Figure 3 | Scratching behaviour is reduced in GRPR mutant mice. **a**, The scratching behaviour induced by intradermal injection of compound 48/80 (100 μ g per 50 μ l) is significantly decreased in GRPR mutant mice ($n = 17$; filled circles) compared with wild-type mice ($n = 14$; open circles); repeated measures ANOVA (ANOVA); $*P < 0.05$. **b**, The scratching behaviour induced by intradermal injection of PAR2 agonist SLIGRL-NH2 (100 μ g per 50 μ l) in wild-type ($n = 11$; open circles) and GRPR mutant mice ($n = 11$;

filled circles) shows GRPR mutant mice have a severely blunted response; repeated measures ANOVA (ANOVA); $*P < 0.05$. **c**, The scratching behaviour induced by intradermal injection of chloroquine (200 μ g per 50 μ l) in wild-type ($n = 11$; open circles) and GRPR mutant mice ($n = 11$; filled circles) shows GRPR mutant mice have a significantly reduced response; repeated measures ANOVA (ANOVA); $**P < 0.01$. All data are presented as means \pm s.e.m. Error bars represent s.e.m.

such as trypsin and tryptase^{14,15}. PAR2 mediates itch in human skin, and PAR2 agonist (SLIGRL-NH2) is a histamine-independent itch inducer^{16,17}. In wild-type mice, intradermal injection of SLIGRL-NH2 (100 µg per 50 µl) induced robust scratching behaviour within 30 min. In contrast, the number of scratches decreased significantly in GRPR mutant mice ($P < 0.05$, Fig. 3b). Finally, we used the chloroquine model to assess scratching behaviour in GRPR mutant mice^{18,19}. The scratching behaviour induced by intradermal injection of chloroquine (200 µg per 50 µl) was significantly reduced in GRPR mutant mice compared with wild-type mice ($P < 0.01$, Fig. 3c). The reduction in the number of scratches was not due to a defect in locomotor activity because there was no significant difference in spontaneous locomotor activity between wild-type and GRPR mutant mice (Fig. 2f). Importantly, these differences were only found in response to known pruritogenic agents, but not to the algisogenic agent (Supplementary Fig. 6a). Thus, the number of scratches did not differ significantly between GRPR mutant and wild-type mice after intradermal injection of vehicle (data not shown). These results suggest that GRPR is a receptor that is important to the transmission of itch information in the spinal cord circuits.

We postulated that if GRPR mediates itch sensation, then activation of GRPR at the spinal level may initiate the transmission of itch signals, which would subsequently result in scratching behaviour. To test this hypothesis, we intrathecally administered the GRPR agonist GRP₁₈₋₂₇ (ref. 20) and found that GRP₁₈₋₂₇ indeed induced scratching behaviour in a dose-dependent manner (Fig. 4a, Supplementary Fig. 7). At these doses, intrathecal GRP₁₈₋₂₇ did not affect the pain sensitivity tested by tail-flick assay (data not shown). When GRP₁₈₋₂₇ was injected into GRPR mutant mice intrathecally, the level of scratching behaviour was significantly lower compared to wild-type mice ($P < 0.01$, Fig. 4a). Moreover, intrathecal injection of the GRPR antagonist²¹ (10 min before injection of GRP₁₈₋₂₇) significantly inhibited GRP₁₈₋₂₇-induced scratching behaviour (Fig. 4b), whereas

this antagonist itself did not induce any scratching behaviour (data not shown). Finally, we intrathecally injected the GRPR antagonist 10 min before intradermal injection of each of the pruritogenic agents studied above and found a significant reduction of the scratching behaviour (Fig. 4c, d, e). In contrast, the algisogenic agent (formalin)-induced scratching behaviour was not significantly affected by the GRPR antagonist (Supplementary Fig. 6b). Thus, our results suggest that GRP acts through the spinal GRPR to mediate the transmission of information that drives scratching behaviour in response to pruritogenic stimuli only.

Taken together, our data provide genetic, pharmacological and behavioural evidence supporting the hypothesis that GRPR is a specific itch-signalling molecule in the spinal cord. Although itch and pain are intimately related and may share similar peripheral and central mechanisms^{2,22,23}, we believe that the reduced scratching behaviour of GRPR mutant mice reflects a defect in itching, rather than a defect in pain sensation, for several reasons. First, our results showed that pain sensitivities were not compromised in GRPR mutant mice. This is also supported by the observation that GRPR mutant mice showed normal response to foot shock²⁴. Second, the scratching behaviour responding to the pruritogenic agents was significantly reduced in GRPR mutant mice, but remained normal in the same mice in response to the algisogenic agent formalin. Finally, activation of the GRPR receptor at the spinal level induced dose-dependent scratching behaviour without affecting pain behaviour. One interesting observation is that GRPR mutant mice showed differential sensitivity in different itch models: the reduced scratching behaviours of GRPR mutant mice are much more notable in PAR2 and chloroquine models than in the compound 48/80 model. Unlike compound 48/80, PAR2 agonist SLIGRL-NH2 and chloroquine are believed to act through a histamine-independent mechanism^{17,18}. Therefore, it is possible that itch signals may be processed and relayed through distinct types of central mediators in the spinal cord in

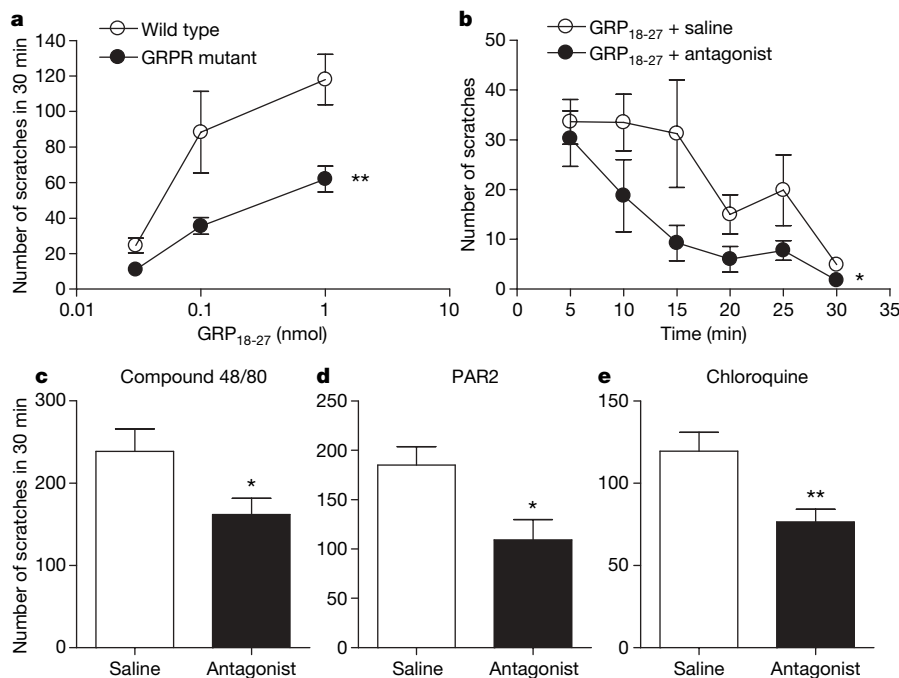


Figure 4 | Effects of GRPR agonist and antagonist on scratching behaviour. **a**, The scratching behaviour is monitored for 30 min after intrathecal injection of GRP₁₈₋₂₇ (0.03, 0.1 or 1.0 nmol per 5 µl). GRP₁₈₋₂₇ induced dose-dependent scratching behaviour in wild-type mice ($n = 7$; open circles). The number of scratches was markedly reduced in GRPR mutant mice ($n = 7$; filled circles) when compared to wild-type littermate controls; repeated measures ANOVA (ANOVA); ** $P < 0.01$. **b**, The effect of GRP₁₈₋₂₇ (1.0 nmol per 2.5 µl) was significantly blocked by intrathecal injection of GRPR antagonist (D-Phe-6-Bn(6-13)OMe, 1.0 nmol per 2.5 µl, $n = 8$; filled

circles) compared with vehicle (2.5 µl, $n = 8$; open circles); repeated measures ANOVA (ANOVA); * $P < 0.05$. **c–e**, Compared with the control group (white bars), intrathecal injection of the GRPR antagonist (1.0 nmol, black bars) significantly inhibited scratching behaviour induced by intradermal injection of compound 48/80, PAR2 agonist SLIGRL-NH2, or chloroquine ($n = 10, 9$ and 10 for compound 48/80, SLIGRL-NH2, and the chloroquine model, respectively). Student's t -test comparing genotypes within treatment; * $P < 0.05$, ** $P < 0.01$. All data are presented as means \pm s.e.m. Error bars represent s.e.m.

response to distinct types of pruritogenic stimuli. Alternatively, GRPR signalling may be differentially recruited in response to different types of pruritogenic stimuli. It is also possible that other bombesin-like receptors in the spinal cord may produce a compensatory effect in GRPR mutant mice²⁵. Although our results suggest that GRPR is specifically involved in itch not pain sensation, the possibility that GRPR-expressing neurons are involved in pain sensation can not be excluded, given the fact that the selective histamine-sensitive neurons also respond to capsaicin^{11,12}. Nevertheless, our results strongly suggest the existence of an itch-specific GRPR-mediated molecular signalling pathway in the dorsal horn of the spinal cord. Our study should have important clinical implications for the treatment of pruritus. For example, chloroquine has been used to treat malaria fever in Africa, but it often induced intractable pruritus in these patients²⁶. GRP/GRPR signalling pathway may provide a central target for therapeutic treatment of chronic and intractable pruritus, without compromising the ability to sense acute noxious stimulus, which itself would be detrimental to the patient.

METHODS SUMMARY

Behaviour tests. GRPR mutant mice and littermate wild-type mice were used in the behaviour experiments²⁷. Mice were shaved at the back of the neck where intradermal injections were then given. Hindlimb scratching behaviour directed towards the shaved area at the back of the neck was observed for 30 min at 5-min intervals¹⁷. Pain behaviours were assessed as described previously²⁸. Locomotor activity of mice was evaluated by an open-field test over a 1-h period in transparent (48 × 25 × 21 cm) polystyrene enclosures as previously described²⁹.

Immunocytochemical staining and *in situ* hybridization. Immunocytochemical staining and *in situ* hybridization were performed as previously described²⁸. The following primary antibodies were used: rabbit anti-GRP (Immunostar), guinea pig anti-CGRP (Peninsula), mouse anti-peripherin (Chemicon), and mouse anti-NF200 (N52, Sigma). The nonpeptidergic primary afferents were identified with IB4-biotin (Vector Laboratories) staining and were visualized with avidin coupled to FITC (Vector Laboratories). For double-staining, secondary antibodies (Jackson ImmunoResearch), including donkey anti-rabbit IgG coupled to Cy3 for GRP, donkey anti-guinea pig IgG coupled to FITC for CGRP, and donkey anti-mouse IgG coupled to FITC for NF200 or peripherin were used.

Data analysis. Statistical comparisons were performed with two-way ANOVA (ANOVA) and Student's *t*-test. All data are expressed as the mean ± standard error of the mean (s.e.m.) and error bars represent s.e.m. *P* < 0.05 was considered statistically significant.

Full Methods and any associated references are available in the online version of the paper at www.nature.com/nature.

Received 4 August 2006; accepted 18 June 2007.

Published online 25 July 2007.

1. Paus, R., Schmelz, M., Biro, T. & Steinhoff, M. Frontiers in pruritus research: scratching the brain for more effective itch therapy. *J. Clin. Invest.* **116**, 1174–1186 (2006).
2. Ikoma, A., Steinhoff, M., Stander, S., Yosipovitch, G. & Schmelz, M. The neurobiology of itch. *Nature Rev. Neurosci.* **7**, 535–547 (2006).
3. Greaves, M. W. Itch in systemic disease: therapeutic options. *Dermatol. Ther.* **18**, 323–327 (2005).
4. Roesler, R., Henriques, J. A. & Schwartzmann, G. Gastrin-releasing peptide receptor as a molecular target for psychiatric and neurological disorders. *CNS Neurol. Disord. Drug Targets* **5**, 197–204 (2006).
5. Battey, J. & Wada, E. Two distinct receptor subtypes for mammalian bombesin-like peptides. *Trends Neurosci.* **14**, 524–528 (1991).
6. Cowan, A., Khunawatt, P., Zhu, X. Z. & Gmerek, D. E. Effects of bombesin on behavior. *Life Sci.* **37**, 135–145 (1985).

7. Gmerek, D. E. & Cowan, A. Studies on bombesin-induced grooming in rats. *Peptides* **4**, 907–913 (1983).
8. Gmerek, D. E. & Cowan, A. Bombesin—a central mediator of pruritus? *Br. J. Dermatol.* **109**, 239 (1983).
9. O'Donohue, T. L. *et al.* A role for bombesin in sensory processing in the spinal cord. *J. Neurosci.* **4**, 2956–2962 (1984).
10. Moody, T. W. & Merali, Z. Bombesin-like peptides and associated receptors within the brain: distribution and behavioral implications. *Peptides* **25**, 511–520 (2004).
11. Schmelz, M., Schmidt, R., Bickel, A., Handwerker, H. O. & Torebjork, H. E. Specific C-receptors for itch in human skin. *J. Neurosci.* **17**, 8003–8008 (1997).
12. Andrew, D. & Craig, A. D. Spinothalamic lamina I neurons selectively sensitive to histamine: a central neural pathway for itch. *Nature Neurosci.* **4**, 72–77 (2001).
13. Kuraishi, Y., Nagasawa, T., Hayashi, K. & Satoh, M. Scratching behavior induced by pruritogenic but not algogenic agents in mice. *Eur. J. Pharmacol.* **275**, 229–233 (1995).
14. Nystedt, S., Emilsson, K., Wahlestedt, C. & Sundelin, J. Molecular cloning of a potential proteinase activated receptor. *Proc. Natl Acad. Sci. USA* **91**, 9208–9212 (1994).
15. Steinhoff, M. *et al.* Agonists of proteinase-activated receptor 2 induce inflammation by a neurogenic mechanism. *Nature Med.* **6**, 151–158 (2000).
16. Steinhoff, M. *et al.* Proteinase-activated receptor-2 mediates itch: a novel pathway for pruritus in human skin. *J. Neurosci.* **23**, 6176–6180 (2003).
17. Shimada, S. G., Shimada, K. A. & Collins, J. G. Scratching behavior in mice induced by the proteinase-activated receptor-2 agonist, SLIGRL-NH₂. *Eur. J. Pharmacol.* **530**, 281–283 (2006).
18. Inan, S. & Cowan, A. Kappa opioid agonists suppress chloroquine-induced scratching in mice. *Eur. J. Pharmacol.* **502**, 233–237 (2004).
19. Green, A. D., Young, K. K., Lehto, S. G., Smith, S. B. & Mogil, J. S. Influence of genotype, dose and sex on pruritogen-induced scratching behavior in the mouse. *Pain* **124**, 50–58 (2006).
20. Ladenheim, E. E., Taylor, J. E., Coy, D. H., Moore, K. A. & Moran, T. H. Hindbrain GRP receptor blockade antagonizes feeding suppression by peripherally administered GRP. *Am. J. Physiol.* **271**, R180–R184 (1996).
21. Wang, L. H. *et al.* des-Met carboxyl-terminally modified analogues of bombesin function as potent bombesin receptor antagonists, partial agonists, or agonists. *J. Biol. Chem.* **265**, 15695–15703 (1990).
22. Stander, S. & Schmelz, M. Chronic itch and pain—similarities and differences. *Eur. J. Pain* **10**, 473–478 (2006).
23. McMahon, S. B. & Koltzenburg, M. Itching for an explanation. *Trends Neurosci.* **15**, 497–501 (1992).
24. Shumyatsky, G. P. *et al.* Identification of a signaling network in lateral nucleus of amygdala important for inhibiting memory specifically related to learned fear. *Cell* **111**, 905–918 (2002).
25. Kroog, G. S., Jensen, R. T. & Battey, J. F. Mammalian bombesin receptors. *Med. Res. Rev.* **15**, 389–417 (1995).
26. Sowunmi, A., Walker, O. & Salako, L. A. Pruritus and antimalarial drugs in Africans. *Lancet* **2**, 213 (1989).
27. Hampton, L. L. *et al.* Loss of bombesin-induced feeding suppression in gastrin-releasing peptide receptor-deficient mice. *Proc. Natl Acad. Sci. USA* **95**, 3188–3192 (1998).
28. Chen, Z. F. *et al.* The paired homeodomain protein DRG11 is required for the projection of cutaneous sensory afferent fibers to the dorsal spinal cord. *Neuron* **31**, 59–73 (2001).
29. Wozniak, D. F. *et al.* Apoptotic neurodegeneration induced by ethanol in neonatal mice is associated with profound learning/memory deficits in juveniles followed by progressive functional recovery in adults. *Neurobiol. Dis.* **17**, 403–414 (2004).

Supplementary Information is linked to the online version of the paper at www.nature.com/nature.

Acknowledgements We thank J. Yin, C.-S. Qiu and K.-H. Zhang for technical assistance and J. Battey for providing GRPR mutant mice. We are grateful to A. Basbaum, E. Carstens, L. Hampton and J. Battey for critical comments on the manuscript. We also thank D. H. Coy for providing the GRPR antagonist. The work was supported by an NIH RO1 to Z.F.C.

Author Information Reprints and permissions information is available at www.nature.com/reprints. The authors declare no competing financial interests. Correspondence and requests for materials should be addressed to Z.F.C. (chenz@wustl.edu).

METHODS

Animals. GRPR mutant mice and littermate wild-type mice were used in the behaviour experiments²⁷. Mice were backcrossed to C57BL/6J strain for more than 10 generations. C57BL/6J mice (Jackson laboratory) were used in the GRPR antagonist experiment. Male mice between 8 and 12 weeks of age were acclimated to the experimental room and were used for experiments. All behavioural tests were done by the observer blind to the treatment or genotype of the animals. All the experiments were performed in accordance with the guidelines of the National Institutes of Health and the International Association for the Study of Pain and were approved by the Animal Studies Committee at the Washington University School of Medicine.

Drugs. GRP₁₈₋₂₇ (0.03, 0.1, 1.0 nmol, Bachem), and the GRPR antagonist, D-Phe-6-Bn(6-13)OMe, (1.0 nmol, kindly provided by D. H. Coy) were dissolved in sterile saline and administered intrathecally with a volume of 5 μ l, unless specified. Compound 48/80 (100 μ g, Sigma-Aldrich), chloroquine (200 μ g, Sigma-Aldrich), and PAR2 agonist, H-Ser-Leu-Ile-Gly-Arg-Leu-NH₂, (SLIGRL-NH₂, 100 μ g, Bachem) were dissolved in sterile saline and administered by intradermal injection at a volume of 50 μ l.

Itch behaviour tests. Prior to experiments, mice were given 30 min to acclimate to a small plastic chamber (15 \times 26 \times 12 cm). For intradermal injections of drugs, mice were briefly removed from the chamber and intradermally injected with drugs. Hindlimb scratching behaviour directed towards the shaved area at the back of the neck was observed for 30 min at 5-min intervals. One scratch is defined as a lifting of the hind limb towards the injection site and then a replacing of the limb back to the floor, regardless of how many scratching strokes take place between those two movements¹⁷.

Pain behaviours. Pain behaviours were assessed as described previously²⁸. Thermal sensitivity was determined using hotplate (48, 52, or 56 °C), paw-flick (method of Hargreaves) or water immersion tail-flick methods (48, 50, or 52 °C). For the hotplate test, the latency for the mouse to lick its hindpaw or jump was recorded. For the Hargreaves test, thermal sensitivity was measured using a Hargreaves-type apparatus (IITC Inc.). The latency for the mouse to withdraw from the heat source was recorded. For the water immersion tail-flick test, tails were dipped beneath the water in a temperature-controlled water bath (IITC Inc.). The latency to withdrawal was measured with a 10-s cutoff. Mechanical sensitivity was assessed using a set of calibrated von Frey filaments (Touch-Test kit, Stoelting). Each filament was applied 5 consecutive times and the smallest filament that evoked reflexive flinches of the paw on 3 of the 5 trials was taken as the paw withdrawal threshold. Inflammatory pain was determined using a formalin test by intraplantar injection of formalin (Sigma, 10 μ l of 5% formalin in saline) into the plantar surface of the right hindpaw. The total time spent in licking and flinching of the injected paw was monitored for 60 min.

Intrathecal injections and scratching behaviour analysis. Intrathecal injections into the lumbar region of unanaesthetized mice were performed as described previously³⁰. For the GRPR agonist experiment, different doses of GRP₁₈₋₂₇ or vehicle were injected at a volume of 5 μ l, and the number of scratching responses was counted for 30 min at 5-min intervals. For the GRPR antagonist experiment, GRPR antagonist was injected 10 min before either intrathecal injection of GRP₁₈₋₂₇ or intradermal injection of the pruritogenic agents, and the number of scratching responses was counted for 30 min at 5-min intervals after the injection of the pruritogenic agents or GRP₁₈₋₂₇.

30. Hylden, J. L. & Wilcox, G. L. Intrathecal morphine in mice: a new technique. *Eur. J. Pharmacol.* **67**, 313–316 (1980).

LETTERS

Global changes to the ubiquitin system in Huntington's disease

Eric J. Bennett¹, Thomas A. Shaler², Ben Woodman³, Kwon-Yul Ryu¹, Tatiana S. Zaitseva¹, Christopher H. Becker², Gillian P. Bates³, Howard Schulman² & Ron R. Kopito¹

Huntington's disease (HD) is a dominantly inherited neurodegenerative disorder caused by expansion of CAG triplet repeats in the huntingtin (*HTT*) gene (also called *HD*) and characterized by accumulation of aggregated fragments of polyglutamine-expanded HTT protein in affected neurons^{1,2}. Abnormal enrichment of HD inclusion bodies with ubiquitin, a diagnostic characteristic of HD and many other neurodegenerative disorders including Alzheimer's and Parkinson's diseases^{3,4}, has suggested that dysfunction in ubiquitin metabolism may contribute to the pathogenesis of these diseases^{5,6}. Because modification of proteins with polyubiquitin chains regulates many essential cellular processes including protein degradation, cell cycle, transcription, DNA repair and membrane trafficking⁷, disrupted ubiquitin signalling is likely to have broad consequences for neuronal function and survival. Although ubiquitin-dependent protein degradation is impaired in cell-culture models of HD^{8–11} and of other neurodegenerative diseases^{12,13}, it has not been possible to evaluate the function of the ubiquitin–proteasome system (UPS) in HD patients or in animal models of the disease, and a functional role for UPS impairment in neurodegenerative disease pathogenesis remains controversial^{14–16}. Here we exploit a mass-spectrometry-based method to quantify polyubiquitin chains¹⁷ and demonstrate that the abundance of these chains is a faithful endogenous biomarker of UPS function. Lys 48-linked polyubiquitin chains accumulate early in pathogenesis in brains from the R6/2 transgenic mouse model of HD, from a knock-in model of HD and from human HD patients, establishing that UPS dysfunction is a consistent feature of HD pathology. Lys 63- and Lys 11-linked polyubiquitin chains, which are not typically associated with proteasomal targeting, also accumulate in the R6/2 mouse brain. Thus, HD is linked to global changes in the ubiquitin system to a much greater extent than previously recognized.

Lys 48-linked polyubiquitin conjugates are the proximal substrates of proteasomal proteolysis⁷, so their steady-state abundance in the cell should reflect proteasome function in cells or tissues without the use of artificial reporters. We used a ubiquitin-association domain from human ubiquitin 2 (UBQLN2, also known as PLIC-2), which we called human P2UBA¹⁸, to capture polyubiquitin chains from lysates of HEK293 cells expressing the cytoplasmic UPS reporter NESGFP¹⁹ (ref. 9), exposed to the irreversible proteasome inhibitor clasto-lactacystin β -lactone (Lc, Supplementary Fig. 1 and Supplementary Discussion). The captured polypeptides were eluted, digested with trypsin, and the resulting peptides and isopeptides were separated by reverse-phase liquid chromatography in line with an electrospray time-of-flight mass spectrometer (LC-ESI-TOF-MS analysis). The abundance of the Lys 48-linked ubiquitin isopeptide (LIFAGK-(GG)-QLEDGR, abbreviated to UbK48) in the digest was

determined by comparison of the extracted UbK48 ion (mass-to-charge ratio, $m/z = 487.60$) to a 'spiked' internal standard consisting of the corresponding synthetic isopeptide labelled with ¹³C and ¹⁵N (Fig. 1b)^{17,19,20}.

This analysis revealed that the concentration of Lys 48-linked chains in cell lysates increased in proportion to the Lc concentration; this signal was eliminated by pretreatment of cell lysates with the deubiquitylating enzyme Usp2c²¹ (Fig. 1a–c). In contrast, the relative abundance of non-isopeptide-linked ubiquitin (EMF-ubiquitin), determined by subtracting the amount of human P2UBA-captured ubiquitin chains from the linear ubiquitin-derived ESTLHLVLR peptide (Fig. 1a, right), was not much affected by exposure to Lc (Fig. 1c). This increase in UbK48 relative to EMF-ubiquitin is not caused by preferential capture of Lys 48-linked chains by the human P2UBA domain, because each of the ubiquitylated species present in the human P2UBA-binding reaction is at a concentration more than tenfold lower than the experimentally determined dissociation constant for human P2UBA binding¹⁸ (Supplementary Fig. 2 and Supplementary Discussion).

Comparison of the magnitude of increase in UbK48 intensity in HEK293 cells treated with Lc with the extent of irreversible modification of the proteasome active site, assessed *in vitro* by cleavage of the fluorogenic substrate Suc-LLVY-AMC, demonstrates that the concentration of UbK48 isopeptide correlates strongly with a loss of proteasome activity, reaching a half-maximal level at ~43% inhibition (Fig. 1d). This dose–response profile is indistinguishable from that obtained by measurement of the fluorescent UPS reporter NESGFP¹⁹ (ref. 9) in the same cells (Fig. 1e). We conclude that cellular levels of UbK48 isopeptide can serve as a sensitive and valid tool to assess UPS impairment. This approach offers distinct advantages over previous methods in that it measures an endogenous and global parameter of UPS function and permits assessment of UPS status in any cell or tissue without the need to express an artificial reporter substrate^{8,22}.

To assess the effect of protein aggregation on UPS function, we measured UbK48 isopeptide levels in a mouse neuroblastoma cell line (N2a) harbouring a gene fusion between green fluorescent protein (GFP) and human huntingtin (*HTT*) exon 1 containing 16 glutamines (*HTTQ16GFP*) or 150 glutamines (*HTTQ150GFP*), expressed under the control of an inducible promoter¹⁰ (Fig. 2). In control experiments, we confirmed that immunoreactive high-molecular-mass ubiquitin conjugates begin to accumulate rapidly after exposure to the proteasome inhibitor MG132 in these cell lines; as in HEK293 cells, this increase was paralleled by a rapid rise in UbK48 but not in EMF-ubiquitin (Supplementary Fig. 4). *HTT* (exon 1) expression, assessed by GFP fluorescence (Fig. 2a) or immunoblot analysis (data not shown), was low or undetectable in untreated cells.

¹Department of Biological Sciences, Stanford University, Stanford, California 94305, USA. ²PPD Biomarker Discovery Inc., 1505 O'Brien Drive, Menlo Park, California 94025, USA.

³Department of Medical and Molecular Genetics, King's College London School of Medicine, London SE1 9RT, UK.

GFP intensity increased in both Q16 and Q150 cells after *HTT* (exon 1) induction, remaining diffuse in cells expressing *HTTQ16GFP* and forming multiple puncta that eventually coalesced into a single juxtanuclear inclusion body after two days in cells expressing *HTTQ150GFP* (Fig. 2a, b). The increase in *HTT* (exon 1) expression was paralleled by a much greater extensive rise in high-molecular-mass ubiquitin immunoreactivity in cells expressing *HTTQ150GFP* compared to *HTTQ16GFP* (Fig. 2c, d). Analysis of the human P2UBA-captured protein by mass spectrometry confirmed that Lys 48-linked chains increased to a much greater extent after induction of *HTTQ150GFP* compared to *HTTQ16GFP* (Fig. 2e). In cells expressing *HTTQ150GFP*, increased UbK48 levels were first detectable at one day post-induction, confirming that UPS impairment is present in cellular models of HD before the formation of microscopically detectable inclusion bodies⁹. UbK48 isopeptide levels were elevated 4–5-fold above the initial uninduced values after three days of induction, whereas the levels of EMF-ubiquitin increased more modestly (≤ 1.8 -fold) in the same cells. These data validate the use of UbK48 isopeptide levels as a biomarker for UPS impairment in a well-characterized cellular model of HD.

To determine whether UPS function is compromised by expression of mutant *HTT* *in vivo* we measured UbK48 isopeptide and EMF-ubiquitin concentrations in extracts from brains of R6/2 mice, a widely used mouse model of HD²³, which express a CAG-expanded *HTT* exon 1 transgene (Fig. 3). R6/2 mice are phenotypically normal at 2 weeks of age, motor impairment can be detected from 5–6 weeks of age, and the disease phenotype is pronounced at 12 weeks (ref. 23). Mass spectrometry analysis revealed that UbK48 isopeptide levels were significantly elevated at 6 and 12 weeks of age in the cortex (Fig. 3a, c) and the striatum (Fig. 3b, c) of R6/2 mice compared to non-transgenic littermates. In contrast, total ubiquitin levels, measured by enzyme-linked immunosorbent assay (ELISA) in unfractionated cortex homogenates (Supplementary Fig. 5a) or by mass spectrometry of human P2UBA-captured material (Supplementary Fig. 5b), were only slightly affected by the *HTT* transgene. Thus, the amount of ubiquitin present in Lys 48-linked chains, expressed either as a fraction of EMF-ubiquitin (Fig. 3d) or as a fraction of total ubiquitin (Supplementary Fig. 6a), was significantly elevated in R6/2 mice at both 12 and 6 weeks of age, signifying a shift of the total ubiquitin pool into higher-order conjugates and not merely an

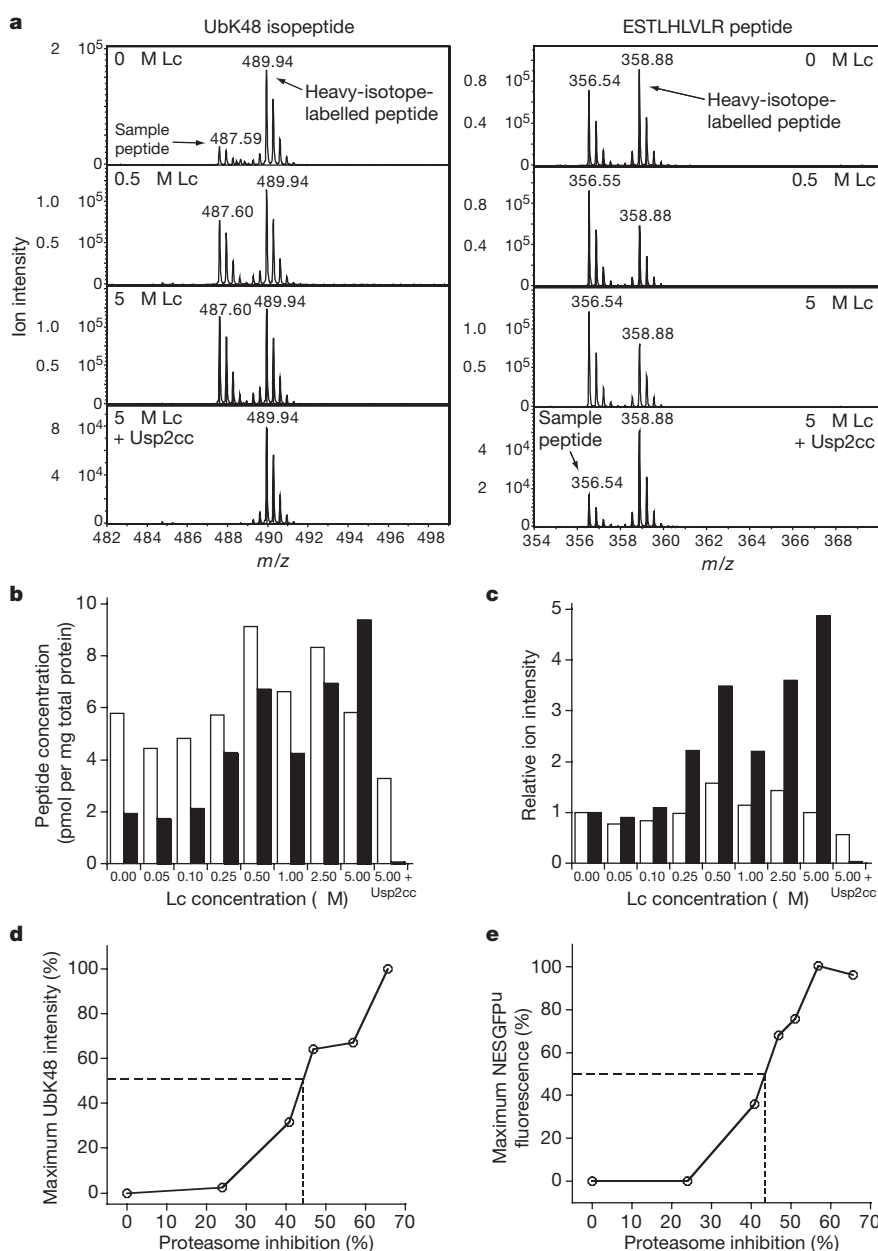


Figure 1 | UbK48 ion intensity correlates with a loss of UPS function. **a**, Extracted mass chromatograms of the UbK48 isopeptide (left, $m/z = 487.60$) and a linear ubiquitin peptide ESTLHLVLR (right, $m/z = 356.55$) (and their corresponding ^{13}C , ^{15}N labelled standards). Ubiquitin species were captured with human P2UBA from lysates of NESGFP^u HEK293 cells exposed to the indicated concentrations of Lc and were digested with Usp2cc where indicated. **b**, **c**, Absolute concentrations (**b**) and relative levels (**c**) of UbK48 isopeptide (filled bars) and non-chain ubiquitin (EMF-ubiquitin, made up of end-cap, mono-ubiquitin and free ubiquitin; open bars). **d**, **e**, Plots of relative changes in UbK48 (**d**) and NESGFP^u fluorescence (**e**, measured by flow cytometry) in Lc-treated NESGFP^u HEK293 cells plotted against proteasome inhibition (measured by Suc-LLVY-AMC cleavage). The dashed lines represent the half-maximal inhibition.

increase in total ubiquitin abundance. Notably, we observed a decrease in total ubiquitin (Supplementary Fig. 5), EMF-ubiquitin (Supplementary Fig. 7a) and UbK48 (Supplementary Fig. 7b) levels in mice of both genotypes between 2 and 4 weeks of age. The decline in cortical EMF-ubiquitin continued in non-transgenic mice until 12 weeks of age; this decrease was largely abrogated by 6 weeks of age in R6/2 mice (Supplementary Fig. 7a), probably offset by increased ubiquitin gene expression in response to HTT-induced UPS stress (data not shown). These data indicate that ubiquitin levels in brain are developmentally regulated.

To determine whether the observed UPS perturbation is a general feature of HD pathology, we analysed UbK48 levels in cortex homogenates from *Hdh*^{Q150/Q150} mice at 8 and 22 months of age (where *Hdh* is the mouse orthologue of human *HTT*). These 'knock-in' mice²⁴ exhibit only modest levels of HTT aggregates and have variable expression of other pathological phenotypes at eight months of age²⁴. However, at 22 months of age, *Hdh*^{Q150/Q150} mice share extensive behavioural and molecular phenotypes with R6/2 mice of 12 weeks of age²⁵. Consistent with this, we observed a small but significant increase in UbK48 isopeptide levels, but not in EMF-ubiquitin levels, in

Hdh^{Q150/Q150} mice at 22 months of age (Fig. 3e). Thus, UPS impairment is observed in two distinct, but comparable, mouse models of HD, and is not simply an artefact of overexpressed *HTT* exon 1. We also found that UbK48 isopeptide levels were elevated by 50% in the striatum and the cortex of human HD patients when compared to control, non-HD cortex (Fig. 3f). A similar elevation is also seen when HD cortex alone is compared to control cortex. This increase is specific to UbK48, because EMF-ubiquitin levels were not significantly altered in human HD brains (Fig. 3f). Thus, UPS impairment is a consistent feature of HD pathology in humans and in mouse HD models.

To investigate whether the observed perturbation of cellular ubiquitin pools by mutant *HTT* (exon 1) expression is specific for Lys 48-linked polyubiquitin chains, or whether it represents a more generalized dysregulation of ubiquitin metabolism, we exploited the same methodology to assess the impact of expression of aggregation-prone HTT protein on polyubiquitin chains that are not known to be associated with proteasomal degradation, as the human P2UBA domain is non-selective with respect to the isopeptide linkage¹⁸ (Fig. 4). Strikingly, we observed that both UbK11 (TLTGK-(GG)-TITLVEPSDTIENVK) and UbK63 (TLDYNIQK-(GG)-ESTLHLVLR)

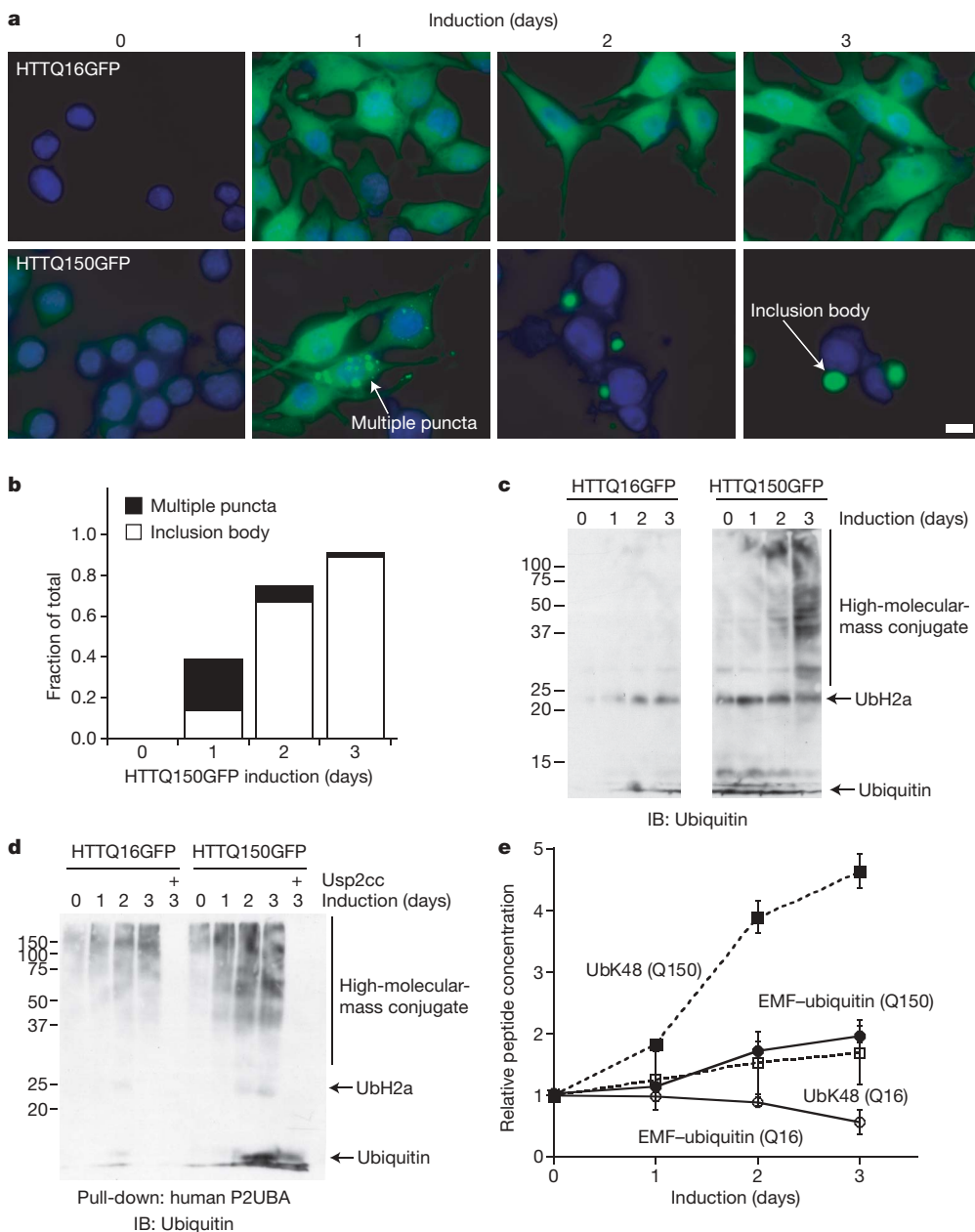


Figure 2 | HTTQ150 aggregation in an inducible cell model of HD correlates with elevated UbK48 levels.

a, Fluorescence micrograph of HTTQ16GFP (top) and HTTQ150GFP (bottom) expression (green) induced for the indicated number of days. Nuclei were visualized with bisbenzimidazole (blue). Scale bar represents 2 μ m.

b, Quantification of HTTQ150GFP distribution scored at the positions indicated by the arrows in the representative panels of **a**. **c**, **d**, Ubiquitin immunoblot (IB) analysis of whole-cell lysates (**c**) and human P2UBA-captured protein (**d**) from cells in **a**. **e**, Relative changes in levels of the indicated ubiquitin species determined by mass spectrometry from human P2UBA pull-down assays of cells in **a** ($n = 3$). Data are presented as mean \pm s.e.m.

isopeptides increased in lysates of N2a cells treated with MG132 to a relatively similar extent as did UbK48 (Fig. 4a). Although UbK11 isopeptides accumulated with similar kinetics to those of UbK48, the increase in UbK63 chains was delayed and transient. Induction of HTTQ150GFP, but not HTTQ16GFP, expression also led to an increase in the relative abundance of UbK11 and UbK63 chains

(Fig. 4b), consistent with the conclusion that expression of aggregation-prone proteins globally alters ubiquitin pools. Lys 63-linked chains were also significantly elevated in homogenates from R6/2 mouse brains when expressed either as absolute isopeptide concentrations (Fig. 4d) or as relative to total ubiquitin levels (Supplementary Fig. 6b). Lys 11-linked chains showed a similar trend, but failed to reach the same level of statistical significance (Fig. 4c and Supplementary Fig. 6c). Thus, both expression of aggregation-prone proteins and direct proteasome inhibition led to alterations in polyubiquitin chains not typically associated with proteasome function. Whether these findings reflect a role for UbK63 and UbK11 chains in proteasome targeting^{17,26}, or perhaps in other ubiquitin-dependent processes such as trafficking to inclusion bodies or autophagy, will require further investigation.

The data reported here demonstrate that the UPS is impaired in two mouse models of HD as well as in the human disease, providing *in vivo* evidence that UPS dysfunction occurs during HD pathogenesis. The demonstration that elevated levels of polyubiquitin chains are evident in the brains of 6-week-old R6/2 mice indicates that UPS dysfunction—and its broad consequences for cellular homeostasis—is temporally poised to contribute to the cascade of events that result in the neuronal dysfunction and death that characterize these disorders. Previous attempts to establish a definitive link between UPS impairment and neurodegenerative disease pathogenesis, first suggested from ubiquitin immunohistochemical studies as early as 1989 (ref. 4), have been hitherto hampered by the lack of

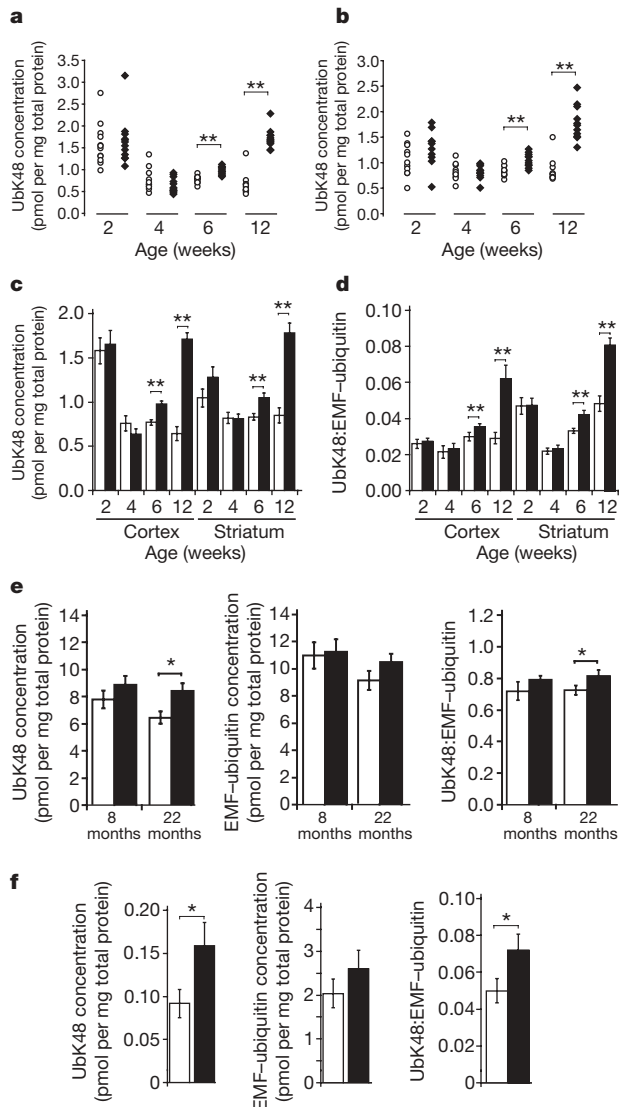


Figure 3 | UbK48 isopeptide ion intensity is elevated in mouse models of HD and in the human HD brain. **a–c,** Elevated brain Lys 48-linked polyubiquitin chain levels in a transgenic model of HD. Polyubiquitylated material from cortex (**a**) and striatum (**b**) homogenates of R6/2 mice (filled diamonds) and non-transgenic littermate mice (open circles) at the indicated ages was captured with human P2UBA. Each symbol represents an individual animal. **c,** Mean UbK48 isopeptide concentrations for R6/2 mice (filled bars) and non-transgenic littermates (open bars) ($n = 12$ for each genotype at each age). **d,** Mean UbK48:EMF-ubiquitin concentration ratio for R6/2 mice (filled bars) and non-transgenic littermates (open bars). **e,** Mean UbK48 isopeptide concentration (left panel), EMF-ubiquitin concentration (middle panel) and UbK48:EMF-ubiquitin ratio (right panel) in human P2UBA-captured cortex homogenates from *Hdh*^{Q150/Q150} mice (filled bars) and age-matched non-transgenic littermates (open bars) ($n = 6$ and 8 for 8-month- and 22-month-old mice of each genotype, respectively). **f,** Mean UbK48 isopeptide concentration (left), EMF-ubiquitin concentration (middle) and UbK48:EMF-ubiquitin ratio (right) in human P2UBA-captured brain homogenates from human control (open bars) and HD (filled bars) patients ($n = 14$). All data are presented as mean \pm s.e.m. Significance levels were determined using Student's *t*-test. Single asterisk and double asterisk denote $P \leq 0.05$ and $P \leq 0.01$, respectively.

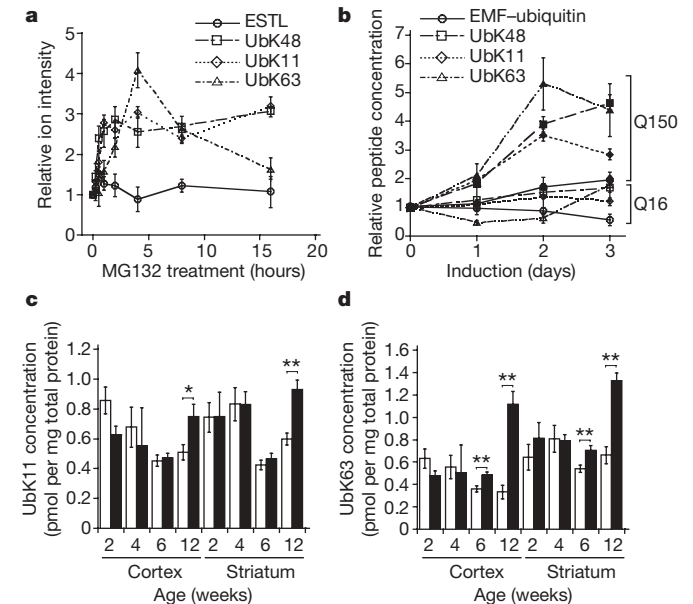


Figure 4 | Elevated levels of polyubiquitin chain linkages not typically associated with proteasomal targeting in cellular and mouse models of HD. **a,** Ubiquitin isopeptide levels in human P2UBA-captured material from extracts of uninduced, differentiated N2a cells exposed to MG132 (10 μ M) for the indicated times. Relative ion intensities from extracted ion chromatograms were normalized to the levels of the same ions in untreated cells ($n = 3$). **b,** Ubiquitin isopeptide levels in human P2UBA-captured material from extracts of differentiated N2a cells after induction of HTTQ16GFP or HTTQ150GFP expression for the indicated times. Filled and open symbols represent data from HTTQ150GFP- and HTTQ16GFP-expressing cells, respectively. Absolute peptide concentration values were normalized to the levels in uninduced cells ($n = 3$). **c, d,** Concentrations of UbK11 (**c**) and UbK63 (**d**) isopeptides in human P2UBA-captured material from brain homogenates from R6/2 mice (filled bars) and non-transgenic littermates (open bars) ($n = 12$ for each genotype at each age). **b–d,** Reported peptide concentrations were measured using LC-ESI-TOF-MS analysis with spiked heavy-isotope-labelled standards. All data are presented as mean \pm s.e.m. Significance levels were determined using Student's *t*-test. Single asterisk and double asterisk denote $P \leq 0.05$ and $P \leq 0.01$, respectively.

suitable analytic tools to assess UPS function *in vivo*. Although artificial reporters of UPS activity on the basis of destabilized GFP^{8,9,11} have proved to be useful tools to probe the effects of protein aggregation on UPS activity in cell-culture models of disease, the intrinsic difficulties associated with these transgenic reporters *in vivo*¹⁵ have precluded definitive assessment of the time course of UPS impairment relative to disease pathogenesis in animal models. The broadly applicable method described here should be useful in achieving deeper insight into the molecular basis of a wide variety of neurodegenerative diseases in humans and in animal models.

METHODS SUMMARY

The amount of total human P2UBA-captured ubiquitin was determined as described¹⁷ from the sum of ubiquitin in polyubiquitin chains (approximated by the sum of UbK48, UbK63 and UbK11 isopeptides) and EMF-ubiquitin (determined by subtracting the UbK48 and UbK11 concentrations from the concentration of the linear peptide ESTLHLVLR¹⁷). The EMF-ubiquitin value represents ubiquitin molecules that are completely unconjugated, present as mono-ubiquitin conjugates or present as the end-cap ubiquitin on a polyubiquitin chain that has a length greater than two. Although the chain and ESTL signal can come from ubiquitin chains linked by lysines other than lysines 48, 11 or 63, analysis of the ion intensities from these isopeptides in our samples reveals that they are present at levels much below those of the three main linkages (often below the level of detection) and thus do not contribute significantly to our calculations.

Full Methods and any associated references are available in the online version of the paper at www.nature.com/nature.

Received 8 May; accepted 14 June 2007.

- MacDonald, M. E. *et al.* A novel gene containing a trinucleotide repeat that is expanded and unstable on Huntington's disease chromosomes. *Cell* **72**, 971–983 (1993).
- Tobin, A. J. & Signer, E. R. Huntington's disease: the challenge for cell biologists. *Trends Cell Biol.* **10**, 531–536 (2000).
- Lowe, J. *et al.* Ubiquitin is a common factor in intermediate filament inclusion bodies of diverse type in man, including those of Parkinson's disease, Pick's disease, and Alzheimer's disease, as well as Rosenthal fibres in cerebellar astrocytomas, cytoplasmic bodies in muscle, and Mallory bodies in alcoholic liver disease. *J. Pathol.* **155**, 9–15 (1988).
- Mayer, R. J., Lowe, J., Lennox, G., Doherty, F. & Landon, M. Intermediate filaments and ubiquitin: a new thread in the understanding of chronic neurodegenerative diseases. *Prog. Clin. Biol. Res.* **317**, 809–818 (1989).
- DiFiglia, M. *et al.* Aggregation of huntingtin in neuronal intranuclear inclusions and dystrophic neurites in brain. *Science* **277**, 1990–1993 (1997).
- Ross, C. A. & Pickart, C. M. The ubiquitin–proteasome pathway in Parkinson's disease and other neurodegenerative diseases. *Trends Cell Biol.* **14**, 703–711 (2004).
- Pickart, C. M. & Fushman, D. Polyubiquitin chains: polymeric protein signals. *Curr. Opin. Chem. Biol.* **8**, 610–616 (2004).
- Bence, N. F., Sampat, R. M. & Kopito, R. R. Impairment of the ubiquitin–proteasome system by protein aggregation. *Science* **292**, 1552–1555 (2001).
- Bennett, E. J., Bence, N. F., Jayakumar, R. & Kopito, R. R. Global impairment of the ubiquitin–proteasome system by nuclear or cytoplasmic protein aggregates precedes inclusion body formation. *Mol. Cell* **17**, 351–365 (2005).
- Jana, N. R., Zemskov, E. A., Wang, G. & Nukina, N. Altered proteasomal function due to the expression of polyglutamine-expanded truncated N-terminal huntingtin induces apoptosis by caspase activation through mitochondrial cytochrome c release. *Hum. Mol. Genet.* **10**, 1049–1059 (2001).
- Verhoef, L. G., Lindsten, K., Masucci, M. G. & Dantuma, N. P. Aggregate formation inhibits proteasomal degradation of polyglutamine proteins. *Hum. Mol. Genet.* **11**, 2689–2700 (2002).
- Petrucelli, L. *et al.* Parkin protects against the toxicity associated with mutant α -synuclein: proteasome dysfunction selectively affects catecholaminergic neurons. *Neuron* **36**, 1007–1019 (2002).
- Urushitani, M., Kurisu, J., Tsukita, K. & Takahashi, R. Proteasomal inhibition by misfolded mutant superoxide dismutase 1 induces selective motor neuron death in familial amyotrophic lateral sclerosis. *J. Neurochem.* **83**, 1030–1042 (2002).
- Wang, H. L. *et al.* Polyglutamine-expanded ataxin-7 decreases nuclear translocation of NF- κ B p65 and impairs NF- κ B activity by inhibiting proteasome activity of cerebellar neurons. *Cell Signal.* **19**, 573–581 (2007).
- Bowman, A. B., Yoo, S. Y., Dantuma, N. P. & Zoghbi, H. Y. Neuronal dysfunction in a polyglutamine disease model occurs in the absence of ubiquitin–proteasome system impairment and inversely correlates with the degree of nuclear inclusion formation. *Hum. Mol. Genet.* **14**, 679–691 (2005).
- Kabashi, E., Agar, J. N., Taylor, D. M., Minotti, S. & Durham, H. D. Focal dysfunction of the proteasome: a pathogenic factor in a mouse model of amyotrophic lateral sclerosis. *J. Neurochem.* **89**, 1325–1335 (2004).
- Kirkpatrick, D. S. *et al.* Quantitative analysis of *in vitro* ubiquitinated cyclin B1 reveals complex chain topology. *Nature Cell Biol.* **8**, 700–710 (2006).
- Raasi, S., Varadan, R., Fushman, D. & Pickart, C. M. Diverse polyubiquitin interaction properties of ubiquitin-associated domains. *Nature Struct. Mol. Biol.* **12**, 708–714 (2005).
- Barr, J. R. *et al.* Isotope dilution–mass spectrometric quantification of specific proteins: model application with apolipoprotein A-I. *Clin. Chem.* **42**, 1676–1682 (1996).
- Dass, C., Fridland, G. H., Tinsley, P. W., Killmar, J. T. & Desiderio, D. M. Characterization of β -endorphin in human pituitary by fast atom bombardment mass spectrometry of trypsin-generated fragments. *Int. J. Pept. Protein Res.* **34**, 81–87 (1989).
- Baker, R. T. *et al.* Using deubiquitylating enzymes as research tools. *Methods Enzymol.* **398**, 540–554 (2005).
- Lindsten, K., Menendez-Benito, V., Masucci, M. G. & Dantuma, N. P. A transgenic mouse model of the ubiquitin/proteasome system. *Nature Biotechnol.* **21**, 897–902 (2003).
- Mangiarini, L. *et al.* Exon 1 of the *HD* gene with an expanded CAG repeat is sufficient to cause a progressive neurological phenotype in transgenic mice. *Cell* **87**, 493–506 (1996).
- Lin, C. H. *et al.* Neurological abnormalities in a knock-in mouse model of Huntington's disease. *Hum. Mol. Genet.* **10**, 137–144 (2001).
- Woodman, B. *et al.* The *Hdh*^{Q150/Q150} knock-in mouse model of HD and the R6/2 exon 1 model develop comparable and widespread molecular phenotypes. *Brain Res. Bull.* **72**, 83–97 (2007).
- Hanna, J. *et al.* Deubiquitinating enzyme ubp6 functions noncatalytically to delay proteasomal degradation. *Cell* **127**, 99–111 (2006).

Supplementary Information is linked to the online version of the paper at www.nature.com/nature.

Acknowledgements We are grateful to P. Howley, R. Baker and N. Nukina for reagents. We thank D. Kirkpatrick and N. Hathaway for suggestions, and J.-P. Vonsattel and the New York Brain Bank for the human brain tissue. This work was supported by a predoctoral training grant from NIGMS (E.J.B.), a small business innovation research grant from NINDS (H.S.), grants from the Huntington's Disease Society of America Coalition for the Cure, Hereditary Disease Foundation and High Q Foundation (G.P.B. and R.R.K.), and a grant from the Wellcome Trust (G.P.B.).

Author Contributions E.J.B., T.A.S., C.H.B., H.S. and R.R.K. devised the overall proteomic approach. E.J.B. performed all of the biochemical analyses, the pull-down assays and, together with T.A.S., obtained and analysed all the mass spectrometry data. All of the mouse breeding and dissection was performed by B.W. and G.P.B. T.S.Z. performed all experiments in Supplementary Fig. 2 and the analysis of the *Hdh*^{Q150/Q150} knock-in mice. K.-Y.R. contributed the real-time RT-PCR data in Supplementary Fig. 3 and performed the ubiquitin ELISA on R6/2 and control mice. E.J.B. and R.R.K. wrote the manuscript. All authors discussed the results and contributed to the manuscript.

Author Information Reprints and permissions information is available at www.nature.com/reprints. The authors declare competing financial interests: details accompany the full-text HTML version of the paper at www.nature.com/nature. Correspondence and requests for materials should be addressed to R.R.K. (kopito@stanford.edu).

METHODS

Reagents. MG132 and Lc were purchased from Affiniti. RapiGest was purchased from Waters. Monoclonal ubiquitin antibody was obtained from Chemicon (MAB1510). Sequencing grade trypsin was purchased from Promega. ^{13}C , ^{15}N labelled peptides and isopeptides were synthesized by Cell Signaling Technology. **Plasmids.** The ubiquitin-association domain of human PLIC-2 (amino acids 575–624) was amplified from a full-length human PLIC-2 construct by PCR and cloned into the pet21a bacterial expression vector (Novagen).

Mice. The R6/2 colony was maintained by backcrossing R6/2 males to (CBA \times C57BL/6) F₁ females (B6CBAF1/OlaHsd, Harlan Olac). Mouse husbandry, genotyping and CAG-repeats sizing were performed as previously described²⁵. The CAG-repeat size of the R6/2 mice used in this study was (195.5 \pm 5.8). The *Hdh*^{Q150/Q150} knock-in mice²⁴ were maintained and bred as described²⁵.

Protein purification. The human PLIC-2 UBA-his6 protein (human P2UBA) was purified using NiNTA resin (Qiagen) and coupled to Affigel-10 agarose (BioRad) using the manufacturer's guidelines. The human P2UBA concentration was $\sim 1 \text{ mg ml}^{-1}$ on the resin after coupling. The Usp2cc was expressed and purified as previously described²¹.

Cell lines. HEK293 cells stably expressing the NESGFP^u reporter were described previously⁹. N2a cells were maintained and induced as previously described¹⁰.

Microscopy. Cells grown on polylysine-coated coverslips were fixed with 4% paraformaldehyde. DNA was stained by $10 \mu\text{g ml}^{-1}$ bisbenzimidazole. Images were acquired with a Zeiss Axiovert 35 microscope with a $\times 100$ objective.

Proteasome activity assay. Proteasome activity was measured from cell lysates essentially as described²⁷.

Quantitative real-time RT-PCR. Ten nanograms total RNA was used as a template for real-time PCR with reverse transcription (RT-PCR). We used iScript one-step RT-PCR with SYBR green kit (BioRad) and iCycler system with iCycler iQ software ver 3.1 (BioRad). The transcript levels of UbC, UbB, Uba52 and Uba80 were normalized to the level of 18S ribosomal RNA. The primers used for real-time RT-PCR were as follows: UbC-F, 5'-GTTACCACCAAGAGGTC-3'; UbC-R, 5'-GGGAATGCAAGAACTTTATTC-3'; UbB-F, 5'-CACTGAGCTCAGTGACGAGAG-3'; UbB-R, 5'-CACGAAGATCTGCATTGAC-3'; Uba52-F, 5'-GTCAGCTTGCCAGAGTAC-3'; Uba52-R, 5'-ACTTCTTCTTGCGGCAGTTG-3'; Uba80-F, 5'-TGGCAAAATTAGCCGACTTCG-3'; Uba80-R, 5'-AACACTTGCCACAGTAATGCC-3'; 18S rRNA-F, 5'-CGGCTACCACATCCAAGGAA-3'; and 18S rRNA-R, 5'-GCTGGAA-TTACCGCGGCT-3'. Control plasmid DNA was generated by subcloning each complementary DNA fragment into pCR2.1 vector (Invitrogen), and 10^8 to 10^3 copies of plasmid DNA was used as a standard.

Polyubiquitin affinity capture. Cells were lysed in 1% Triton X-100, 150 mM NaCl, 20 mM Tris, pH 8.0, and complete protease inhibitor tablets (Roche). One milligram of protein was diluted to a final volume of 300 μl in IP buffer (10 mM Hepes, pH 7.2, 0.5% Triton X-100 and 150 mM NaCl), to which 75 μl human P2UBA resin (1:1 slurry) was added and incubated at 4 $^{\circ}\text{C}$ for 5 h with constant rotation. The beads were collected by centrifugation, washed twice with IP buffer and twice in cold PBS. Protein was eluted in 50 μl SDS sample buffer for immunoblot analysis or with 50 μl 0.1% RapiGest in 50 mM ammonium bicarbonate, pH 7.8, for mass spectrometry analysis. We observed that addition of 5 mM *N*-ethylmaleimide to the cell lysis buffer to reduce deubiquitylating enzyme activity increased the total intensities of all ubiquitin peptides without altering their respective proportions, as described above.

Tissue preparation. Dissected mouse cortex and striatum were mixed with 300 μl IP buffer and homogenized using a Teflon micro-rotator homogenizer with three ten-second pulses. The sonicated lysates were centrifuged for 5 min at 14,000g at 4 $^{\circ}\text{C}$. Human HD and control post-mortem cortex and striatum were obtained from the New York Brain Bank at Columbia University. Details of ages and genders of HD and control donors are provided in Supplementary Table 1. Dissected brain regions were mixed with 5 ml IP buffer, homogenized using a glass-glass Dounce homogenizer and prepared as above.

Sample preparation for mass spectrometry. RapiGest eluted material was mixed with 10 pmol of heavy-isotope-labelled peptide. The eluate was incubated with 1 μg sequencing grade trypsin at 37 $^{\circ}\text{C}$ for 16 h. The trypsin digestion was then mixed with 1 μl 1 M hydrochloric acid for 30 min at 37 $^{\circ}\text{C}$.

Mass spectrometry. The digested samples were analysed on a LC-MS system that consisted of an ESI-TOF mass spectrometer (MicroTOF System, Bruker Daltonics) coupled to a capillary HPLC (Agilent). The peptide mixtures were separated on a 0.32 mm inner diameter \times 150 mm length C-18 reversed-phase column at a flow rate of approximately $10 \mu\text{l min}^{-1}$ using a linear gradient of acetonitrile (0% to 40%) over 110 min. Eluant from the column was directly electrosprayed into the source of the mass spectrometer at a spray voltage of approximately 4 kV. To identify the peptides, a second portion of each sample was analysed by an undirected LC-MS/MS analysis on a linear ion-trap mass spectrometer (LTQ, ThermoElectron) using the same chromatography conditions as those used in the LC-MS profiling analyses. The acquired MS/MS spectra were searched against a database of protein sequences using a commercial software package (model Mascot, Matrix Sciences). Absolute quantification was performed using the ion intensities of the tracked endogenous peptides relative to the spiked labelled peptides. The ions that were tracked were: LIFAGK-GG-QLEDGR (UbK48) isopeptide unlabelled ($m/z = 487.60$) and heavy-isotope-labelled ($m/z = 489.94$), ESTLHLVLR (ESTL) peptide unlabelled ($m/z = 356.55$) and heavy-isotope-labelled ($m/z = 358.88$), TLTKG-(GG)-TITLEVEPSDTIENVK (UbK11) isopeptide unlabelled ($m/z = 801.43$) and heavy-isotope-labelled ($m/z = 803.43$), and TLDYNIQK-(GG)-ESTLHLVLR (UbK63) isopeptide unlabelled ($m/z = 561.81$) and heavy-isotope-labelled ($m/z = 563.56$). The peak heights (intensity) of the molecular ions were used at the chromatographic peak maxima for relative quantification. Approximately 40% of total eluted material was injected into the mass spectrometer. Negligible background was observed under all circumstances at the positions of the endogenous and labelled peptides. Signal-to-noise ratios of the labelled peptides at their spike concentrations were ~ 300 . A dynamic range approaching 10,000 was available for the experiment, although typically only a dynamic range of 1,000 was used. The limit of detection was estimated to be approximately 25 fmol mg^{-1} of extracted protein and was similar for all the peptides used.

Statistical analysis. All data are presented as mean \pm s.e.m. Significance levels were determined using Student's *t*-test. Single asterisk and double asterisk denote $P \leq 0.05$ and $P \leq 0.01$, respectively.

Ubiquitin ELISA. Total ubiquitin concentrations were measured as described²⁸.

27. Kisselev, A. F. & Goldberg, A. L. Monitoring activity and inhibition of 26S proteasomes with fluorogenic peptide substrates. *Methods Enzymol.* **398**, 364–378 (2005).

28. Ryu, K. Y., Baker, R. T. & Kopito, R. R. Ubiquitin-specific protease 2 as a tool for quantification of total ubiquitin levels in biological specimens. *Anal. Biochem.* **353**, 153–155 (2006).

Hebbian STDP in mushroom bodies facilitates the synchronous flow of olfactory information in locusts

Stijn Cassenaer¹ & Gilles Laurent¹

Odour representations in insects undergo progressive transformations and decorrelation^{1–3} from the receptor array to the presumed site of odour learning, the mushroom body^{4–7}. There, odours are represented by sparse assemblies of Kenyon cells in a large population². Using intracellular recordings *in vivo*, we examined transmission and plasticity at the synapse made by Kenyon cells onto downstream targets in locusts. We find that these individual synapses are excitatory and undergo hebbian spike-timing dependent plasticity (STDP)^{8–10} on a ± 25 ms timescale. When placed in the context of odour-evoked Kenyon cell activity (a 20-Hz oscillatory population discharge), this form of STDP enhances the synchronization of the Kenyon cells' targets and thus helps preserve the propagation of the odour-specific codes through the olfactory system.

Olfactory processing in insects begins in an array of receptor neurons that express collectively many tens of olfactory receptor genes (~ 60 in *Drosophila*^{11,12}; ~ 150 in honeybees¹³). The representations of general odours are then decorrelated by local circuits of projection neurons and local neurons in the antennal lobe^{1–3}. In locusts and other insects, the antennal lobe output is distributed in space and time and can be described as stimulus-specific time-series of projection-neuron activity vectors, updated at each cycle of a 20-Hz collective oscillation^{1,14,15}. Distributed projection-neuron activity is then projected to Kenyon cells, the intrinsic neurons of the mushroom body. In contrast to projection neurons, Kenyon cells respond very specifically and fire extremely rarely². The mechanisms underlying this sparsening are starting to be understood^{2,16}. Such sparse representations are advantageous for memory and recall¹⁶, consistent with established roles of the mushroom bodies in learning^{4–7}. In *Drosophila*, experiments combining molecular inactivation with behaviour indicate that synaptic output from Kenyon cells in the lobes is required for memory retrieval⁵. Little is known, however, about the electrophysiological properties of these synapses.

We studied the connections made by Kenyon cells onto a small population of extrinsic neurons¹⁷ in the β -lobe of the locust mushroom body (Fig. 1a), using an intact, *in vivo* preparation (Methods). β -lobe neurons (β -LNs) respond to odours; their responses are odour-specific and their tuning is sensitive to input synchrony¹⁷. We recorded intracellularly from pairs of Kenyon cells and β -LNs: randomly selected Kenyon cells were impaled in their soma; β -LNs were impaled in a dendrite in the β -lobe. We focused on one β -LN anatomical subtype¹⁷, which comprises many individual neurons. Neurons of this subtype, called β -LNs here, could be recognized also by their physiological characteristics (see below). Each β -LN has extensive dendrites (Fig. 1a, and Supplementary Fig. 1) that intersect many of 50,000 Kenyon cell axons. Monosynaptic connections were found in $\sim 2\%$ of tested Kenyon cell (KC)– β -LN pairs (Fig. 1b). All were excitatory. The delay between Kenyon cell spike and β -LN-excitatory post-synaptic potential (EPSP) onset was 6.5 ± 0.70 ms,

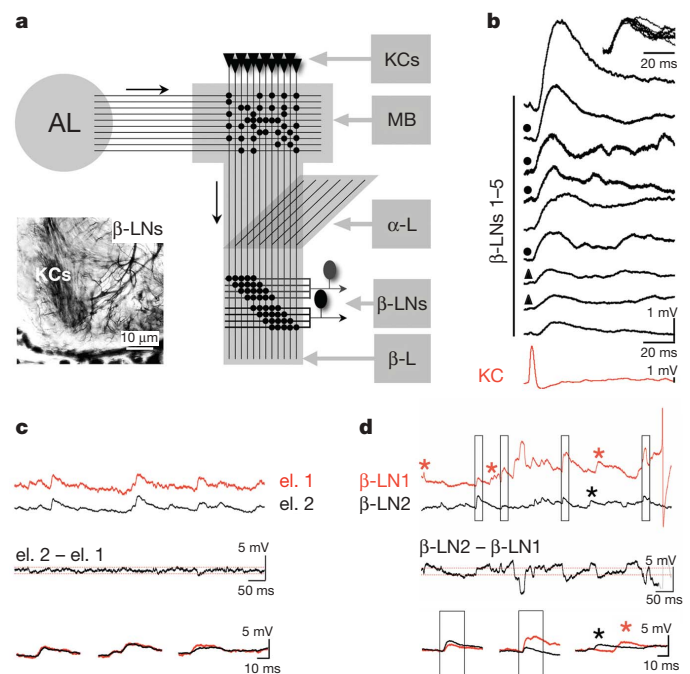


Figure 1 | Synaptic connections between individual Kenyon cells and β -LNs are excitatory, powerful and varied in gain. **a**, Schematic of the locust olfactory circuits: Projection neuron axons ($n = 830$) exit the antennal lobe (AL) and send collaterals into the mushroom body (MB) calyx. There, they excite Kenyon cells ($n = 50,000$) with $\sim 50\%$ average connectivity¹⁶. Kenyon cells each send a bifurcating axon into the α - and β -lobes (α -, β -L), forming 'beams' of thousands of tightly packed axons (inset). The finer dendrites of β -LNs run normal to Kenyon cell axons in β -LN-specific sectors: two of these can be seen in the inset (a photomicrograph of a $10\text{-}\mu\text{m}$ -thick section of the distal end of the β -lobe). **b**, Spike-triggered averages of β -LN intra-dendritic recordings from nine different KC– β -LN pairs (9 Kenyon cells, 5 β -LNs). All β -LNs and Kenyon cells are recorded *in vivo*, with intracellular electrodes. Note the wide-range of spike-triggered average amplitudes. Same-symbol-marked spike-triggered averages are from the same β -LNs, with different presynaptic Kenyon cells sampled successively. Inset, scaled spike-triggered averages in **b**, illustrating similarity of kinetics. **c**, Simultaneous dendritic impalements of one β -LN with two separate electrodes (el. 1, 2). el. 2 – el. 1 is the difference between the two voltage traces; note the high correlation of amplitudes (noise envelope is 2 s.d., red stipples), indicating similar electrotonic access to synaptic sites. Lower panel, overlay of selected EPSPs from above. **d**, Simultaneous dendritic impalements of two different β -LNs (1 and 2). Note some common EPSPs (boxes) and EPSPs specific to either β -LN (*). β -LN2 – β -LN1 is the difference between the two voltage traces; note significant variations on each side of the noise envelope (stippled lines as in panel **c**). Lower panel, overlay of selected EPSPs from above.

¹California Institute of Technology, Division of Biology, 139-74, Pasadena, California 91125, USA.

including 5.4 ± 0.25 ms for spike propagation from Kenyon cell soma to the β -lobe. The remaining (synaptic) delay (~ 1 ms) is similar to that at another chemical synapse in the locust brain¹⁶. Unitary EPSPs were large (1.58 mV \pm 1.11 , $n = 9$ pairs), in contrast to those generated in Kenyon cells by individual projection neurons (86 μ V \pm 44)¹⁶. The fact that Kenyon cell outputs are powerful is consistent with Kenyon cell spikes being rare and therefore highly informative. EPSP amplitude varied greatly across connected pairs (0.55 – 4 mV). This could reflect a distribution of electrotonic distances between synapses and recording sites. Simultaneous impalements of different dendrites in the same β -LN ($n = 2$ experiments), however, show that the amplitudes of most events were the same across recording sites (Pearson's correlation > 0.9) (Fig. 1c). Consistent with this, unitary EPSP kinetics (10 – 90% rise time, 8.3 ms \pm 2.3 ; time to $1 - (1/e)$ of peak, 13.2 ms \pm 4.4) were independent of the β -LN recorded and, thus, of the impalement site (inset, Fig. 1b). Simultaneous dendritic recordings of different β -LNs ($n = 5$ experiments), however, revealed that their synaptic backgrounds overlapped only partly (Fig. 1d; Pearson's correlation or fraction of common EPSPs, 0.1 – 0.3). Common EPSPs rarely had the same amplitude (Fig. 1d). Hence, β -LNs may each receive inputs from hundreds to thousands ($\sim 2\%$ of $50,000$ Kenyon cells) of Kenyon cells, in overlapping subsets; KC– β -LN connections are strong on average, with target-specific strength.

Odour-evoked activity in projection neurons and Kenyon cells consists principally of sequential volleys of synchronized spikes—generally, one spike per responding neuron per oscillation cycle^{1,2,15}. β -LN responses to odours also consisted typically of sequences of single phase-locked spikes, timed around the trough of several local field potential (LFP) oscillation cycles (Fig. 2a, b). The cycles when a spike was produced (usually with probability < 1) depended on β -LN and stimulus identity, as illustrated in Fig. 2c, d. We conclude that, to each oscillation cycle corresponds a particular activity vector in the projection neuron², Kenyon cell² and β -LN populations. By recording from pairs of β -LNs simultaneously during odour trials, we also observed that, when the two β -LNs fired one action potential during the same oscillation cycle ($n = 4$ pairs; Fig. 2d, upper panel, asterisks), those action potentials were tightly synchronized (± 2 ms, Fig. 2d, middle and lower panels).

A fortuitous observation provided hints of plasticity at the KC– β -LN synapse (Fig. 3a). At trial 4 of a Kenyon cell stimulus sequence intended to explore β -LN integration, the β -LN fired a spontaneous action potential roughly at the time of the first (of 2) Kenyon-cell-evoked EPSP (Fig. 3a). At trial 5, 10 seconds after this single fortuitous pairing, the first EPSP of the pair was greatly enhanced (Fig. 3a). This suggested the possibility of spike-timing-dependent plasticity (STDP), a phenomenon thus far unknown in invertebrates but well characterized in vertebrates, in which the gain of a connection can be changed according to the temporal relationship between pre- and post-synaptic spikes^{8–10}. We explored the consequence of pre-post temporal relationships on the KC– β -LN synapse. A β -LN was impaled and stimulated alternately by two independent Kenyon cell pathways—one for pairing, one for unpaired control (Fig. 3b). Each stimulus was repeated every 10 s, with a 5-s delay between pairing and control stimuli. Pairing consisted of a single Kenyon cell (pre) stimulus and a 5-ms supra-threshold β -LN (post) current pulse, timed such that the delay ($dt = t_{\text{post}} - t_{\text{pre}}$) between pre- and post-synaptic spikes varied between -60 and $+50$ ms. Test trials, used to measure connection strength before and after pairing, were identical to the pairing trials in all respects except in the temporal relationship between pre- and post-synaptic spike times (2.5 s apart, Fig. 3b). Two examples with controls are shown in Fig. 3c, d (for $dt = 10$ ms and -4 ms, 25 pairings each). For $dt = 10$ ms (Fig. 3c), the paired input underwent potentiation; for $dt = -4$ ms (Fig. 3d), it underwent depression. For both conditions, the control pathway (same β -LN, different Kenyon cell input) remained unchanged (Fig. 3c, d, lower panels). The changes were thus input-specific; they were

often detectable after a single pairing (see also Fig. 3a), and could be maintained for up to 25 min. We tested 26 values of dt between -60 and $+50$ ms. The resulting changes (Fig. 3e) define a classical hebbian profile^{8,10}: the synapse is potentiated when pre- precedes post-, and depressed when post- precedes pre-, with symmetrical profiles. The changes could be fitted well with two exponential decays flanking a narrow linear range around $t = +4$ ms ($\tau_1 = 10.4$ ms for $dt < -9$ ms; $y = 3.78t - 13.1$ for -9 ms $< dt < 17.5$ ms; $\tau_2 = 11.6$ ms for $dt > 17.5$ ms). Several connections were tested successively with two (or more) values of dt (some positive, others negative): the same connections could undergo both depression and potentiation, depending on the value of dt . The STDP profile thus seems to be a property of each connection and not only a collective one.

We observed that the values of dt over which synaptic weights change correspond to the period of single odour-evoked oscillation cycles; hence, only within-cycle 'coincidences' may modify the connections between a Kenyon cell and its targets. The features of the STDP curve, when considered together with the timing of Kenyon cells and β -LNs during odour-evoked activity, have interesting

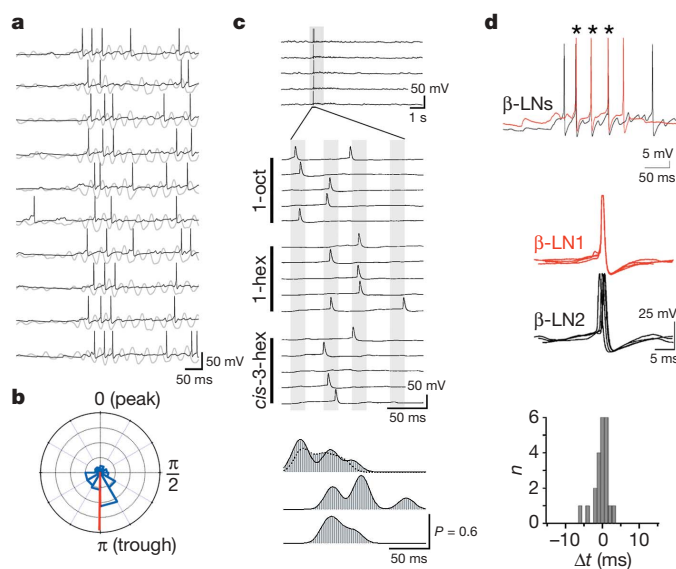


Figure 2 | β -LN tuning and spike-time precision during responses to odours. **a**, Responses of one β -LN to ten successive trials with odour *cis*-3-hexen-1-ol (LFP shown in grey). Note non-random timing of β -LN action potentials during each trial and during each oscillation cycle (calibration LFP, 250 μ V). **b**, β -LN action potentials lock to the trough of LFP during odour responses. Phase plot of β -LN action potentials during odour responses (phases plotted clockwise). Distribution (blue) constructed with data from 8 β -LNs (average in red). **c**, β -LN responses are structured in time and are odour-specific (see also ref. 17). This β -LN responds to different odours with different discharge patterns: upper panel, response to odour 1-octanol (grey bar); middle panels, same 5 trials as in upper panel on an expanded time base, showing approximate timing of relevant oscillation cycles (grey bars) and also showing responses to 1-hexanol and *cis*-3-hexen-1-ol. Apparent spike-time jitter is due to variability of oscillation cycle duration within and across trials. In contrast, spike-time jitter across β -LNs, but within the same oscillation cycle of the same trial, is low (see panel **d**). Lower panel, smoothed peri-stimulus time-histogram from the trials and odours in the middle panels (in the same order). The y axis measures firing probability. Stippled line in the top peri-stimulus time-histogram shows responses to a second set of 5 trials with this odour, delivered after trials with the 2nd and 3rd odours. **d**, Spike discharges in response to odours are precisely locked across β -LNs. Upper panel, simultaneous recording of two β -LNs during odour stimulus, with spikes from both neurons in several oscillation cycles (*). Note precise overlap. Middle panels, zoom on those action potentials, superimposed and triggered on β -LN1 action potential. Lower panel, distribution of spike-time jitter. Recordings as in the middle panels; Δt is the time difference between spikes in β -LNs 1 and 2, when they occur in the same oscillation cycle.

consequences. Consider the phases of Kenyon cell and β -LN spikes (Fig. 4a). Owing to propagation delays, Kenyon cell spikes reach their targets just before the trough of the LFP, a little before β -LN firing (Fig. 2a, b). Consider a cycle in which a β -LN spikes early ($dt < 0$): some KC– β -LN connections will undergo depression (Fig. 3e); at the next trial, β -LN spike time at this cycle should be delayed (Fig. 4b). If, in contrast, a β -LN spikes late, STDP should potentiate Kenyon cell drive to it, and thus advance spike time for that cycle (Fig. 4b). In short, the cycle-by-cycle action of STDP suggests adaptive control of β -LN spike phase. The need for such regulation is not unique to this system: models of cortical networks indicate that, as activity propagates through successive ‘layers’, accumulating noise can rapidly smear the temporal structure that may exist^{18,19}. Modelling studies^{20–22} predict that STDP, given appropriate parameters, could preserve the temporal discretization of activity through such layers.

We generated a reduced model of the KC– β -LN circuit (Methods) and introduced the STDP rule derived from our experiments (Fig. 4c). To control the relative phases of Kenyon cells and β -LNs, we drew Kenyon cell spike phases from experiments², and input weights from uniform distributions with different means: with low weights, β -LN spikes tended to occur late ($dt > 0$, Fig. 4d); with larger weights, they occurred early ($dt < 0$, Fig. 4d). After several trials (each with a random draw of inputs from the same distribution), STDP was allowed to modify synaptic weights for the following trials: when β -LN spikes occurred late ($dt > 0$), Kenyon cell outputs became potentiated and β -LN spikes were advanced; for $dt < 0$, time shifts were inverted. The histograms in Fig. 4d represent spike-time distributions for 1,000 trials before (red) and after (black) STDP, for each of three conditions. These simulations were repeated 200 times (50 trials each), with 11 different Kenyon cell input distributions (Fig. 4e). Once STDP was turned on (trial 1), the evolution was

systematic and rapid, leading to the adaptive up- or downregulation of input weights, firing phase and response intensity (top, middle and bottom, respectively, all averages; Fig. 4e). Given that the model is entirely constrained by experiments, it is noteworthy that the mean phase of the first β -LN spike at steady state (π rad, Fig. 4e), matches precisely that measured experimentally (Fig. 2b).

To test directly the effect of STDP on β -LN output, we next manipulated β -LN spike timing during responses to odours *in vivo*: if our model is correct, such manipulations should change the output of the odour-activated Kenyon cells onto that β -LN and, thus, generate predictable shifts in its spike phase. During odour stimuli, short current pulses locked to selected cycles of the LFP were injected in a β -LN: a negative pulse (b, Fig. 4f) was injected during the cycles and phase when the β -LN would naturally fire (to prevent stimulus-evoked spikes), and a positive pulse (c, Fig. 4f) was injected at a desired phase, for those same cycles (that is, at an abnormal time relative to the Kenyon cell inputs that would normally drive the recorded β -LN). An example is shown for four consecutive cycles in Fig. 4g. After several such pairing trials, current injection was terminated and β -LN-firing phase over the next trials was compared to that before pairing. Figure 4h plots the effects of one such manipulation ($dt > 0$): as predicted, an artificial phase-delay caused a corrective phase-advance. Twenty distinct experiments were carried out in six β -LNs; the expected phase shifts were observed in 16 of those 20 (Mann–Whitney: $P < 0.001$) (Fig. 4i). This is consistent with an adaptive role for STDP in the fine-tuning of β -LN spike-phase, and may explain the tight synchronization of β -LNs (Fig. 2d). Hence, STDP helps preserve the discrete and periodic structure of olfactory representations as they flow through the mushroom bodies.

We showed that the connections made by Kenyon cells to β -LNs are excitatory, strong on average, variable across pairs, and plastic. Plasticity follows time-sensitive hebbian associativity rules^{8–10} and

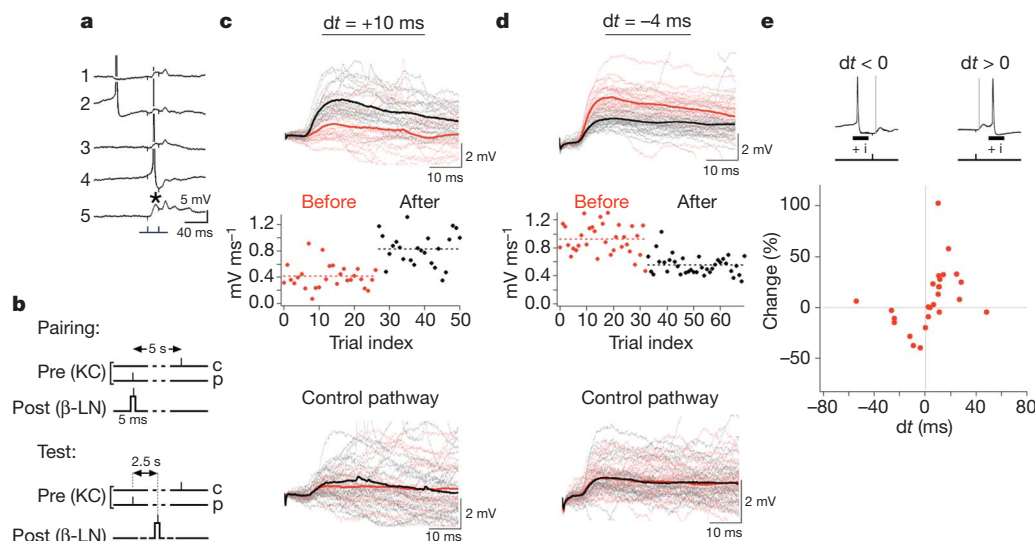


Figure 3 | Hebbian spike-time-dependent plasticity at the KC– β -LN synapse. **a**, Effect of single, near-coincident spikes in pre- and post-synaptic neurons on the Kenyon cell to β -LN synapse. The β -LN is held from a dendrite at normal resting potential *in vivo*, and subjected to paired Kenyon cell stimuli at 20-ms intervals (first and second stimuli in train are from different Kenyon cell electrodes). At trial 4, the effect of the first stimulus sums with an on-going slow depolarization, causing a β -LN action potential. At trial 5, the first EPSP (asterisk) is dramatically enhanced. **b**, Stimulation protocols to probe STDP. For ‘pairing’, the β -LN is depolarized with a 5-ms DC pulse, causing a single β -LN spike in a window around the time of the Kenyon cell pairing stimulus (p). We tested the effects of 5 to 25 successive pairings (10-s intervals); all evoked STDP. Control Kenyon cell stimulus (c) is offset by 5 s relative to the β -LN current pulse. ‘Test’, same protocol as pairing, except that Kenyon cell and β -LN stimuli are 2.5 s apart.

c, Potentiation of KC– β -LN connection after 25 pairings with $dt = 10$ ms. Upper panel, superimposed before- and after-trials, with their averages (bold lines). Middle panel, EPSP slope against trial index, with 25 pairings between the before- and after- periods. Stippled lines are average slopes over corresponding trials. Lower panel, a control, recorded at the same time with a second Kenyon cell pathway, offset by 5 s with respect to the β -LN spike, and showing no significant change. **d**, Depression of KC– β -LN connection after 25 pairings with $dt = -4$ ms. Panels as in panel **c**. **e**, STDP plot for 26 values of $dt = t_{\text{post}} - t_{\text{pre}}$, where dt is measured as the delay between the β -LN spike (t_{post} , caused by intracellular current injection, + i) and the β -LN EPSP onset (t_{pre} , grey line, upper panels). EPSP onset time is used (rather than Kenyon cell stimulus time) because Kenyon cell spike time at the β -LN synapse is delayed from stimulus time, owing to spike propagation (see Fig. 4a). Note the zero-crossing is slightly offset from $dt = 0$ (lower panel).

is constrained to within-cycle interactions between pre- and post-synaptic neurons. STDP is therefore not specific to vertebrates or cortical architectures. We do not know the molecular underpinnings of STDP in this system, or whether STDP might confer the associative features usually ascribed to mushroom bodies^{4–7}. The fly and honey-bee genomes both reveal coding sequences for *N*-methyl-D-aspartate (NMDA) receptor subunits^{13,23} and some *Drosophila* behavioural results²⁴ are compatible with STDP learning rules²⁵. One hypothesis, readily testable here, is that STDP provides associativity by tagging transiently the subset of synapses activated simultaneously by the odour, before the conditional arrival of a slower, non-specific reward signal²⁶.

Our results reinforce the proposed importance of spike timing for this, and possibly other, olfactory system(s)^{1,2}: Kenyon cells act as coincidence detectors for synchronized projection neuron input², β -LNs act as coincidence detectors for Kenyon cell input; because STDP helps enhance β -LN synchronization, we infer that spike

timing must be relevant also for the processing of β -LN output. These results indicate that the oscillation cycle—a temporal unit of processing first defined by negative feedback in the antennal lobe¹⁴—is actively preserved in at least three successive layers of processing (projection neurons, Kenyon cells and β -LNs). It will be interesting to assess whether all Kenyon cell outputs obey the same STDP rules, and if these rules are themselves subject to learning-related modifications. Indeed, Kenyon cells seem to communicate with one another through axo-axonal chemical synapses²⁷. Given the dynamics of projection neuron/Kenyon cell activity vectors in response to odours^{1,2,15}, the possibility that Kenyon cell–Kenyon cell synapses also undergo STDP suggests a mechanism for sequence learning²⁸, similar to principles proposed for spatial map formation in rodents^{29,30}; here, however, the learned sequences have no relation to movement in physical space. The existence of such similarities (synaptic learning rules, and synchronized and sequential neural activity patterns) may bring us closer to understanding the

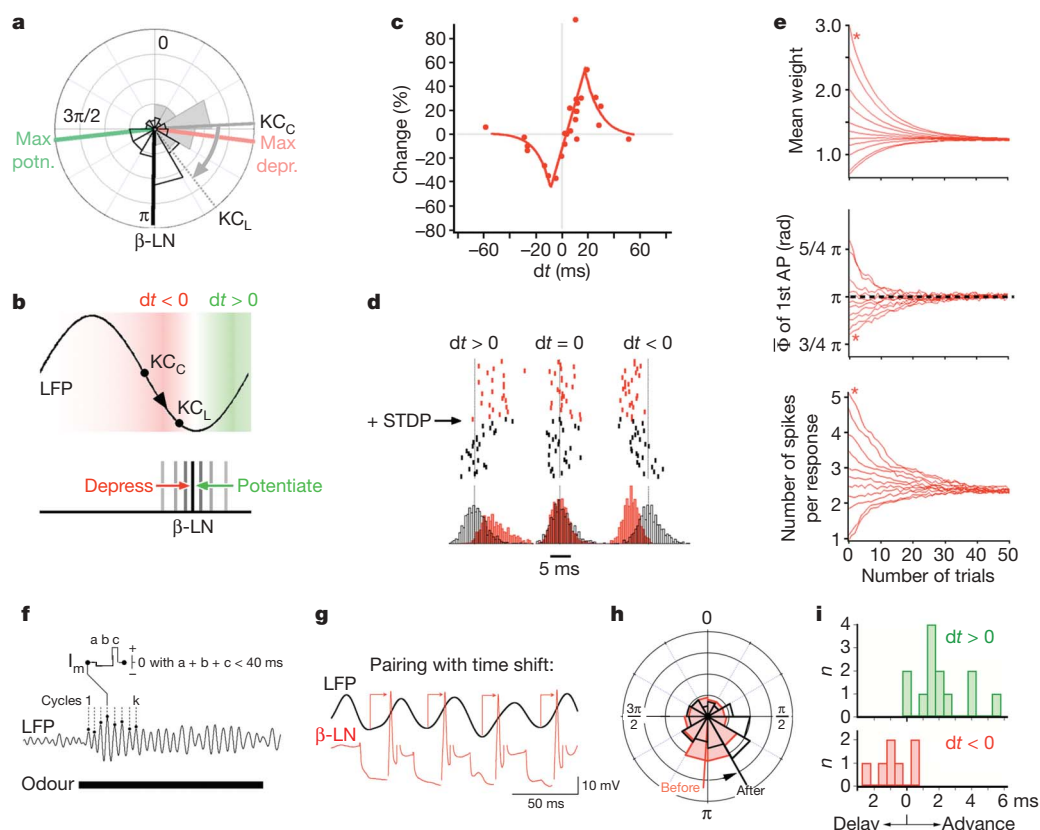


Figure 4 | The effect of STDP on β -LN spike timing. **a**, Polar plot of Kenyon cell spike phase in the calyx (somata) (KC_C) and in the β -lobe (KC_L), and β -LN spike phase (from dendrites in the β -lobe) relative to the LFP (in the calyx). All measurements from experiments. Green and red lines indicate extrema of the STDP curve (see panel **c**). **b**, Schematic of temporal relationships between LFP, Kenyon cell spike time, β -LN spike time and the STDP rule. The Kenyon cell mean spike time in the calyx (KC_C) is about $\pi/2$ after the LFP peak, and near the LFP trough in the β -lobe (KC_L), owing to propagation delay. β -LN mean spike time in the β -lobe is at the LFP trough (π rad). The STDP curve is represented in colour gradients. The predicted effect of STDP on β -LN spike time is schematized underneath. If the β -LN spike occurs early, STDP should depress late Kenyon cell inputs (in this oscillation cycle), delaying this β -LN spike at the next opportunity. The converse applies if the β -LN spike occurs late. **c**, The STDP fit (two exponentials flanking a linear segment, see text) overlaid on experimental data. **d**, Simulations of STDP on β -LN spike time (rasters) (model β -LN excited by 10 model Kenyon cells during one LFP cycle). First trial at top. Three conditions are illustrated: left panel, low input weights (mean, 1.8 mV; range, 3 mV), causing late β -LN-spike times ($dt > 0$); when STDP is turned on, potentiation shifts β -LN spikes to earlier times. Right panel, high input

weights (mean, 9 mV; range, 3 mV); when STDP is turned on, depression delays β -LN-spike times. Middle panel, intermediate weights, causing no change. Histograms show the distribution of β -LN spike times before (red) and after (black) STDP (1,000 runs per condition). **e**, Evolution of KC– β -LN weights (upper panel), β -LN mean spike phase (middle panel) and number of spikes per response (lower panel) over 50 trials following onset of STDP (at trial 1). AP, action potential. Each curve is an average of 200 simulations (11 different input distribution means). Asterisks indicate a corresponding condition in the three plots. **f**, Schematic of experimental design. LFP cycles (1...k) during which the recorded β -LN-produced action potentials are selected. Peaks of LFP are used to trigger a sequence of current (I_m) pulses (a, b, c) into the β -LN (one such sequence per oscillation cycle). The a-b-c sequence lasts less than one oscillation cycle, and is repeated for all selected cycles, over several trials. **g**, Example of protocol described in panel **f**, such that the β -LN spike is phase-delayed to $\sim 3/2\pi$ (arrows). (Interrupted segments of β -LN potential trace are bridge-balance artefacts.) **h**, Phase plot of spikes in one β -LN before and after pairing (10 trials each), as in panel **g**. Fifteen pairing trials (estimated $dt = 17$ ms). **i**, Distributions of pairing-induced mean phase shifts, measured in 20 separate experiments (6 β -LNs; mean \pm s.e.m. = -0.74 ± 0.4 ms versus 2.0 ± 0.4 ms).

relationships between circuit dynamics, architecture and learning in the brain.

METHODS SUMMARY

All results were obtained *in vivo* from locusts (*Schistocerca americana*) in an established, crowded colony. Odours were delivered by injection within a constant stream of dessicated air. The results presented here originate from recordings of over 50 β -LNs in 40 locusts. Kenyon cells were stimulated electrically from their soma, using gold-electroplated tetrodes or intracellular electrodes. β -lobe neurons were recorded from their dendrites in the β -lobe with glass micropipettes. Field potential recordings were carried out from the Kenyon cell soma cluster, using twisted-wire tetrodes. Stimulation protocols and data analysis were carried out using specialized software (LabView, National Instruments; Igor, Wavemetrics).

Full Methods and any associated references are available in the online version of the paper at www.nature.com/nature.

Received 26 April; accepted 1 June 2007.

Published online 20 June 2007.

- Mazor, O. & Laurent, G. Transient dynamics versus fixed points in odor representations by locust antennal lobe projection neurons. *Neuron* **48**, 661–673 (2005).
- Perez-Orive, J. *et al.* Oscillations and sparsening of odor representations in the mushroom body. *Science* **297**, 359–365 (2002).
- Wilson, R. I., Turner, G. C. & Laurent, G. Transformation of olfactory representations in the *Drosophila* antennal lobe. *Science* **303**, 366–370 (2004).
- deBelle, J. S. & Heisenberg, M. Associative odor learning in *Drosophila* abolished by chemical ablation of mushroom bodies. *Science* **263**, 692–695 (1994).
- Dubnau, J., Grady, L., Kitamoto, T. & Tully, T. Disruption of neurotransmission in *Drosophila* mushroom body blocks retrieval but not acquisition of memory. *Nature* **411**, 476–480 (2001).
- Yu, D., Keene, A. C., Srivatsan, A., Waddell, S. & Davis, R. L. *Drosophila* DPM neurons form a delayed and branch-specific memory trace after olfactory classical conditioning. *Cell* **123**, 945–957 (2005).
- Zars, T., Fischer, M., Schulz, R. & Heisenberg, M. Localization of a short-term memory in *Drosophila*. *Science* **288**, 672–675 (2000).
- Bi, G. Q. & Poo, M.-M. Synaptic modifications in cultured hippocampal neurons: dependence on spike timing, synaptic strength, and postsynaptic cell type. *J. Neurosci.* **18**, 10464–10472 (1998).
- Markram, H., Lubke, J., Frotscher, M. & Sakmann, B. Regulation of synaptic efficacy by coincidence of postsynaptic APs and EPSPs. *Science* **275**, 213–215 (1997).
- Roberts, P. D. & Bell, C. C. Spike timing dependent synaptic plasticity in biological systems. *Biol. Cybern.* **87**, 392–403 (2002).
- Clyne, P. J. *et al.* A novel family of divergent seven-transmembrane proteins: candidate odorant receptors in *Drosophila*. *Neuron* **22**, 327–338 (1999).
- Vosshall, L. B., Wong, A. M. & Axel, R. An olfactory sensory map in the fly brain. *Cell* **102**, 147–159 (2000).
- The Honeybee Genome Sequencing Consortium. Insights into social insects from the genome of the honeybee *Apis mellifera*. *Nature* **443**, 931–949 (2006).
- MacLeod, K. & Laurent, G. Distinct mechanisms for synchronization and temporal patterning of odor-encoding neural assemblies. *Science* **274**, 976–979 (1996).
- Wehr, M. & Laurent, G. Odour encoding by temporal sequences of firing in oscillating neural assemblies. *Nature* **384**, 162–166 (1996).
- Jortner, R., Farivar, S. S. & Laurent, G. A simple connectivity scheme for sparse coding in an olfactory system. *J. Neurosci.* **27**, 1659–1669 (2007).
- MacLeod, K., Backer, A. & Laurent, G. Who reads temporal information contained across synchronized and oscillatory spike trains? *Nature* **395**, 693–698 (1998).
- Diesmann, M., Gewaltig, M. O. & Aertsen, A. Stable propagation of synchronous spiking in cortical neural networks. *Nature* **402**, 529–533 (1999).
- Vogels, T. P., Rajan, K. & Abbott, L. F. Neural network dynamics. *Annu. Rev. Neurosci.* **28**, 357–376 (2005).
- Arthur, J. V. & Boahen, K. *Advances in Neural Information Processing*. (eds Sholkopf, B. & Weiss, Y.) 75–82 (MIT Press, 2006).
- Suri, R. E. & Sejnowski, T. J. Spike propagation synchronized by temporally asymmetric Hebbian learning. *Biol. Cybern.* **87**, 440–445 (2002).
- Zhigulin, V. P., Rabinovich, M. I., Huerta, R. & Abarbanel, H. D. Robustness and enhancement of neural synchronization by activity-dependent coupling. *Phys. Rev. E* **67**, 021901 (2003).
- Ultsch, A., Schuster, C. M., Laube, B., Betz, H. & Schmitt, B. Glutamate receptors of *Drosophila melanogaster*. Primary structure of a putative NMDA receptor protein expressed in the head of the adult fly. *FEBS Lett.* **324**, 171–177 (1993).
- Tanimoto, H., Heisenberg, M. & Gerber, B. Experimental psychology: event timing turns punishment to reward. *Nature* **430**, 983 (2004).
- Drew, P. J. & Abbott, L. F. Extending the effects of spike-timing-dependent plasticity to behavioral timescales. *Proc. Natl Acad. Sci. USA* **103**, 8876–8881 (2006).
- Frey, U. & Morris, R. G. Synaptic tagging: implications for late maintenance of hippocampal long-term potentiation. *Trends Neurosci.* **21**, 181–188 (1998).
- Leitch, B. & Laurent, G. GABAergic synapses in the antennal lobe and mushroom body of the locust olfactory system. *J. Comp. Neurol.* **372**, 487–514 (1996).
- Nowotny, T., Rabinovich, M. I., Huerta, R. & Abarbanel, H. D. Decoding temporal information through slow lateral excitation in the olfactory system of insects. *J. Comput. Neurosci.* **15**, 271–281 (2003).
- Blum, K. I. & Abbott, L. F. A model of spatial map formation in the hippocampus of the rat. *Neural Comput.* **8**, 85–93 (1996).
- Mehta, M. R., Lee, A. K. & Wilson, M. A. Role of experience and oscillations in transforming a rate code into a temporal code. *Nature* **417**, 741–746 (2002).

Supplementary Information is linked to the online version of the paper at www.nature.com/nature.

Acknowledgements This work was supported by an NIH training grant, grants from the NIDCD, and the Lawrence Hanson Fund. We thank E. Schuman, I. Fiete, M. Murthy, M. Papadopoulou, O. Mazor, V. Jayaraman and the reviewers for their helpful comments.

Author Information Reprints and permissions information is available at www.nature.com/reprints. The authors declare no competing financial interests. Correspondence and requests for materials should be addressed to G.L. (laurentg@caltech.edu).

METHODS

Preparation and stimuli. All results were obtained *in vivo* from locusts (*Schistocerca americana*) in an established, crowded colony. Young adults of either sex were immobilized, with two antennae intact for olfactory stimulation. The brain was exposed and de-sheathed as previously described². Odours were delivered by injection of a controlled volume of odourized air within a constant stream of dessicated air. Teflon tubing was used at and downstream from the mixing point to prevent odour lingering and cross-contamination. Odours were used at 10% vapour pressure further diluted in the dessicated air stream. The results presented here originate from recordings of over 50 β -LNs in 40 locusts.

Electrical stimulation. Twisted-wire tetrodes obtained from FHC (number CE4B75) were modified for monopolar stimulation, with the casing serving as the anode. The tips of the tetrodes were splayed such that the distance between the exposed tips was approximately equal to 60% of the diameter of the mushroom body calyx. The exposed end of the stimulating electrode was embedded among Kenyon cell somata. The tetrodes were electroplated with gold solution to reduce the impedance to between 200 and 350 k Ω at 1 kHz. Stimulating currents (5–50 μ A, 0.1 ms) were generated by an STG1000 Multichannel System. The number of consecutive pairing trials varied between 5 and 25, at 10-s intervals. Propagation delays for the Kenyon cell action potentials were measured as the delay between a Kenyon cell soma stimulus and the extracellular spike volley recorded in the β -lobe, at the level of the β -LN dendritic recordings³¹.

Intracellular recordings. Sharp electrode recordings from the dendrites of β -lobe neurons were made with borosilicate glass micropipettes (DC resistance, 100 M Ω) filled with 3 M K acetate. Input resistance was around 300 M Ω . The cell type from which the data are derived could be recognized by several characteristics, including response to odour, sub-threshold baseline activity profile, and response to electrical stimulation of Kenyon cells. A series of pilot experiments, in which the cells were stained intracellularly by injection of 6% cobalt hexamine, confirmed that cells with these physiological characteristics belong to a specific morphological class (see Supplementary Fig. 1). EPSP slopes were measured from linear fits to voltage trace between 10% and 90% of rising phase. Recordings from β -LNs were always made from dendrites in the β -lobe (the largest dendrites are often several μ m in diameter). That these recordings were not from Kenyon cell axons is guaranteed by the fact that Kenyon cell axons are too small for intracellular impalement (100–400 nm diameter²⁷). This identity of β -LNs was confirmed by dye injection. Kenyon cell intracellular recordings were always made from their somata (5–7 μ m diameter).

Field recordings. Twisted-wire tetrodes obtained from FHC (number CE4B75) were used for extracellular recordings of the local field potential (LFP). For these recordings, the tip was cut with fine scissors and each channel tip was electroplated with gold solution to reduce the impedance to between 200 and 350 k Ω at 1 kHz. These recordings were made with a custom-built 16-channel pre-amplifier and amplifier. Two to four tetrodes were used simultaneously. The pre-amp has a unitary gain, and the amplifier gain was set to 10,000 \times . For pairing experiments during odour stimuli (Fig. 4f–i), the LFP was low-pass filtered on line and fed through a real-time peak-detection algorithm. Each detected peak was given a rank order (1...k) and the cycles during which the recorded β -LN produced an action potential were identified. Because of inter-trial variability of LFP and small uncertainty about cycle ranking in each trial, we typically selected eight consecutive oscillation cycles centred on the cycles of interest. During each one of those 8 consecutive cycles, a current-pulse sequence (a–c, Fig. 4f) was injected into the β -LN dendrite so as to phase-advance ($b > 0$; $c < 0$) or phase-delay ($b < 0$; $c > 0$) its odour-evoked spikes. This pulse sequence was started again at each LFP peak of the selected cycles.

Simulations. A leaky integrate-and-fire model ($R = 300$ M Ω , $\tau = 20$ ms) was implemented in Igor (Wavemetrics, Lake Oswego, Oregon). Spiking threshold and after-hyperpolarization were estimated from intracellular recordings. A single oscillation cycle was modelled as 10 inputs convolved with a current waveform derived from dual KC– β -LN recordings. The number of inputs per cycle was based on KC– β -LN connectivity estimates from dual intracellular recordings and from β -LN baseline sub-threshold activity, as well as on the average Kenyon cell population response time course^{1–3} and response probability². The specific Kenyon cell spike times were drawn randomly at every trial from the Kenyon cell spike time distribution. The weights at the start of each simulation were drawn randomly from a distribution similar to that observed experimentally, and scaled for different simulations to evaluate the effect on the spiking response in the presence and absence of STDP. The STDP rule was modelled, as described in the text, by two exponentials flanking a linear region (fitted to data by minimizing Chi-square; Igor curve-fitting). When STDP was invoked, every trial was followed by an update of the weights, on the basis of dt , as dictated by the fitted STDP curve (Fig. 4).

31. Perez-Orive, J., Bazhenov, M., Stopfer, M. & Laurent, G. Intrinsic and circuit properties favor coincidence detection for decoding oscillatory input. *J. Neurosci.* **24**, 6037–6047 (2004).

LETTERS

DNMT3L connects unmethylated lysine 4 of histone H3 to *de novo* methylation of DNA

Steen K. T. Ooi^{1*}, Chen Qiu^{2*}, Emily Bernstein^{3*}, Keqin Li^{2*}, Da Jia², Zhe Yang², Hediye Erdjument-Bromage⁴, Paul Tempst⁴, Shau-Ping Lin⁵, C. David Allis³, Xiaodong Cheng² & Timothy H. Bestor¹

Mammals use DNA methylation for the heritable silencing of retrotransposons and imprinted genes and for the inactivation of the X chromosome in females. The establishment of patterns of DNA methylation during gametogenesis depends in part on DNMT3L, an enzymatically inactive regulatory factor that is related in sequence to the DNA methyltransferases DNMT3A and DNMT3B^{1,2}. The main proteins that interact *in vivo* with the product of an epitope-tagged allele of the endogenous *Dnmt3L* gene were identified by mass spectrometry as DNMT3A2, DNMT3B and the four core histones. Peptide interaction assays showed that DNMT3L specifically interacts with the extreme amino terminus of histone H3; this interaction was strongly inhibited by methylation at lysine 4 of histone H3 but was insensitive to modifications at other positions. Crystallographic studies of human DNMT3L showed that the protein has a carboxy-terminal methyltransferase-like domain and an N-terminal cysteine-rich domain. CocrySTALLIZATION of DNMT3L with the tail of histone H3 revealed that the tail bound to the cysteine-rich domain of DNMT3L, and substitution of key residues in the binding site eliminated the H3 tail–DNMT3L interaction. These data indicate that DNMT3L recognizes histone H3 tails that are unmethylated at

lysine 4 and induces *de novo* DNA methylation by recruitment or activation of DNMT3A2.

Null alleles of *Dnmt3L* are lethal when transmitted through the maternal germ line as a result of a failure to establish maternal genomic imprints during oogenesis, and mutant males show reactivation of retrotransposons and extreme meiotic defects in spermatocytes. The loss of DNA methylation in DNMT3L-deficient male germ cells also causes hyperacetylation of histones and a loss of methylation from lysine 9 of histone H3 (ref. 3). DNMT3L stimulates *de novo* methylation by DNMT3A2 (refs 4,5) but does not enhance the binding of DNMT3A2 to DNA, and DNMT3L alone does not bind to DNA^{5,6}. However, the nature of the cues that regulate DNMT3L are unknown.

Embryonic stem (ES) cells express both DNMT3L and DNMT3A2, a germ-cell-specific isoform of DNMT3A that is also required for genomic imprinting^{4,7}. ES cells show much higher rates of *de novo* methylation than do differentiated somatic cells, and methylation imprints are gained and lost at high rates in ES cells^{8,9}. ES cells are therefore an appropriate cell type in which to carry out biochemical identification of proteins that interact with DNMT3L. We introduced a tandem His₆-FLAG tag into the N terminus of the

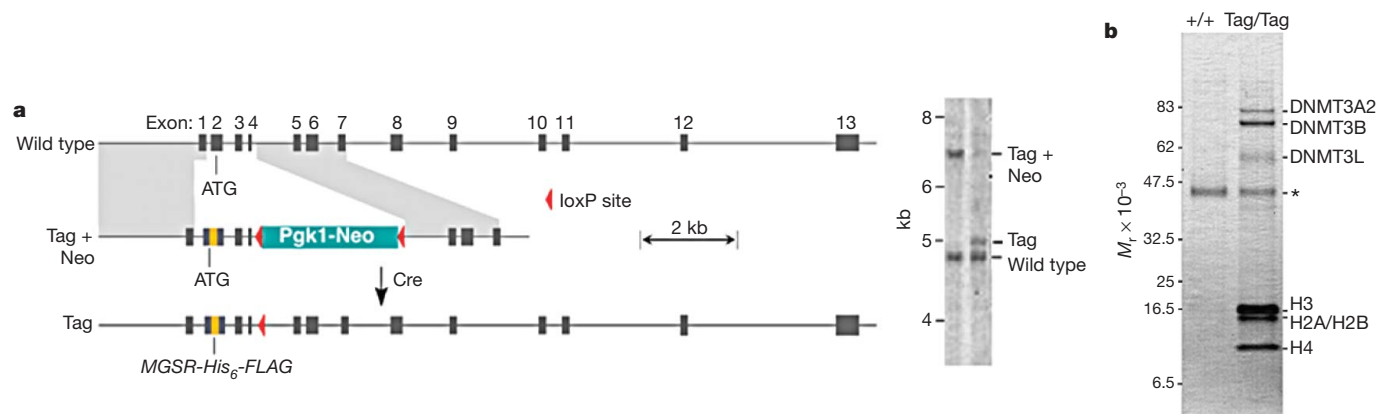


Figure 1 | Generation of epitope-tagged *Dnmt3L* locus and DNMT3L protein interaction screen in ES cells. **a**, Targeting of the endogenous mouse *Dnmt3L* locus with a replacement cassette that introduces an N-terminal His₆-FLAG epitope tag. The tag was introduced immediately after the first four amino acids of DNMT3L (Supplementary Fig. S1). The neo resistance cassette was deleted by transient exposure to Cre recombinase. Mice homozygous for the *Dnmt3L*^{Tag/Tag} allele are fertile and were used to generate homozygous *Dnmt3L*^{Tag/Tag} ES cells. The southern blot on the right shows

that homologous recombination and Cre-mediated excision of the marker occurred as predicted. **b**, Protein interaction screen in wild-type and *Dnmt3L*^{Tag/Tag} ES cells by FLAG immunoprecipitation. Coomassie-stained bands were subjected to MALDI-reTOF and mass spectra were screened against a non-redundant protein database to identify interacting proteins. The protein band marked by the asterisk is actin, a common contaminant in anti-FLAG immunoprecipitation.

¹Department of Genetics and Development, College of Physicians and Surgeons of Columbia University, New York, New York 10032, USA. ²Department of Biochemistry, Emory University, Atlanta, Georgia 30322, USA. ³Laboratory of Chromatin Biology, The Rockefeller University, New York, New York 10021, USA. ⁴Molecular Biology Program, Memorial Sloan-Kettering Cancer Center, New York, New York 10021, USA. ⁵Institute of Biotechnology, National Taiwan University, Taipei 106, Taiwan.

*These authors contributed equally to this work.

endogenous *Dnmt3L* gene by homologous recombination in ES cells to generate the *Dnmt3L^{Tag}* allele (Fig. 1a and Supplementary Fig. S1). Southern blotting (Fig. 1a) and DNA sequencing confirmed that the tag was targeted correctly, and expression of the tagged DNMT3L protein was confirmed on immunoblots probed with an anti-FLAG antibody (Supplementary Fig. S1). Mice that were homozygous for the tagged allele were of normal phenotype and both sexes were fertile, which indicated that the tag did not interfere with the function of DNMT3L.

We conducted anti-FLAG immunoprecipitation on lysates derived from *Dnmt3L^{Tag/Tag}* ES cells. Mass spectrometry of polypeptides specific to eluates derived from *Dnmt3L^{Tag}* samples (Fig. 1b) identified DNMT3A2 and DNMT3B, which have been reported to interact with *Dnmt3L* *in vitro*^{4,5,10}. DNMT3A2 has been reported to be required for *de novo* DNA methylation in germ cells, and germ-cell-specific conditional alleles of *Dnmt3A2* phenocopy null alleles of *Dnmt3L* (ref. 7). We also found that DNMT3L was associated with the four core histones (Fig. 1b).

Peptide interaction assays with biotinylated tails of the four core histones showed that recombinant human DNMT3L bound only to the N-terminal tail of histone H3 (Fig. 2a). Peptide interaction assays using different regions of the N-terminal histone H3 tail revealed that DNMT3L binding required the first seven N-terminal amino acids of H3 (Fig. 2a, right). The binding of DNMT3L to histone H3 was abolished by mono-, di- or trimethylation of lysine 4 on histone H3, but was insensitive to modifications at other positions (Fig. 2b). These data indicate that the interaction between DNMT3L and the N-terminal tail of histone H3 depends on the methylation state of H3 lysine 4. Fluorescence polarization data showed that the dissociation constant (K_d) for the interaction between the unmodified H3 N-terminal tail and full-length DNMT3L was 2.1 μ M; a single methyl group increased the K_d to 38.5 μ M, and no interaction could be detected when the pep-

tide was di- or trimethylated at lysine 4 (Fig. 2d). Isolation of mononucleosomes by treatment of nuclei with micrococcal nuclease before anti-FLAG immunoprecipitation showed that DNMT3L is associated with nucleosomes that are depleted for H3 methylated at lysine 4 (Fig. 2e). These data confirm that the interactions shown in Fig. 2a, b also occur *in vivo*.

The results of crystallographic studies have suggested a mechanism for the histone–DNMT3L interaction. The structure of full-length human DNMT3L was determined to a resolution of 3.29 Å. The three endogenous zinc ions within the cysteine-rich region established X-ray phasing (Fig. 3a and Supplementary Table T1). Although the classical methyltransferase fold that is characteristic of S-adenosyl L-methionine-dependent methyltransferases was present¹¹, the DNA recognition domain¹² was absent and a cysteine-rich region organized around the three zinc ions was located opposite to the region where the catalytic centre is located in active DNA (cytosine-5) methyltransferases (Fig. 3a).

A peptide corresponding to the first 24 amino acids of histone H3 was soaked into the DNMT3L crystal shown in Fig. 3a. Crystallographic analysis of the complex showed electron density for approximately seven amino acids bound to the zinc-binding domain; the remainder of the peptide was unstructured (Fig. 3b). On the basis of the binding data (Fig. 2) and the structural comparison with the PHD-like domain of BHC80, a component of the LSD1 histone H3 lysine 4 demethylation complex¹³, we deduced that the structured portion of the peptide is the first seven amino acids of H3. BHC80 selectively binds unmethylated H3 lysine 4 peptides, and this binding is mediated by a PHD-like domain that has strong structural similarities to the cysteine-rich domain of DNMT3L (Supplementary Fig. S2 and ref. 14). Mutations that introduce a bulky tryptophan side chain into the H3 binding site of DNMT3L (I107W) or that disrupt the interaction of an aspartic acid side chain with the amino group of H3 lysine 4 (D90A) eliminate the interaction of the H3 tail with

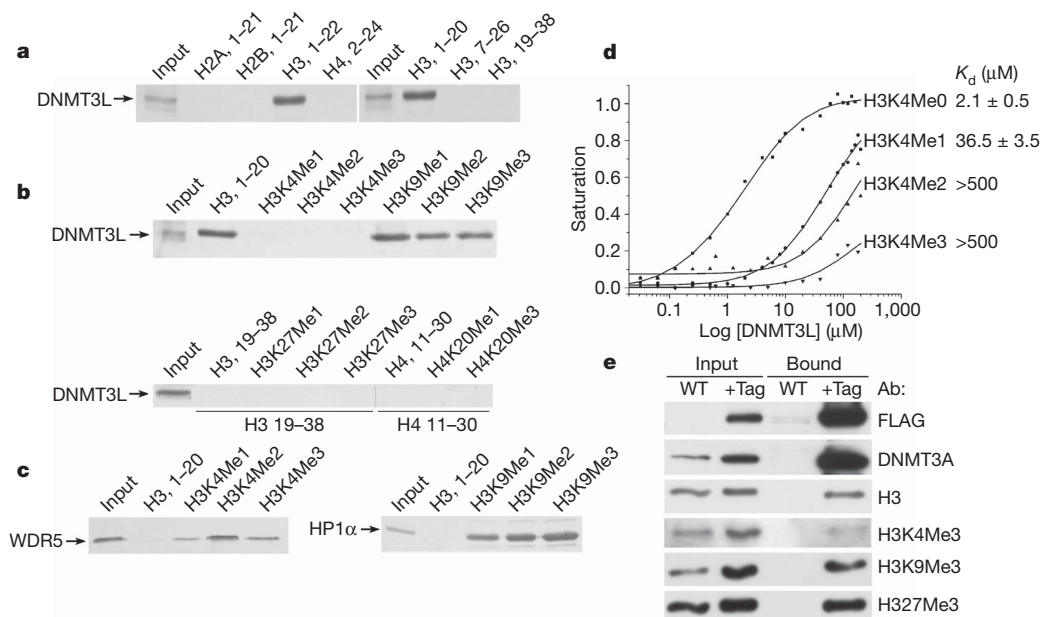


Figure 2 | Interaction of DNMT3L with the N terminus of histone H3 is abolished by methylation of H3 lysine 4. **a**, Peptide interaction assays with unmodified histone tails as indicated, incubated with full-length human DNMT3L. DNMT3L interacts only with the N-terminal tail of H3 (left), and this interaction requires only the first seven amino acids of H3 (right). **b**, Peptide interaction assays with DNMT3L and modified histone tails as indicated. DNMT3L bound only to the H3 tail that is unmodified at lysine 4. **c**, WDR5 (WD repeat domain 5) and the chromodomain of HP-1 α (heterochromatin protein 1 α) were used as controls for peptide binding specificity. **d**, Dissociation constants as determined by fluorescence

polarization with C-terminal fluoresceinated peptides. K_d values are shown on the right. The 18-fold increase in K_d caused by monomethylation of H3 lysine 4 prevented detection of DNMT3L binding in **b**. **e**, Histones associated with DNMT3L *in vivo* are depleted in H3 that is trimethylated at lysine 4. Nuclear extract was treated with micrococcal nuclease before immunoprecipitation followed by separation of proteins by SDS-polyacrylamide gel electrophoresis. Immunoblot was performed with the antibodies indicated. A specific depletion in H3 trimethylated at lysine 4 can be seen in the fourth immunoblot from the top.

DNMT3L (Fig. 3c). The basis for methylation-sensitive binding of H3 to DNMT3L is steric occlusion of the interaction between aspartic acid 90 in DNMT3L and lysine 4 of histone H3 (Fig. 3b, c and data not shown).

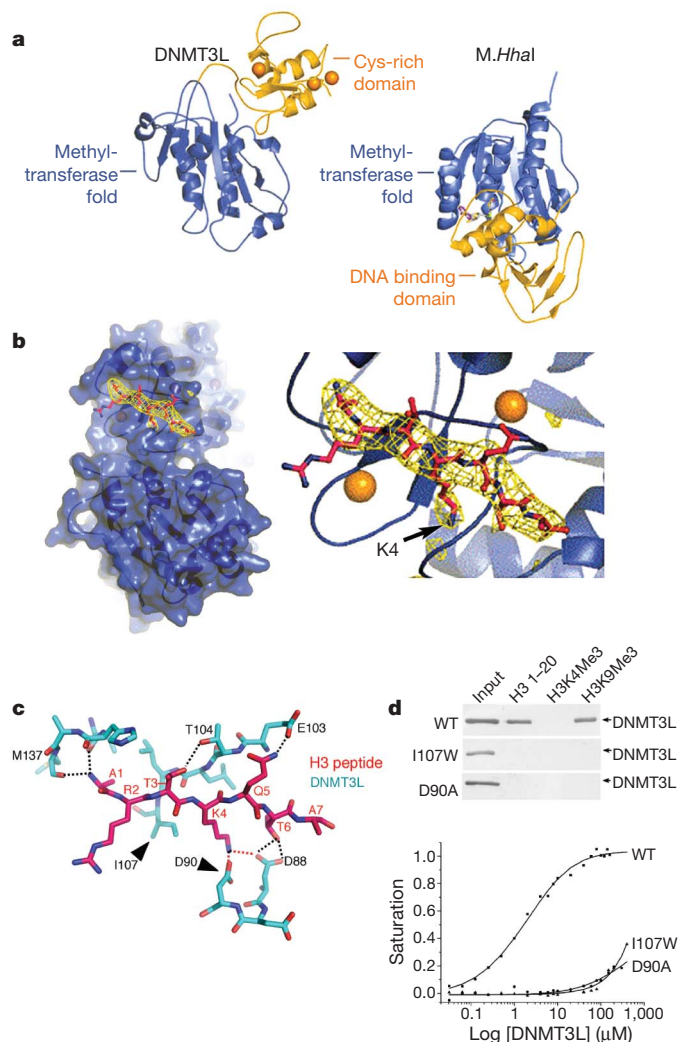


Figure 3 | Structure of DNMT3L and mode of recognition of histone H3 unmethylated at lysine 4. **a**, DNMT3L contains a classical methyltransferase fold as well as a cysteine-rich region organized around three zinc ions (indicated in yellow; zinc ions in orange). The structure of DNMT3L alone was determined to a resolution of 3.29 Å. **M.HhaI** is a bacterial DNA cytosine-5 methyltransferase that contains a classical methyltransferase fold¹². **b**, Structure of DNMT3L after incorporation of the H3 N-terminal tail into the DNMT3L crystal by soaking with peptide. The omit electron density (orange) is contoured at 4.0σ. At the resolution of 3.69 Å, the electron density map alone does not provide an unambiguous position of the bound peptide. The model shown here is based on stereochemical principles and on the strong structural similarity with BHC80, which also binds specifically to histone H3 unmethylated at lysine 4 (Supplementary Fig. S2 and ref. 14). Only the N-terminal seven amino acids of the 24-amino-acid peptide were structured. The side chain of R2 was also disordered in the crystal. **c**, Detailed interaction between the H3 N terminus (amino acids numbered in red) and DNMT3L (numbered in black). The dashed lines indicate potential interactions between amino-acid side chains. H3 lysine 4 makes contacts with the carboxylates of DNMT3L D90 and D88, and methylation of lysine 4 will occlude these interactions. **d**, Mutagenesis of residues in the peptide binding site of DNMT3L abolished binding. Arrowheads in **c** indicate positions of I107W and D90A mutations. Each mutation abolished the interaction of DNMT3L with the unmethylated N-terminal peptide as shown by binding assay (top) and fluorescence polarization (bottom). K_d for binding to the wild type was 2.1 μM and for each of the two mutated proteins was >500 μM.

These data indicate that *Dnmt3L* responds to states of histone modification to regulate *de novo* DNA methylation. Under this model, DNMT3L triggers *de novo* DNA methylation by activation or recruitment of DNMT3A2 upon contact with nucleosomes that contain unmethylated H3 lysine 4, while other sequences are masked from DNMT3L by the inhibitory effects of nucleosomes that contain histone H3 methylated at lysine 4.

Methylation of lysine 9 on histone H3 is required for DNA methylation in vegetative cells of the ascomycete *Neurospora crassa*, and for methylation of some non-CpG sequences in *Arabidopsis thaliana*^{15,16}. Mouse ES cells that lack the H3 lysine 9 methyltransferases Suv39h1 and Suv39h2 show slight demethylation of satellite DNA¹⁷. In each of these cases, the signal for DNA methylation is the presence of methylation at H3 lysine 9 rather than the absence of methylation at H3 lysine 4. Methylation of lysine 4 on histone H3 has recently been suggested to protect gene promoters from *de novo* DNA methylation in mammalian somatic cells^{18,19}, and this suggestion is fully compatible with the findings presented here.

DNMT3L is required for the *de novo* methylation of imprinting control regions in female germ cells and for the *de novo* methylation of dispersed repeated sequences in male germ cells. The data presented here point towards a novel mechanism whereby DNMT3L could convert patterns of histone H3 lysine 4 methylation, which are not known to be transmitted by mitotic inheritance, into patterns of DNA methylation that mediate the heritable transcriptional silencing of the affected sequences.

METHODS SUMMARY

Generation of *Dnmt3L*^{Tag} allele. A synthetic oligonucleotide coding for His₆ followed by the FLAG epitope was introduced into the *Dnmt3L* gene by homologous recombination in ES cells. Once we had confirmed correct targeting, we excised the neomycin resistance cassette by transient exposure to Cre, before injecting the cells into blastocysts to generate chimaeric mice. *Dnmt3L*^{Tag/Tag} ES cells were derived from blastocysts from homozygous breedings.

Immunoprecipitation. We immunoprecipitated clarified lysates from wild-type and *Dnmt3L*^{Tag/Tag} ES cells using EZview Red Anti-FLAG M2 Affinity Gel (Sigma) and eluted them with FLAG peptide (Sigma) according to the manufacturer's protocol.

Peptide interaction assays. The interaction of DNMT3L with biotinylated histone tails was assayed essentially as described²⁰.

Mass spectrometry. Protein bands were excised and digested with trypsin and then batch fractionated on a RP micro-tip, and the peptide mixtures were analysed by matrix assisted laser desorption/ionization reflectron time-of-flight (MALDI-reTOF) mass spectrometry (UltraFlex TOF/TOF; Bruker Daltonics) as described^{21, 22}. We took selected experimental masses (m/z) to search a non-redundant protein database ('NR'; ~3.7 × 10⁶ entries; National Center for Biotechnology Information; Bethesda, Maryland), using the PeptideSearch algorithm (M. Mann, Southern Denmark University, Odense, Denmark). Mass spectrometric sequencing of selected peptides was done by MALDI-TOF/TOF (MS/MS) analysis on the same prepared samples, using the UltraFlex instrument in 'LIFT' mode. We used fragment ion spectra to search the NR database using the MASCOT MS/MS Ion Search program (Matrix Science Ltd.).

X-ray crystallography. We solved the structure of full-length human DNMT3L by three-wavelength Zn anomalous diffraction data (Supplementary Table T1).

Full Methods and any associated references are available in the online version of the paper at www.nature.com/nature.

Received 12 February; accepted 4 June 2007.

1. Bourc'his, D. & Bestor, T. H. Meiotic catastrophe and retrotransposon reactivation in male germ cells lacking *Dnmt3L*. *Nature* **431**, 96–99 (2004).
2. Bourc'his, D., Xu, G. L., Lin, C. S., Bollman, B. & Bestor, T. H. *Dnmt3L* and the establishment of maternal genomic imprints. *Science* **294**, 2536–2539 (2001).
3. Webster, K. E. et al. Meiotic and epigenetic defects in *Dnmt3L*-knockout mouse spermatogenesis. *Proc. Natl Acad. Sci. USA* **102**, 4068–4073 (2005).
4. Chen, T., Ueda, Y., Xie, S., Li, E. A novel *Dnmt3a* isoform produced from an alternative promoter localizes to euchromatin and its expression correlates with active *de novo* methylation. *J. Biol. Chem.* **277**, 38746–38754 (2002).
5. Suetake, I., Shinozaki, F., Miyagawa, J., Takeshima, H. & Tajima, S. DNMT3L stimulates the DNA methylation activity of *Dnmt3a* and *Dnmt3b* through a direct interaction. *J. Biol. Chem.* **279**, 27816–27823 (2004).

6. Karet, M. S., Botello, Z. M., Ennis, J. J., Chou, C. & Chedin, F. Reconstitution and mechanism of the stimulation of de novo methylation by human DNMT3L. *J. Biol. Chem.* **281**, 25893–25902 (2006).
7. Kaneda, M. *et al.* Essential role for de novo DNA methyltransferase Dnmt3a in paternal and maternal imprinting. *Nature* **429**, 900–903 (2004).
8. Lei, H. *et al.* De novo DNA cytosine methyltransferase activities in mouse embryonic stem cells. *Development* **122**, 3195–3205 (1996).
9. Humpherys, D. *et al.* Epigenetic instability in ES cells and cloned mice. *Science* **293**, 95–97 (2001).
10. Chen, Z. X., Mann, J. R., Hsieh, C. L., Riggs, A. D. & Chedin, F. Physical and functional interactions between the human DNMT3L protein and members of the de novo methyltransferase family. *J. Cell. Biochem.* **95**, 902–917 (2005).
11. Goll, M. G. & Bestor, T. H. Eukaryotic cytosine methyltransferases. *Annu. Rev. Biochem.* **74**, 481–514 (2005).
12. Klimasauskas, S., Kumar, S., Roberts, R. J. & Cheng, X. HhaI methyltransferase flips its target base out of the DNA helix. *Cell* **76**, 357–369 (1994).
13. Shi, Y. *et al.* Histone demethylation mediated by the nuclear amine oxidase homolog LSD1. *Cell* **119**, 941–953 (2004).
14. Lan, F. F. *et al.* Recognition of un-methylated histone H3 lysine 4 links BHC80 to LSD1-mediated gene repression. *Nature* doi:10.1038/nature06034 (this issue).
15. Tamaru, H. *et al.* Trimethylated lysine 9 of histone H3 is a mark for DNA methylation in *Neurospora crassa*. *Nature Genet.* **34**, 75–79 (2003).
16. Jackson, J. P., Lindroth, A. M., Cao, X. & Jacobsen, S. E. Control of CpNpG DNA methylation by the KRYPTONITE histone H3 methyltransferase. *Nature* **416**, 556–560 (2002).
17. Lehnertz, B. *et al.* Suv39h-mediated histone H3 lysine 9 methylation directs DNA methylation to major satellite repeats at pericentric heterochromatin. *Curr. Biol.* **13**, 1192–1200 (2003).
18. Weber, M. *et al.* Distribution, silencing potential and evolutionary impact of promoter DNA methylation in the human genome. *Nature Genet.* **39**, 457–466 (2007).
19. Appanah, R., Dickerson, D. R., Goyal, P., Groudine, M. & Lorincz, M. C. An unmethylated 3' promoter-proximal region is required for efficient transcription initiation. *PLoS Genet.* **3**, e27 (2007).
20. Wysocka, J. *et al.* WDR5 associates with histone H3 methylated at K4 and is essential for H3 K4 methylation and vertebrate development. *Cell* **121**, 859–872 (2005).
21. Sebastiaan Winkler, G. *et al.* Isolation and mass spectrometry of transcription factor complexes. *Methods* **26**, 260–269 (2002).
22. Erdjument-Bromage, H. *et al.* Examination of micro-tip reversed-phase liquid chromatographic extraction of peptide pools for mass spectrometric analysis. *J. Chromatogr. A* **826**, 167–181 (1998).

Supplementary Information is linked to the online version of the paper at www.nature.com/nature.

Acknowledgements We thank C.S. Lin for advice and assistance, D. Bourc'his, M. Damelin, C. Schaefer, X. Zhang and R. E. Collins for helpful discussions, J. R. Horton for collection of X-ray diffraction data, A. Ruthenberg for recombinant WDR5 protein, and K. Anderson, D. Bourc'his and C. Schaefer for criticism of the manuscript. This work was supported by grants from the National Institutes of Health to C. D. A., X. C., P. T. and T. H. B. and by a fellowship from the European Molecular Biology Organisation to S.K.T.O.

Author Information The X-ray structures of DNMT3L and the DNMT3L-H3 tail complex have been submitted to PDB as 2PVO and 2PVC, respectively. Reprints and permissions information is available at www.nature.com/reprints. The authors declare no competing financial interests. Correspondence and requests for materials should be addressed to T.H.B. (THB12@columbia.edu) or X.C. (XCheng@emory.edu).

METHODS

Generation of *Dnmt3L*^{Tag} allele. We synthesized the right and left homologous arms of the *Dnmt3L* targeting construct by cloning the indicated PCR products into pBluescript SK (Stratagene). We designed forward and reverse primers using the available mouse genome sequence data. The synthetic oligonucleotide (5'-GG CAC CAT CAC CAC CAT CAC GAC TAC AAA GAC GAT GAC GAT AAA TCC C-3') encoding a His₆ tag followed by FLAG epitope was introduced into a *Sma*I site within exon 2, which contains the ATG start codon. An additional *loxP* site in inverse orientation was introduced into a *Clal* site between exons 1 and 2 using the synthetic oligonucleotide 5'-ATA ACT TCG TAT AAT GTA TGC TAT ACG AAG TTA TAT CG-3'. The floxed neomycin resistance cassette was introduced from plasmid pEasyFlox (a gift from T. Ludwig) into *Not*I and *Xba*I sites within the pBluescript SK multiple cloning site between exons 3 and 4. Following gene targeting and G418 selection of 129Sv/Ev ES cell, we identified clones that had been correctly targeted by homologous recombination at the endogenous *Dnmt3L* locus by southern blotting with a 516-bp PCR-amplified probe, generated with 5'-AGA ATT CGC GGG CCC TAT GGA GAT ATA CAA GT-3' forward and 5'-ATG GAT CCG AAG TTC AGG AAG GTG TGT GTG T-3' reverse primers. The neomycin cassette was removed by Cre-mediated excision after transfection of the Cre-expressing plasmid pCAGGS-Cre (a gift from V. E. Papaioannou). Cre-mediated site-specific recombination was verified by southern blotting and sequencing of PCR products that spanned *LoxP* sites. Targeted clones that had deleted the neomycin cassette were injected into blastocysts and chimaeric mice were identified by southern blotting. Both male and female animals that are homozygous for the *Dnmt3L*^{Tag} allele are viable and fertile. *Dnmt3L*^{Tag/Tag} ES cells were derived from blastocysts from homozygous breedings.

LETTERS

Recognition of unmethylated histone H3 lysine 4 links BHC80 to LSD1-mediated gene repression

Fei Lan^{1*}, Robert E. Collins^{2*}, Rossella De Cegli^{1,4†}, Roman Alpatov¹, John R. Horton², Xiaobing Shi³, Or Gozani³, Xiaodong Cheng² & Yang Shi¹

Histone methylation is crucial for regulating chromatin structure, gene transcription and the epigenetic state of the cell. LSD1 is a lysine-specific histone demethylase that represses transcription by demethylating histone H3 on lysine 4 (ref. 1). The LSD1 complex contains a number of proteins, all of which have been assigned roles in events upstream of LSD1-mediated demethylation^{2–4} apart from BHC80 (also known as PHF21A), a plant homeodomain (PHD) finger-containing protein. Here we report that, in contrast to the PHD fingers of the bromodomain PHD finger transcription factor (BPTF) and inhibitor of growth family 2 (ING2), which bind methylated H3K4 (H3K4me3)^{5,6}, the PHD finger of BHC80 binds unmethylated H3K4 (H3K4me0), and this interaction is specifically abrogated by methylation of H3K4. The crystal structure of the PHD finger of BHC80 bound to an unmodified H3 peptide has revealed the structural basis of the recognition of H3K4me0. Knockdown of BHC80 by RNA inhibition results in the de-repression of LSD1 target genes, and this repression is restored by the reintroduction of wild-type BHC80 but not by a PHD-finger mutant that cannot bind H3. Chromatin immunoprecipitation showed that BHC80 and LSD1 depend reciprocally on one another to associate with chromatin. These findings couple the function of BHC80 to that of LSD1, and indicate that unmodified H3K4 is part of the 'histone code'⁷. They further raise the possibility that the generation and recognition of the unmodified state on histone tails in general might be just as crucial as post-translational modifications of histone for chromatin and transcriptional regulation.

Recent studies have identified a subset of PHD fingers that bind methyl lysine^{5,6,8,9}. To investigate the role of BHC80, a PHD finger-containing protein (Fig. 1a) of the LSD1 co-repressor complex, in transcriptional repression, we determined whether BHC80 also binds histone tails through its PHD finger. As shown in Fig. 1b, BHC80 binds the first 21 residues of histone H3 (lane 3), but not residues 21–44 or histones H4, H2A or H2B (lanes 4, 8–11). Unexpectedly, the BHC80–H3 interaction is disrupted by methylation of K4, but is insensitive to modifications at K9 or K14 (Fig. 1b, lanes 5–7 and Supplementary Fig. 1a). Native BHC80 in the LSD1 complex also binds H3K4me0, and this binding is similarly compromised by H3K4 dimethylation (Fig. 1c). BHC80 in a reconstituted, three-component complex (LSD1, the co-repressor CoREST and BHC80) also retains the ability to bind H3K4me0 (Supplementary Fig. 1b).

Although full-length BHC80 binds H3K4me0, deletion of the PHD finger (BHC80 Δ PHD) significantly impairs this interaction (Fig. 1d). A glutathione *S*-transferase (GST) fusion of the finger (BHC80 residues 486–543) binds the H3 tail and retains the histone-binding specificity of full-length BHC80 (Fig. 1e), indicating that the PHD

finger alone is necessary and sufficient for binding the H3K4me0 peptide. Furthermore, all three methylation states of H3K4 inhibit binding, with mono-methylation having the least adverse effect (Fig. 1f). Isothermal titration calorimetric (ITC) analysis of the PHD finger determined a dissociation constant (K_D) of $\sim 30 \mu\text{M}$ for the unmodified H3 peptide, $\sim 460 \mu\text{M}$ for H3K4me1, and no binding to H3K4me2 (Fig. 1g), consistent with the pulldown results.

The co-crystal structure of the BHC80 PHD domain (residues 486–543) bound to the unmodified H3 tail (residues 1–10) was solved at the resolution of 1.43 Å (Supplementary Table 1). All ten residues of the H3 peptide were observed (Supplementary Fig. 2) bound to one of the two molecules in the asymmetric unit (Supplementary Fig. 3a). Like all structurally characterized PHD (and RING) fingers, the BHC80 PHD finger adopts a 'cross-braced' topology of Zn^{2+} -coordinating residues (Fig. 2a, b). The H3 peptide binds to the surface of the PHD finger as an anti-parallel β -sheet, with H3R2–H3R8 forming backbone hydrogen bonds with G498–M502 of BHC80 (Fig. 2b). The cognate PHD finger contacts the first 8 residues of the H3 peptide, but H3 residues 9 and 10 interact with a neighbouring PHD molecule (Supplementary Fig. 3b). The substrate specificity of the BHC80 PHD finger is determined primarily through the recognition of the H3 amino terminus, H3K4 and H3R8 (Fig. 2c). Three main chain carbonyl oxygen atoms (residues 523, 524 and 525) form a hydrogen bond 'cage' that recognizes the N terminus of H3. The side chain of H3A1 inserts into a shallow hydrophobic pocket formed by L512, W527 and P523 (Fig. 2c, inset). The H3 peptide-binding site is further defined by M502, which inserts between H3R2 and H3K4, and the side chain of D489, which inserts between the side chains of H3K4 and H3R8, forming an electrostatic bridge between the two (Fig. 2c). The importance of D489 and M502 to H3 binding was confirmed by mutagenesis; mutation of D to A and M to W, respectively, abolished PHD binding to the unmodified histone H3 tail (Fig. 2d).

As well as interacting with D489, the epsilon amino group of H3K4 forms a hydrogen bond with the main chain carbonyl oxygen of E488 (Fig. 2c, inset). A β -carbon from H487, 4.0 Å away, further restricts the lysine-binding site. Indeed, a modelled mono-methyl lysine is allowed only a 15° range of motion before clashing with other atoms (Supplementary Fig. 4). This might account for the >15-fold reduction in binding of BHC80 to the H3K4me1 peptide when compared with the H3K4me0 peptide (Fig. 1g). A second or third methyl group would clash with the D489 side chain, E488 carbonyl, or H487 β -carbon, consistent with the observation that the BHC80 PHD finger does not bind H3K4me2 or H3K4me3 peptides (Fig. 1f, g). Therefore, molecular recognition of unmodified lysine

¹Department of Pathology, Harvard Medical School, 77 Ave Louis Pasteur, Boston, Massachusetts 02115, USA. ²Department of Biochemistry, Emory University School of Medicine, 1510 Clifton Road, Atlanta, Georgia 30322, USA. ³Department of Biological Sciences, Stanford University, Stanford, California 94305, USA. ⁴Dipartimento di Biochimica e Biotecnologie Mediche, Università di Napoli 'Federico II', Via S. Pansini 5, 80131 Napoli, Italy. [†]Present address: Telethon Institute of Genetics and Medicine (TIGEM), Via P. Castellino 111, 80131 Naples, Italy.

*These authors contributed equally to this work.

is primarily through bonds to the unmodified epsilon amino group, and steric exclusion of methyl groups. This mode of binding is distinct from the caging of di- and tri-methyl lysine by aromatic residues, as identified in the polycomb and heterochromatin protein 1 (HP1) chromodomains^{10–13}.

The aromatic cage, though absent from BHC80, is also present in structurally characterized methyl-lysine-binding PHD fingers, such as those of BPTF and ING2 (refs 14,15). The PHD fingers of BHC80, BPTF and ING2 adopt highly similar folds (Fig. 3a). All engage the H3 peptide as an anti-parallel β -sheet on the same face, with recognition of the H3 N-amine and the H3A1 side chain. H3R2 is buried in a pocket in BPTF and ING2, but is not contacted by BHC80. In BHC80, M502 occupies the space left open for R2 binding by a

conserved glycine (G) in BPTF and ING2 (ref. 12). Only BHC80 contacts H3R8, whereas in BPTF and ING2, the H3 peptide meanders off the face of the PHD finger before R8. The BPTF PHD finger features a full aromatic cage (Fig. 3b) reminiscent of the binding of the HP1 or polycomb chromodomain to trimethyl lysine^{12,13}, whereas ING2 has only half a hydrophobic cage, with a serine and methionine finishing the H3K4 binding pocket, similar to recognition of H3K4me3 by the chromo-ATPase/helicase-DNA-binding double chromodomain^{16,17}. As a family, PHD fingers show flexibility in peptide binding (Fig. 3c), making it difficult to predict whether an individual PHD finger is a histone-binding module, and whether it binds lysine or methyl lysine, on the basis of its primary sequence. Indeed, the robustness of the PHD scaffold, and its plasticity as a binding module, have been noted¹⁸. Our data indicate that the array of PHD fingers in chromatin-interacting and -modifying proteins, many of which lack the consensus binding sequence for H3K4me3

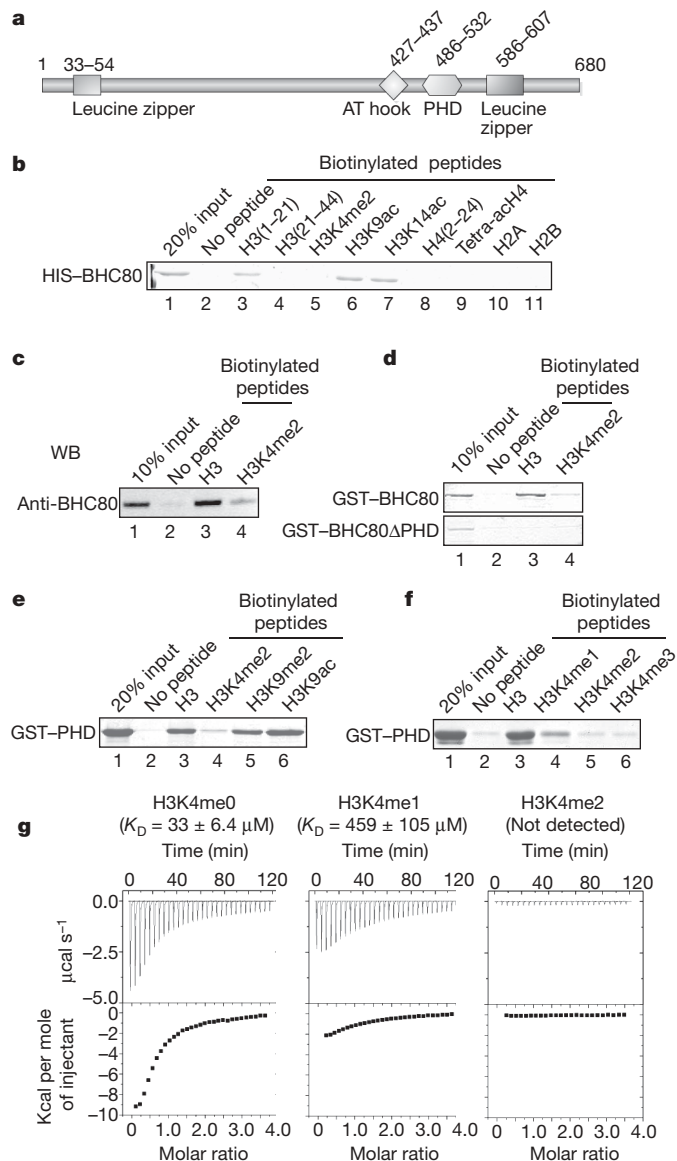


Figure 1 | BHC80 binds histone H3 through the PHD zinc finger. **a**, Diagram of BHC80 domain architecture. AT hook, a motif that binds AT-rich DNA. **b**, *In vitro* assays of binding of recombinant BHC80 to histone tail peptides. ac, acetyl group. **c**, Native BHC80 in purified LSD1 complex also preferentially binds unmodified H3 tail. WB, western blot, using antibodies against BHC80. **d**, PHD finger of BHC80 is necessary for H3 tail binding. **e**, The PHD finger is sufficient for H3 tail binding. **f**, Methylation of H3K4 inhibits PHD finger binding to the H3 tail. **g**, ITC measurement of binding of the BHC80 PHD finger to unmodified, mono-, or di-methylated H3K4 peptides (residues 1–10). K_D values are means (\pm s.d.) of at least three experiments using varied peptide and protein concentrations.

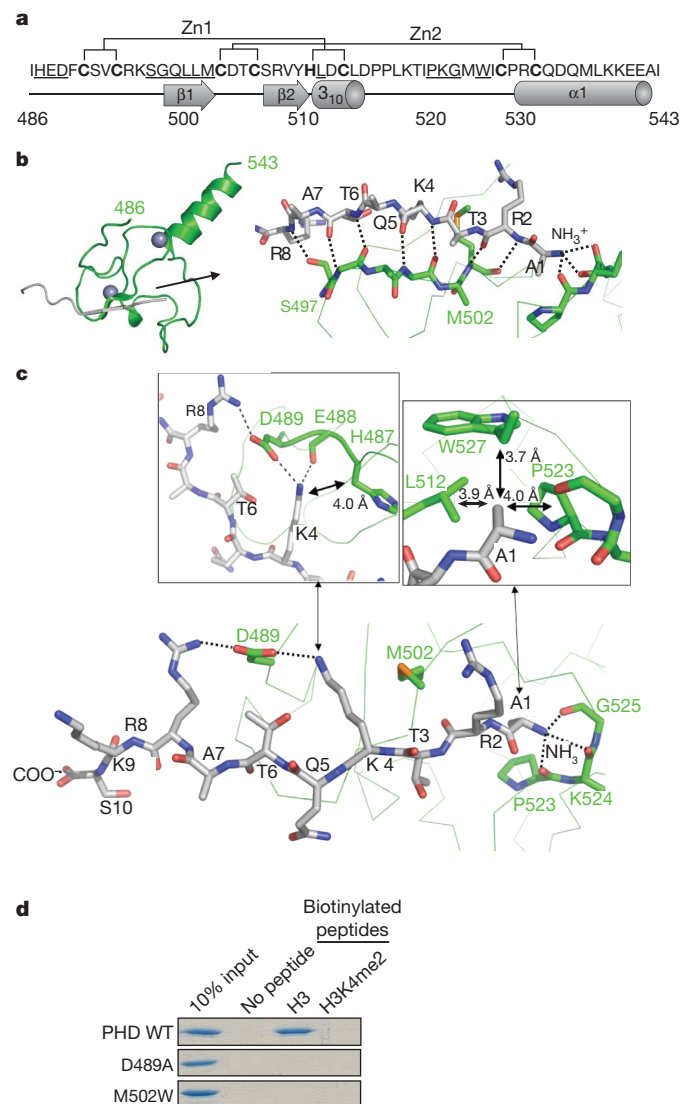


Figure 2 | Structure of BHC80 PHD with H3 1–10. **a**, Cross-brace topology of the PHD domain. Residues involved in peptide binding are underlined. Bold residues are those involved in chelating Zn. **b**, The H3 peptide binds BHC80 as an anti-parallel β -strand (grey). **c**, Peptide binding is specified by the insertion of M502 between H3R2 and H3K4 and D489 between H3K4 and H3R8. D489 and E488 bind H3K4, and H487 (4.0 Å away) restricts methyl-lysine binding (Supplementary Fig. 4). The N-terminal amine of H3 is caged by carbonyl oxygens, and H3A1 is recognized by a shallow hydrophobic pocket. **d**, Mutation of D489 and M502 disrupt PHD binding to unmodified H3. WT, wild type.

that is found in the BPTF and ING PHD fingers, might have histone-binding activities of unknown specificity. In this regard, the DNA methyltransferase 3-like protein, Dnmt3L, a regulatory factor that is required for *de novo* DNA methylation of imprinting control regions in female germ cells and of retro-transposons in male germ cells^{19–21}, was found to bind H3K4me0 through its Cys-rich PHD-like domain²². Structural comparison reveals that the N-terminal Cys-rich domain of DNMT3L is similar to the PHD finger of BHC80 (Supplementary Fig. 5). The structural similarity as well as their common mode of interaction with histone H3K4me0 raises the question of whether *de novo* DNA methylation (by DNMT3) is linked to the action of H3K4 demethylases and their associated complex components.

Having established the specificity of BHC80 for H3K4me0, we next investigated whether LSD1-mediated demethylation of H3K4me2 affects BHC80 binding at target promoters *in vivo*. Previous studies reported that depletion of LSD1 by RNA interference (RNAi) resulted in an increase in H3K4me2 at the synapsin 1 (*SYN1*) and voltage-gated sodium channel 1 α (*SCN1A*) promoters¹⁴. Importantly, chromatin immunoprecipitation (ChIP) analysis showed that the binding of BHC80 to these promoters was reduced in the LSD1-depleted cells, although the global level of BHC80 was unaffected (Fig. 4a and data not shown). These data are consistent with a model in which LSD1-mediated demethylation of H3K4me2 is important for the association of BHC80 with chromatin.

We further investigated the function of BHC80 in LSD1-mediated transcriptional repression by depleting BHC80 using two independent short hairpin RNA (shRNA) constructs (Fig. 4b, top). The inhibition of BHC80 expression resulted in a consistent depression of a number of LSD1 target genes, including *SCN1A*, *SCN3A* and *SYN1* (Fig. 4b). Introduction of the RNAi-resistant wild-type BHC80, but not the RNAi-resistant PHD finger mutant D489A, into the BHC80 knockdown cells restored the repression of LSD1 target genes, indicating that binding of H3K4me0 by BHC80 is important for LSD1-mediated gene repression. D489A was expressed at a similar level to that of the wild-type protein (Fig. 4c) and assembled into the LSD1 complex in the transfected cells (data not shown).

The binding of BHC80 to H3K4me0, which is a demethylation product of LSD1, indicates that BHC80 functions downstream of LSD1. How is a downstream effector of LSD1 required for efficient LSD1-mediated repression? Recent studies have indicated that the regulation of histone methylation is highly dynamic, and might involve the actions of both methylases and demethylases at the same target promoters²³. BHC80 may be necessary to help to maintain LSD1 at the target promoters, thereby preventing the re-methylation of H3K4. Consistent with this idea, BHC80 has been shown to interact physically with LSD1 (ref. 24). To address this model experimentally, we compared the binding of LSD1 to H3 using LSD1 complexes prepared from either wild-type or BHC80-knockdown cells. A reduction of BHC80 in the LSD1 complex resulted in decreased binding of LSD1 to K4 unmethylated histone H3 peptides *in vitro* (Fig. 4d), indicating that BHC80 is important for the association of LSD1 with its reaction product H3K4me0. Consistent with this, recombinant BHC80 could significantly increase binding of LSD1 to the H3K4me0 peptide in the presence of CoREST *in vitro* (Supplementary Fig. 1b). These findings indicate that BHC80 is required for the association of LSD1 with histone H3 after demethylation.

We further investigated the effect of depletion of BHC80 on the LSD1 protein complex and its occupancy at target promoters. Knockdown of BHC80 had no effect on the assembly of the LSD1 complex in solution by co-immunoprecipitation analysis (Fig. 4e). In contrast, occupancy of LSD1 at its target gene loci was reduced as a result of BHC80 knockdown (Fig. 4e). These findings support a model in which BHC80 is required for stable association of the LSD1 complex with its target promoters. An alternative, but not mutually exclusive, model is that binding of BHC80 to the demethylated H3 might be important for LSD1 to mediate demethylation of the neighbouring nucleosome. This propagation mechanism is similar to the one that has been proposed for the H3K9 methyltransferase Suv39H and HP1, in which the Suv39H methylase and the H3K9me-binding HP1 function together to propagate the repressive signal at the target loci^{25–27}. Many histone demethylases contain histone tail-binding modules in the form of PHD or Tudor domains. It will be interesting to determine whether some of these histone tail-binding modules function similarly to what has been reported here for LSD1

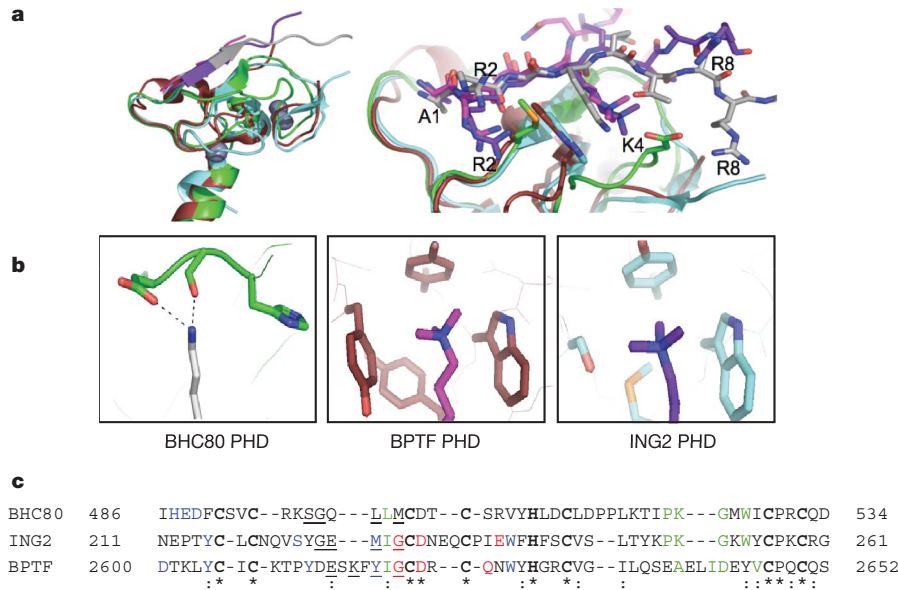


Figure 3 | Structural comparison of PHD fingers. **a**, Superimposition of PHD domains of BHC80 (PDB 2PUY, green, H3 grey), BPTF (PDB 2F6J, red, H3 pink) and ING2 (PDB 2GQ6, blue, H3 purple). **b**, Recognition of H3K4 by BHC80 (left) and binding of H3K4me3 by BPTF (middle) and ING2 (right); colours as in **a**. **c**, Sequence alignment of the PHD fingers of

BHC80, BPTF and ING2. Zinc-binding residues are bold, K4-binding residues blue and the R2-binding pocket, red. Residues that form the N-amine and A1 binding pockets are green. Residues that form the anti-parallel β -sheet with peptide are underlined. Stars mark invariant residues, and colons denote conservation.

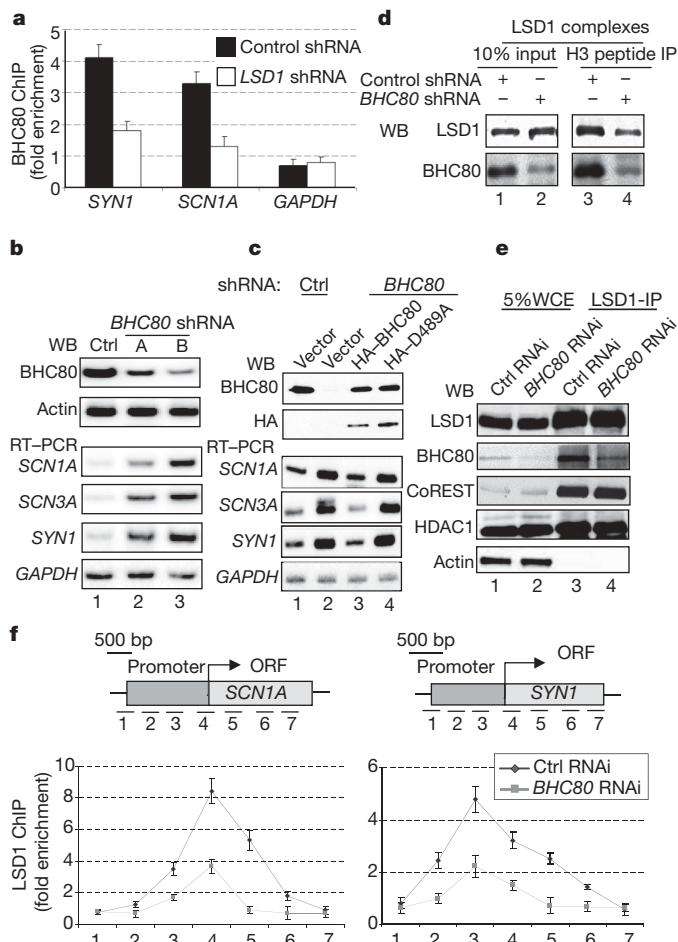


Figure 4 | BHC80 binding to the H3 tail is important for LSD1-mediated repression. **a**, The occupancy of promoters by BHC80 is reduced in HeLa cells where LSD1 is knocked down by RNAi. Glyceraldehyde-3-phosphate dehydrogenase (*GADPH*) is used as a control. **b**, BHC80 was effectively depleted by BHC80 shRNAs and expression of *SCN1A*, *SCN3A* and *SYN1* were de-repressed in the BHC80 RNAi cells. Ctrl, control. **c**, RNAi-resistant wild-type BHC80, but not the PHD point mutant D489A, restored target gene repression in BHC80 RNAi cells. **d**, Reduction of BHC80 in the LSD1 complex reduced the association of LSD1 with H3 peptide. IP, immunoprecipitate. **e**, Inhibition of BHC80 does not affect LSD1 complex formation in solution. **f**, RNAi of BHC80 results in decreased LSD1 occupancy at its target genes. Error bars in **a** and **f** represent s.e.m. calculated from three independent experiments.

and BHC80, or facilitate cross-talk among modifications at different residues on histone tails^{9,28,29}. Together, our findings indicate that each and every subunit of the LSD1 complex has a unique role in coordinating and setting up a chromatin environment that is important for repression.

In sum, we have identified a PHD finger with a new histone tail-binding specificity (H3K4me0), and provided structural insights into the specific recognition and functional importance of unmethylated lysine. We speculate the existence of more such binding modules in the human proteome that are dedicated to recognizing the unmodified state of amino-acid residues on histone tails that are otherwise modified by various post-translational modification events. We anticipate that the identification of these modules and insights into their functions will shed significant new light on dynamic chromatin regulation.

METHODS SUMMARY

BHC80 (BC015714)-derived recombinant proteins were purified from bacteria with either 6×His or GST tags. The LSD1 complex was purified from a stable HeLa cell line with Flag-HA-LSD1 expression⁴. We carried out *in vitro* binding

assays using purified recombinant BHC80 proteins or LSD1 complex with a panel of biotinylated histone peptides with specific modifications at indicated lysine residues. We used tranylcypromine in the LSD1 complex binding assays to inhibit its demethylase activity. The bound fractions were visualized by either Coomassie blue staining or western blotting after immobilization by streptavidin beads. shRNA vectors were made as described³⁰ and cotransfected with the puromycin resistance gene into HeLa cells. Chromatin samples and RNA samples were prepared from drug-selected cells. The semi-quantitative ChIP assay and PCR with reverse transcriptase were done by adding ³²P-dCTP during PCR amplification and analysed by phosphor-image quantification. PCR reactions were optimized within the linear range. ChIP control oligonucleotides were designed to amplify the intron region of the RNA *PolIII* gene, which in principle is not affected by either LSD1 or BHC80 knockdown. For crystallography and ITC, the BHC80 PHD finger was expressed as a 6×His-SUMO fusion, and cleaved, leaving HisMet fused to the recombinant protein. The structure of the BHC80 PHD domain in complex with histone peptide was solved by three-wavelength Zn anomalous diffraction data (Supplementary Table 1). ITC was performed on a MicroCal VP-ITC by injecting synthetic H3 peptide (residues 1–10, K4me0, 1 or 2) into BHC80 at various concentrations.

Full Methods and any associated references are available in the online version of the paper at www.nature.com/nature.

Received 8 May; accepted 20 June 2007.

- Shi, Y. *et al.* Histone demethylation mediated by the nuclear amine oxidase homolog LSD1. *Cell* **119**, 941–953 (2004).
- Hakimi, M. A. *et al.* A core-BRAF35 complex containing histone deacetylase mediates repression of neuronal-specific genes. *Proc. Natl Acad. Sci. USA* **99**, 7420–7425 (2002).
- Lee, M. G., Wynder, C., Cooch, N. & Shiekhattar, R. An essential role for CoREST in nucleosomal histone 3 lysine 4 demethylation. *Nature* **437**, 432–435 (2005).
- Shi, Y. J. *et al.* Regulation of LSD1 histone demethylase activity by its associated factors. *Mol. Cell* **19**, 857–864 (2005).
- Shi, X. *et al.* ING2 PHD domain links histone H3 lysine 4 methylation to active gene repression. *Nature* **442**, 96–99 (2006).
- Wysocka, J. *et al.* A PHD finger of NURF couples histone H3 lysine 4 trimethylation with chromatin remodelling. *Nature* **442**, 86–90 (2006).
- Strahl, B. D. & Allis, C. D. The language of covalent histone modifications. *Nature* **403**, 41–45 (2000).
- Shi, X. *et al.* Proteome-wide analysis in *Saccharomyces cerevisiae* identifies several PHD fingers as novel direct and selective binding modules of histone H3 methylated at either lysine 4 or lysine 36. *J. Biol. Chem.* **282**, 2450–2455 (2007).
- Iwase, S. *et al.* The X-linked mental retardation gene *SMCX/JARID1C* defines a family of histone H3 lysine 4 demethylases. *Cell* **128**, 1077–1088 (2007).
- Jacobs, S. A. & Khorasanizadeh, S. Structure of HP1 chromodomain bound to a lysine 9-methylated histone H3 tail. *Science* **295**, 2080–2083 (2002).
- Nielsen, P. R. *et al.* Structure of the HP1 chromodomain bound to histone H3 methylated at lysine 9. *Nature* **416**, 103–107 (2002).
- Fischle, W. *et al.* Molecular basis for the discrimination of repressive methyl-lysine marks in histone H3 by Polycomb and HP1 chromodomains. *Genes Dev.* **17**, 1870–1881 (2003).
- Min, J., Zhang, Y. & Xu, R. M. Structural basis for specific binding of Polycomb chromodomain to histone H3 methylated at Lys 27. *Genes Dev.* **17**, 1823–1828 (2003).
- Pena, P. V. *et al.* Molecular mechanism of histone H3K4me3 recognition by plant homeodomain of ING2. *Nature* **442**, 100–103 (2006).
- Li, H. *et al.* Molecular basis for site-specific read-out of histone H3K4me3 by the BPTF PHD finger of NURF. *Nature* **442**, 91–95 (2006).
- Flanagan, J. F. *et al.* Double chromodomains cooperate to recognize the methylated histone H3 tail. *Nature* **438**, 1181–1185 (2005).
- Sims, R. J. III *et al.* Human but not yeast CHD1 binds directly and selectively to histone H3 methylated at lysine 4 via its tandem chromodomains. *J. Biol. Chem.* **280**, 41789–41792 (2005).
- Kwan, A. H. *et al.* Engineering a protein scaffold from a PHD finger. *Structure* **11**, 803–813 (2003).
- Bourc'his, D. & Bestor, T. H. Meiotic catastrophe and retrotransposon reactivation in male germ cells lacking Dnmt3L. *Nature* **431**, 96–99 (2004).
- Bourc'his, D., Xu, G. L., Lin, C. S., Bollman, B. & Bestor, T. H. Dnmt3L and the establishment of maternal genomic imprints. *Science* **294**, 2536–2539 (2001).
- Hata, K., Okano, M., Lei, H. & Li, E. Dnmt3L cooperates with the Dnmt3 family of de novo DNA methyltransferases to establish maternal imprints in mice. *Development* **129**, 1983–1993 (2002).
- Ooi, S. K. T. *et al.* DNMT3L connects unmethylated lysine 4 of histone H3 to de novo methylation of DNA. *Nature* doi:10.1038/nature05987 (this issue).

23. Garcia-Bassets, I. *et al.* Histone methylation-dependent mechanisms impose ligand dependency for gene activation by nuclear receptors. *Cell* **128**, 505–518 (2007).
 24. Iwase, S. *et al.* Characterization of BHC80 in BRAF-HDAC complex, involved in neuron-specific gene repression. *Biochem. Biophys. Res. Commun.* **322**, 601–608 (2004).
 25. Lachner, M., O'Carroll, D., Rea, S., Mechtler, K. & Jenuwein, T. Methylation of histone H3 lysine 9 creates a binding site for HP1 proteins. *Nature* **410**, 116–120 (2001).
 26. Bannister, A. J. *et al.* Selective recognition of methylated lysine 9 on histone H3 by the HP1 chromo domain. *Nature* **410**, 120–124 (2001).
 27. Nakayama, J.-I., Rice, J. C., Strahl, B. D., Allis, C. D. & Grewal, S. I. S. Role of histone H3 lysine 9 methylation in epigenetic control of heterochromatin assembly. *Science* **292**, 110–113 (2001).
 28. Huang, Y., Fang, J., Bedford, M. T., Zhang, Y. & Xu, R. M. Recognition of histone H3 lysine-4 methylation by the double tudor domain of JMJD2A. *Science* **312**, 748–751 (2006).
 29. Shi, Y. & Whetstone, J. R. Dynamic regulation of histone lysine methylation by demethylases. *Mol. Cell* **25**, 1–14 (2007).
 30. Sui, G. & Shi, Y. Gene silencing by a DNA vector-based RNAi technology. *Methods Mol. Biol.* **309**, 205–218 (2005).
- Supplementary Information** is linked to the online version of the paper at www.nature.com/nature.
- Acknowledgements** We thank S. Iwase and T. Baba for the gift of BHC80 antibody and Yujia Shi for discussion. This work was supported by grants from the NIH to X.C. and Y.S..
- Author Information** The X-ray structure of the BHC80 PHD domain in complex with the H3 tail peptide has been deposited to PDB as 2PUY. Reprints and permissions information is available at www.nature.com/reprints. The authors declare no competing financial interests. Correspondence and requests for materials should be addressed to Y.S. (yshi@hms.harvard.edu) and X.C. (xcheng@emory.edu).

METHODS

In vitro binding assays. Histone peptides (0.5 µg) were incubated with 2–5 µg purified recombinant BHC80 or GST-PHD finger or 50 ng LSD1 complex for 2 h at 4 °C in binding buffer (20 mM Tris-HCl 7.5, 150 mM NaCl, 0.1% Triton X-100). LSD1 complexes were purified by Flag-immunoprecipitation from a stable cell line with Flag-HA-LSD1 followed by 2× elution using 3Flag peptide (Sigma)⁴. After 1 h incubation, Streptavidin beads (Upstate 16-126) were washed four times and subjected to Coomassie blue staining. Tranylcyromine (Sigma P8511) was used in Fig. 1c at a concentration of 50 µM to inhibit the demethylation reaction.

RNAi and PCR with reverse transcriptase (RT-PCR). Two BHC80 shRNAs were designed to target the sequences (5'-GGAGGCTCTTAAAGTGGAAAT-3' and 5'-GGGCAGAGGCTGTCCAAAT-3'), and subcloned into a pBS-U6 vector. LSD1 shRNA was done as described¹. HeLa cells were cotransfected with shRNA and pBabe-puro vectors. After 12 h of transfection, cells were split and selected by 1.5 µg ml⁻¹ puromycin for 60 h. RNA extraction and RT-PCR were performed as described^{1,4}. The RT-PCR results in Fig. 4b, c were achieved by radioactive PCR.

Chromatin immunoprecipitation. LSD1 ChIP experiments were done using primers that have been described¹. Chromatin samples from 10⁷ cells were sonicated to 200–500 bp in ChIP lysis buffer (50 mM HEPES/KOH pH 7.5, 500 mM NaCl, 1 mM EDTA, 1% Triton X-100, 0.1% Na-deoxycholate and protease inhibitors), and incubated with 3 µg LSD1 antibody (ab-17221) or BHC80 antibody¹⁰ for each chromatin IP experiment. The recovered DNA was amplified in radioactive PCR by the indicated primers and quantified by phosphor image, and an unrelated genomic region was used as a PCR internal control for normalization.

Crystallography. The BHC80 PHD finger (residues 486–543) was expressed in BL21-Gold (DE3) *E. coli* cells (Stratagene) as a 6×His-Smt3 (yeast SUMO) fusion construct (generated in-house: see ref. 31) harboured in a modified pET28b vector (Novagen). Protein expression was induced with 0.4 mM isopropyl-β-D-thiogalactopyranoside for 3 h at 37 °C in Luria-Bertani broth supplemented with 50 µM ZnCl₂. The fusion protein was isolated on nickel-charged HiTrap Chelating HP (GE Healthcare). Following imidazole elution, the fusion was cleaved off by Ulp1 protease³¹, leaving two amino acids (HisMet) fused to the BHC80 PHD finger. The protein was further purified by HiTrap-Q and Superdex-75 (GE Healthcare). For co-crystallization, the PHD finger (final concentration ~40 mg ml⁻¹ in 20 mM Tris, pH 7.2, 100 mM NaCl, 5 mM DTT, and 25 µM ZnCl₂) was mixed in a 1:1.5 ratio with an H3 peptide (residues 1–10, dissolved in the protein buffer and neutralized with NaOH). Clusters of

rod-shaped crystals were obtained using the sitting drop vapour-diffusion method at 16 °C, with mother liquor containing 100 mM sodium citrate, pH 5.6, 20% polyethylene glycol 4000, and 20% isopropanol. In follow-up screens, we obtained single rhombohedral crystals with the hanging-drop vapour diffusion method, in mother liquor containing MES 6.2–6.5, 5–10% polyethylene glycol 4000, and 20% isopropanol. Both crystal forms diffract in the C2 space group with similar cell dimensions, but the latter were used to determine the structure. Crystals were cryoprotected by soaking in mother liquor supplemented with 40% glycerol. To prevent the evaporation of isopropanol, drops containing crystals were submerged in paraffin oil during handling.

All data were collected at the SER-CAT 22-ID beamline at the Advanced Light Source at Argonne National Laboratory on a MAR300 CCD detector. Zinc anomalous diffraction data were collected from two crystals and processed using HKL2000. SOLVE³² found four zinc sites. We used SOLOMON solvent flipping³³ for density modification, which gave a clear solvent boundary and traceable density. Model building with O³⁴ and refinement with CNS³⁵ continued by using a 1.43-Å data set (from a third crystal).

Isothermal titration calorimetry. A SUMO-tagged fusion of the BHC80 PHD was exchanged into 25 mM Tris-HCl buffer, 50 mM NaCl, 2 mM β-mercaptoethanol (pH 7.2) by gel-filtration chromatography. Extensively lyophilized H3 1–10 peptides were dissolved in the same buffer. ITC measurements were carried out from 100–500 µM protein concentration, with 3–7 mM peptide concentration, on a MicroCal VP-ITC instrument at 25 °C. For each peptide, a reference titration of peptide into SUMO alone was subtracted from experimental data to control for heat of dilution and non-specific binding. Binding constants were calculated by fitting the data using the ITC data analysis module of Origin 7.0 (OriginLab Corporation).

31. Malakhov, M. P. *et al.* SUMO fusions and SUMO-specific protease for efficient expression and purification of proteins. *J. Struct. Funct. Genomics* **5**, 75–86 (2004).
32. Terwilliger, T. C. & Berendzen, J. Automated MAD and MIR structure solution. *Acta Crystallogr. D Biol. Crystallogr.* **55**, 849–861 (1999).
33. Abrahams, J. P. & Leslie, A. G. Methods used in the structure determination of bovine mitochondrial F₁ ATPase. *Acta Crystallogr. D Biol. Crystallogr.* **52**, 30–42 (1996).
34. Jones, T. A. *et al.* Improved methods for building protein models in electron density maps and the location of errors in these models. *Acta Crystallogr. A* **47**, 110–119 (1991).
35. Brunger, A. T. *et al.* Crystallography & NMR system: a new software suite for macromolecular structure determination. *Acta Crystallogr. D Biol. Crystallogr.* **54**, 905–921 (1998).

naturejobs

**JOBS OF
THE WEEK**

For scientists, much like for everyone else, the course of true love rarely runs smooth. But after we discussed the hurdles faced by career-conscious researchers as they pursue romantic relationships (see *Nature* **446**, 463; 2007), we received a flood of letters underlining just how hard it is to mix love and the lab. Fortunately, not all the stories were of love lost. One note described a marriage that has lasted despite each person's professional ambitions. It took ten years for the pair to take a chance on love — they worried that a relationship combined with their careers would make things too complicated. Once they got married, things got very complicated. Far-flung job opportunities meant living apart and left them making frequent flights to meet up — while watching their bank accounts rapidly empty.

In a search for data on lab relationships, another reader conducted an informal survey of 52 scientists. She found that 14 were married to other scientists based in the same lab or others, nearly as many were single, about half as many were in relationships with other scientists, and a few were divorced.

Other stories showed how intrusive lab life can be. One boss insisted that the best science takes place between 5 p.m. and midnight — even while he lamented his own fractured family life. Another told his graduate students that travel and love lives are not conducive to being a successful scientist.

One reader offered his secrets to success. He and his wife, PhD candidates in applied physics and mechanical engineering, respectively, have a one-year-old child. He attributes their success to working under fixed-term contracts — which helps them plan ahead — mutual personal and career support, and remembering to count one's blessings when work and family life seem overwhelming.

Career-related obstacles to relationships aren't unique to science, of course. But scientists would do well to recognize that the search for love, especially among career-driven professionals, can be every bit as complicated as the secrets of nature they are attempting to unravel.

Gene Russo, acting editor of *Naturejobs*

CONTACTS

Acting Editor: Gene Russo

European Head Office, London

The Macmillan Building,
4 Crinan Street,
London N1 9XW, UK
Tel: +44 (0) 20 7843 4961
Fax: +44 (0) 20 7843 4996
e-mail: naturejobs@nature.com

European Sales Manager:

Andy Douglas (4975)
e-mail: a.douglas@nature.com
**Business Development
Manager:**
Amelie Pequignot (4974)
e-mail: a.pequignot@nature.com

Natureevents:

Claudia Paulsen Young
(+44 (0) 20 7014 4015)
e-mail: c.paulsenyoung@nature.com

France/Switzerland/Belgium:

Muriel Lestringuez (4994)

Southwest UK/RoW:

Nils Moeller (4953)

Scandinavia/Spain/Portugal/Italy:

Evelina Rubio-Hakansson (4973)

Northeast UK/Ireland:

Matthew Ward (+44 (0) 20 7014 4059)

North Germany/The Netherlands:

Reya Silao (4970)

South Germany/Austria:

Hildi Rowland (+44 (0) 20 7014 4084)

Advertising Production Manager:

Stephen Russell
To send materials use London
address above.
Tel: +44 (0) 20 7843 4816
Fax: +44 (0) 20 7843 4996
e-mail: naturejobs@nature.com
Naturejobs web development:
Tom Hancock

Naturejobs online production:

Jasmine Myer
US Head Office, New York
75 Varick Street, 9th Floor,
New York, NY 10013-1917
Tel: +1 800 989 7718
Fax: +1 800 989 7103
e-mail: naturejobs@natureny.com

US Sales Manager:

Peter Bless

Japan Head Office, Tokyo

Chiyoda Building,
2-37 Ichigayatamachi,
Shinjuku-ku, Tokyo 162-0843
Tel: +81 3 3267 8751
Fax: +81 3 3267 8746

Asia-Pacific Sales Manager:

Ayako Watanabe
Tel: +81-3-3267-8765
e-mail: a.watanabe@natureasia.com

What I did on my holidays

Travel broadens the mind.

Ian Stewart

At first I was disappointed when Dad said we weren't going to Blackpool this year. Yes, I know — like Mum told him — it's crowded and noisy and the entertainment's a bit naff, but there's a lot for the kids (that's me and Treec), and we've been there for the past ten years so we know it and we feel comfortable.

"We ought to be more adventurous," Dad said.

"The Wilkinsons have been to Majorca," said Mum.

"A bit more adventurous than that," Dad said.

"Like what?" I butted in. I'm Gemstone-Sally Worthington, aged twelve, and this is my blog.

"Eatyworld," Dad said. Well, it's really 'E-T World', which is the bloids' name for Gliese-581c, but everyone pronounces it that way.

"We can't afford Eatyworld," Mum said.

"Special introductory deal," Dad said. "They've built a new themeplex beside that big lake where the shark-things live."

"Selachinoids," said Treecreeper-Darren, my step-half-brother. Treec does that kind of thing in his avatar classes. He's a pain.

"It's the wormgate tickets we can't afford," Mum objected, "not the entry to the themeplex. You know how much extraterrestrial costs! Why, even the Yeghiazarians decided against it." Pagoda-Sue Yeghiazarian is almost my friend, she's eleven and three quarters.

"Not if we go via Hanoi," Dad said. "Speedijump have opened up a new budget wormgate. It costs less than the local gate to Blackpool." Mum gave him that quizical look of hers. "Of course there's the return trip to Hanoi as well, but we still save a lot."

So it was decided. Mum started listing the things we ought to pack, I downloaded a blogplate and uploaded the resultant blog so all my friends would know we were going, especially Pagoda-Sue Yeghiazarian, and Treec found some really gross virts about aliens that we both watched until Mum found out and banned him from the site.

By the time we set off we were really looking forward to Eatyworld. It's got a gigantomorph reserve, and a world-

girdling forest with millions of pandamoniums. Apparently the Eaties themselves are a bit weird, but they're allowed to be because they live there. I can't tell you how excited we all were!

Well, what Speedijump doesn't tell you, Mum complained at length on our arrival in Hanoi, is that actually their gate to Eatyworld is on the outskirts of Louangphrabang. So there's a train ride (yes, a genuine old-fashioned train — there were people riding on



the roof but we went first class, which meant we had seats), which costs extra. As does the food, the drink, the ticket for the toilet queue, border tax from 'Nam into Laos, baggage surcharge and carbon debit.

Too late, Treec discovered that there used to be a virtsite warning potential customers, but it was taken down by a bot battalion. Still, we were going to Eatyworld! A little extra expense and discomfort would be a small price to pay, Dad said.

The actual wormgate transit was over before we'd realized. You join a queue shuffling down a long corridor, and just after the fifth security check there's a red line on the floor and a sign that says 'Welcome to Gliese-581c, please mind the gravitational discontinuity, this courtesy holo sponsored by Lonely Star Insurance'.

The hotel was pretty good. The lake was frozen at this time of year, and the shark-things were hibernating. But the room did have a holovirt projector exactly like the one we've got in Finchley. So Treec and I watched holos of selachinoid packs, showing what we would have seen if we'd come during high season — a two-week period when the lake isn't covered in ice. Of course the special offer isn't available then, Dad said.

Most of the time we stayed in the themeplex. You don't actually see any Eaties, because they're not like real aliens with ten legs and six eyes and either scary or cuddly or just sort of grey versions of us. They're difficult to describe — a bit like colonies of vertical slugs glued together — and they're slimy and they smell bad. But we smell even worse to them, so they stay well away from the tourist compound. The themeplex has people in alien suits to show you where the rides are, anyway, so you get the genuine extraterrestrial experience.

We did visit the gigantomorph reserve, but new health and safety rules meant that we had to stay at least two kilometres away from the creatures. Apparently some kid had jumped off the hovertrax and a gigantomorph had sat on him and licked up the mess. The kid was insured but the gigantomorph wasn't, and it died from blood poisoning. Dad bought some binoculars so we could see enough of the beasts to appreciate how impressive they would have been close up.

The world-girdling forest, it turned out, had been opened up to sustainable logging, and only a few patches of the former Planetary Parks were still standing. But that wasn't quite the same, especially as the remaining pandamoniums had all died from a virus brought in by a tourist from Pittsburgh. So we mostly stayed in the themeplex.

The trip back was a breeze until we got to Louangphrabang, only to find that the railway to Hanoi was closed because terrorists had blown up a bridge. So we had to go standby via Kamchatka and Tierra del Fuego, while our bags went to Tokyo and then disappeared. How can you lose four bags in an enclosed corridor? I was upset because I'd packed my souvenirs in the checked baggage, but Mum said they were all made in Taiwan and transported to Eatyworld anyway. So she'll replace the set of plastic gigantomorphs and we'll forget the other stuff.

Treec and I want to go back to Eatyworld next year. But Mum and Dad say we're going to Blackpool.

Ian Stewart is co-author of *Wheeler's, Heaven and the Science of Discworld* trilogy. When not writing books, he does serious mathematics at the University of Warwick, UK.

JACEY